UNIVERSITÀ
DEGLI STUDI
FIRENZE

Dottorato di ricerca in Fisica ed Astronomia

CICLO XXXIII

COORDINATORE: Prof. Raffaello D'Alessandro

Reaction mechanisms and particle correlations in light-ion reactions at Fermi energies

Settore Scientifico Disciplinare FIS/04 Fisica Nucleare e Subnucleare

Tutori

Dott. Giovanni Casini

Prof. Andrea Stefanini

Dottorando

Dott. Catalin Frosin

Coordinatore

Prof. Raffaello D'Alessandro

Anni 2017-2020

TABLE OF CONTENTS

NOMENCLATURE

Acronyms / Abbreviations

ADC Analog to Digital Converter

b_{gr} grazing impact parameter

BF Heavy Fragments (Z>5)

CM Center of Mass system

CN Compound Nucleus

DI Direct Reaction

DIC Deep Inelastic Collisions

FAZIA **F**orward-angle **A** and **Z** **I**dentification **A**rray

IED Incomplete Energy Deposition

IMF Intermediate Mass Fragments (Z=3, 4 and 5)

LCP Light Charged Particles (Z=1 and 2)

LO Light Output

NN Nucleon-Nucleon collisions

PSA Pulse Shape Analysis

QP Quasi-Projectile

QT Quasi-Target

INTRODUCTION

In nuclear reactions with heavy ions it is interesting to observe the time evolution of collisions from a highly out of equilibrium situation (two colliding nuclei in their ground state) towards a possible situation where one or more equilibrated pieces of nuclear matter with high excitation energy and angular momentum are formed. The stronger the nuclear excitation the larger becomes the number of quantum mechanical states which can be explored and consequently more nuclear properties far from the ground state can be studied. In the Fermi energy regime (20-100 MeV/u) a wide range of phenomena take place, ruled by the competition of the nuclear mean field contribution and by the nucleon-nucleon collisions; their respective weights in first approximation depend on the initial bombarding energy. Thus, the associated phenomenology is extremely rich when exploring the impact parameter range from peripheral towards more central reactions. In particular, the peripheral and semi-peripheral collisions mainly manifest in the exit channel a binary nature, with two heavy fragments (called QP, for "Quasi-Projectile" and QT for "Quasi-Target", see chap. 1). On the other hand, for central collisions, the formation of a short-living single source is more probable. This general picture of the Fermi domain is fairly understood and was deeply studied for the medium-heavy mass region where the transition between reaction mechanism are well delineated. However, understanding the scaling of the reaction mechanism moving towards lighter systems (A_{tot}<40) is less obvious and experimental data in this region are scarce or relatively dated. The reaction phase-space is more limited and different reactions mechanisms are intertwined over the impact parameter range. Moreover, finite size fluctuations and structure effects can have more influence on the outcome of light-ion collisions than for heavier systems.

The present PhD work is focused on the study of the reaction mechanisms in light-ion reactions and aims at presenting some new detailed data in this field. In particular we wanted to study the decay of nuclei produced by means of different mechanisms, i.e. from fusion to inelastic collisions at Fermi energies. In this work, we will present the results for the ^{32}S,^{20}Ne+^{12}C reactions at 25 and 50 AMeV beam energies, investigated in the frame of the

FAZIA collaboration program at LNS laboratories. The experiment, referred to as FAZIACor, employed four FAZIA blocks and is one of the first measurements performed with the FAZIA array. In this reaction context and energy domain, the FAZIA multi-telescope (Si-Si-CsI) array represents the "state of art" from the point of view of the isotopic identification of nuclear fragments, its performances competing for ions up to Z=25 with those of a mass spectrometers (see Chap. 2 and 3). The apparatus is the result of a long R&D phase which particularly optimized the functioning of silicon detectors in terms of identification capabilities, reaching isotopic identification up to Z=25 with ΔE-E Si-Si telescopes. A part of this Thesis (see Chap.4) reports on one of the latest study on the detectors performances investigated by the collaboration, namely the response of the CsI crystals to energetic light particles (protons). I was actively involved in both the experiment preparation and data analysis on this subject, thus representing an important part of my PhD grant.

A second specific aim of this Thesis is the use of particle-particle correlations as a tool to reconstruct unbound states of excited fragments formed during the collisions and decaying via particle emission. This analysis is important for the FAZIA collaboration because it is a pioneering analysis performed with our three-layer telescopes and represents a first attempt to reconstruct part of the decay chains. Whilst the design characteristics are not fully optimized for this technique, the good angular and energy resolution allows to still obtain promising results as we will see in chapter 6. A third objective of this work is the comparison of the measured findings, both general features and some specific details, with theoretical models describing the production and decay of the fragments along the nuclear interactions. This comprehensive comparison has been carried on using combinations of two type of models, one describing the dynamical phase and the other the following decay. In this respect it must be pointed out the recent robust expertise gained by our group in handling these codes as it appears from our recent publications. Indeed, this expertise made it possible to mix different approaches and compare the final distributions with the experimental ones, so better evidencing the successes or the limits of the various model ingredients or approaches. More precisely, for the dynamical part two models have been considered: the microscopic transport model AMD and the more phenomenological one HIPSE. For the statistical part we use both SIMON and HFl (see chapter 5 for the model details). As said, the use of such simulations resulted to be quite useful to guide the data analysis and to better understand the nuclear dynamics of (light-) heavy ion reactions at Fermi energies, therefore we regarded as important to keep this approach also in this work.

This thesis is organized as follows. In chapter 1 we introduce the physics case presenting a survey on heavy ion collisions in the Fermi energy domain with particular emphasis on the mechanisms relevant to light ions collision. Chapter 2 contains a complete description

of the FAZIA multi-telescope array highlighting the main features that allowed to perform these experiments. Chapter 3 is dedicated to the description of the FAZIACor data reduction with a detailed description of the identification and calibration processes. Then, before discussing the results of the analysis, the mentioned specific study on the CsI(Tl) response to energetic protons (up to 200 MeV) is presented in chapter 4. In particular, the light output and detection efficiency are evaluated for the FAZIA scintillators when bombarded with these particles. The results obtained here, although not directly used in the physics analysis, are important for the collaboration in view of the new experiments scheduled for FAZIA at GANIL. In chapter 5 we proceed with the description of the theoretical models used in this work and a first comparison with the experimental data. Then, in chapter 6, the core of the FAZIACor analysis is reported, starting from the event selections, passing to the general reaction characteristics and focusing to more specific results. The conclusions are then summarized at the end of this thesis.

CHAPTER 1

PHYSICS CASE

An important concept in nuclear reactions is thermalization. It corresponds to the property of an excited system of reaching chemical and thermal equilibrium just after the nuclear reaction. In this way one can define a temperature of this equilibrated system and to consider its following decay channels from a statistical point of view. The Fermi energy domain of nuclear reactions, typically assumed between 20 and 100 MeV/u bombarding energies, is the transition domain from low to relativistic energies. In this region the energy relaxation and equilibration is characterized by a strong competition between one-body and two-body processes which govern the interaction of the nucleons. Two-body effects mainly dissipate energy through elastic nucleon–nucleon collisions. On the other hand, one-body processes dissipate energy through the interaction of individual nucleons with the nuclear mean field.

At these Fermi energies, whatever the dissipation mechanisms, the thermalization time is comparable to the interaction time. This latter is of the order of $\tau_{inter} = R/v_{rel}$ in which v_{rel} is the relative velocity between the two partners in the entrance channel and R is the sum of the radii of the two nuclei [1]. A typical value is $\tau_{inter} = 30$ fm/ c for a medium mass system at 50 MeV/u beam energy. From the fact that the thermalization time is comparable with the reaction time, one may draw the following conclusions:

- A sizable fraction of the available energy may be thermalized during the reaction process itself therefore creating as a consequence nuclei with large excitation energies.

- However, a sizable fraction of the available energy may not be thermalized during the collision, leading to a fast emission prior to thermalization. This emission is called in a wide sense pre-equilibrium emission [2, 3]. Event fluctuations will lead to various final situations, i.e. to a varying proportion of pre-equilibrium emission with respect to thermalization even for a fixed impact parameter ("b"). Therefore, even for a given b,

strong fluctuations are observed in the properties of the produced nuclei at the end of the reaction.

Since in this work we study the ^{32}S,^{20}Ne+^{12}C reactions at 25 and 50 AMeV beam energies (FAZIACor experiment), hereafter we will describe the main reaction mechanisms taking place at the Fermi energies focusing on the reactions between light nuclei which are the topic of this experimental Thesis. The general picture is first drawn then the specific features which we would address with our study are reported.

1.1 Reaction mechanisms in light heavy-ion collisions

In the considered beam energy range (20-50 AMeV), the energy dissipated in a nucleus cannot be used to excite intrinsic states of the nucleon. Thus, the initial energy is available to heat the matter. However, part of the energy is also used to excite collective degrees of freedom associated with deformation, rotation and/or compression. The proportion of energy stored in a given mode depends on the typical timescales for the excitation of the mode and also on the initial conditions, i.e. the entrance channel characteristics. The features of each

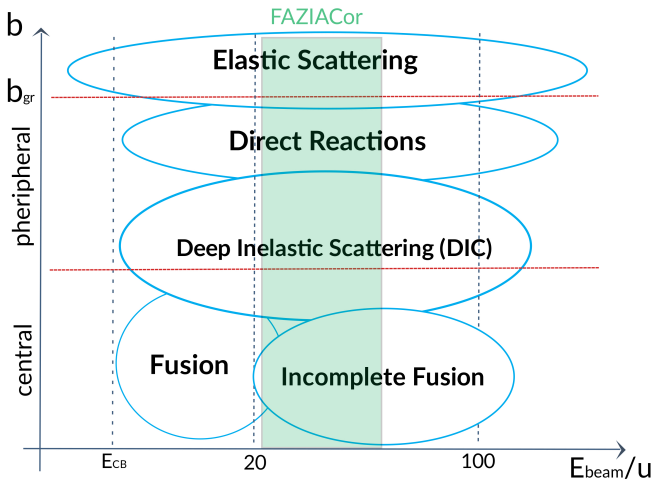

Fig. 1.1 Schematic qualitative representation (axis not in scale) of the reaction mechanisms as a function of the beam energy (E_{beam}) and impact parameter (b). E_{CB} indicates the Coulomb barrier energy. The regime explored by the FAZIACor experiment is also shown by the light green shadow.

kind of collision change with the bombarding energy E_{beam} and are different for different impact parameters (see fig.1.1). At low beam energies (below 20 MeV/u), the Pauli exclusion principle is effective in reducing the nucleon-nucleon collisions (NN). Consequently, the

interaction can be mainly described by means of a mean field approach (one-body). The interaction times, growing with reaction centrality, can be relatively long and the system has the time to evolve to complete thermal and chemical equilibrium. An extreme and quite important case is that of complete fusion. Here, in central collisions, a thermodynamical equilibrated source can be formed from the fusion of projectile and target nuclei, without memory of the entrance channel apart for energy-momentum conservation. This source is called a Compound Nucleus (CN) and is in general excited well above its ground state.

Going towards peripheral collisions, the Deep Inelastic Collisions (DIC) represents the dominant channel, especially for heavy systems; only a part of the available energy is transferred to the internal degrees of freedom, and the reaction products keep memory of their initial characteristics. The more peripheral the reaction, the less effective the energy dissipation. At the end of the interaction phase two heavy fragments are present, called Quasi-Projectile (QP) and Quasi-Target (QT). Finally, around the grazing impact parameter the kinematics of the two nuclei is only slightly perturbed with small energy and/or mass exchange in the case of direct reactions (transfer/pick-up of few nucleons).

As the beam energies increase (over 20 MeV/u), the NN collisions become more probable and "fast" emissions of nucleons or clusters can occur. These pre-equilibrium emissions affect the further development of the interaction. For example, the complete fusion tends to disappear because part of the initial momentum, charge and mass is removed before thermalization: indeed, the incomplete fusion channel sets in. Similarly, also the other reaction modes typical of more peripheral collisions are affected by the fast emissions (also referred to as dynamical emissions because of their origin clearly related to the reaction dynamics). Thus, the primary QP and QT after the interaction, do not retain the total mass and charge of the system. For light systems the direct reactions (DI) and DIC are naturally much less separated. We can rapidly pass from direct to fusion-like processes with the formation of only one main excited source.

In the exit channel, a strong evolution of the decay modes of hot nuclear matter is expected as one goes from very moderate excitation energy up to values close to or even larger than the total binding energy of the system ($E^*/A \sim$ 6-8 MeV/u), for which a complete system dissolution is expected (sometimes referred to as vaporization). The low-energy deexcitation includes evaporation of particles with the production of evaporation residues, fission and radiative giant resonances. Particle evaporation is associated with the chaotic thermal motion of the nucleons and the subsequent emission of light charged particles (Z=1, 2 also abbreviated as LCP), neutrons and light fragments. When the excitation energy decreases below the particle separation energy the de-excitation process goes on through gamma ray emission. The fission is a very general nuclear process which is favored in large-size systems

thanks to the stronger repulsive Coulomb field; for the systems here studied this is a negligible reaction channel. At higher energies one observes the rise of the multifragmentation process, where three or more IMF are produced, without heavy fragments in the exit channel. Then, as the energy continues to grow, the reaction will end up in the vaporization of the system into LCP constituents. For FAZIACor we focus our attention on both central and peripheral (or mid-peripheral) collisions. We will not directly study the direct o elastic region of fig.1.1. However being the phase-space more limited for light-ion reactions, they are expected to be included as a background, although the adopted trigger selection helps to reject them from the analysis as we will see later on in chapters 3, 5 and 6.

1.1.1 Peripheral and mid-central collisions

In peripheral and mid-central collisions, an excited quasi-projectile (QP) and an excited quasi-target (QT) are produced at the end of the collision. As a function of the initial excitation, the decay chain can be complex and/or long and the final products can be quite different from the original (primary) QP and QT nuclei. Conversely, for quasi-elastic collisions, the QP and QT residues closely resemble the initial projectile and target nuclei. The binary channel is generally accompanied by light particles and IMFs. In particular, for medium-heavy systems (A>70-80) a sizable contribution is observed at mid-rapidity (i.e. in the phase space between those of the QP and the QT). According to the many experimental observations [4, 5] and theoretical models [6, 7], this emission phase-space is compatible with the formation and decay of a low density region between the separating QP-QT also referred to as "neck" region. The neck zone is subjected to fast breakup due to the rise of "mechanical" instabilities caused by temperature and pressure effects. Emission of LCP and IMF, attributed to the decay of the neck and also pushed by the Coulomb repulsion, has indeed been observed. The remaining excited QP and QT further decay following the statistical weights of the open exit channels. The presence of a neck structure is strongly supported by many studies for heavy or medium mass systems. Instead, as expected, the formation of a neck-like structure in light systems has less experimental evidence though it is not excluded, especially with increasing beam energies; some dynamical polarized emission can occur also for the Ne+C and S+C reactions here investigated.

1.1.2 Competition between complete and incomplete fusion

We now come to the main features concerning the most central collisions. By "central" we mean those collisions which can lead ultimately to the formation of a main single system, in contrast to the reaction patterns depicted earlier, in which two or more sources emerge.

In general, central collisions correspond to the largest dissipated energies and the largest compression. At low incident energy, fusion reactions are easily selected by searching for the signatures of the compound nucleus. Since this CN is not exceedingly excited, its decay products can be easily recognized: these correspond either to an evaporation residue or to two fission fragments (efficiently produced for heavy enough nuclei). Both channels are accompanied by the emission of light particles. As said before, at high energies (FAZIACor

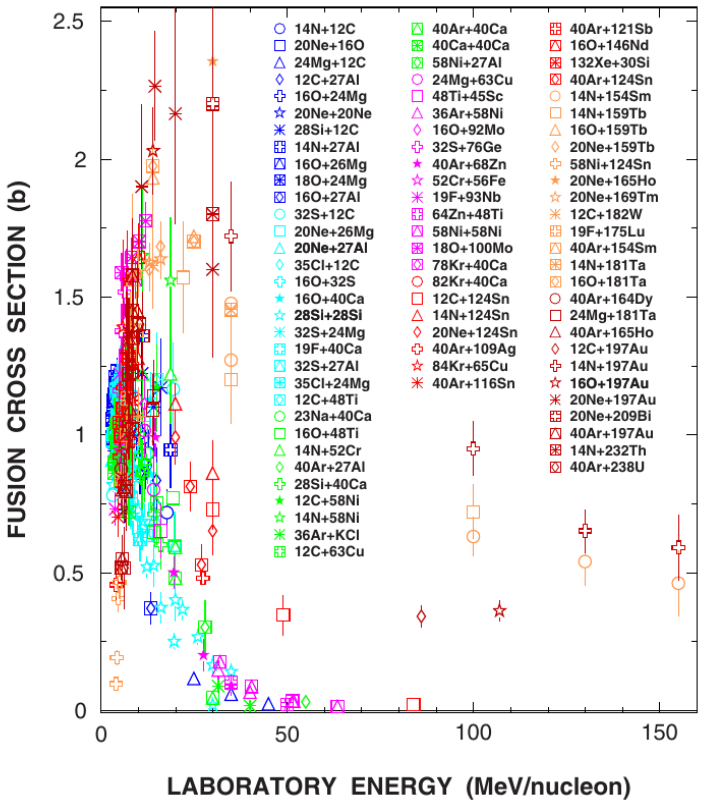

Fig. 1.2 Evolution of the fusion cross-section (sum of incomplete and complete) as a function of the incident energy for a variety of systems. Image taken from [8].

included) on average, fast emission and possible clusterization effects can occur and not all nucleons of the projectile and the target fuse during the interaction. Some of them may individually escape because of elastic NN collisions and also fast clusterization can occur with the (pre-equilibrium) emission of small fragments (typically Z=3,4). As a consequence also central reactions do not lead to the formation of a precise source with the total initial mass, charge and momentum of the system; instead we observe the formation of a distribution (for an event set) of single sources characterized by a reduced mass, charge and momentum with respect to the initial ones. This process is called incomplete fusion [9–11] and, together with the neck emissions for semi-peripheral collisions, represents a typical process at Fermi

energies as those here investigated. Different theoretical models have been devised to interpret this complex phenomenology and they can be related to two main ideas which were proposed starting from the studies on heavy systems at low-energy reactions. The first one suggests that fusion cross section is limited by the entrance channel effects [12, 13], while the second one attributes the limitation to compound nucleus properties [14, 15]. From the experimental point of view, a large body of data shows (see [8, 16, 17] and references therein) the fast decrease and even the disappearance of fusion as a function of the incident energy around E_{lab} =40 MeV/u as shown in fig.1.2. An energy limit of about 6.5 $\pm$ 1.0 MeV/nucleon (in CM) roughly corresponding to the maximum excitation energy which can be reached by a thermalized nucleus decaying by means of evaporation was extracted by Eudes et al. [8] from a review of many experiments over a broad range of beam energies and system mass values. Therefore, from these systematics we expect complete fusion to be a very rare process above 30-40 MeV/u of beam energy.

In the early works on incomplete fusion, the signals for this process were searched in the deviation from the full momentum transfer scenario. For example, in the work of Morgenstern et al. [9], the degree of momentum transfer was related to the mean ER velocity and they were able to extract the ratio of complete to fusion-like processes on the basis of few simple assumptions. For instance, assuming a Maxwellian velocity distribution of the ER's and an isotropic or 1/sin angular distribution, the corresponding transformation into the laboratory yields the following Lorentz-invariant cross section as a function of the velocity:

$$\frac{1}{v^2}\cdot\frac{d^2\sigma}{d\Omega dv} = N\cdot exp\left(-\frac{V_{CN}^2 sin^2\theta}{2s^2}\right)\cdot exp\left(\frac{(v-V_{CN}cos\theta)^2}{2s^2}\right) \tag{1.1}$$

From eq.1.1 it can be seen that the observed velocity spectrum should be a Gaussian centered at $V_{CN}\cdot cos\theta$ with θ the laboratory scattering angle, N a normalization constant, and s the standard deviation. The data can then be fitted by eq.1.1 with N and s as free parameters. The components of incomplete fusion are parametrized in an analogous way with V'_{CN} being the velocity of the reduced CN. In fig.1.3, this kind of analysis is shown for two asymmetric reactions at Fermi energies taken from [10]. As it can be seen, the shapes are well reproduced and the observed velocity centroids show clearly deviations from the expected compound-nucleus velocities (indicated in the figure by vertical bars sitting at zero). The observation of compound velocities smaller than the value expected for complete fusion, as found for ^{20}Ne+^{27}Al, is indicative of the presence of pre-equilibrium emission and incomplete fusion. One may chose to view the process in this case as a breakup of the projectile in the vicinity of the target nucleus, and a following fusion of one of the remaining pieces with the target. In the case of the ^{40}Ar+^{12}C system, instead, it was found that the average recoil velocities are

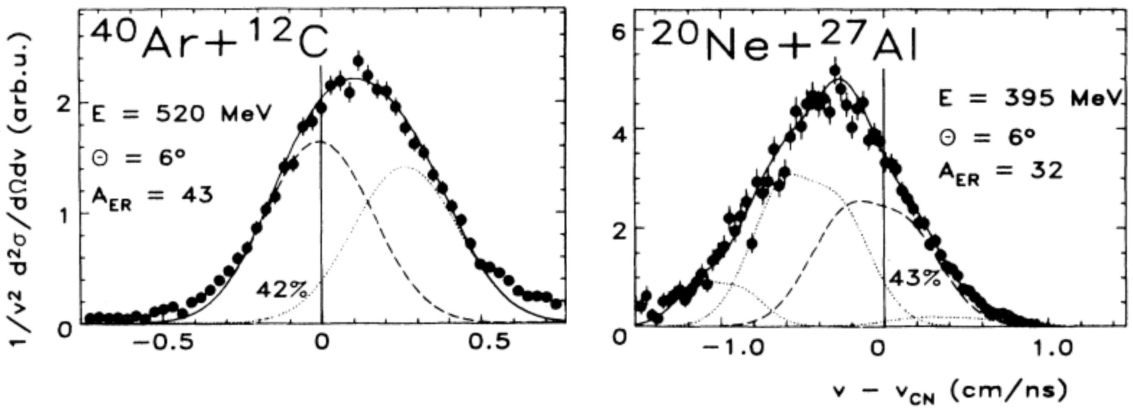

Fig. 1.3 Velocity spectra of evaporation residues (ER) indicated in each panel with A_{ER} at a specific laboratory angle for two asymmetric reactions. On the left the reverse kinematics ^{40}Ar+^{12}C at 520 beam energy while on the right the direct kinematics ^{20}Ne+^{27}Al at 395 beam energy are shown. The quoted numbers indicate the fraction of complete fusion (CF) obtained from a deconvolution fit. Figure taken and adapted from [10].

slightly higher. In the spirit of the incomplete-fusion picture such an observation could be an indication that the projectile is fusing with only a fragment of the target, i.e. in this case it is the light partner which preferentially "breaks up" and part of it is fusing with the incoming beam nucleus. However, it is not obvious how one might easily verify it since the process will not present a clear signature unlike the incomplete-fusion process involving projectile breakup which should be accompanied by a beam velocity light fragment.

A more recent study of incomplete and complete fusion for the ^{32}S+^{12}C (one of the FAZIACor systems) reaction at 20 AMeV beam energy was attempted by Pirrone et al. [16]. They tried to separate the different reaction components by means of a kinematical analysis of the fragment velocity spectra coupled to a fit deconvolution. The contributions found have been interpreted as originating from complete fusion, incomplete fusion, and direct reaction mechanisms showing for each evaporation residue the relative weight.

As can be seen from fig.1.2, a great deal of reactions were performed between 0-20 AMeV, including both heavy and light systems. What seems to be missing is the higher energies measurements, especially for light systems. In addition, there are scarce data on the persistence of nuclear structure effects (such as alpha-clusters in N=Z nuclei) at high energies. These effects play a role as clearly shown for the lower energy domain also by our collaboration [18–20] but their occurrence in the Fermi domain has not been clearly demonstrated. Adopting the parametrization from the systematics of ref.[8], we estimated

Table 1.1 Fusion (total and complete) extrapolation for the FAZIACor systems from the functional dependence of [8]. The values are normalized to the total reaction cross-section calculated with the Tripathi formula [21].

Reaction	25 AMeV		50 AMeV	
	$\sigma_f/\sigma_R(\%)$	$\sigma_{cf}/\sigma_R(\%)$	$\sigma_f/\sigma_R(\%)$	$\sigma_{cf}/\sigma_R(\%)$
^{20}Ne+^{12}C	9.8	2.3	1.1	0
^{32}S+^{12}C	12.7	6	2.7	0

the complete and incomplete cross section ratios for the FAZIACor reactions shown in table 1.1. One of the objective of the present work is to add some further pieces of information in this range of system size versus energy where our FAZIACor experiment well fits this context. Following the velocity deconvolution method previously described, the complete and incomplete components of fusion events have been estimated when possible using our data. Since at these relatively high energies and these small systems the various mechanisms largely overlap, it is rather hard to disentangle the contribution of fusion-like mechanisms from that of damped non-thermalized processes, thus we use the prediction of a transport model MonteCarlo (including clusterization as explained in chapter 5) to better constrain the velocity intervals of the different components and compare their spectra. This latter is necessary as the DIC and DI reactions may not by easily approximated with a Gaussian distribution as the fusion-like components. When possible, via an elastic cross section normalization, the absolute cross section for the CF and ICF components will be given.

1.1.3 Multifragmentation

The contributions of complete and of incomplete fusion are anyhow associated to the detection of a kind of evaporation residue, representing the biggest fragment, with possible coincident smaller fragments. When the energy available to the reaction increases, other more violent mechanisms can occur in particular for central collisions. These mechanisms results in the more or less complete disassembly of the system in short times without the sequence of two phases of excitation and decay decoupled in time. Processes such as multifragmentation and vaporization cannot be excluded in the reactions here studied but they do not represent our main focus due to the low cross section and the limited angular acceptance. Indeed, while for the detection of the main fragment the apparatus is relatively efficient also thanks to the reverse kinematic condition, for reactions producing many small nuclei and flying in a wider solid angle the coverage is not sufficient.

Nevertheless, it is useful in this introduction to present some features of this many-body channels because some trace of them can be present in our events when comparing the low and the high bombarding energy data. Multi-fragment decay modes are expected as the deposited energy reaches values close to the binding energy. In particular, fragmentation (i.e. the almost contemporary disassembly of hot nuclei into at least three fragments) becomes a competitive process both for central and semi-central collisions. This transition has been extensively studied for systems with medium-heavy mass [22, 23] and has been associated to nuclear phase transitions [24, 25], during the intense scientific debate demonstrated by the rich literature around the years 2000's. Experimentally, the indication of the change in the reaction modes is obtained by counting the events in which only two massive fragments are observed and events in which at least three fragments have been emitted. As an example, in figure 1.4, the yield of three-body (Y3, fragmentation) versus two-body (Y2, binary decay) mechanisms is shown as a function of excitation energy per nucleon ε^*. A clear evolution is observed with the 3-fragment channel reaching 10% of the 2-body one at around 3 MeV/u. From this point on, fragmentation starts to be a competitive process, although evaporation

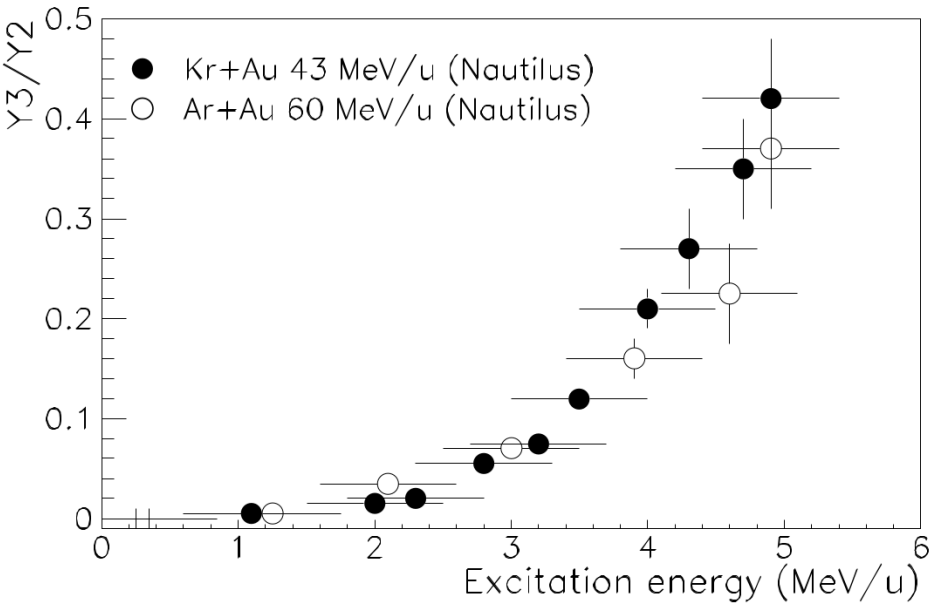

Fig. 1.4 Evolution of the competition between two-body (Y2) and three-body (Y3) decay as a function of ε^*. Image taken from [1, 25].

and/or fission are still present. Interestingly enough, the ratio Y3/Y2 displayed in figure 1.4 is independent of the entrance channel (i.e. both the system size and the bombarding energy) and thus largely of the mechanism that led to the production of the hot sources. This evidence

supported the hypothesis that multifragmentation production is essentially governed by the excitation energy and thus also that the fragment multiplicity is, to a large extent, dictated by the excitation energy deposited in the system, independently of the incident energy. Although multifragmentation becomes sizable at excitation energies around 3 MeV/nucleon, the maximum for IMF fragment production is found around 9 MeV/nucleon (see fig. 1.5), i.e. close to the binding energy of nuclei. At higher excitation energy, as a consequence of the disassembly of the systems in lighter particles (neutrons and Z=1, 2 isotopes), the fragment production reduces. Average time intervals between successive emissions can be

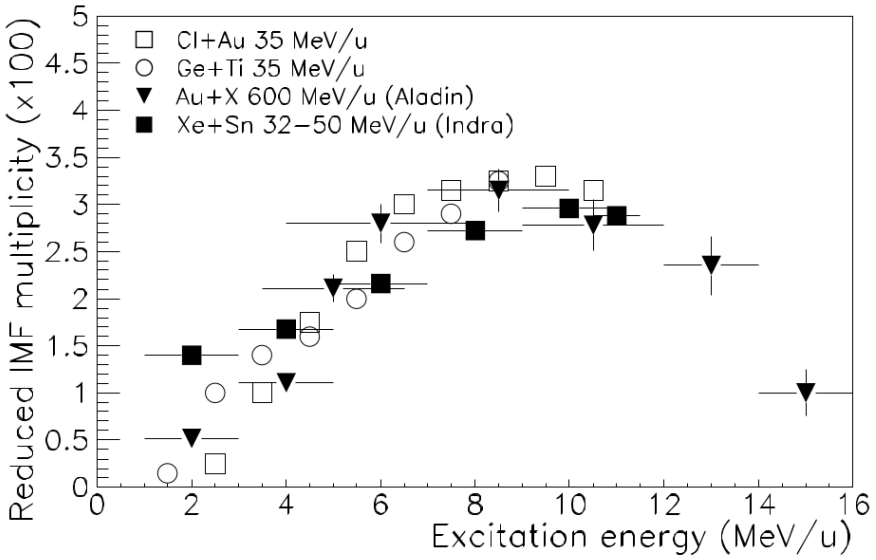

Fig. 1.5 Evolution of the average fragment multiplicity, normalized to the size of the multi-fragmenting system, as a function of the excitation energy per nucleon deposited into the system. Image taken from [1].

estimated by analyzing space-time correlations (explained in the following section) between fragments, taking advantage of proximity effects induced by Coulomb repulsion[26]. A strong decrease of measured times with the increase of excitation energy is observed up to around 5 MeV/nucleon with saturation that appears around 50-100 fm/c [27], reflecting the limit of sensitivity of the method. For such short times fragments can be considered as emitted quasi simultaneously and fragment emissions cannot be treated independently.

For light systems, at the energies of FAZIACor, the multifragmentation regime could be accessible because the energy deposited in the system is above the threshold for the onset of this process. The question is rather if the dissipation process can really lead to the formation of a heated nuclear matter around/over 3 AMeV. The works of [28, 29], have shown how

this scenario is indeed supported by data for the ^{24}Mg+^{12}C system investigated at 25, 35, and 45 MeV/nucleon beam energies. A study of such type has also been performed for the ^{16}O+^{12}C reaction at 32.5 AMeV by Scarpaci et al. [17]. The authors investigated, for selected measured residues, the event shape following methods typical of high-energy physics. Specifically, they studied the event sphericity of the Mg decay into the 5·He+2·H channel in central collisions. Based on the comparison with a statistical and multi-fragmentation decay model they concluded that the former was more compatible. Generally speaking the characteristics of many fragment events in (mainly) central collisions have been studied and interpreted for relatively heavy systems. The literature dealing with light systems is scarce. On the other hand, this scarcity also reflects the idea that for light nuclei various effects that can enhance the fragmentation channel are reduced. For example one might argue if reasonable picture of compression followed by expansion with spinoidal instabilities and then clusterization emerged for the multifragmentation of heavy ions is still valid also when the available nuclear charge and mass are small. Also, one can wonder whether the alpha or (in general) the cluster structure revealed by many light nuclei can influence the most dissipative collisions at high energies. For example, one can guess that the reaction channels are intensely related to the emission of alpha particles whose abundance prohibits the production of larger fragments. Moreover, there are indications that the multifragmentation threshold is higher with lower mass already from the Natowitz et al. [30] studies on the mass dependence of the caloric curve. The study of the multi-fragment events needs a rather large acceptance detector as demonstrated by our recent studies [18–20, 31, 32] at the lower energies in the fusion regime at Legnaro, with the Garfield-RCo array [33]. Here we cannot endeavor a specific investigation of the explosive events because, as said, we are employing the first 64 telescopes of the FAZIA array that are not enough. Although, since previous studies [17, 28, 29] suggest that indeed such high energy densities can be reached also in light systems, we will try to at least marginally consider this aspect in the current work. In this respect, the goal would be to give some limits for the occurrence of many-body events (resembling multifragmentation) as possible residuals from the classification of the main studied channels. In this direction it is useful to exploit the comparison among the four measured reactions, at two energies, and the guide offered by the models containing both dynamic and statistical features as we will see in the final chapters.

1.2 Particle correlations

The decay of excited nuclei by means of particle emission can be studied by trying to correlate the phase-space kinematical properties of the decay products. Indeed, one can reconstruct the

time evolution at "the n-1" step, with "n" being the detection time. The study of correlation functions has been used as a powerful tool to explore certain spectroscopic properties of unbound states of nuclei [34–36], such as spin [37] and branching ratios [32, 38] with respect to new decay channels and/or specific ones. In fact, unstable states of several loosely bound nuclear species produced during the dynamical evolution of a system can be identified and explored by detecting their particle decay products in coincidence. Correlations have also been shown to provide important quantitative information about space-time properties of emitting sources produced in different stages of the reaction dynamics [39–42].

In this section we will first provide a general introduction to the particle-particle correlation technique and then some of the applications of correlation techniques will be presented. In particular, a detailed description of the application to the reconstruction of the excited states is given as an introduction for what done in the FAZIACor analysis. From this point of view, an interesting challenge with particle-correlations is to study the evolution of the correlation patterns, like the possible change of population of excited states as a function of the initial system energy and size; this could help providing information on collision dynamics and characterizing prevailing dissipative regimes [40, 43]. We want to stress that, according to the originary aim of the Faziacor experiment, we here test the feasibility to access some resonance decay and to study its characteristics and branching ratios in order to signal possible in-medium effects. This means, in particular, to put into evidence if the decay of some excited fragments changes when the parent system is formed in a "standard" hot environment at ground state density or when it is produced in a diluted nuclear medium. This kind of analysis is surely challenging and here it is faced for the first time in the collaboration. In this context the present Thesis represents a pioneer study that can open to further investigations with new data, collected by our group in experiments using the full Fazia array coupled to the Indra multi-detector and thus featuring a much larger acceptance.

1.2.1 The correlation function

Intensity interferometry via particle correlations was first studied in astrophysics [44, 45]. This idea has later been generalized to correlations in nuclear physics involving various types of particles. The early example of correlations involved identical bosons and fermions. It has been applied to relativistic energy nuclear physics studying angular correlation of pions emitted in proton-antiproton annihilation processes at energies of 1 GeV [46]. At lower energies, proton-proton [47] have been widely used for studying the properties of the sources of particles emitted in heavy ion reactions. Subsequently, non-identical particle correlations such as d-alpha correlations [48] and correlations involving heavier fragments [49, 50] (up to Carbon) have also been studied.

Hereafter we introduce the notion of correlation function and briefly describe its interpretation following the Konin-Pratt formalism [47, 51] in the non-relativistic limit. For two particles with momenta $\vec{p}_1$, $\vec{p}_2$, total momentum $\vec{P} = \vec{p}_1 + \vec{p}_2$ and momentum of relative motion $\vec{q} = \mu(\ \vec{p}_1$ /m1 - $\vec{p}_2$/m2), the two-particles correlation function, 1 + R($\vec{q}$, $\vec{P}$), is defined experimentally as:

$$\sum Y_{12}(\vec{p}_1, \vec{p}_2) = C_{12}[1 + R(\vec{q}, \vec{P})] \cdot \sum Y_1(\vec{p}_1) \cdot Y_2(\vec{p}_2) \tag{1.2}$$

In this equation $Y_{12}(\vec{p}_1, \vec{p}_2)$ is the two-particles coincidence yield while $Y_1(\vec{p}_1)$ and $Y_2(\vec{p}_2)$ are the single-particle yields. The normalization constant C_{12} is commonly determined by the requirement R($\vec{q}$, $\vec{P}$) = 0 at large relative momentum values where the correlations due to final state interactions and quantum statistics can be neglected. The sums in eq.1.2 are performed over all detectors and particle energy combinations satisfying a specific gating condition. Experimental studies have focused on two types of observables: directionally gated and angle-averaged correlation functions. Directionally gated correlation functions are constructed by selecting particles pairs with specific conditions on the orientation between the relative momentum, $\vec{q}$, and the total momentum, $\vec{P}$. In many cases however, to obtain sufficient statistics one generally studies angle-averaged correlation functions by integrating over the relative angle between the vectors $\vec{q}$ and $\vec{P}$. The resulting correlation function therefore depends only on the magnitude of the relative momentum, q:

$$\sum Y_{12}(\vec{p}_1, \vec{p}_2) = C_{12}[1 + R(q)] \cdot \sum Y_1(\vec{p}_1) \cdot Y_2(\vec{p}_2) \tag{1.3}$$

where the product of the single yields, $Y_1(\vec{p}_1) \cdot Y_2(\vec{p}_2)$ in eqs.1.2 and 1.3, is normally approximated with the uncorrelated two-particles yields $Y_{12}^{uncor}(\vec{p}_1, \vec{p}_2)$ constructed via the so-called event-mixing technique [52, 53]. This technique consists in taking particle 1 and 2 from two different events to calculate $Y_{12}^{uncor}(\vec{p}_1, \vec{p}_2)$ and the the correlation function is given by:

$$1 + R(q) = C_{12} \cdot \frac{Y_{12}(\vec{p}_1, \vec{p}_2)}{Y_{12}^{uncor}(\vec{p}_1, \vec{p}_2)} \tag{1.4}$$

The validity of approximation $Y_{12}^{uncor}(\vec{p}_1, \vec{p}_2) = Y_1(\vec{p}_1) \cdot Y_2(\vec{p}_2)$ calculated with the event-mixing technique requires that the mixing is made using events of the same class (similar phase-space, impact parameter gate etc.). However, one needs to keep in mind that the evaluation of the denominator is difficult when leading with low multiplicity events because of the trivial correlations induced by conservation laws [52, 53].

Fig.1.6 shows an example [39] of angle-averaged proton-proton correlation function measured in ^{14}N + ^{197}Au collisions at E/A = 75 MeV, represented as a function of the relative

momentum q between the particle pairs. At small relative momentum strong deviations from unity are registered. In fact, if the two emitted particles are totally uncorrelated, the probability of detecting them in coincidence would be equal to the product of the probabilities of detecting the single yields, resulting in a flat correlation function, R(q) = 0, at all q values. Experimentally, it is easily observed that this is not the case. These deviations are due to quantum statistics and to the so-called final-state interactions (FSI) [47]. In the case of identical fermions (bosons), the relative wave function must respect anti-symmetrization (symmetrization) rules that induce measurable effects in the correlation function at small relative momenta. Furthermore, the coincident particles can interact with their mutual Coulomb and nuclear interaction. The Coulomb repulsion is responsible for the anti-correlation (yield depletion) at small q-values while the nuclear attractive force is responsible for the observed prominent peak.

Theoretically, the proton-proton correlation function is calculated by the so-called Koonin-Pratt equation [51]:

$$C(q) = 1 + R(q) = 1 + \int d\vec{r} S(\vec{r}) K(\vec{r}, \vec{q}) \tag{1.5}$$

where $S(\vec{r})$ is defined as the probability distribution for the emission of a pair of particles with relative distance *"r"* at the time when the second particle is emitted. It should be normalized to unity if all the emission components are included. The angle-averaged kernel, $K(\vec{r}, \vec{q})$, is obtained from the radial part of the antisymmetrized two-proton relative wave function as follows:

$$K(\vec{r}, \vec{q}) = |\Phi_q(r)|^2 - 1 \tag{1.6}$$

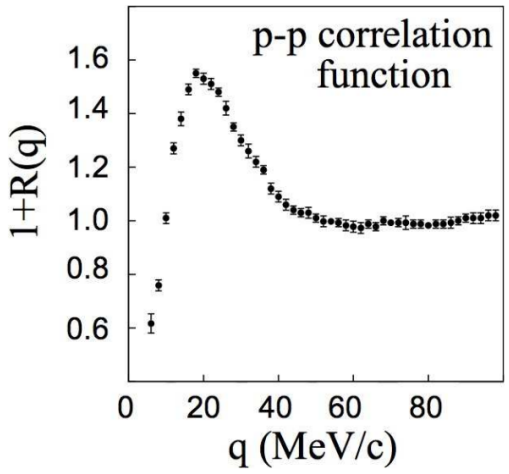

Fig. 1.6 Proton-proton correlation function measured in ^{14}N + ^{197}Au collisions at E/A = 75 MeV. Image taken from [39].

The kernel contains all the information about anti-symmetrization of the proton-proton wave function, due to their fermionic nature, the mutual Coulomb and nuclear final-state interactions (FSI). The goal of intensity interferometry consists of solving eq.1.5 from the measured correlation function and this corresponds to extract the unknown source function, $S(\vec{r})$. Different approaches have been proposed in literature. For example, single Gaussian functions $S(\vec{r}) \propto exp(r^2/2r_0^2)$ with unit normalization have been extensively used due to their simplicity. This function depends on only one parameter defined as size or radius, r_0 [54].

1.2.2 Nuclear structure and particle spectroscopy

In the context of this Thesis, particle correlations are a useful way to study the decay of unbound states produced during nuclear reactions. In this framework correlation techniques and invariant-mass spectroscopy have became a tool to explore spectroscopic properties such as spins, branching ratios and the existence of new states. A practical expression for the correlation function in terms of relative energy E_{rel} [55, 56] is:

$$1 + R(E_{rel}) = 1 + R_{Coul}(E_{rel}) + R_{Nucl}(E_{rel}) \tag{1.7}$$

where the Coulomb contribution can be expressed in an empirical way [35, 57] by:

$$1 + R_{Coul}(E_{rel}) = 1 - exp(-[E_{rel}/E_C]^{\alpha}) \tag{1.8}$$

and the nuclear part can be expressed within the Breit-Wigner formalism as:

$$R_{Nucl}(E_{rel}) = \frac{h^3}{4\pi V_{eff}(2S_1+1)(2S_2+1)} \cdot \frac{1}{\mu\sqrt{2\mu E_{rel}}} \cdot exp(-E_{rel}/T_{eff}) \cdot \frac{1}{\pi} \cdot \sum_i (2J_i+1) \frac{\Gamma_i/2}{(E_{rel}-E_i^*)^2 + \Gamma_i^2/4} \cdot (B.R.) \tag{1.9}$$

where S_1 and S_2 are the spins of the considered particles, μ is their reduced mass, V_{eff} is the effective emitting source volume, T_{eff} is the effective temperature, J_i , E_i, Γ_i are the spin, excitation energy, width of the level "i", B.R. is the branching ratio for the decay to the measured channel. V_{eff} , T_{eff} would represent volume and temperature of a physical source only in the idealized situation of a single decay step of a fully equilibrated source in the absence of any collective flow and experimental deformation. For example, collective energy components act in the direction of increasing V_f with respect to a physical volume, which leads to a suppression of high-lying resonances. Because of these effects, no physical meaning can be attributed to the V_{eff}, T_{eff} extracted values [55, 58].

Usually, a fitting procedure is performed on experimental data with the Coulomb background parameters E_C and α, the nuclear ones and the weight of different contributions of excited states as free parameters. In this way the weight of different excited levels of the source can be determined. An example of a rather complicated analysis attempted by

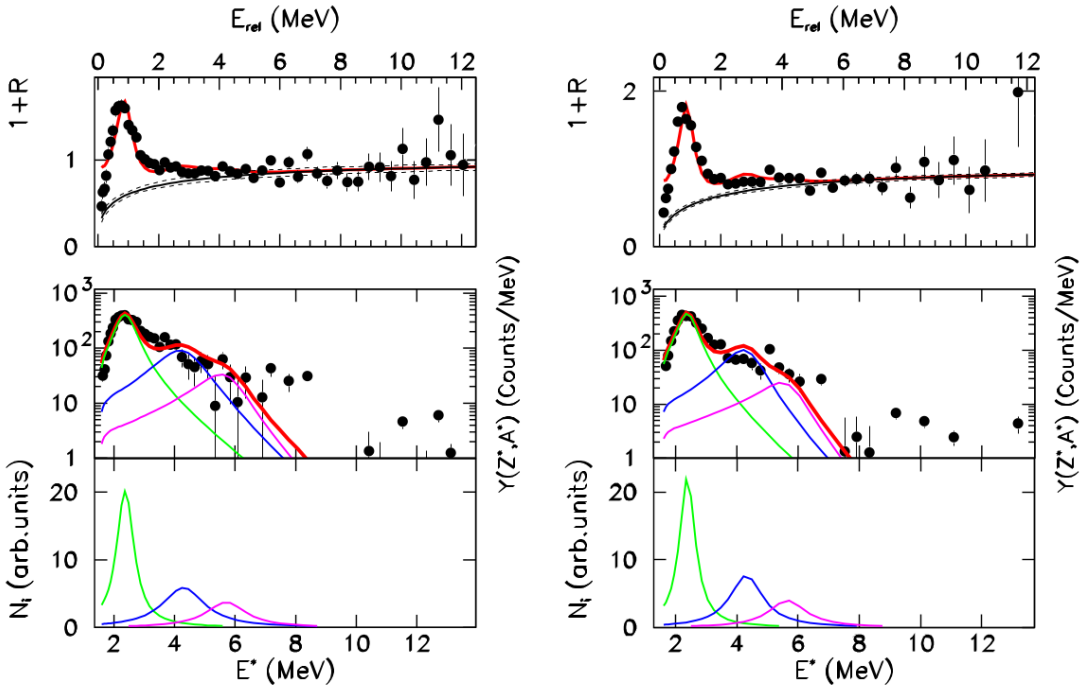

Fig. 1.7 d+α correlation functions obtained for peripheral (left) and central (right) ^{32}S + ^{58}Ni collisions at 14.5 AMeV. Upper panels: experimental correlation (symbols) and theoretical expectation from the known excited state information of ^{6}Li (red lines). The average Coulomb background is given by a full black line. The dashed lines give the uncertainty on the Coulomb fit. Middle panels: deduced population of ^{6}Li excited states. Both the population of the different states and the total population are given. Lower panels: Breit Wigner distributions corresponding to the states presented in the middle panels. Picture taken from refs.[58, 59]

our group at lower energies is shown in fig.1.7 for the deuteron-alpha pair looking for ^{6}Li excited state population in peripheral (left panels) and in central (right panels) collisions. In this case the reaction is ^{32}S + ^{58}Ni. Thus the source for semi-peripheral events is assumed to be a quasi-projectile excited ion similar to Sulphur; in central collisions, instead, one hypothesizes the formation of a bigger source close to the total system mass after fusion. In principle, the primary yields (i.e. those of the excited fragments) are calculated by multiplying the nuclear contribution R-R_{Coul} of the correlation function for the uncorrelated yield: $Y_{12}(E^*) = (R(E^*) - R_{Coul}(E^*))\sum_E Y_1 Y_2$ where $E^* = E_{rel} + Q_{value}$. At high E* values

the only contribution is generally due to the Coulomb interaction, thus no excited states are present and R-R_{Coul} tends to zero. On the other hand, at intermediate energies and close to the decay threshold one has several of these states depending on the specific nucleus. If the experimental resolution is good enough, by exploiting this technique, one can study the population of fragments excited well above the particle separation threshold, prior to their decay.

To conclude, we remind that one of the FAZIACor purpose, is indeed to test the particle-particle correlation analysis in order to study the population of excited fragments produced at Fermi energies also in relation to the reaction mechanisms. Exploiting the Fazia detector high mass discrimination and its good granularity ($\Delta\theta = \pm\ 0.7°$), one can explore these correlations to a degree which has not been yet fully achieved as a technique by the collaboration.

CHAPTER 2

EXPERIMENTAL APPARATUS: FAZIA

In heavy-ion reactions at Fermi energy (less than 20-100 MeV/u roughly), one has to detect a large number of different particles (from protons to fission fragments) with a wide range of energies which can vary from a few tens of keV to GeV. These reaction products are the clues we need to put together in order to study the behavior and evolution of a nuclear system during and after the collision. Therefore, one has to be able to recover information as much and as precisely as possible from their detection in terms of charge, mass, energy, velocity etc.

In the following sections, we briefly describe the main features and working principles of the experimental apparatus (F.A.Z.I.A [1])used to perform the experiment. This apparatus is based on a segmented geometry employing a three layer telescope configuration (Silicon-Silicon-Cesium Iodide). This allows for the use of both ΔE-E and Pulse Shape Analysis (PSA) methods for particle identification purposes. The chapter is organized as following. After a short introduction to the FAZIA collaboration and projects, we will detail the key aspects of each stage, namely the Silicon and CsI detectors. Later on, the electronics, the trigger part and the acquisition system will be explained, with particular emphasis on the signals which are acquired for the online and/or offline analysis. Finally, the ΔE-E and Pulse Shape Analysis (PSA) methods will be introduced in order to understand the following identification procedure used in Chapter 3.

2.1 FAZIA

The multi-detector array FAZIA aims at detecting and identifying particles and fragments produced in heavy-ion reactions in the Fermi energy domain. The challenge was to design an

[1] **F**orward-angle **A** and **Z** **I**dentification **A**rray

apparatus that is able to completely identify (Z, A and energy) the nuclear reaction products keeping in mind also the advent of exotic beams from present and future facilities. Two of the design requirements of FAZIA were modularity and portability: this would allow the use of FAZIA in various laboratories, in different setups and coupled to several detectors. Currently, FAZIA is coupled with the INDRA multidetector [60] (see Fig. 2.1 where 12 operating blocks are shown) at the GANIL laboratories in Caen.

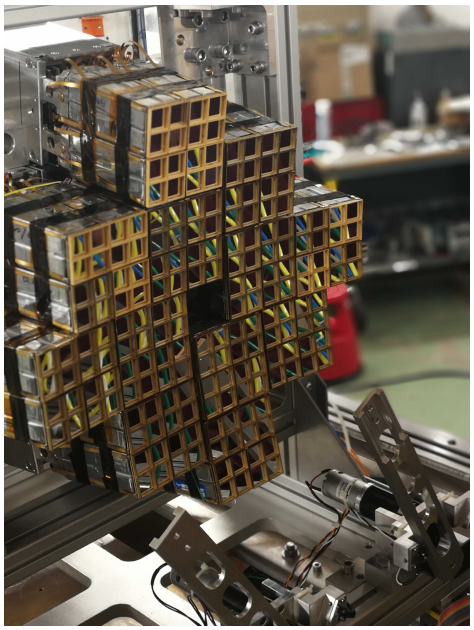

Fig. 2.1 Current 12 blocks FAZIA configuration at Ganil coupled with the INDRA detector in order to cover the forward angles (between 2° and 14°) in a 4π detection system.

As already mentioned, an important objective of the collaboration, is to maximize the charge and mass identification capabilities for the detected nuclei. In the present configuration, FAZIA is able to discriminate charges up to Z$\sim$55 and masses up to Z$\sim$25. This was achieved after a long R&D activity [61] which produced a specific custom "recipe" for the production of the next generation detectors. Among other things, it involves a careful selection of the materials (eg. the quality of the silicon detectors) and their manufacturing [62, 63], and the use of custom electronics with novel pulse-shape analysis techniques [64–66]. Moreover, a distinctive cutting-edge feature of this apparatus is the whole electronics being embedded in the proximity of the telescopes inside the vacuum chamber in a very compact and versatile block configuration, as we will discuss towards the end of this chapter. To summarize, FAZIA was thought as an array comprising a large number (192 in present day) of three-stage telescopes; two silicon detectors Si1 of 300 μm and Si2 of 500 μm, followed by a 10 cm thick Cesium Iodide scintillator (CsI(Tl)). The array is organized in blocks of 16

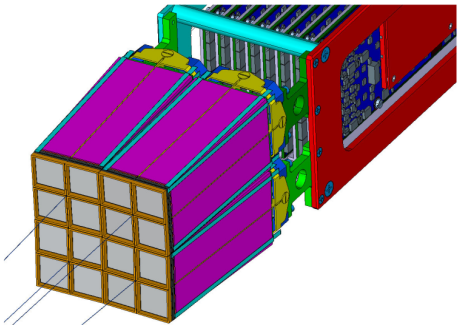

(a) Rendering of a FAZIA block

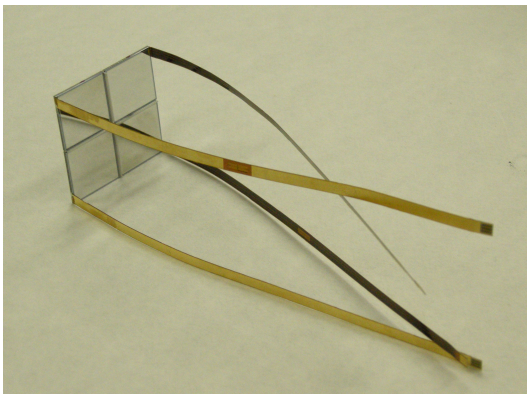

(b) Single Fazia silicon quartetto

Fig. 2.2 a) Rendering of a FAZIA block, seen from the detectors and their supporting mechanics. Silicon are shown in grey while the CsI are in purple. Orientation axes of quartettos and quartet frames (gold color) are also shown [72]. b) Silicon detectors organized in "quartetto" configuration with the flexible polymide connections to the Front-End electronics.

telescopes grouped in 4x4 matrices (see Fig.2.2a). The desired low identification thresholds are provided, not by means of a first gas stage detectors, but by employing the PSA of the signals for the particles stopped in the first silicon layer. Additionally, an improvement of the identification thresholds is expected, especially for very slow light particles, with the help of time of flight measurements, which cannot be recovered by the PSA from Si1 [67, 68].

After the R&D phase, starting from 2015 the FAZIA collaboration performed several experiments at the INFN Laboratori Nazionali del Sud (LNS). The first ones were made with a FAZIA four block demonstrator, namely ISO-FAZIA (^{80}Kr+^{40,48}Ca at 35 MeV/u) [69], FAZIA-SYM (^{40,48}Ca+^{40,48}Ca at 35 MeV/u) [70] and FAZIA-COR (^{32}S,^{20}Ne+^{12}C at 25, 50 MeV/u) in 2017, the latter being the subject of this thesis. More recently in 2018, a six block configuration was mounted, and used in the FAZIA-PRE (^{40,48}Ca+^{12}C at 25,40 MeV/u [71]) experiment. The conclusion of LNS campaign was the FAZIA-ZERO (^{12}C+^{12}C at 62 MeV/u) experiment in July 2018. Following the LNS experiments, there was a test performed with just one block (POLITA) at CCB (Bronowice Cyclotron Center) in Poland dedicated to the study of the CsI scintillator, which we will discuss also later on in chapter 4. Generally speaking, the physical motivations for studying nuclear collisions with FAZIA is to improve the knowledge of the nuclear equation of state, and particularly of the density dependence of its symmetry energy term, E_{sym} [7, 73]. This means studying for example, isospin transport phenomena in dissipative collisions such as the isospin diffusion process [74] but also topics like the isotopic composition of quasi-projectile fission fragments [70, 75], the pre-equilibrium component at Fermi energy [71] and the formation and decay of clusters in the nuclear medium and/or fragmentation cross sections.

2.1.1 Si detectors

The details of what summarized in this paragraph have been published in many articles[63, 65, 66, 76, 77] which we refer to for the reader who would like to know more on this subject. Most of the silicon detectors (shown for example in Fig.2.2b) mounted until now are manufactured by CiS [2] and are ion implanted of the n-TD type [62], with bulk resistivity values in the range 2000–3000 Ω·cm and an active area of 20×20 mm^2. However, the Fazia collaboration has also started to employ in the last year or so the new UHPS (Uniform High Purity Silicon) manufactured by TOPSIL [3]. They all present a thin metallic layer (about 20 nm of aluminum) on both sides to ensure a very low sheet resistance thus preserving good timing properties. The silicon detectors have a thickness uniformity of ± 1 μm as required to build a good Si1-Si2 telescope. This removes the impact position dependence by keeping constant the energy deposition in the telescope, therefore avoiding large variations in the ΔE variable. In order to achieve the best charge (mass) separation and to obtain the lowest identification energy threshold, a meticulous evaluation of the generated silicon signals had to be taken. In particular the R&D program focused on several aspects that can influence the shape of the signal obtaining considerable improvements for both the standard ΔE-E technique and the PSA in each of the silicon stages. Being critical to the identification procedure, a great part of the efforts were being devoted to the latter technique for ions which are stopped in the first Si-layer and cannot be identified via the ΔE-E method. Indeed, what is exploited with this PSA method are the different energy loss profiles (different stopping powers) inside the detector for different particles of the same initial kinetic energy. This results in different charge collection times, i.e. in different pulse shapes. Therefore, using only one detector (a Si layer in this case), it is possible to identify in charge (mass) stopped ions by correlating the measured energy of the ion and a parameter related to the shape of the charge or current signal.

Hereafter we present briefly the main results of a series of several adjustments and settings which were made during the R&D preparatory phase, in order to improve the identification of particles:

"Random" cut: The silicon wafers were cut from the ingot in such a way that impinging direction was tilted with respect to the major crystal axis. This makes the crystal appear similar to an amorphous material for the incoming particles and reduces the effects related to the crystal channeling as demonstrated by Bardelli et al. [63]. Indeed, for ions entering the detector along directions parallel to major crystal planes and/or axes,

[2] https://www.cismst.de/en/loesungen/strahlungsdetektor/
[3] http://www.topsil.com/

a sizable increase of fluctuations is found with respect to other directions. Instead, impinging directions far from any crystal axis or plane correspond to minimal fluctuations in quantities such as the measured energy and the signal waveforms for fixed energy deposit in the bulk. Referring to ref. [63], one clearly observes that, where crystal orientation effects are present (i.e. (i) and (ii) in Fig. 2.3), the measured distributions are not only much wider than along "random" directions (iii in Fig. 2.3), but they are also is bimodal. On the contrary, the "random" incidence region shows a better resolution with regular Gaussian shapes.

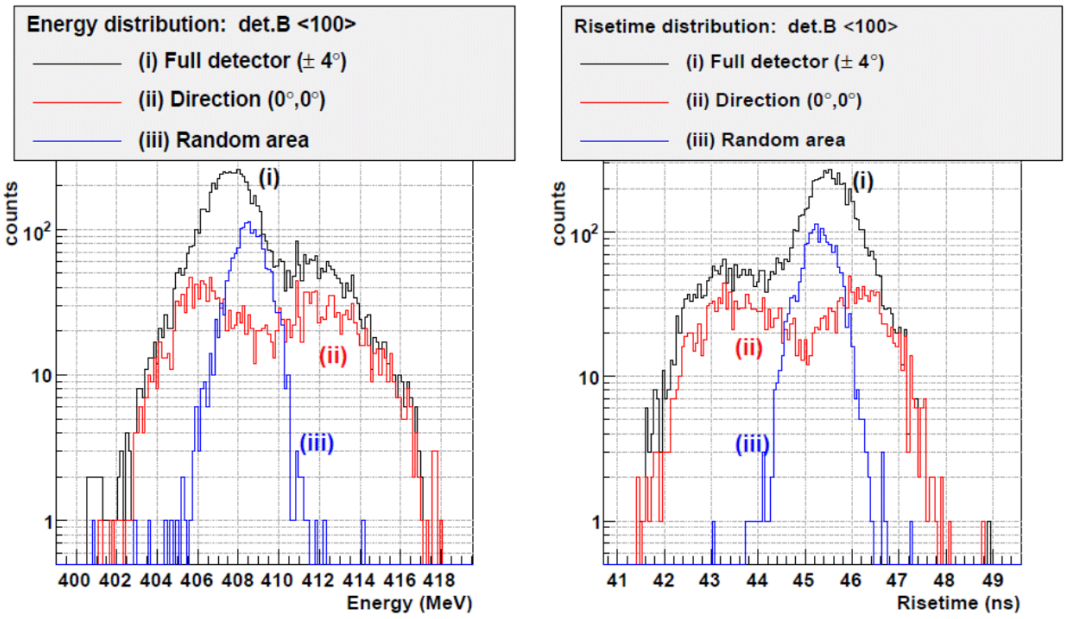

Fig. 2.3 Left: energy distribution for a ^{82}Se ion of 408 MeV energy stopped in a <100> cut detector. Black histogram (i) refers to full detector, while red histogram (ii) refers to the center of detector (“channeling” position) and blue histogram (iii) to "random" direction. Right: current rise-time distribution for the same detector with the same angular cuts as in the left panel. Picture taken from [63].

Dopant homogeneity [66]: the use of silicon detectors with good dopant homogeneity is mandatory, especially for discrimination by PSA as shown in Fig. 2.4. In fact, the signal development in Si detectors is strictly related to the charge collection times which are affected by local inhomogeneities of the electric field generated in the diode by the applied voltage due to variations of doping concentration (i.e. resistivity). To limit these variations, one has to start with a highly uniform silicon material commonly obtained via the the n-TD process. Control and further selection can then be done with

a non-destructive laser-based method [76] developed by the collaboration, that allows to build a map of the resistivity as a function of the position on the silicon. In Fig. 2.4 the PSA results obtained with different Si-detectors from the test experiment with the ^{32}S+Al at 474 MeV reaction, are shown: the resistivity uniformity increases from left to right, going from around 5% FHWM down to ∼0.7% FHWM, (the other relevant parameters were kept constant during the measurement). From the picture it is easily seen how the resistivity non-homogeneity plays a key role in the particle identification properties, in particular for particles having small penetration in the detector region towards long rise-times. Since the requirements are so strict for PSA, detectors with doping inhomogeneities less than 5% have been chosen for final telescopes.

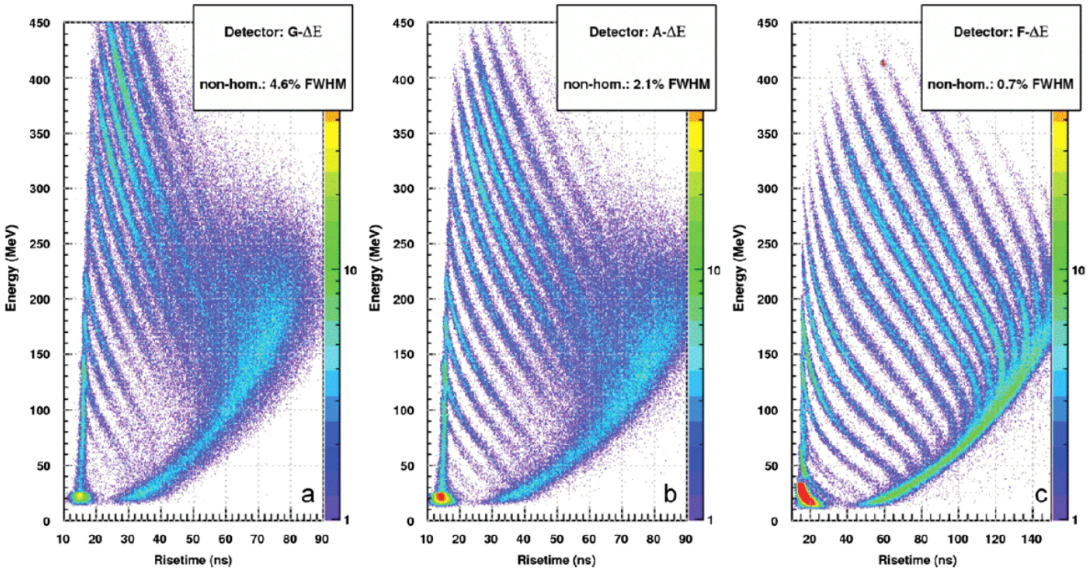

Fig. 2.4 Pulse-shape particle identification plots (energy vs. charge rise-time) obtained with three different detectors having different resistivity non-homogeneities (as shown in the insets). Picture taken from [66].

Reverse mounting and operation stability: this reverse mounting type of configuration of silicon detectors is employed so that the particles enter from the low-field side. In this way it is possible to maximize the rise-time differences of the charge signals produced by different stopped nuclei of the same energy [65, 77] since the shape of the signals is very sensitive to the strength and the configuration of the electric field inside the detector. In the front configuration the signals are faster and rise-times are less spread for different particles and energies, thus limiting the ion identification sensitivity. Moreover, the constancy of the electric field inside the detectors as a function of time is

of course beneficial for PSA applications. Therefore, FAZIA implemented an automatic correction tool used during the experiments: for each detector, we periodically check the changes of reverse current which induce change in the bias resistor (20 MΩ) and we compensate these changes by modifying accordingly the supply voltage in real time.

2.1.2 CsI detectors

The CsI scintillator length was fixed to 10 cm, to make FAZIA performant up to around 200 AMeV (depending on Z) by stopping all light charged particles which punch through the two silicon layers. The crystals (pictured in Fig.2.5) have a paralleled shape with a slight tapered geometry to keep the same angular aperture at both ends. In fact, this choice is dictated by the FAZIA conventional operation distance from the target of 1 meter. In order to favor scintillation efficiency for heavy ions, a Tl concentration of around 2000 ppm was chosen [78] with a doping uniformity along its main direction of about $\pm 5\%$. The light response and resolution, as well as its homogeneity along the detector length were improved by wrapping the crystals with a highly reflective material, 3M Vikuity^{TM} ESR [79]. The CsI(Tl) are coupled to 18x18 mm^2 active area photodiodes, manufactured according to the FAZIA design by the CIS company or FBK [4], which are generally tested before mounting with a ^{60}Co source. The coupling is made with an optical glue between the two surfaces (CsI-Si) and wrapped in the same reflective foil which is furthermore tightened by an opaque tape. The fast and slow components of the light output are obtained afterwards

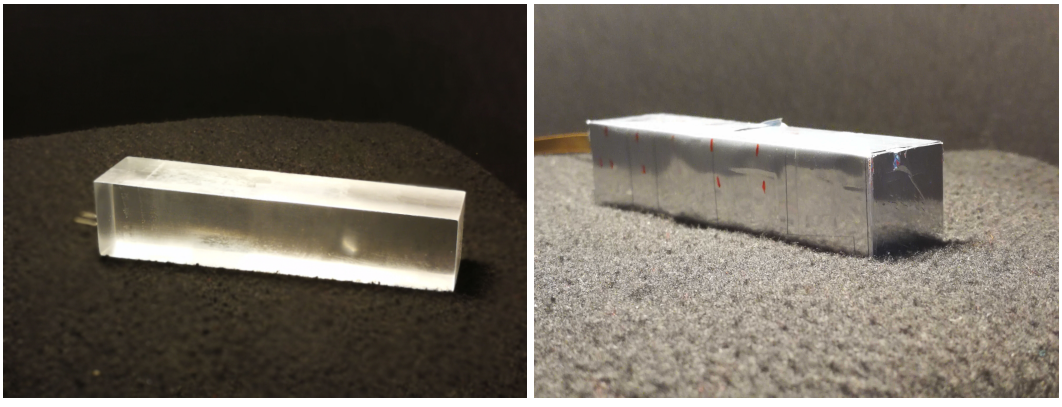

(a) Naked CsI (b) Wrapped CsI

Fig. 2.5 Fazia CsI crystal from a telescope. In a) is the naked crystal with only the PD glued on and in b) the same one wrapped.

[4] https://iris.fbk.eu/

(both online and offline) by means of trapezoidal filters with different shaping parameters in order to achieve particle identification by means of the PSA correlation between these two components. A detailed study of the behavior of these detectors in terms of Light Output (L.O) and identification efficiency for energetic protons will be discussed in chapter 4.

2.1.3 Electronics

In this subsection we will give a quick overview of the Fazia block, and in particular we will focus on the electronics and the data acquisition part of the apparatus. For more details we refer the reader to [61, 72, 80]. The main feature which can be noticed when looking at a FAZIA experiment, is the absolute scarcity of electronics outside the scattering chamber (see Fig. 2.6). In fact, the so-called *Regional Board* (RB) is the only electronic component of the acquisition system placed outside the scattering chamber and it performs the functions of an "event building" card. Only two connections per block are necessary to connect the inside with the outside: a 48 V (6 A) power supply line and a 3 Gbit/s full-duplex optical link used for multiple functions such as the transfer of data, the synchronization of the clocks, the transmission of triggers and the management of any block parameter via slow control. For a full description of each of these parts and their detailed functioning see Valdré et al. [72]. Apart from the RB, outside a cooling system is also present since the average power consumption of a single FAZIA block is almost 300 W. A refrigeration liquid (water with 30% alcohol or glycol) is distributed by a powerful chiller (ACW LP60) and flows from the outside through all the blocks under vacuum. Inside, each block is mounted upon a supporting bottom plate consisting of 8 mm of copper on which the front-end electronics is screwed on. The heat conduction is improved by a thermal grease coated between the electronic cards and the copper surface. This design allows to efficiently distribute the refrigeration liquid along the entire electronic holding surface and to generally maintain the temperature below 60 °C.

Inside the vacuum chamber, the basic element of the FAZIA array is the block, which consists of 16 detector telescopes. Each telescope is directly connected with 3 flexi cables of about 15 cm length to 8 *Front-End Electronic Cards* (FEE). Therefore, up to two telescopes can be connected to each front-end card. As shown in Fig. 2.6, all the FEE cards are connected to a *Block Card* (BC) via a common backplane, which hosts also the Power Supply (PS) and *Half Bridge* (HB) cards. The block card is mainly devoted to handle I/O operations and to merge data coming from the FEE cards. The power supply and half bridge cards produce and monitor the voltages needed to the other boards on the block. The FAZIA blocks then communicate with the regional board via the BC through the 3 Gbit/s optical link. The electronics, from the FEE to the BC and HB, are nested inside a metallic cover which should guarantee furthermore the screening of additional noise present inside the scattering chamber.

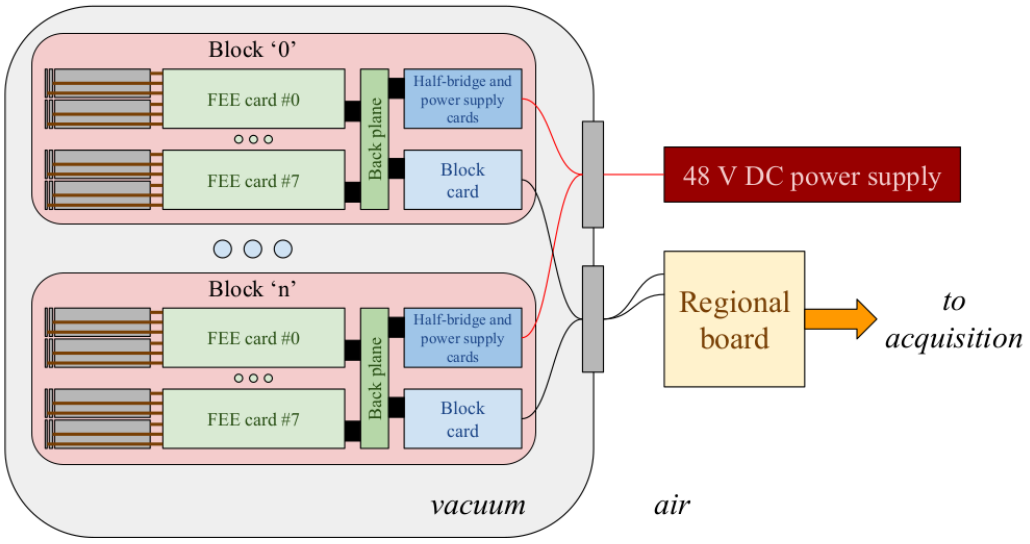

Fig. 2.6 Schematic representation of the FAZIA electronic cards inside and outside the scattering chamber. For a detailed description see the text. Picture taken from [72].

As mentioned, each of the detectors of the FAZIA telescopes (silicon detectors and CsI scintillators coupled to photo-diodes) are connected to custom-designed Front-End Electronics [80] which are an innovative and important part of the FAZIA project. They are basically composed of three stages. The first stage embeds all the low-noise analogue electronics (charge sensitive pre-amplifiers [81], current signal differentiators, amplifiers and anti-aliasing filters). In the middle part, among many other components, two Xilinx Virtex-5 [5] FPGA chips (one for each telescope and called "A" and "B" from now on), a PIC microcontroller and 12 ADCs are mounted [80, 82]. At the end, the FEE hosts the switching power-supplies which are sources of electromagnetic disturbances and thus placed, by design, far from the analogue stage. Starting from the front, six charge pre-amplifiers (three per telescope) are placed on each front-end card just next to the detector connectors providing an output dynamic range of 8 V for a total energy of 4 GeV (300 MeV Si-equivalent for the CsI(Tl) channels). The analogue lines then are split to accommodate for multiple channels per detector. For the first Si stage, we have three paths: a high range (low gain) charge signal (QH1), a low range (high gain) charge signal (QL1) and a current signal (I1). In the second Si stage we have the high range charge signal (Q2) and the current signal (I2). Finally, for the CsI stage we have only one charge signal (Q3). The low gain signals (QH1, Q2 and Q3) must be attenuated by a factor 4, to adapt the 8 V dynamic range of the pre-amplifiers to the 2 V input range of the ADCs while the high gain signal (QL1) is amplified by a factor 3.

[5] Xilinx Virtex-5: model XC5VLX50

The current signals (I1 and I2) are obtained by analogue differentiation of the Si1 and Si2 pre-amplifier outputs. Lodged in the FEE there is also a square pulse generator, which is user configurable (amplitude, frequency and duty cycle) via slow controls, in order to control the analogue chain response during data taking.

Moving towards the middle we find twelve ADCs with different specifications which digitilize the signals for the following two FPGAs of the front-end cards. The first ADC type is dedicated to the high range channels (QH1,Q2 and Q3) and has a sampling frequency of 100 MS/s with 14 bit resolution. The second type is dedicated instead to the low range (QL1) and current signals (I1 and I2) which are sampled at 250 MS/s with 14 bit resolution. In fact the current signals, because of their fast time evolution, need a higher sampling rate so as their shape can be faithfully reconstructed and used for PSA purposes. Both FPGAs of the FEE-cards include four trapezoidal shaping filters to calculate in real time the energy released in each stage of the telescope. There is one shaper on the QH1 signal, one on Q2 and two on Q3. In fact, the CsI(Tl) signal has a "fast" and a "slow" filter in order to exploit the well known fast-slow technique to identify the light ions that stop in this last stage of the telescope. All the rising edge and flat top lengths of the filters are user adjustable. Usually, the filters on QH1 and Q2 are set at a rise time of 2 μs and a flat top of 1 μs. Rise time and flat top for Q3 shapers were set respectively at 2 μs and 10 μs for the slow filter and at 2 μs and 500 ns for the fast one. All the flat top values are set according to the slowest acquired signal in order to avoid ballistic deficit; no pole-zero cancellation is applied, anyway its effect was found to be negligible since the pre-amplifier constant decay (approximately 260 μs) is much longer than the flat top. In addition to being shaped, all the signals (including also QL1, I1 and I2 that have no shaper) are continuously stored in adjustable circular buffers with dimension $N < 1024$. The FAZIA collaboration adopts both online and offline signal processing to extract the information required for the ΔE-E and PSA methods. For example the energy information from the charge signals is obtained in the following way both online and offline. Using a the first portion of the signal the baseline amplitude (BL) is evaluated and subtracted from each signal sample. Then the signal is shaped by means of the trapezoidal digital filter and the deposited energy is evaluated as the filter output maximum.

2.1.4 Trigger system and signal processing

The basic principle of the trigger logic in FAZIA is multiplicity based. First, "local triggers" are generated by the FEEs by means of fast trapezoidal shaping filters (200 ns of both flat top and rise time) implemented on the QH1, Q2 and Q3 signals inside the FPGAs. Here, the user can choose the type of trigger source, i.e logic OR among any combination of the three layers (Si1, Si2 and CsI) and the threshold configuration. One can use either a low threshold

(trigger is produced when the maximum amplitude of shaped signal is larger than it) or both low and high thresholds (trigger is produced when the maximum amplitude of shaped signal is between them). Once the local trigger is produced, they are then sent through 16 dedicated lines (one per each telescope) to the block card in the backplane. The BC counts and sends the total number of local triggers to the regional board every 40 ns through the optical link.

Inside the RB, the multiplicity values from each block are checked and compared to the trigger logic of the experiment. Via slow control, the user can set up to eight experiment triggers and also select which block individually should answer to the triggers, the multiplicity threshold and a downscale factor K if necessary. The regional board will then integrate inside a time window the multiplicities coming only from the blocks specified by the slow control settings, and it will produce an "experiment trigger" only if the integrated value overcomes the multiplicity thresholds. The trigger is then accepted based on the scaling factor K, i.e once every K occurrences. The logic OR among all the "experiment triggers" is eventually the global trigger signal. At this point, the RB has to check if there are any alerts: FPGA data buffers are almost full or there is an external veto from the “veto in” LEMO connector available on the RB card. If there is at least one alert, then a veto flag is issued. In these cases, except when there is only an external veto, the flag is also sent to the “veto out” LEMO connector of the RB card. A validation signal is produced if there is a global trigger without any veto flag issued. As an alternative to the global trigger, an external trigger coming from the “trigger in” LEMO connector can be accepted in order to produce the validation signal. This feature allows to couple FAZIA to a separate apparatus as for example INDRA in the currently used setup at GANIL.

In both these cases, the validation signal, together with an event number generated by a counter on the regional board FPGA, is sent at a 25 MHz rate to every block via the optical links, captured by the block cards and distributed to every FEE through the backplanes. When a front-end card FPGA receives a validation, all the raw signals are transferred from their circular buffers to FIFO memories, whose lengths are adjustable via slow control. The validation signal has different effects on each telescope depending on the acquisition thresholds and on the local trigger. These acquisition thresholds are again user programmable via slow control and act on the energy shaped signals. If the telescope has not generated the local trigger, but any of the QH1, Q2, Q3 "fast" and Q3 "slow" shaped signals exceeds its respective acquisition threshold, then all the telescope signals are marked for acquisition. Otherwise, a zero-suppression is applied for the whole telescope, meaning that the whole telescope is not set to be acquired. If marked for acquisition, the local event from the telescope (six waveforms, four maximum values of the shaped signals and the event number sent by the RB) is first saved in a large FIFO memory and then sent to the acquisition.

The overall sustainable rate and the data flow are limited by the maximum acquisition rate (approximately 2000 ev/s). However, one has to also keep in mind to avoid pile-up and the increasing of dead time. Therefore, for FAZIACor the acquisition rate was kept between 500-1200 Hz depending on the beam intensity fluctuations.

2.2 Identification methods

In this subsection, we will try to remind the reader the basic physics behind the identification methods, namely the ΔE-E and PSA in Si or CsI. Here, examples of these correlations will be shown from the current experiment FAZIACor. Given the multi-layer telescope configuration of FAZIA, the ΔE-E technique is possible whenever the particles punches through at least one layer (Si1-Si2 and Si2-CsI) while the PSA can be applied to a detector standalone. In particular, this last method is extremely useful for particles stopped in the first layer which would be otherwise unidentified, thus significantly lowering the identification thresholds. As already mentioned in the introduction of this chapter, the use of the "energy *vs*. time of flight" method for mass identification of ions stopped in first silicon layer (as performed by many other experiments [83–86]) is currently under investigation in FAZIA and so far used only for some specific tests [68].

2.2.1 ΔE-E

The ΔE-E identification technique is based on the well-known Bethe-Block expression [87] for the energy loss of a charged particle in an absorber of given density. Indeed, the energy loss of a fragment with atomic number Z, mass A, and velocity v, through a material with electron number density n and mean excitation potential I, can be expressed by:

$$-\left\langle \frac{dE}{dx} \right\rangle = \frac{4\pi}{m_e c^2} \frac{nZ^2}{\beta^2} \frac{e^2}{4\pi\varepsilon_0} ln\left(\frac{2m_e c^2 \beta^2}{I(1-\beta^2)} - \beta^2 \right) \tag{2.1}$$

where $\beta = \frac{v}{c}$, $n = \frac{N_A Z_{abs} \rho_{abs}}{A_{abs} M_u}$ with N_A, Z_{abs}, ρ_{abs}, A_{abs} and M_u the Avogadro number, atomic number, density, mass and molar mass of the absorber. In the non-relativistic limit however, the energy loss is a simple function of the particle charge, mass and incident energy [87] and eq. 2.2 can be reduced to:

$$-\left\langle \frac{dE}{dx} \right\rangle \propto \frac{Z^2 A}{E} \tag{2.2}$$

Therefore, the energy loss inside a material increases quadratically with the impinging particle charge and linearly with its mass, while it decreases with the impinging energy.

Exploiting the dependencies in eq. 2.2, one has the possibility to identify particles by using a sequence of detectors with the requirement that at least one must be entirely crossed by the particle and then stopped in the following detector. The correlation between the energy loss (ΔE) in the first layer and the residual energy (E) in the second is what gives the ΔE-E matrix for particle identification. Depending on the quality of the detectors one can discriminate both the Z and A of the impinging particle up to some intrinsic limit. For example, the isotopic resolution of the fragments which is more critical, is reached if the energy resolution of the detectors employed in the telescope, mainly the ΔE stage, is high. In this sense, the strict specifications of the production of Si1 and Si2 detectors, summarized in the FAZIA recipe, are essential to the quality of the fragment identification, since the silicon layers are the ΔE pairs of Si1-Si2 and Si2-CsI telescope, respectively. Nevertheless, depending on the energy domain and detector thickness, the amount of energy deposited in the ΔE can become so low that the sensitivity needed to separate different ions is lost due to energy straggling (i.e. large deposited energy fluctuations). This can happen especially for low ionizing particles such as protons and alpha particles in experiments with high energy beam (more than 50 MeV/u). To mend this problem one has to use the PSA of the final CsI detector where these

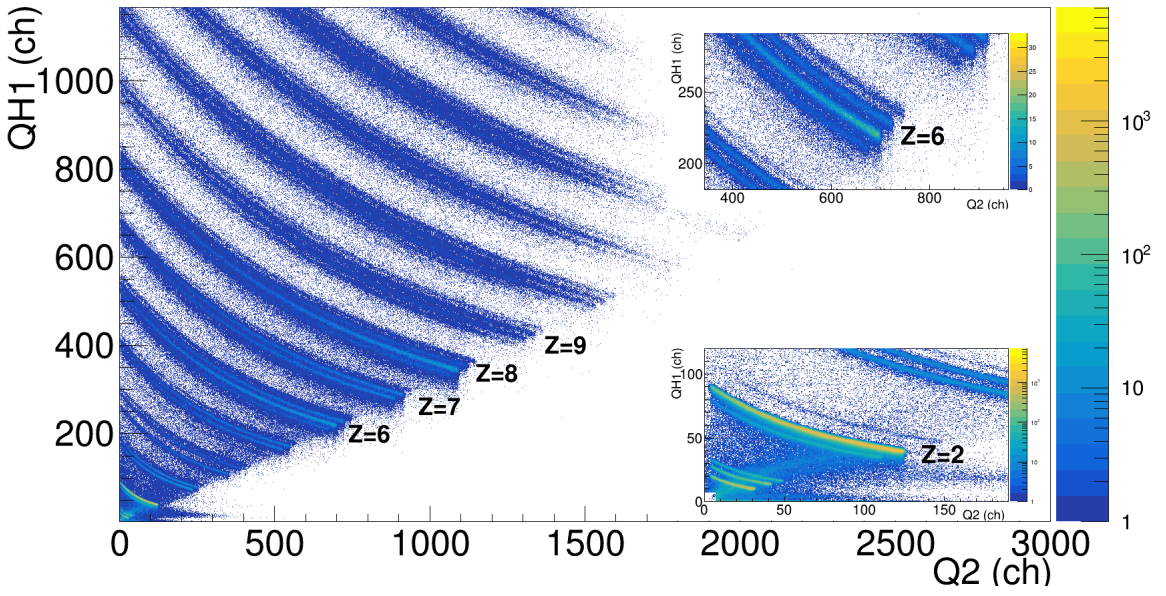

Fig. 2.7 A typical Si1-Si2 ΔE-E matrix of a FAZIA telescope (Tele111). Punching through fragments in the Si2 stage are vetoed by the CsI signal. In the main-panel a few Z are indicated. In the panels to the right, a zoomed portion is shown in the low-Z region and in the Carbon ridge. The data refers to the entire statistics, i.e ^{32}S+^{12}C and ^{20}Ne+^{12}C at 25 and 50 AMeV.

particles are indeed stopped and not rely on the Si detector. This technique will be explained in the following paragraphs.

In fig. 2.7, a ΔE-E matrix for a typical Telescope (here Tele111) is shown from the FAZIACor data-set with the two systems (i.e ^{32}S+^{12}C and ^{20}Ne+^{12}C at 25 and 50 AMeV) summed in order to fully populate every ridge. The ridge of Z of Carbon, Nitrogen, Oxygen and Fluorine are indicated in the main panel as an example. In the panels, two zooms of the loci representing alpha particles and Carbon isotopes are shown in order to evidence the mass discrimination of this method in our systems and with the FAZIA apparatus. In this experiment, Z up to 17-18 can be recognized, especially in the heavier system (^{32}S+^{12}C), and mass A can be discriminated up to Z=15. The difference in mass discrimination between Z=17 and Z=15 is given mainly by the low statistics which populates the higher Z ions. More details will be illustrated in the next Chapter where the identification and calibration process will be fully described. However, during the R&D phase, it was demonstrated that the charge and mass separation with FAZIA can extend up to Z=55 and Z=25 respectively [61], well beyond the range accessible with the FAZIACor experiment.

2.2.2 Pulse Shape Analysis (PSA)

As introduced above, the Pulse Shape Analysis [64] is a technique which relies on the different shape of signals produced by ions with different Z-A but fixed energy E, and can be applied to a single detector. The full potential of this method is exploited if used with digital systems which ease the use of algorithms on the digitized signals in terms of performance, speed and upgradability. In FAZIA, the PSA is applied to both the silicon and CsI detectors taking advantage of different intrinsic physical processes which produce the signals.

Si PSA

For the Si detectors, the difference in signals is due to the process of carrier collection inside the detector [65, 88, 89]. In particular, the different shapes are due to a variation with Z, A and E of the penetration depth and of the ionization density profile along the particle track. Initially, a narrow straight clouds of carriers (i.e. electron-hole pairs) is formed. Then the carriers density evolve following the Bragg curve as a function of the penetration depth. The maximum is generally reached near the end of the track where the electron-hole pairs density is so high that it acts like a plasma modifying locally the electric field present inside the depletion region of the junction. Therefore, a longer time ("plasma time" [90, 91]) is needed for the carriers to be separated ad then to reach the respective electrodes depending on the plasma density. Moreover, the electric field changes going from the entrance to the opposite

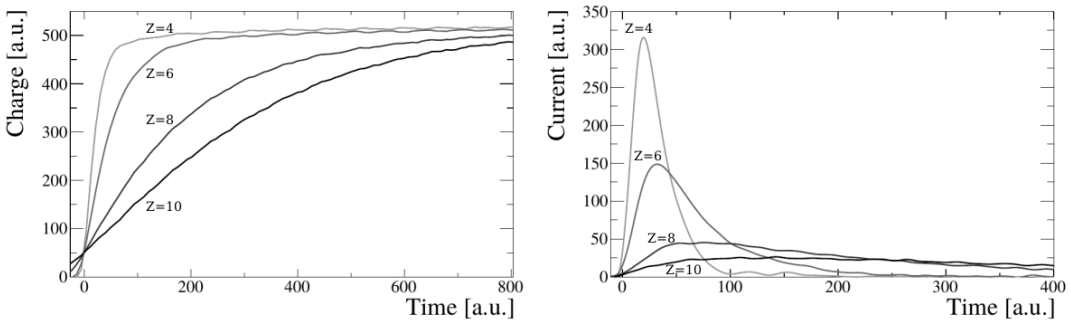

Fig. 2.8 Experimental signals extracted from the Si1 detector for different ions (Z=4, 6, 8 and 10) at an impinging energy of 95.5 MeV. The left panel shows the acquired charge signals while the right panel represents the induced current signal for the same ions. For more details see the text. Picture taken from [92] where some of the first R&D FAZIA data on PSA were presented

side of the detector, thus the intensity of the junction field near the Bragg peak depends on the fragment penetration (i.e. the ion range) into the detector. As a consequence, the collection time depends once more on the Z and A of the impinging ion, even when they have the same impinging energy. To summarize, fixing the incident energy, we observe that signals induced by heavier ions have a slower charge rise time (left panel of fig. 2.8) with respect to light ions. The corresponding effect is of course visible also in the current signal (right panel of fig. 2.8), where the maximum of the induced signals is lower for the heavier fragments with respect to lighter ions (the total produced charge is equal for each fragment). As mentioned in section 2.1.1, to enhance the plasma time difference, the FAZIA collaboration has opted for a reverse mounting configuration [77] of the silicon detectors. In this configuration, the carrier plasma tends to be formed in the low field region for heavy/slow fragments, while it is on average produced in the high field region for light/fast fragments, thus favoring the differences in the charge or current signal waveforms for different ions.

During the R&D phase two parameters have been investigated in order to be used for PSA applications:

- **Rise-time of the charge signal (Q-PSA)**: correlation between the energy deposited in the detector and the charge signal rise time.
- **Maximum of the current signal (I-PSA)**: correlation between the energy deposited and the maximum of the current signal.

Both correlations have shown excellent Z identification being able to reach Z=54, while the isotopic identification performances differ between the two methods. The I-PSA has shown a

better separation of the isotopes compared to the Q-PSA [61, 93], thus FAZIA adopted this choice as the main identification method for particles stopped in the first silicon. In fig. 2.9, a typical PSA correlation matrix, taken from the FAZIACor data-set, is shown. The ridges corresponding to the different Z species can be clearly distinguished (to guide the eye a few Z are indicated). Furthermore, in the right panel, an excellent mass separation can be observed for Z=6, being able to discriminate at least four isotopes.

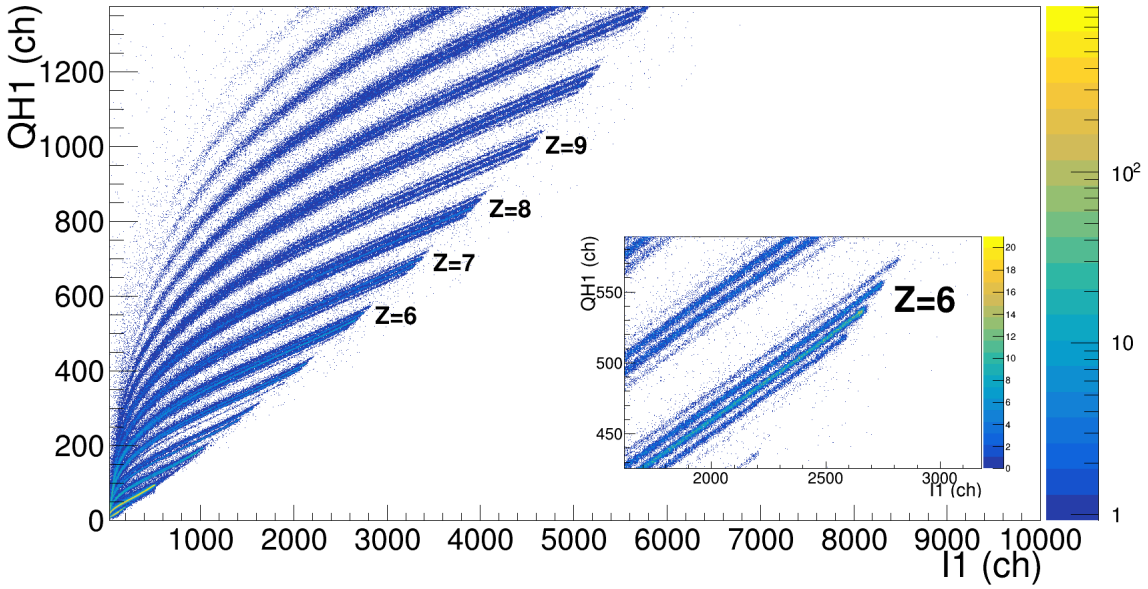

Fig. 2.9 A typical Si1-PSA matrix of a FAZIA telescope (Tele111). Punching through fragments in the Si1 stage are being vetoed by Si2. In the main-panel a few Z are indicated. In the panel to the right, a zoom of the same matrix is shown for the Carbon ridges, well demonstrating that C isotopes are recognized (from A=10 to A=14). The data refers to the entire statistics, i.e ^{32}S+^{12}C and ^{20}Ne+^{12}C at 25 and 50 AMeV.

CsI PSA

The CsI(Tl) scintillators emit light pulses whose shape varies as a function of the type of incident radiation. In particular, the fluorescence produced shows two main components, commonly labeled as *fast* and *slow* with different time decay constants ($\tau_{fast} \approx 0.75\mu s$ and $\tau_{slow} \approx 5\mu s$) and these two are then correlated for particle identification purposes [94].

The nature of the fast and slow components arises from the de-excitation of different states of the scintillator. These states are populated in different proportions depending on the specific energy loss of the incident particle. Therefore, the relative intensities of the two components are different for different dE/dx. In the CsI, for example, a high ionization loss

produces a higher density of free electrons and holes. The high density favors then the pair recombination into loosely bound systems known as "excitons". These excitons moving through the crystal lattice are captured as a whole by impurity centers (Tl), exciting the latter to certain radiative states (fast component). The singly free electrons and holes, on the other hand, are captured successively resulting in the excitation of metastable states (slow component) not accessible to excitons [95].

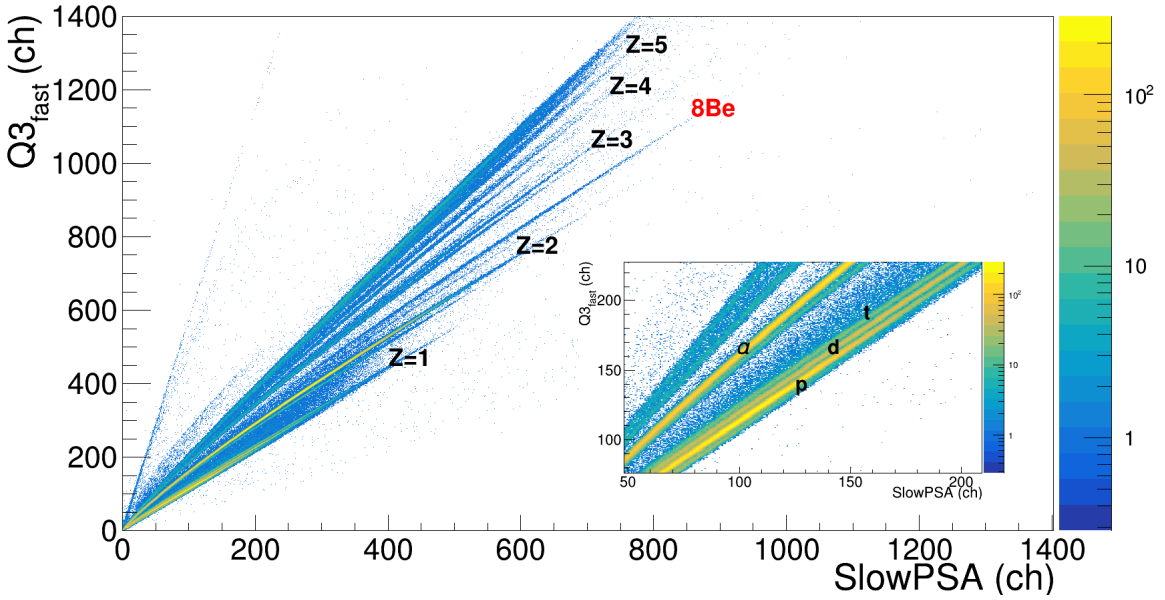

Fig. 2.10 A typical CsI-PSA matrix of a FAZIA telescope (Tele111). The double-α hit of the ^{8}Be decay is also indicated. In the right insert, a zoom of the same matrix is shown around Z=1 (p, d, t) and Z=2 (α). The data refers to the entire statistics, i.e ^{32}S+^{12}C and ^{20}Ne+^{12}C at 25 and 50 AMeV.

As mentioned, in FAZIA, we disentangle the different components of the scintillation light output of our CsI(Tl) by applying two digital trapezoidal filters to the digitized Q3 signal (Q3$_{fast}$ and Q3$_{slow}$), which simply differ in the flat top. Being the fast and slow signals strongly correlated as the latter contains the former, a better discrimination is obtained by using the fast *vs.* a linear combination of the fast and slow components. This variable, from now on called *"SlowPSA"*, is obtained as Q3$_{slow}$-0.8·Q3$_{fast}$ and has become a standard option in the FAZIA collaboration. An example of a Fast-SlowPSA correlation is presented in fig. 2.10. The charge separation is clearly visible up to Lithium-Boron, while on the other hand good isotopic separation is only achieved for hydrogen and helium ions (see the sub-panel in fig. 2.10).

CHAPTER 3

THE FAZIACOR EXPERIMENT

Heavy-ion collisions (HIC) allow exploring the nuclear equation of state (EoS) under laboratory controlled conditions. In such complex dynamical systems particle-particle correlations can probe dynamics and thermodynamics of hot nuclear systems and can also be used as a spectroscopic tool. The original guideline of the FAZIACor proposal was the study of reactions of N/Z-symmetric systems of light masses (^{32}S+^{12}C) and (^{20}Ne+^{12}C) at two beam energies (25 and 50 MeV/u) to explore possible in-medium effects on nuclear structure properties of unbound states (ex. Hoyle and cluster-like states), by means of multi-particle correlations. However, in this Thesis, we wanted to extend the investigation also to the general reaction mechanism characterization for such light systems which we find to be a challenging study in itself. The particle correlation technique will be used as a complementary tool to achieve these purposes.

In this chapter we will give an overview of the entire experiment. First, we give a general description of the experimental setup and the tools used to perform the data analysis. Then we will go into the details of the identification and calibration procedures in order to obtain a set of data ready for the physics case. This part represents a crucial part of the Thesis and therefore particular care and time was devoted to it. Finally, the results of the identification and calibration sections will be summarized and conclusions will be drawn.

3.1 FAZIACor

3.1.1 Experimental setup

The FAZIACor experiment was performed in Catania at the Laboratori Nazionali del Sud (LNS) of Istituto Nazionale di Fisica Nucleare (INFN) inside the Ciclope scattering chamber in march 2017 and used the same configuration as the FAZIASym experiment [70]. This

was composed of four complete Fazia blocks in a wall structure (B000, B001, B002, B003 shown in fig. 3.1) plus a fifth one (called SIMON for SIlicon MONitoring) serving as a single telescope (two-layer Si-Si) for elastic events detection. Each block covers the same polar angles (i.e. from 2° to 8°) but at different azimuthal angles. The experiment consisted of studying of the following systems:

1. $^{20}_{10}$Ne $+^{12}_{6}$C @ 25 and 50 AMeV
2. $^{32}_{16}$S $+^{12}_{6}$C @ 25 and 50 AMeV

In this experiment, not all the telescopes feature the standard 300-500 μm Si-Si configuration but for a part of them we used also 300-300 μm arrangements. A scheme of the Si layer thickness is shown in fig. 3.1. The main data set was acquired for collisions on ^{12}C target of

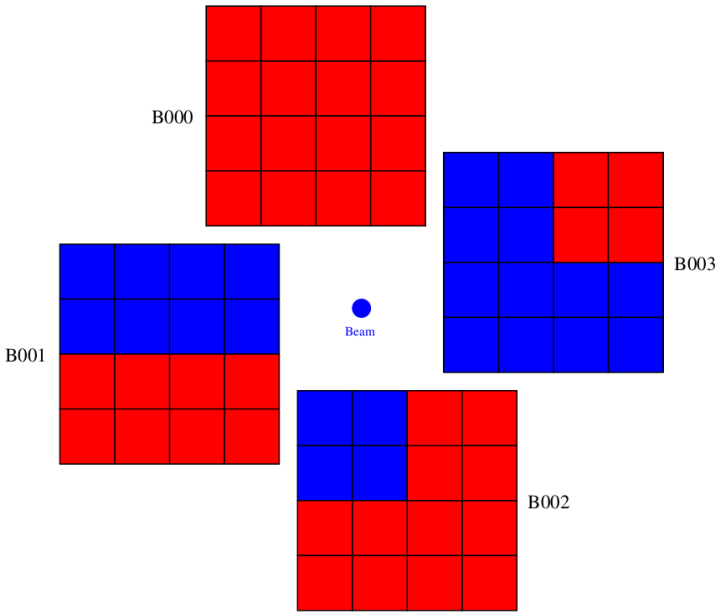

Fig. 3.1 FAZIACor wall configuration. The thicknesses of the silicon layers for the FAZIACor experiment are also shown. Red indicates the 300-300 μm arrangement, and blue means a 300-500 μm arrangement.

239 μg/cm^2 thickness. However, for checks and calibration purposes, several other reaction data are available. Cosmic rays, alpha source (three peaks Pu-Am-Cm) and pulser runs were also acquired. The cosmic rays and alpha source data was mainly acquired in the preparation phase before the actual use of the carbon target while the pulser runs are performed during several phases both for calibration of the silicon detectors and for controls of the electronics, respectively. Moreover, elastic calibration runs were performed with a thin Au foil (154

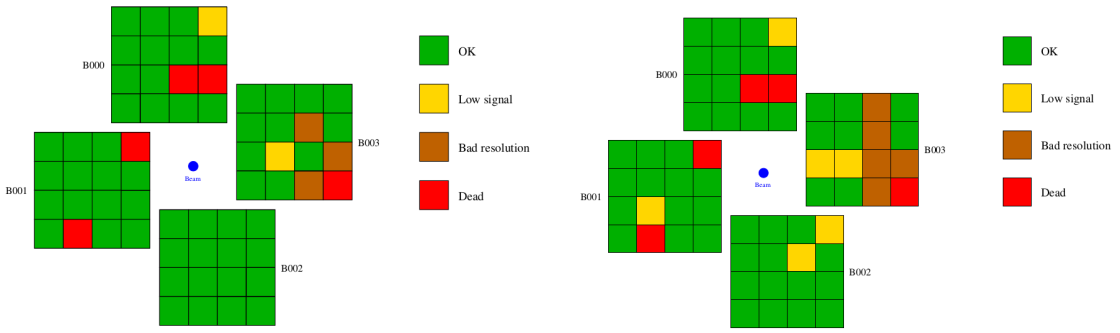

(a) Start of FAZIACor (b) End of FAZIACor

Fig. 3.2 Detectors status for the first layer (Si1) at the beginning (a) and end (b) of the experiment.

μg/cm^2) and a few runs on empty frame for possible background estimation and beam quality checks.

In figures 3.2, 3.3, 3.4, for each block and telescope, the three detector layers (Si1, Si2, CsI) are presented and their status at the beginning (left part) and end (right part) of the experiment are shown. The telescopes were labeled as: *Ok*, *bad resolution*, *low signal* and *misalignment*. "Ok" stands for no problem at all, "bad resolution" means that no mass resolution can be obtained from the ΔE-E/PSA correlations, "low signal" indicates lower amplitudes than typical for the "Ok" telescopes and "misalignment" depicts a situation where the punch through region is not efficiently removed in the Si-Si correlation with the CsI veto. Misalignment is less visible at the end due to the lower beam energy (25 AMeV) with respect to the initial phase (50 AMeV) causing less particles to punch through the Si2. However, this problem still remains. Therefore, in some cases (telescopes) extra care is taken during the identification and calibration process. The low signals cases do not represent a problem if the reduction concerns the signals of the residual energy detector in a ΔE-E matrix; this is the case since the residual energy signal is generally higher (in terms of ADC units) compared to the DE signal. So some telescopes (or equivalently correlation matrices) are not completely lost. Since FAZIACor is designed to study correlation, and mass resolution is extremely important, the bad resolution layer/telescopes have to be discarded. The number of good correlations (or working telescopes) is shown in tab. 3.1 both at the start and end of the FAZIACor experiment. For specific telescopes due to electronic faults some correlations were not available at the beginning but recovered towards the end or have been lost during the experiment so the percentage of available correlation matrices can vary start to end.

As explained in chapter 2, the experiment trigger is multiplicity based. A minimum bias trigger of M$\geq$2 was chosen for the four wall blocks without any reduction.

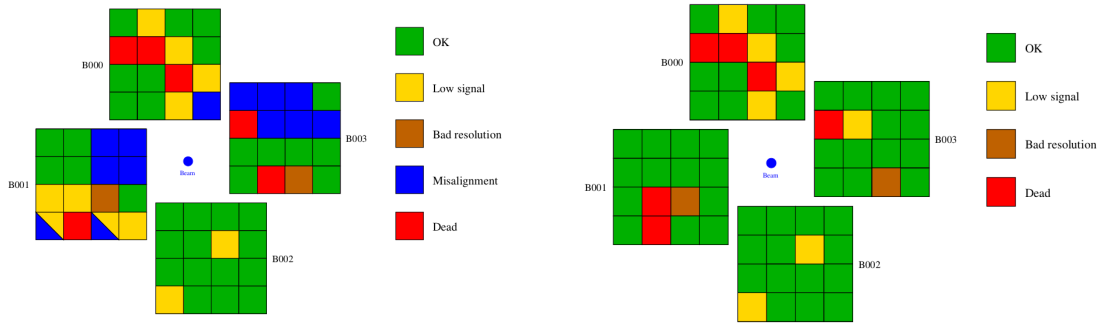

(a) Start of FAZIACor (b) End of FAZIACor

Fig. 3.3 Detectors status for the second layer (Si2) at the beginning (a) and end (b) of the experiment.

(a) Start of FAZIACor (b) End of FAZIACor

Fig. 3.4 Detectors status for the third layer (CsI) at the beginning (a) and end (b) of the experiment.

Table 3.1 Summary of the working telescopes (max number 64) at the beginning (^{32}S+^{12}C @ 50 AMeV) and end (^{20}Ne+^{12} @ 25 AMeV) of the experiment.

Correlation	Start	End	Percentage (Start-End)
Si1	54	49	84%-77%
Si2	45	49	70%-77%
CsI	51	45	80%-70%
Si1-Si2	39	39	60%-60%
Si2-CsI	35	36	55%-56%

3.1.2 KaliVeda: a heavy-ion analysis toolkit

The acquired data during the experiment has been stored at the IN2P3 Computing Center in Lyon (FR) [96]. Here, given the large amount of data (hundreds of GB), the first data reduction phase is also performed by means of KaliVeda [97]. KaliVeda is an object oriented data analysis framework based on ROOT [98] and freely available to download from the GitHub [99] platform. It was originally developed to provide simulation and analysis tools for heavy-ion reaction data collected by the INDRA multidetector and it has been upgraded in order to include the FAZIA telescopes with additional identification features. Nowadays, KaliVeda has evolved being able to manage also experimental data. It allows the management and treatment of large data sets, from the data reduction part, the identification and energy calibration procedures to the final physics analysis. The framework is equipped with several graphical interfaces to ease for example the identification process, i.e it allows to manually place identification grids on the ΔE-E/PSA correlations, but also provides energy loss, stopping power and range calculations for E/A = $1-100$ MeV. During my thesis work, a consistent period (including a 3 months stage at LPC Caen in France) has been spent to become acquainted with the KaliVeda package that then I have used for most of the analysis described hereafter. Due to their importance in this Thesis, most of the features of KaliVeda will be explained and illustrated step by step in the following section devoted to the identification and calibration of the raw data.

3.2 Particle identification

In this section the ion identification procedures adopted in KaliVeda to access the charge and mass of the detected fragments are described. As reference in the examples, the data of all systems will be used if not otherwise specified. All the matrices presented in this section refer to the telescope-111 but the same specifications apply to the others. The vertical scales of the bidim plots shown in this chapter are logarithmic except when specified differently. The telescope identification code is defined in the following way. The enumeration of the blocks is done counterclockwise (looking from the beam direction) while for individual blocks the numbering of the quartets and telescopes inside quartets is done clockwise. The telescope identification code is: $IDTEL = block*100+quartet*10+telescope$. The telescope-111 thus refers to the telescope 1, of the 1 quartet of the block number 1. In the FAZIACor experiment, four FAZIA blocks were employed, for a total of 64 possible telescopes. However, given the requirements of the experiment and operational problems, the real number of well performing sensors is lower and summarized in tab. 3.1.

The very first step of the whole identification procedure, consists in checking the database of the experiment to define subsets of stable and homogeneous runs. Once the runs were selected, the matrices from the four reactions were compared to control whether the entire statistics could be summed together. The correlations are populated differently (due to different physics and energies) but continuously and if the apparatus remains stable the matrices can be superimposed. This step speeds up the construction of the identification grids which is a cumbersome and time consuming task requiring many weeks of work. In our case, except for two telescopes which had powering instabilities, the correlation matrices can be processed by the same set of identification grids.

Depending on the particle type and impinging energy, different correlations have to be used. Slow ions are generally stopped in the Si1 or Si2 layers; therefore, Si1 PSA and Si-Si ΔE-E are enough for their identification while the most penetrating species need the Si-CsI. For the LCP (Z<3), since they generally punch through the Si1 and/or Si2, the Si-Si and Si-CsI ΔE-E are employed. The most energetic ones, such as protons over 100 MeV, however release only small amounts of energy in the silicon layers (especially in the 300-300 μm telescopes) sometimes very close to the noise threshold and require the use of the CsI PSA. Independent of the kind of identification matrix, the KaliVeda software offers specific tools, such as the *ID Grid Manager GUI* and the *ID Grid Editor GUI*, to perform ion identification starting from correlations using graphical interfaces. The former is a graphical interface for visualizing, testing and saving the generated grids. The latter is an identification grid editing interface which selects the canvas with the desired grid with dynamic zoom and "pan & scan" features using the mouse. Grids lines can be translated, rotated about an arbitrary point and scaled. The two graphical tools allows the user to easily draw a line in the present grid by dragging the mouse along a ridge and inserting points which are joined by straight segments. The requirement is to complete the segmented line until the end of the ridge; the users try to follow at best the ridges, aiming at drawing lines equally spaced. An example of identification grids are shown in figs. 3.5 3.7 3.10 superimposed on the Si1 PSA, Si1-Si2 and Si2-CsI correlations, respectively. The variables shown in the axes have been introduced in par 2.1.3. Moreover, the user can choose to draw the lines following two recipes:

- Click only one isotope line for each element Z
- Click each isotope individually for each element Z if the matrix allows it

In the first case, if mass resolution is achieved, in a second step the user is asked to define the peaks and intervals/limits for the different identified isotopes. The two methods can also be combined, as we will see for the Si2-CsI correlations. The grids can be completed by also inserting cuts, to exclude some unwanted regions of the matrix or instead to exclusively

retain parts of that. Each cut is individually drawn on each matrix and then detailed in the text for the various correlations.

The lines are identified by a Particle Identification parameter (PId), corresponding to the atomic number Z of the particle which is given by the user when clicking the line. The final PId distribution of the detected ions is produced by KaliVeda by an interpolation procedure of the particles position in the matrix, between the four closest lines in the grid. The quality of the identification (interpolation) is tracked by means of a quality code which allows later on to perform further checks or to impose more restrictive cuts. The adopted codes, assigned to each particle, are the following depending on which of the two methods is being used. If a Z & A (mass & charge) isotopic identification grid is used:

- IDCode=0 - good Z and A.
- IDCode=1 - Z is reliable but A can be lower by one unit.
- IDCode=2 - Z is reliable but A can be larger by one unit.
- IDCode$\geq$3 - A not well identified.

If Z-only charge identification grid is used:

- IDCode=0 - good Z.
- IDCode=1 - slight ambiguity of Z, which could be larger.
- IDCode=2 - slight ambiguity of Z, which could be smaller.
- IDCode$\geq$3 - Z not well identified.

For example, in correlation between particles is vital to have a good mass identification. Therefore, only those particles with quality code "0" will be selected while if we are interested in less demanding quantities (for instance to globally characterize the system) the other codes can be taken into consideration to increase the statistics.

3.2.1 Si1 PSA

In fig. 3.5, the PSA matrix for Tele111 for the whole statistics together with the identification grid is shown. One can see and clearly distinguish the various isotopes of a single Z. For the line clicking, the first recipe has been followed, i.e. only one isotope line for each Z and identification intervals afterwards. In addition to the lines, two cuts have been inserted in the matrix. The first one is a black contour line defining the region where mass discrimination

is feasible. The limiting left points of the black contour on the ridges are obtained by a semiautomatic procedure. This consists in importing the typical identification thresholds for this technique as reported in [93]. The mass thresholds coordinates in terms of energy (MeV units) and I_1 are transformed in the respective energy and I_1 coordinates in ADC units (ch) and inserted in the grid contour. The electronic settings are of course taken into account when the transformation from MeV to ADC units is made for the Si energy.

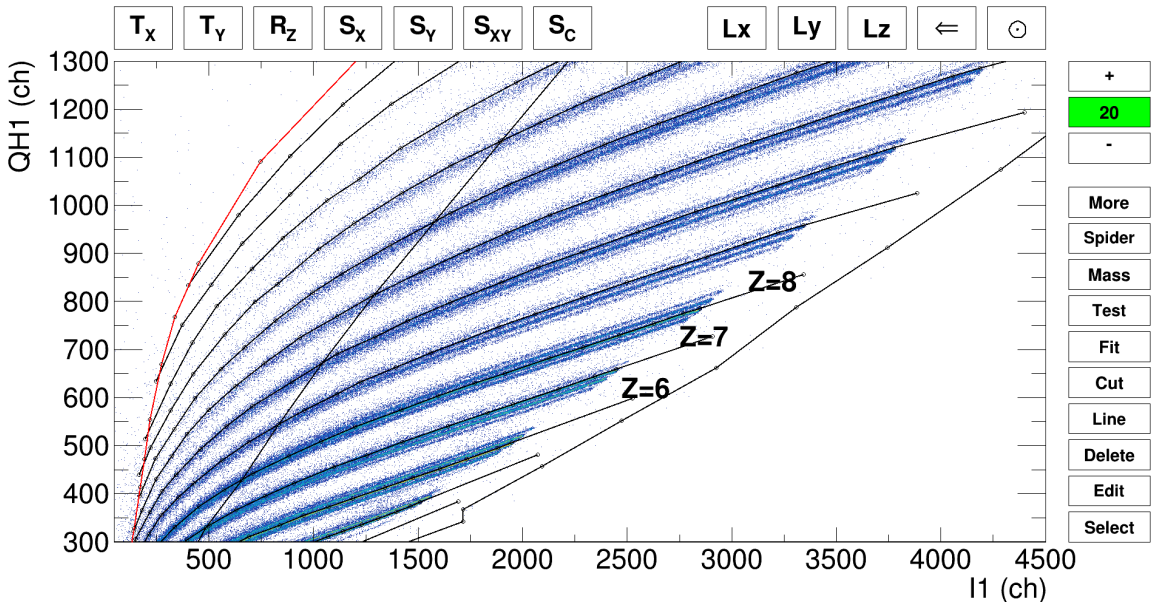

Fig. 3.5 Example of a Si1 PSA for the Telescope 111. The panel shows a zoom around the Z=6,7,8 ions. One can see also the identification lines, drawn one for each Z. Moreover, two cuts are present. The black contour, defining the region of the matrix where mass discrimination is achieved and a red line which marks the limit for achieving at least Z identification.

The second step of the identification procedure (mass intervals) is shown in fig. 3.6a where the PId distribution obtained from the previous grids is illustrated for the Carbon isotopes as an example. The vertical black lines represent the interval of mass identification chosen and the triangles (with (Z,A) coordinates shown atop) indicating the centroid of the isotope distribution. We chose to leave out some particles between two consecutive peaks in order to reduce the A contamination in the mass discrimination. However, Kaliveda still performs a mass assignment based on a nearest peak interpolation. To keep track of the different mass association, every particle is tagged with a code which is "0" for the interpolated mass and "1" for the inside interval mass assignment. The choice is then left to the user whether or not to include both codes. The same considerations and procedures

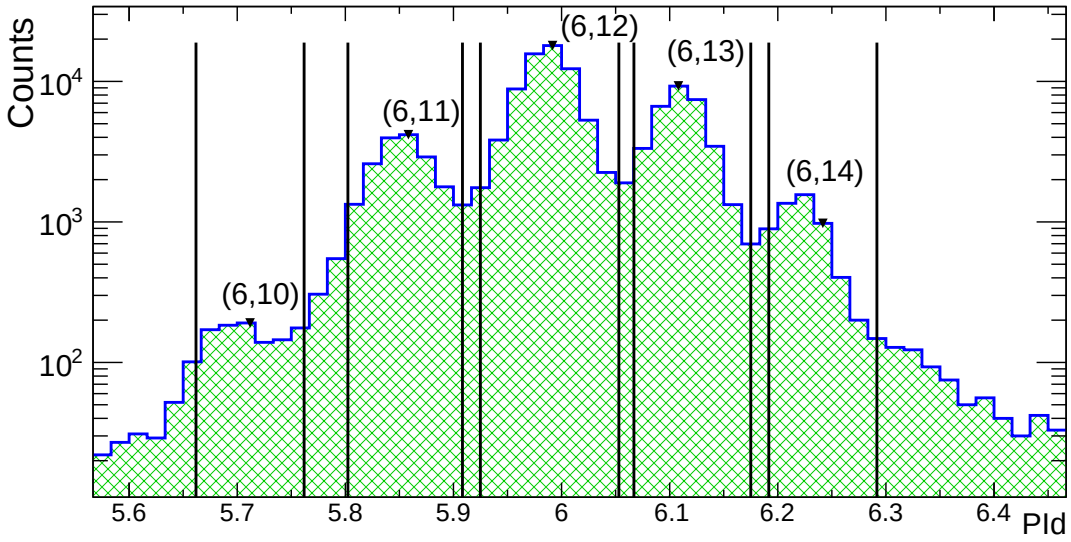

(a)

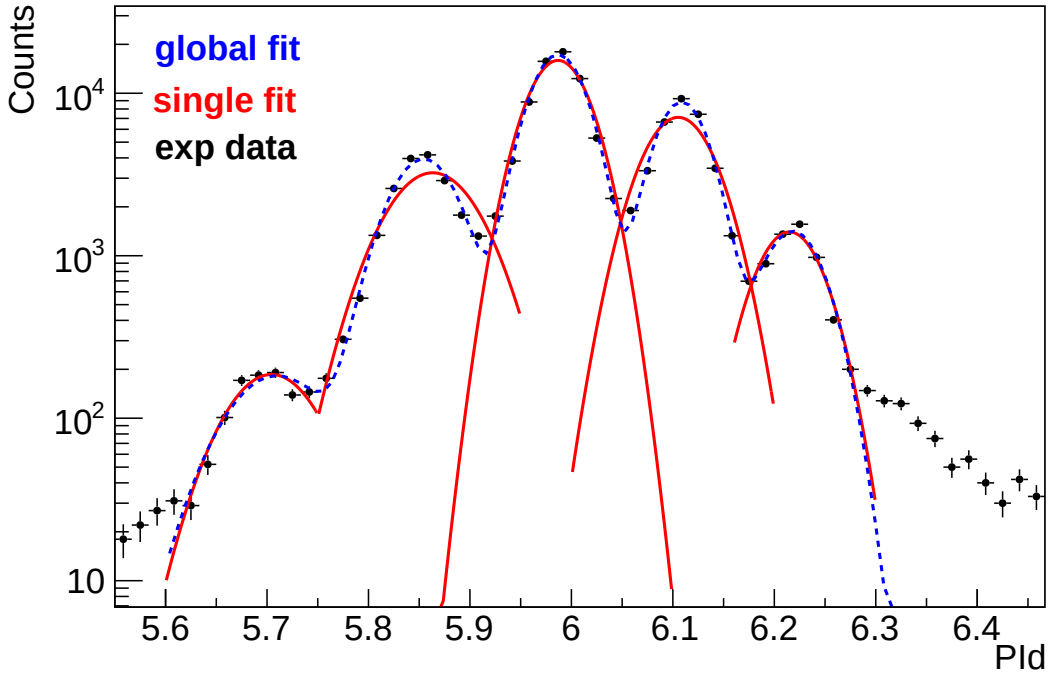

(b)

Fig. 3.6 a) PId distribution for telescope 111 obtained from the grids in fig. 3.5. The vertical black lines represent the interval of mass identification and the triangles show the centroid of the isotope distribution. For each isotope the (Z,A) coordinates are shown on top. b) Multi-gaussian fit procedure: blue dotted line representing the global multi-gaussian function, the red lines are the single fit gaussians serving as an input for the final fit, while the experimental data from pad a) is shown as black points.

are applied to the remaining isotopic identification of the remaining ions in the full PId distribution.

In order to estimate the quality of the identification, a multi-gaussian fit is applied to the isotopic peaks associated with each element and a Figure of Merit (FoM) can be evaluated for pairs of adjacent peaks. The FoM is defined as following:

$$FoM = \frac{PId_2 - PId_1}{FWHM_2 + FWHM_1} \tag{3.1}$$

where $PId_{2,1}$ are the centroids (from fit) of two adjacent peaks in the PId spectrum and $FWHM_{2,1}$ their respective full widths at half maximum. The errors on the FoM values are calculated by simple propagation of the errors of the centroids and FWHM values coming from the fit procedure. For example, in the shown Carbon case of fig. 3.6a, we obtained a FoM(^{11,12}C)=0.93$\pm$0.05 and FoM(^{12,13}C)=1.03$\pm$0.03. A FoM value of 0.7 is usually associated with 5% mutual contamination between the peaks when they have the same height. However, being the peaks populated differently we decided to calculate directly the relative contamination by means of integration of the fit functions. The obtained values are as following: the amount (%) of ^{12}C mistaken for ^{11}C is 3.1% and 2.7% vice versa, while the amount of ^{12}C mistaken for ^{13}C is 2.5% and 2.1% vice versa. Keep in mind that these values are averaged over the two energies (25 and 50 AMeV), however for the Si1-PSA the differences are not significant (ex. FoM(^{11,12}C)$_{25}$=0.95$\pm$0.05 vs FoM(^{11,12}C)$_{50}$=1.06$\pm$0.05) and well above the limit value of 0.7.

3.2.2 Si1-Si2 ΔE-E

For the Si1-Si2 identification matrices, the used method is that of clicking each isotope individually for each Z, as shown in fig. 3.7. This type of identification allows the best isotopic separation and does not require to set any mass intervals as the mass is already set when the grids are placed (each line has to be given initially a (Z, A) coordinate). The quality code is determined after the linearization following this rules: IDCode=0 is set up in the $\pm$0.05 interval from the peak for each isotope, while IDCode>0 are set up by interpolation to the nearest line outside these limits.

The quality of the identification procedure, as for the PSA, can be checked using the FoM and multi-gaussian fit. Taking into account the same carbon pairs of adjacent peaks and same 111 telescope, we obtain the following values: FoM(^{11,12}C)=1.59$\pm$0.04 and FoM(^{12,13}C)=1.53$\pm$0.02. The FoM values are similar for the others telescopes. No particular differences are present for this Z case if the 300-300 and 300-500μm telescopes are compared. For example, for telescope 011 we achieved the following results: FoM(^{11,12}C)=1.73$\pm$0.06

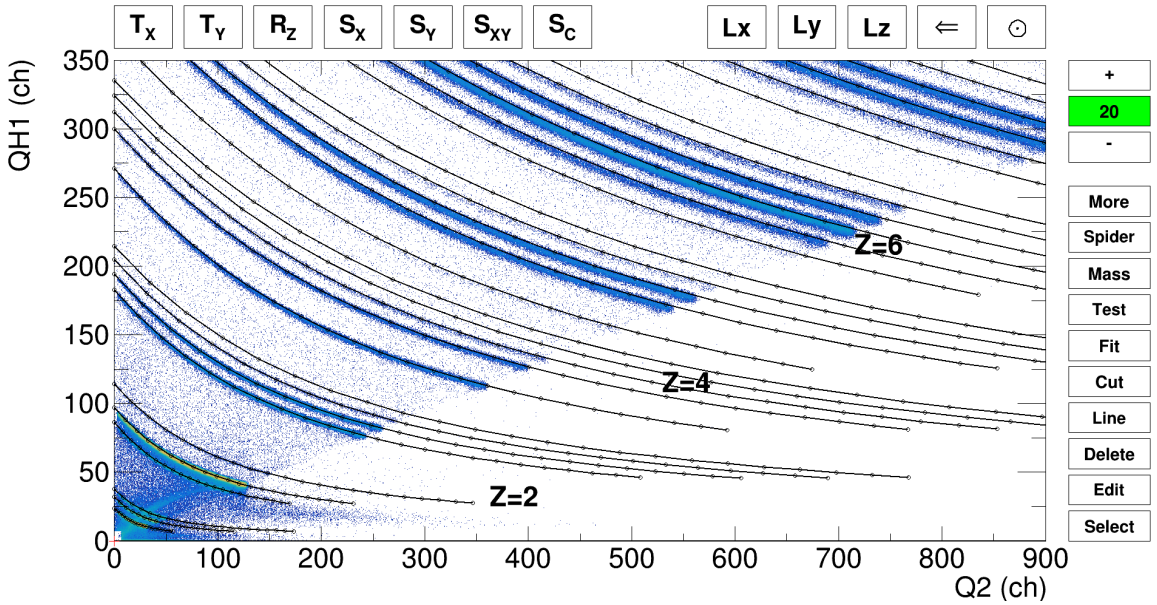

Fig. 3.7 Si1-Si2 correlation matrix for the 111 telescope (zoomed in the Z<7 region). The punching through particles have been vetoed with the CsI behind. A few Z values are indicated with labels to guide the eye.

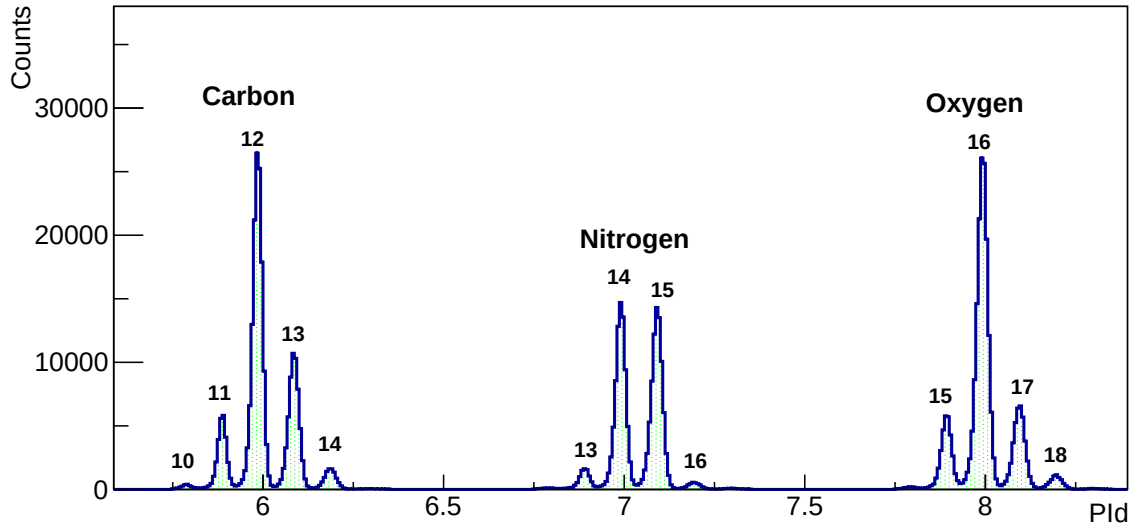

Fig. 3.8 PId distribution (telescope 111) for Z= 6, 7, 8 obtained from the grids in fig. 3.7. For each isotope the mass values are shown next to the corresponding peak.

and FoM(^{12,13}C)=1.77$\pm$0.03. As testified by the high FoM values and further checked with the fit functions, the possible isotopic contamination are well under 1%. On the other hand, the differences produced by the different Si2 thickness are noticeable towards the heavier ions. For example, if we look at the FoM values for the Si isotopes (Z=14) for the same two telescopes:

- FoM(^{28,29}Si)$_{111}$=0.92$\pm$0.04 vs FoM(^{28,29}Si)$_{011}$=0.78$\pm$0.05
- FoM(^{29,30}Si)$_{111}$=0.93$\pm$0.04 vs FoM(^{29,30}Si)$_{011}$=0.76$\pm$0.05

one can notice a significant improvement when using the 500μm Si2.

3.2.3 Si2-CsI ΔE-E

As anticipated, for the Si2-CsI it is necessary a hybrid approach. The identification procedure is separated for LCP and heavier species. In the former case, each isotope is clicked and mass assigned individually while for the latter only one line per Z is enough. The one line for isotope is necessary because the automatic mass interval procedure and interpolation algorithm are not efficient enough and the mass discrimination (especially for hydrogen isotopes) is not achieved. The ΔE-E correlations in these two Z regions are shown in fig. 3.9 and fig. 3.10. The two type of grids superimposed are also shown. The region below the red cut (under the last H line in fig. 3.9) includes two types of spurious particles. The first ones are represented by radiations which deposit energy only in CsI crystals and not in the silicon layers (noise level), such as neutrons or gamma rays. The second ones are basically protons which have undergone nuclear reactions and/or have escaped the crystal geometry without releasing completely their kinetic energy (called in the following incomplete energy deposition (IED) events). These cases, present also for alpha particles (see the tail toward low CsI signals at constant Si2-ΔE values), are excluded (only for Z=1) from the identification procedure and will be carefully discussed in Chapter 4. Moreover, a dotted line (assigned to the ^{5}He isotope), has been inserted in order to better preserve the identification metric and to better gather alpha-particles which would otherwise be lost due to the distance from its line. The particles falsely identified as ^{5}He are lately removed from the analysis. As for heavier ions, in fig. 3.10 we can see that ions up to Sodium can be isotopically separated with decreasing quality.

The quality of identification (telescope 111) is summarized with the following representative FoM values:

- FoM(^{24,25}Mg)=0.65$\pm$0.05 corresponding to ^{24}Mg contamination of 16% into ^{25}Mg

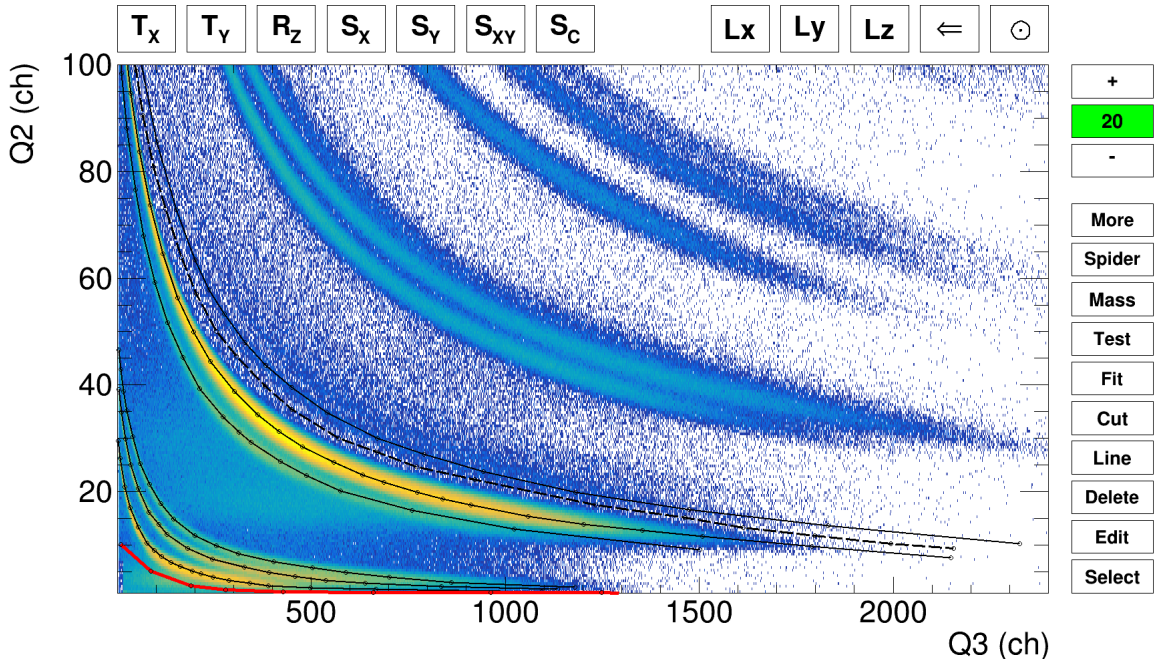

Fig. 3.9 As in 3.10, a Si2-CsI matrix for telescope 111 (zoom LCP) with the grid used for the identification superimposed. The red line delimits the region below which is excluded from the identification procedure (see text for details.) The dotted line is assigned to the ^{5}He location (see text for details).

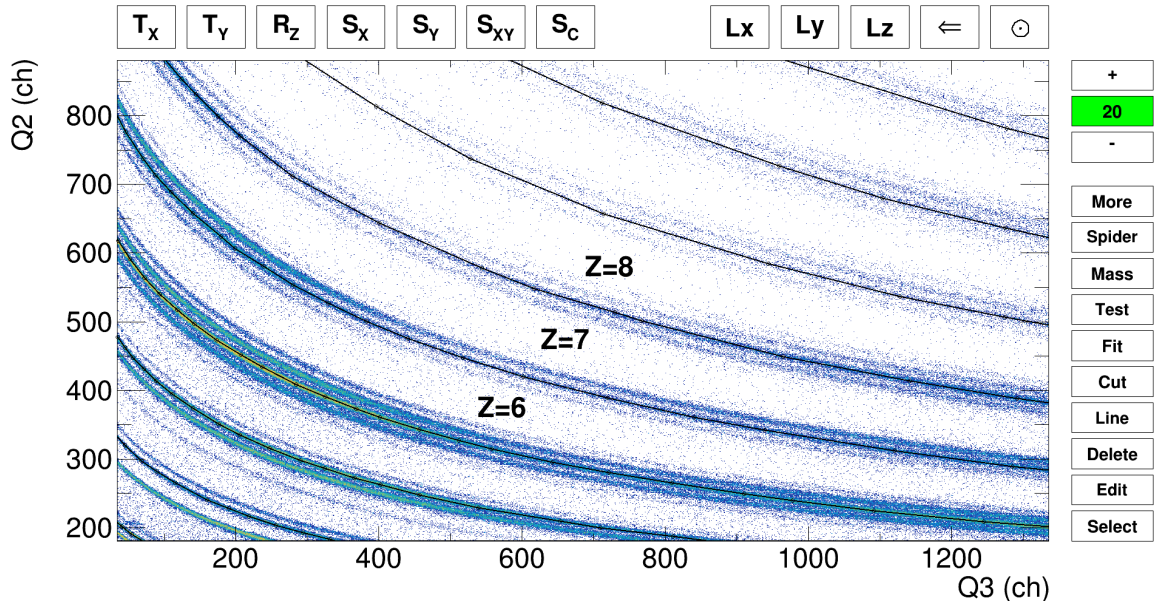

Fig. 3.10 Si2-CsI matrix for telescope 111. The figure is zoomed in the Z=6,7,8 region and the grid used for the fragment identification are shown superimposed. The data refers to all the systems, i.e ^{32}S+^{12}C and ^{20}Ne+^{12}C at 25 and 50 AMeV.

- FoM(^{11,12}C)=0.87$\pm$0.04 and FoM(^{12,13}C)=0.95$\pm$0.05 corresponding to a 3.5% ^{12}C contamination into ^{11}C and 1.3% vice versa and a 2.6% ^{12}C contamination into ^{13}C and 1.5% vice versa
- FoM(^{1,2}H)=0.91$\pm$0.05 and FoM(^{2,3}H)=0.81$\pm$0.08 corresponding to a p-d contamination of 4.5% and a d-t contamination of 8%
- FoM(^{2,3}He)=1.08$\pm$0.03 corresponding to a α-^{3}He of 3.7%

Moreover, the Si2 thickness has now a bigger impact on the identification process than for the Si-Si ΔE-E. If we repeat the same identification quality estimation on telescope 011 we obain the following values;

- FoM(^{24,25}Mg) no mass discrimination
- FoM(^{11,12}C)=0.75$\pm$0.05 and FoM(^{12,13}C)=0.84$\pm$0.05
- FoM(^{1,2}H)=0.70$\pm$0.07 and FoM(^{2,3}H)=0.71$\pm$0.08
- FoM(^{2,3}He)=1.01$\pm$0.05

We can notice from the Mg values that in the heavier ion regions the isotopic discrimination has reached the limit of 0.7 with significant contamination for the 500 μm Si2 and no mass is separated for a 300 μm Si2. Again, here the quoted values are averaged over the two beam energies. In general we noticed a clear improvement of the FoM values as the energy decreases and also a clear improvement with increasing Si2 thickness.

3.2.4 CsI PSA

In fig. 6.10a, a typical Fast vs. SlowPSA correlation matrix of telescope 111 with the grid superimposed is shown for the FAZIACor dataset (sum of all systems). Together with the identification lines (extending up to Boron) there are also two cuts (red line in fig. 6.10a). The lowest, near the Hydrogen lines defines the lower limit for the identification procedure and excludes events related to either neutral events such as gammas and/or neutrons or IED as seen aslo for the SI2-CsI matrices. On the other hand, the highest, defines the upper limit and removes those events related to IMF and heavy ions which cannot be discriminated by the CsI-PSA. This does not mean that they are lost because are well identified with the ΔE-E (SI2-CsI). In fact, the CsI-PSA, as repeated many times, comes in handy for high energy LCP particles characterized by a small release of energy in the Si layers.

Fig. 6.10d shows the PId distribution obtained by this identification method for the LCP region. One can clearly recognize p, d, t for Z=1 and ^{3}He, ^{4}He, ^{6}He for Z=2. The typical

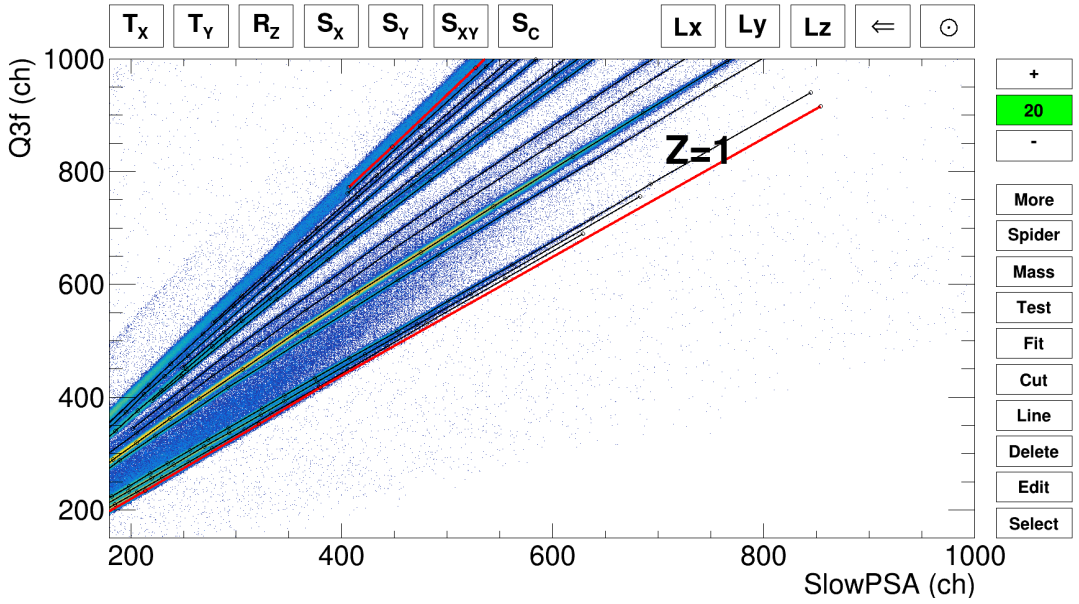

(a)

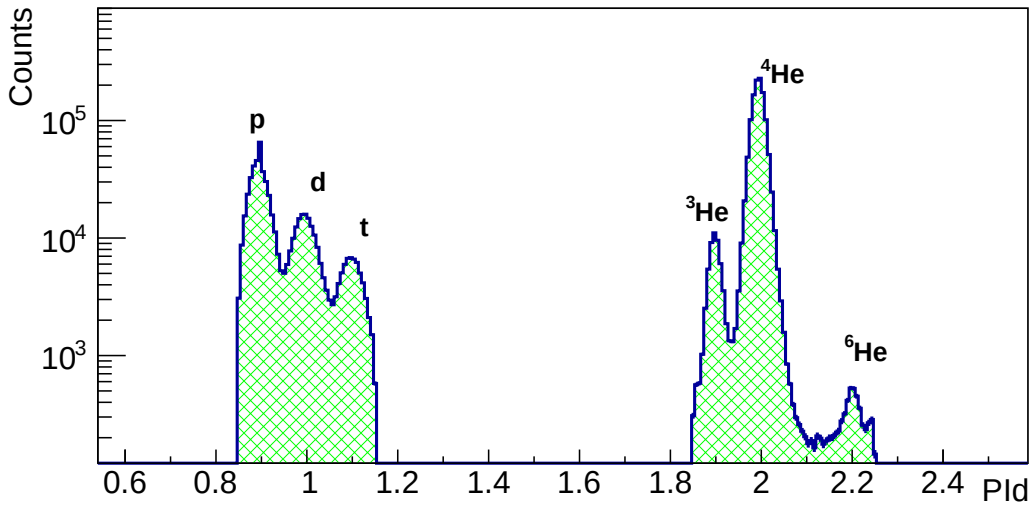

(b)

Fig. 3.11 a) Fast vs. SlowPSA correlation matrix with the grid used for identification superimposed. The matrix is zoomed, in order to show better the H and He ions. The regions below the lowest and above the highest red lines correspond to regions excluded from the identification procedure (see text for details). b) shows the PId distribution obtained for Hydrogen and Helium ions.

quality is again quoted via the FoM values: FoM(^{1,2}H)=1.26±0.05, FoM(^{2,3}H)=1.10±0.06 and FoM(^{2,3}He)=1.39±0.03. These values correspond (from the fitting procedure) to a 1.2 % p-d contamination, 1.9% d-t contamination and 0.8% ^{3}He-α contamination.

3.3 Energy calibration

After the identification step, one can proceed with the second part, namely the energy calibration. Indeed, here one can take advantage of the previous results as the identification has been done in ADC units (channels), therefore uncorrelated to the calibration procedure. The energy calibration of the silicons layers are independent while the CsI calibration will generally be based on the energy release (ΔE) in the previous detectors (Si2 layer).

3.3.1 Si calibration

For the silicon calibration, we exploit the punch-through spots of the ions just arriving up to the CsI layer. These points are fixed references and depend in principle only on the value of the silicon thicknesses. When available, the exact measured (by means of a micrometer) values were used afterwards while when not measured the nominal thickness has been assumed. The effective thickness of the detectors is important as it is used to calculate the energy loss (in MeV) in the specific Si layer. From comparison between the nominal values and a few measured values we observed a 4% and 2 % maximum variation of the thicknesses respectively for the 300 and 500 μm. In this work we used the VedaLoss tables [100] present in the Kaliveda toolkit. The code calculates ranges (and energy) for particles with an energy from 0.1 to 250 AMeV using data integrated from two databases. At low energy (E/A $<$ 2.5 MeV), ranges are taken from Northcliffe and Schilling [101], while above energy-range pairs are taken from Hubert et al. [102]. The corresponding ADC units (channels) values for the punch-through points are sampled from the experimental ΔE-E matrices (Si1-Si2). They produce various cusps in the plot, and correspond to the energy needed by a (Z,A)-ion to cross the silicons. The heavier the ion, the broader the cusp. Therefore, a limited (21 points in total) but sufficient number of ions have been employed as for the heaviest ions the cusps are not well resolved. In fig. 3.12, the correlation between the deposited energy and the measured value in channels can be seen for our reference telescope (tele-111). The calibration parameters for each telescope, have been extracted by means of a fit of the experimental points with a linear function, *i.e.* $E = a * CH + b$, knowing that silicon detectors have a linear response as a function of the deposited energy. The results of the fit (red lines in fig. 3.12) are shown superimposed to the experimental punch through points. The offsets is fixed to

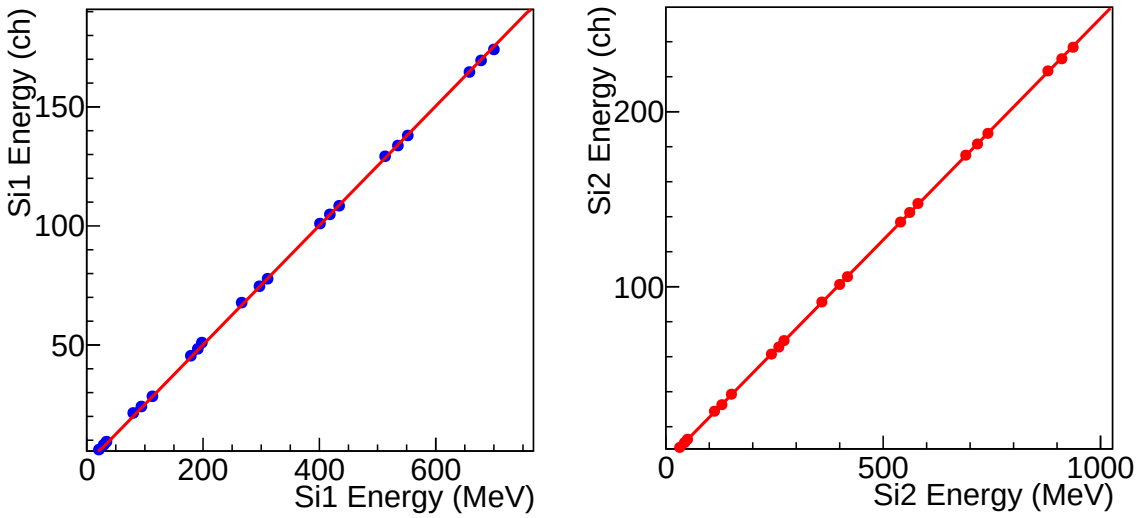

Fig. 3.12 Telescope-111 channel-energy correlation of the Si1(Si2) detector with superimposed the fit result (red line in both cases) in the left (right) panel. Errors are lower than the points size.

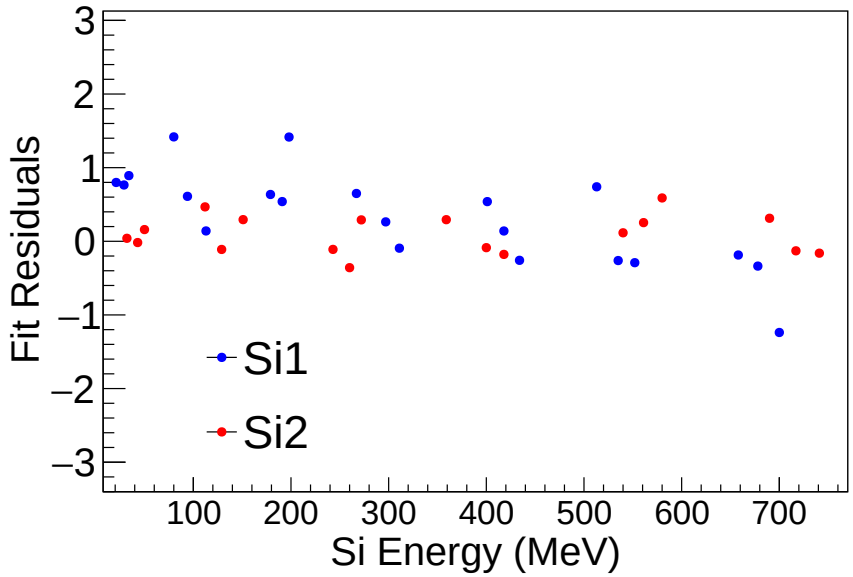

Fig. 3.13 Residues (adc/ch units) of the fit both for Si1 and Si2 of fig. 3.12, according to the legend. Data refer to the representative telescope 111.

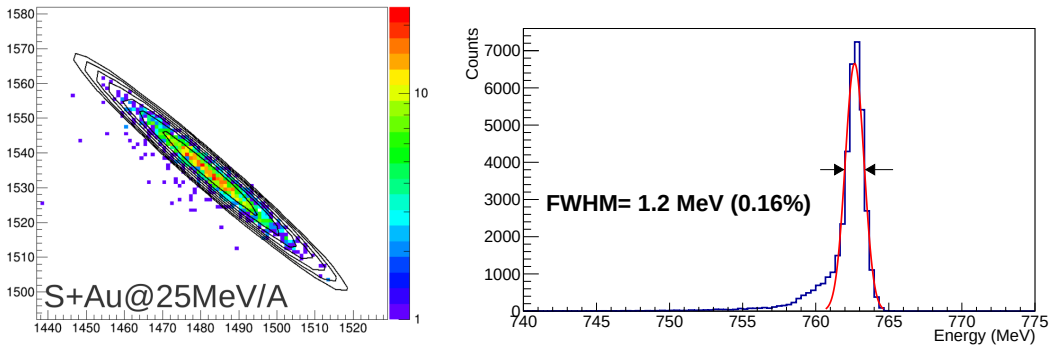

Fig. 3.14 In the left panel, a Si1-Si2 zoomed matrix in the elastic peak area is shown. In the right panel, the elastic peak calibrated with the FWHM (resolution) estimation is shown. The data refers to the ^{32}S+^{197}Au system @ 25 AMeV.

zero as the calibration line must pass through the origin because our digital treatment of the signals and of the baseline subtraction guarantees the absence of a non-zero offset. In fact, we verified that leaving "b" free the value is consistent with zero. For example, for Si2 the offset value (for tele-111) obtained from the fit is: $b = 0.157 \pm 0.131$ MeV.

In fig. 3.13, the residues of the fit procedure are presented. The blue and red points represent Si1 and Si2, respectively. The residues show a good quality (distributed closely around zero) of the energy calibration obtained with the FAZIA detector in a large range of energies. Indeed, we quote an average uncertainty of the Si1 (Si2) calibration of about 0.6% and 0.1% across the whole energy range. A good estimate of the energy resolution of Si2 can also be obtained from the elastic runs using the gold target when the projectile is stopped in the Si layers (*i.e* ^{32}S+^{297}Au and ^{20}Ne+^{297}Au @25 AMeV). An example for ^{32}S+^{12}C is shown in fig. 3.14. The peaks are extracted with a 2D Gaussian fit and then calibrated taking into account random interaction/energy loss in the target, measured silicon thicknesses and the beam energy given by the LNS beam team. This procedure is applied only to the 300-500 telescopes as even at the lower bombarding energy 25MeV/u, the Ne projectile is stopped in the second layer only if it is 500 micron (S projectiles are in any case stopped in the second layer). The obtained results are summarized in tab. 3.2. The residues of the fit can been used to further check the identification procedure. Indeed one can see, that the punch-through points are grouped in subsets of three which correspond to the isotopes of a given element for which the cusps have been resolved. They represent a benchmark for the fragment identification as if the mass would have been wrongly assigned (cannot be excluded especially for high Z tracks), one would have found strong deviations in the fit results (and residues).

Table 3.2 Energy resolution of the Si2 layer for (^{32}S+^{197}Au and ^{20}Ne+^{197}Au @ 25 AMeV).

Projectile	FWHM (MeV)	Resolution (%)
Ne	1.3	0.3
S	1.2	0.2

3.3.2 CsI calibration

The CsI energy calibration becomes mandatory only if the energy loss of impinging particles in the Si layers is very low. In fact, by looking at a Si2 *vs.* CsI matrix (fig. 3.10) one can see the ridges getting flat towards the end and becoming less correlated to the initial energy. For most of the detected ions in FAZIACor this is not the case, as generally for Z>2 the energy release in 300/500 μm of silicon is high enough. Therefore, one can employ the calibration of the Si layers and the measured ΔE to reconstruct the impinging energy of the detected fragments. However, especially for hydrogen ions the correlation is not only flat but also very close to the noise level making difficult to obtain a precise energy calibration for these particles above a certain energy. For example, protons above 100 MeV lose less than 1 MeV in 500 μm of silicon.

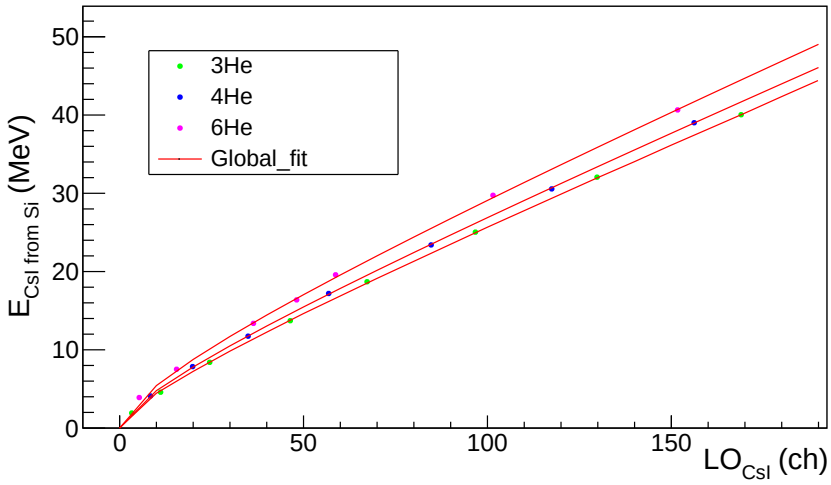

Fig. 3.15 Energy *vs.* Light Output(LO) correlation for Z=2 isotopes for the CsI crystal of the reference tele-111. The results of the global fit, by means of the analytical formula of the total light output reported in [103, 104], is shown by the red lines.

Therefore, the adopted method here is to calibrate Z>2 using the measured ΔE in the Si layer. On the other hand, for LCP (Z<3), to calibrate the CsI detectors, we took advantage

of the interval in the Si2-CsI matrix correlation where the ridges are still well separated. By means of energy loss calculations we calculate the residual energy in the CsI (in MeV) from the ΔE loss in the Si2 layer. Afterwards, one can use a functional, as the one reported in Pârlog et al. [103, 104] and shown below, to fit these points and to obtain the fit parameters a_1, a_2, a_4 characteristic of each CsI detector:

$$LO = a_1 \left\{ E \left[1 - a_2 \frac{Z^2 A}{E} ln \left(1 + \frac{1}{a_2 \frac{Z^2 A}{E}} \right) \right] + a_4 a_2 A Z^2 ln \left(\frac{E + a_2 A Z^2}{E_\delta + a_2 A Z^2} \right) \right\} \tag{3.2}$$

The adopted functional prescription has been successfully employed by the INDRA collaboration for their CsI crystals and is implemented in the KaliVeda toolkit. This fitting function expresses the non-linear relation between the light LO of the crystal and the energy deposited by a charged particle with mass A and charge Z. The parameters are as following:

- a_1: electronic gain parameter
- a_2: quenching parameter
- $\mathrm{E}_\gamma = A \cdot a_3$: the energy per nucleon threshold for the delta-electron contribution
- a_4: fractional energy loss transferred to delta-electron contribution

An example of the CsI energy in MeV units and the Light Output (LO) in channels is shown in fig. 3.15 for Z=2 isotopes, where the points are samples from the identification grid lines. The procedure is then repeated also for Z=1 to obtain a different set of parameters for each CsI detector. The default procedure was to obtain these parameters from a global fit which included both ions (Z=1 & Z=2). However, as stated also in [103, 104], the precision of the calibration is not the same for Z=1 and heavier particles if an unique set of fit parameters are used. To ameliorate the situation, a different gain and quenching parameters a_1, a_2 are needed and separate fits are employed separately for Z=1 and Z=2 lines. Indeed, in chapter4, we will show how the proton light output is practically linear from 1 MeV up to 100 MeV, and possible non linearity effects show up only at high energies while for heavier species the response function is non-linear over a very broad energy range.

To somehow test the quality of the CsI energy calibration, one can look for instance at the excitation energy of fragments that decay through particle emission, as already shown by [70] for FAZIA. By selecting particles stopped in the CsI we perform a particle-particle correlation analysis [31, 105] to access the excited states of nuclei above the particle threshold emission. In fig. 3.16, the ^{6}Li decay in alpha and deuteron particles, is shown together with the fit results of the corresponding energy level. The spectra is obtained summing over all crystals.

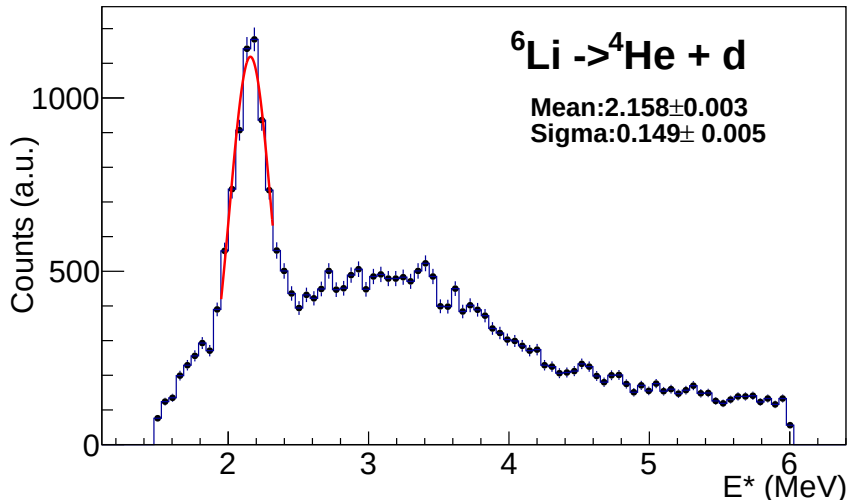

Fig. 3.16 Excitation energy spectra of ^{6}Li reconstructed from the α-d correlation from the ^{32}S+^{12}C reactions at 50 AMeV.

Table 3.3 Velocity parameters for the four FAZIACor reactions.

Reaction	25 AMeV		50 AMeV	
	V_{cm} (mm/ns)	V_{beam}(mm/ns)	V_{cm} (mm/ns)	V_{beam} (mm/ns)
^{20}Ne+^{12}C	44	70	63	100
^{32}S+^{12}C	50	70	73	100

The reconstructed peak position (2.158 MeV) is in very good agreement with the predicted postion (2.186 MeV) [106] validating the CsI energy calibration. No other peaks are easily recognizable also due to the background. This is given mainly by the uncorrelated alpha and deuteron particles arising from non-Lithium sources.

3.4 Summary of the reactions

In this section we summarize the results of the previous identification and calibration procedures. Table 3.3 shows some important reactions parameters which will result useful hereafter [1]. The starting point statistics for the data-set are shown for the four systems in table 3.4.

[1] non-relativistic kinematics: the use of classical kinematics is justified also for the higher beam energy when the gamma parameter is 1.06

Table 3.4 Table containing the available statistics for the further analysis.

Reaction	25 AMeV	50 AMeV
^{20}Ne+^{12}C	15×10^7 events	15×10^7 events
^{32}S+^{12}C	10×10^7 events	7×10^7 events

3.4.1 Identification energy thresholds

The FAZIA identification capabilities, as reported in papers summarizing the R&D phase [93, 107], are shown in fig.3.17. The different region of the identification methods are shown as a function of the fragment charge and their energy (per nucleon). The indicated limits are not as sharp as pictured here but they rather depend on the quality of the different telescopes. For example, the different Si1/Si2 thicknesses can make these boundaries move slightly. Nevertheless, it is instructive to describe the general energy thresholds of FAZIA.

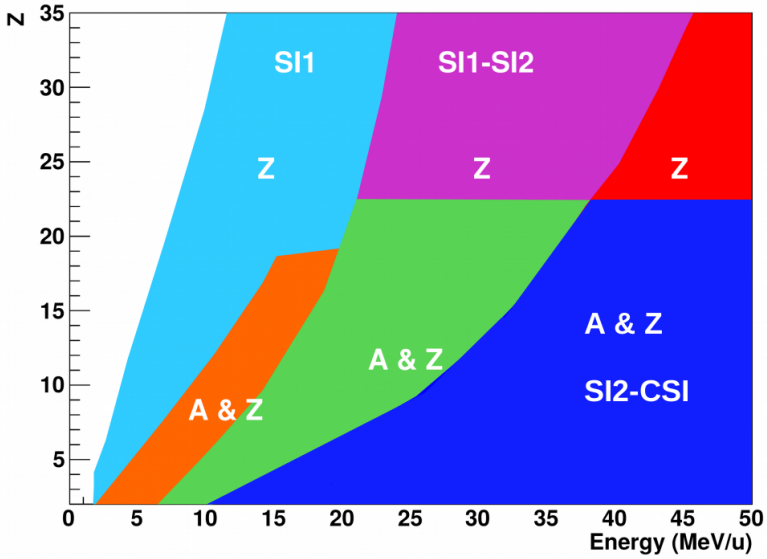

Fig. 3.17 FAZIA identification energy thresholds obtained by combing all the identification methods. The identification via Fast-Slow of CsI has not been included in this plot.

The lower energy threshold of the FAZIA apparatus is represented by the white region. This indicates the minimum energy to resolve the charge of a fragment by means of PSA in Si1. The Si-PSA area is colored cyan and orange, depending on the fragment energy. In fact, with increasing ion energy, also the mass of the fragment results accessible, up to Z$<$20 (see fig. 3.5). The ions punching through the Si1 layer are then identified via the (ΔE-E method) Si1-Si2, in charge and mass up to Z$\approx$25 (green area) and only in charge above (violet area).

Finally, fragments that reach the CsI are identified both in charge and mass (blue area) and only charge (red region) via Si2-CsI (ΔE-E method). The identification region competing to Fast-Slow correlation is not included in fig.3.17. As mentioned in sec. 3.3.2, the PSA in CsI extends the identification of light ions (LCP) above 100 MeV where the energy deposition in the silicon layers is scarce. For the present experiment FAZIACor (where the maximum Z that can be identified is Z=22), we are safely inside the regions where both charge and mass discrimination is feasible. Only a small portion of the PSA in Si1 (cyan region in fig.3.17), where only Z identification is possible, is included. Nevertheless, since for particle-particle correlations mass is important, this area is afterwards unused from this specific analysis.

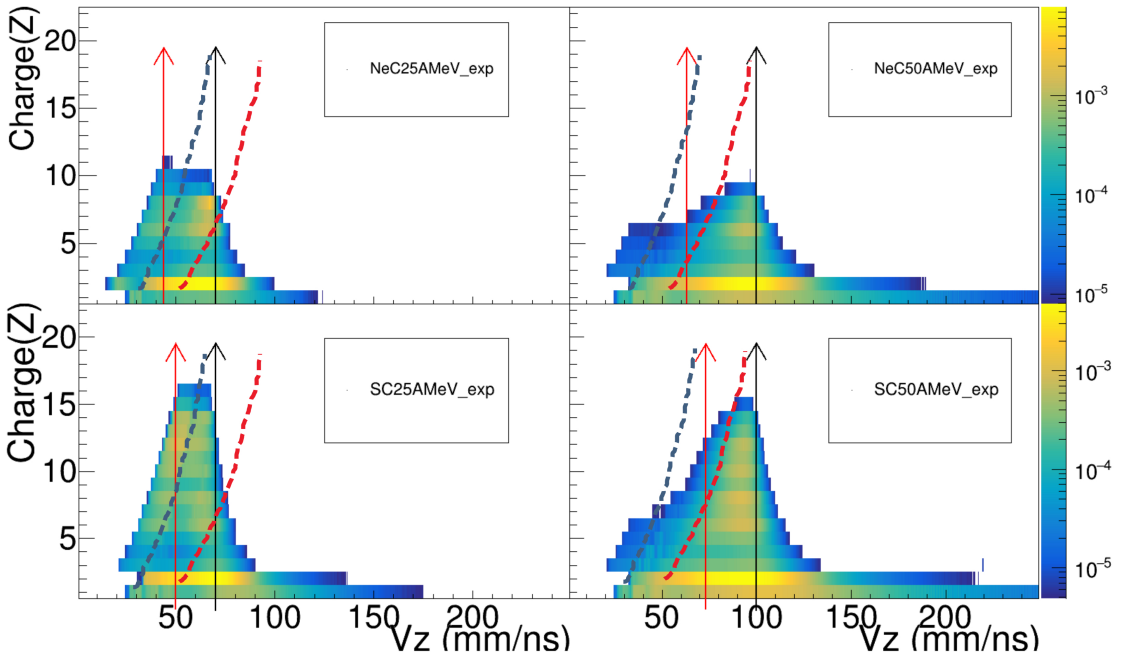

Fig. 3.18 Experimental correlations of ion charge v.s. parallel velocity in the laboratory frame for the four indicated reactions. The blue line represents the average energy threshold between PSA in Si1 and Si1-Si2 ΔE-E, while the red line the one between Si1-Si2 and Si2-CsI ΔE-E. The red arrow indicates v_{cm} and the black one shows v_{beam}.

3.4.2 Calibrated Events

In fig. 3.18 the correlation between the ion charge vs. parallel velocity in the laboratory frame is shown. This well illustrates the phase-space region covered by the different identification

methods for our four reactions. The blue and red lines represent the reference energy threshold between PSA in Si1 and Si1-Si2 ΔE-E and the one between Si1-Si2 and Si2-CsI ΔE-E, respectively. The red one in this case is representative of a 300-500 μm telescope. For the lower energy reactions (25 AMeV), the Si1-Si2 correlation is predominant in the fragment identification, while for the higher energy (50 AMeV) the Si2-CsI is mostly contributing. In general, we observe that the PSA identification method allows to identify fragments with a parallel velocity slightly (25 AMeV) or much (50 AMeV) lower than center of mass velocity. The Si1-Si2 at 25 AMeV includes both light and heavy fragments with parallel velocity above V_{cm} and lower than V_{beam}. Most of the heavy fragments (Z=6-20) are probably associated with QP remnants but incomplete fusion from central events cannot be excluded at this point. On the other hand, being the phase-space more expanded in Vz, for the 50 AMeV reactions it is easier to recognize the QP remnants from complete/incomplete fusion events. In fact, the heavy fragments at 50 AMeV are distributed around a velocity slightly lower than V_{beam} but well separated from the V_{cm} region. Another interesting fact is the change in the population of the Z>5 region. It is striking (though expected) how the beam energy increase (from 25 to 50 AMeV) tends to produce more Z<6 fragments than heavy fragments, suggesting the opening of more violent reaction mechanisms.

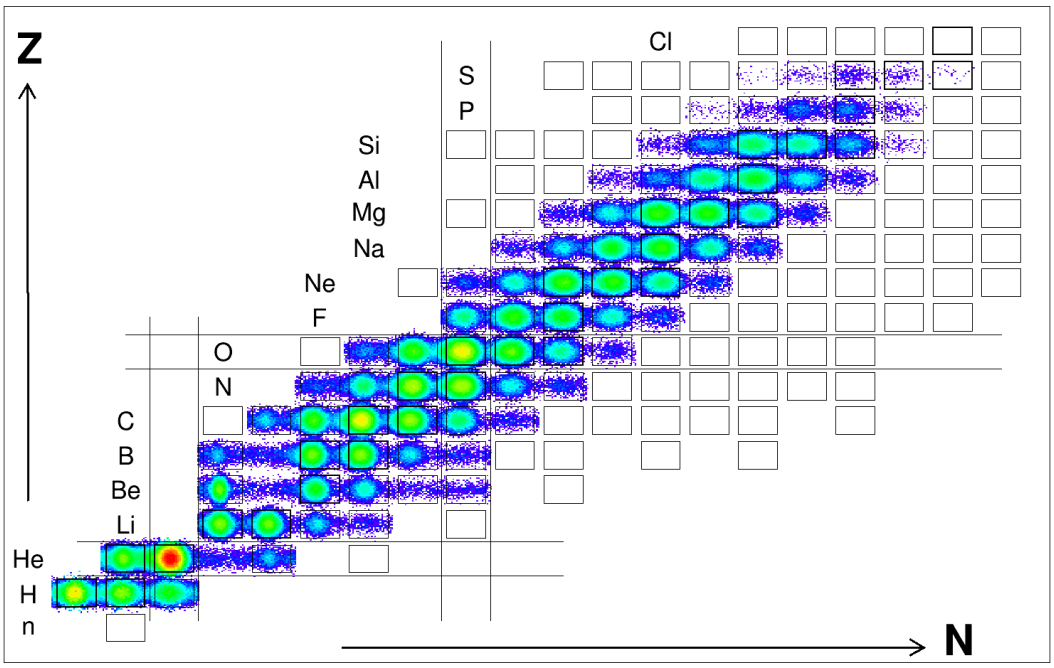

Fig. 3.19 Typical nuclide chart for the FAZIACor data-set obtained summing the ions identified through all identification methods and by all telescopes. Only ions identified both in charge and mass have been here considered.

Summarizing, the identification and calibration procedure led to a satisfactory data-set to use for the following analysis. Indeed, in fig. 3.19, a typical nuclide chart from the ^{32}S+^{12}C reaction at 25 AMeV is illustrated. The results show as a matter of fact how the identification capabilities of FAZIA are of a spectrometer level at least. The identification in charge and mass extends up to the projectile region and on average 3 well populated isotopes per Z can be resolved. The isotopic distributions are however not so broad for our systems, due to the limited entrance channel neutron availability (they are N=Z nuclear systems).

CHAPTER 4

RESPONSE OF CsI TO HIGHLY ENERGETIC PROTONS

4.1 Introduction

Particle correlation studies, besides the necessary angular resolution, request also good energy measurements. For light particles and in particular for high energy protons this is not a simple task. Indeed, with the FAZIA telescopes, like for many detectors based on Si-CsI layers [33, 60, 108], most of their kinetic energy is deposited in the CsI scintillator stage. Therefore, a special care must be paid to the energy calibration of the CsI for protons with energies above 100 MeV. Usually, the CsI energy calibration relies on the measurement of the energy in the preceding Si layers. In this way, for recognized light particles, one can transform the measured light output (LO) in energy. Afterward, one can use a functional as the one reported in Pârlog et al. [103, 104]:

$$LO = a_1 \left\{ E \left[1 - a_2 \frac{Z^2 A}{E} ln \left(1 + \frac{1}{a_2 \frac{Z^2 A}{E}} \right) \right] + a_4 a_2 A Z^2 ln \left(\frac{E + a_2 A Z^2}{E_\delta + a_2 A Z^2} \right) \right\} \tag{4.1}$$

to obtain the fit parameters a_1, a_2, a_4, characteristic of each CsI where A,Z,E refer to the stopped particle. However, for high energy particles, the energy loss in the Si-stage is limited, so the sensitivity needed to calibrate within some percent the LO in absolute energy scale is lost. Therefore, in order to provide an independent direct energy calibration, we decided to perform a test of some FAZIA crystals using monochromatic proton beams, with energies ranging from around 50 MeV to 180 MeV, close to the maximum energy that can be deposited in the crystal before punching through it.

Besides the energy calibration we wanted to address another subject closely related, namely the identification efficiency of protons. This can be spoiled by nuclear processes occurring (especially above 100 MeV) within the scintillator that reduce and/or change the features of the luminescence and thus affecting the detection efficiency. The results obtained in this experiment can be of great importance for the proper reconstruction of the energy and the yield of energetic protons measured in experiments using the FAZIA telescopes (and in general with thick CsI crystals). The subject has been investigated also by other authors and is of general interest for experiments detecting energetic light particles. During my PhD contract, I dedicated a sizable amount of activity to address this point, obtaining results that have been already published [109] and that I want also to report here, too. Most picture shown hereafter are taken/adapted from the mentioned publication.

4.2 Experimental Setup

Two FAZIA telescopes (labeled as F1 and F2 after), composed for this test by two equal Si stages (500 μm each) and a 10 cm thick CsI(Tl), were placed inside the scattering chamber of the experimental hall at Cyclotron Center Bronowice (CCB) in Krakow (see Fig 4.1). Proton beams (5-20 nA), produced with variable energy between 70 MeV and 180 MeV, were

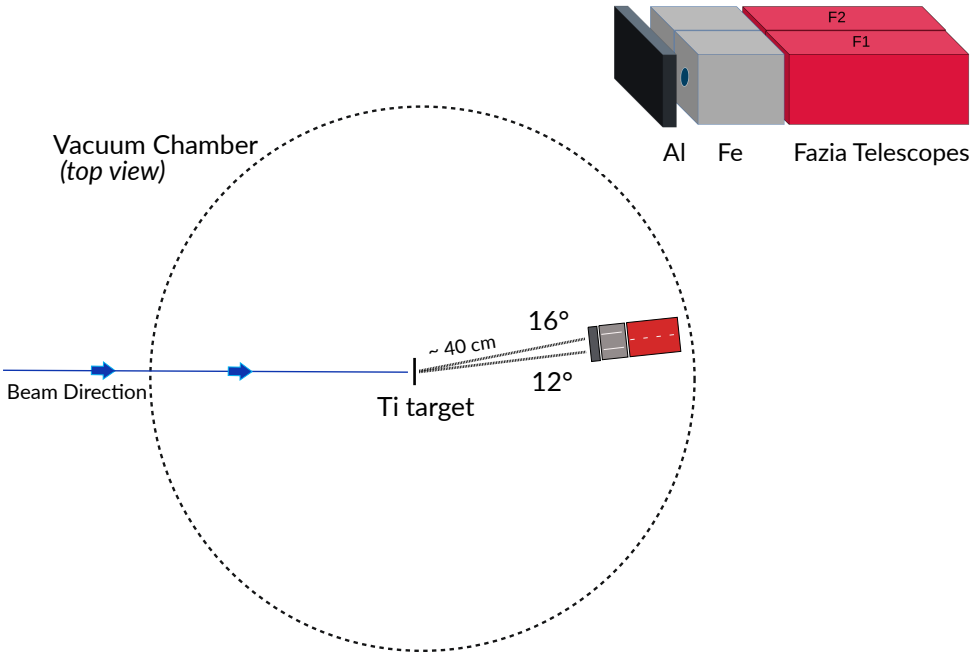

Fig. 4.1 Scheme of the layout of the experimental set-up. The iron collimators (Fe) and the aluminum (Al) absorber are shown. They are placed in front of the two FAZIA telescopes during part of the operation. The beam of protons is scattered on a titanium target and reaches the FAZIA telescopes placed at 12° and 16° on the equatorial plane of the scattering chamber.

elastically scattered by a Ti foil. The telescopes were collimated with a passive iron block (4 cm thick) with a 5 mm diameter hole so that only the central part of the active area was directly hit by protons. To reach the minimum chosen energies we used Al degraders placed in front of the telescopes (see Fig. 4.1) We remind that the FAZIA CsI have a slight tapered shape with front area being 20.4x20.4 mm^2 and the rear one being 21.7x21.7 mm^2. The entrance face is protected by a reflecting aluminized Mylar foil (2μm thick) while the lateral wrapping consists of high reflecting (98%) polymer foil (ESR Vikuiti, 3M). A photodiode (18x18 mm^2) readout is used which is coupled to the crystal with an optical glue. The experiment has been carried out in November 2018. In addition to the mentioned arguments, we also tested the portability and ease of use of the FAZIA equipment (mechanics, electronics and connections) discussed in chap.2. The entire setup, although simplified with only one block, has been mounted and fully operative in about 3 hours.

4.3 Results

4.3.1 Light Output

Figure 4.2 shows the proton energy spectra for F1 and F2 in collimated geometry, at beam energies of 80 and 180 MeV. In the described experimental setup, protons elastically scattered by the target represent only a fraction of the detected events because other contributions arise from reactions in the target and from interaction with iron collimator. To better understand the measured spectra, we started to use the GEANT4 toolkit. With this code, we simulated the experimental conditions and we verified that a sizable background contribution arises from protons scattered and partially degraded in a region next to the collimator hole. All these effects, while contributing to form an extended low-energy tail in the measured proton spectra, yet do not prevent the detection of the sharp elastic peak needed for the energy calibration. The peak position can be extracted for every energy scan with a simple Gaussian fit. Unfortunately, the background will play a major role in the efficiency calculation as we will see later. The upper panel of Fig. 4.3 shows an example (for the F1 crystal) of the measured LO vs. energy for protons. The black points are the experimental results which are being compared with two fitting functions. The first is a linear correlation while the second one is a power law ($LO = a \cdot E^b$) with “a" and “b" as free parameters as in Dell’Aquila et al. [110]. The linear fit passing through the origin (red continuous line) well fits all the measured energies in the lower energy region, while one observes a systematically increasing deviation from a straight line above about 110 MeV. This is particularly evident in the bottom panel of the Fig. 4.3 where the residuals in ADU units (red triangles for the linear fit) are shown.

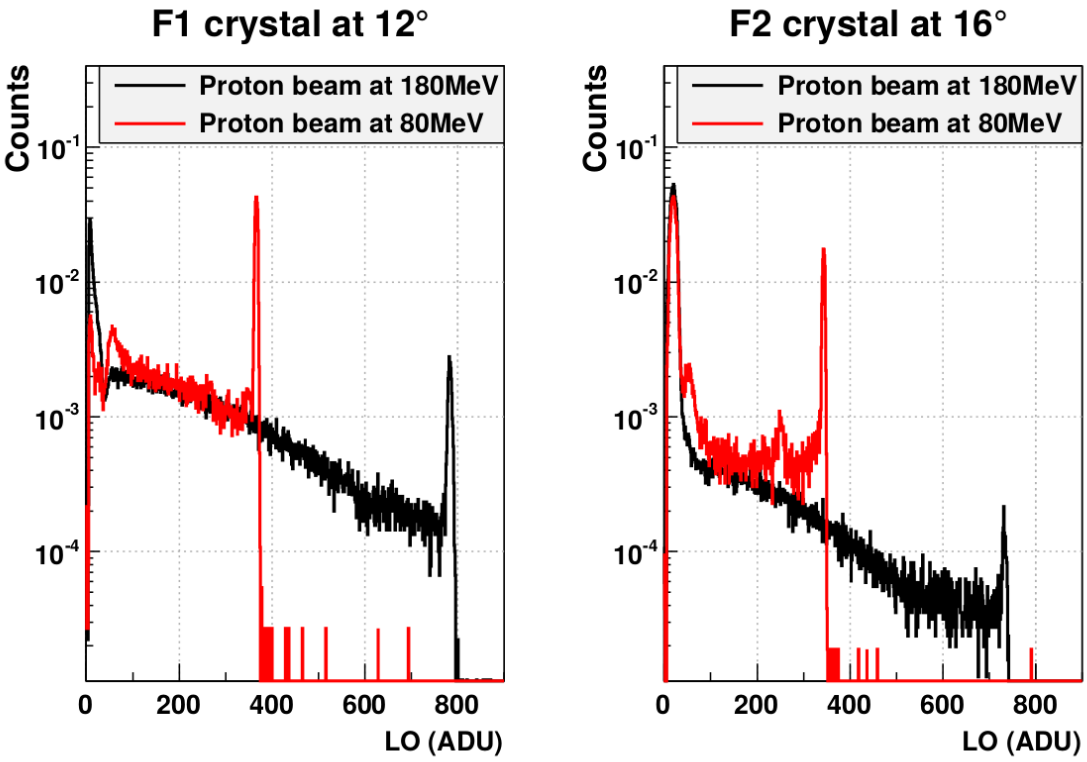

(a)

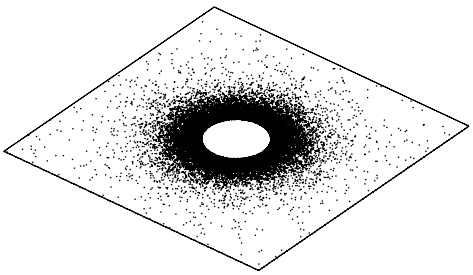

(b)

Fig. 4.2 (a) Proton light output spectra expressed in ADC units (ADU), measured with the two FAZIA CsI(Tl) crystals in the collimated configuration at two beam energies. The histogram areas are normalized to 1. (b) GEANT4 simulation showing the front face of the collimator for protons at 180 MeV. The points surrounding the hole represent the protons responsible for the observed low-E background. Figures taken from Frosin et al. [109].

This observation is in agreement with the findings reported by Dell'Aquila et al. [110] where the same power law is shown to be more suitable to describe the experimental data. The improvement from linear to power law correlation is also better appreciated by looking at the residuals (blue dots, bottom panel in Fig. 4.3) and χ^2/NDF values in tab. 4.1.

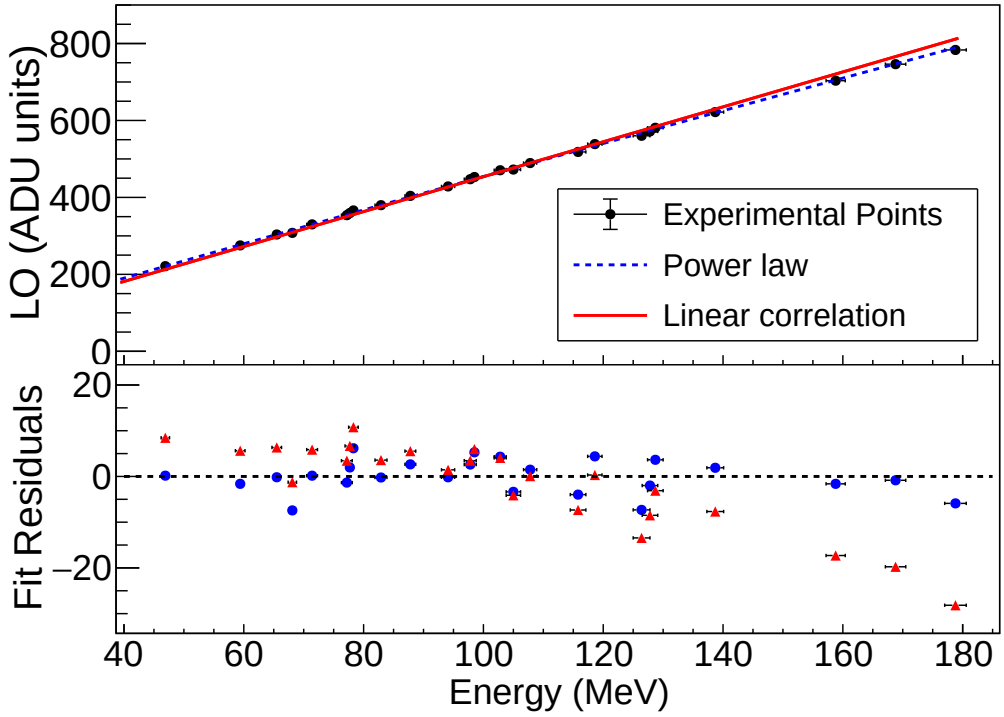

Fig. 4.3 Upper panel: experimental correlation between the Light Output expressed in ADC units (ADU) and the proton energy (black points) for the F1 crystal. The red line represents a linear fit of the experimental points while the blue dotted line is a power law fit of the data. Bottom panel: residuals of the two fits (red triangles: linear fit, blue open dots: power law). Only the statistical errors are considered here (typically 0.5 ADU for y-axis) and the beam energy is known with a nominal accuracy of $\pm 1\%$ (for x-axis). Figures taken from Frosin et al. [109].

Table 4.1 Fit parameter results for the F1 crystal with the two fitting functions (see text).

Function	Parameters	χ^2/NDF
$LO = m \cdot E$	m=4.54±0.01	59.9/20
$LO = a \cdot E^b$	a=5.91±0.02 b=0.94±0.01	9.5/19

Doping uniformity

A first cause of non-linearities can be related to the spatial (longitudinal) non-uniformity of Tl activator concentration which can alter the light output along the 10 cm thickness of the crystal. In order to check this hypothesis we measured the Tl concentrations of some FAZIA crystals exploiting the PIXE (proton induced X-ray emission) technique, available at the LABEC accelerator in Florence. From the PIXE measurements of the Fazia's CsI, shown in Fig 4.4, a 5-10 % non-uniformity of the Tl doping was evinced with the largest variation being present near the front and rear face of the crystal. This percentage of doping disparity is not sufficient to reproduce the 6% observed non uniformity in the light collection toward the rear side (outgoing side), the estimate being just around 1% [111–114]. However, we must add that the PIXE tecqnique explores mainly the most superficial layer of the crystal (20-30 micron) and deeper uniformity measurment are needed.

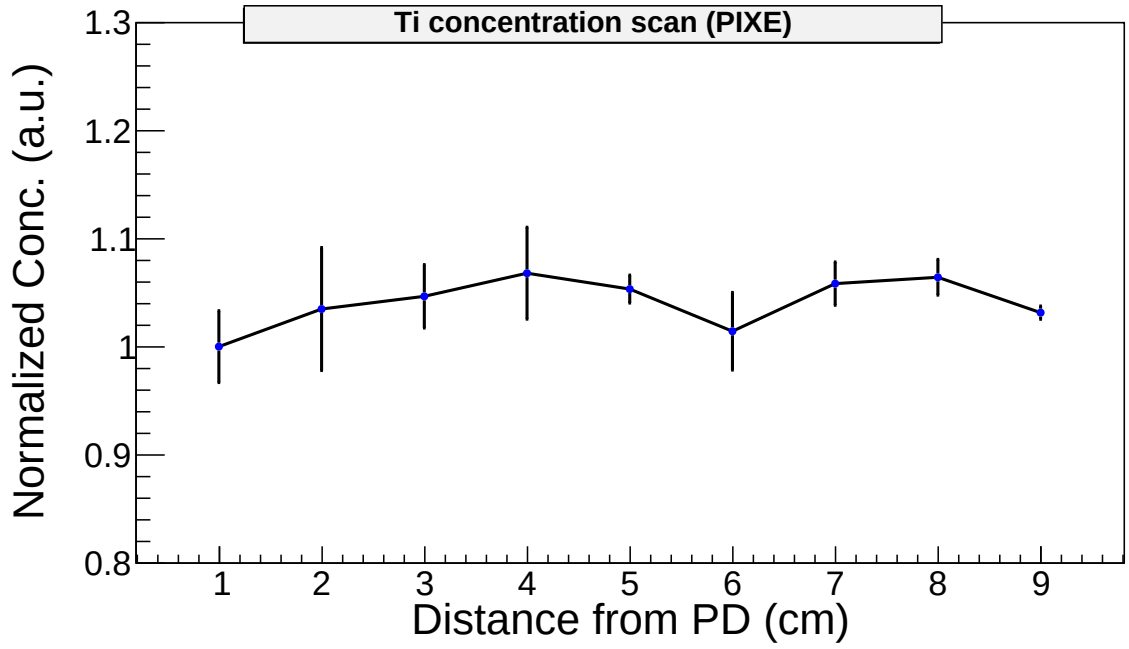

Fig. 4.4 Normalized concentration (respect to the first point) of the Tl activator concentration measured with the PIXE [112] technique as a function of the distance from the photodiode. The measured crystal is taken from the same batch as F1 and F2.

Light collection efficiency

A second cause for the observed non-linear LO response could be related to the fluorescence propagation and collection to the photodiode, namely to the light collection efficiency. Such subject has been already investigated in literature, where different geometrical shaped

(tapered/parallel) [115–117] and different materials used for the wrapping and polishing [118–121] of the crystals have been tried out. In particular, the authors of [115, 116] have shown how the light collection non-uniformity as a function of depth is effecting the energy resolution in PWO (or $PbWO_4$) and CsI crystals for shower measurements. They highlight the influence of a tapered geometry which introduces a non uniformity depending on the light generation point due to a focusing effect. Similar position sensitive response measurements were made by [117, 118] where also the roughness and wrapping of the crystals side faces have been considered together with a MonteCarlo simulation in the latter reference. In the case of a parallel crystal geometry, the main factor to influence the collected light is the intrinsic self-absorption. Therefore, a nearly homogeneous response can be observed for all regions of the crystal, if the absorption length is significantly larger than the longitudinal dimensions of the crystal which is generally the case for 10-20 cm crystals. On the contrary, tapered crystals produce a focusing of the light due to the reflection on the tapered side faces. This focussing increases the opening angle of the photons traveling towards the photo sensor and the photons have to travel a shorter distance due to a lower number of reflections until they are detected. In fact, light that undergoes specular reflections on the surface of a polished tapered crystal will, for each reflection at incoming angle θ_i, with respect to the normal relative to the central axis of the crystal, reflect into an angle $\theta_i + 2\beta$, where β is the tapering angle. The net result is therefore a relative increase in detected intensity with distance, i.e the detected light yield is enhanced, if the light is generated in the front part of the crystal. A MonteCarlo simulation was performed with the Geant4 toolkit [122] in order to convince ourselves of this effect. The treatment of the light collection is simulated by means of special Geant4 particles called optical photons with the Fazia CsI crystal. The results of such simulation is shown in fig.4.5 for a lateral gamma-ray scan where the comparison with experimental data was also made. The tapered geometry which introduces a non uniformity depending on the light generation point is overall well reproduced by the simulation although the region very close to the photodiode (PD) needs a better characterization. The disagreement between simulation and data can be related to the naive schematization in Geant due to unknowns in the experimental configuration.

As stated, the effects of non-uniformity in the light collection observed when irradiating with gamma-rays is present also for other particles such as protons. In particular, ref.[115] observed the same behavior if instead of gamma the scan is performed with energetic protons. In both the γ-rays and proton scan above, the particles were entering from the lateral sides, however if one shoots the protons from the front side with increasing energies up to the punch-through the experimental energy-range relation is the same. In fact, the Bragg peak for protons corresponds to a big energy deposition at a well defined position. Therefore, one

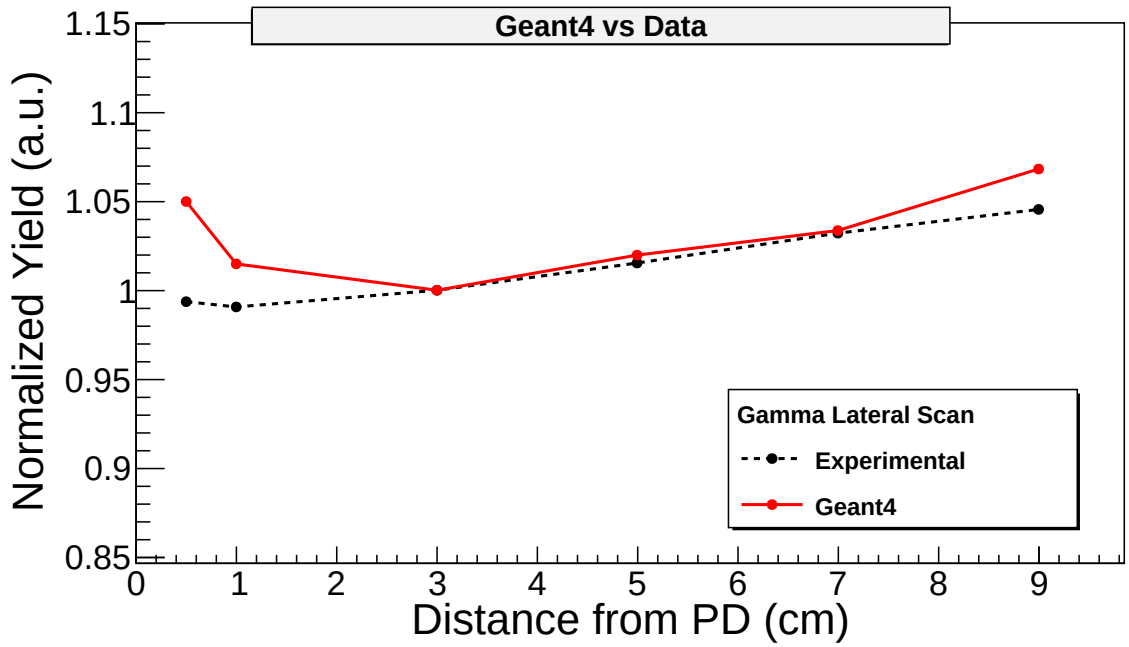

Fig. 4.5 Experimental (black points) and Geant4 (red points) results from a collimated ^{60}Co gamma source scan of a tapered Fazia crystal. The lines with the same color are drawn to guide the eye. The normalized yield to a reference point (3 cm) is shown as a function of the photodiode distance.

can perform a longitudinal scan by changing the impinging beam energy on the front face (the corrispondence is shown in table 4.2). This is the same experimental condition as in

Table 4.2 Range and distance from the photodiode of protons impinging with different energies calculated with the energy-loss tables of KaliVeda [100].

Energy (MeV)	Range (cm)	Distance from PD (cm)
190	9.6	0.4
180	8.8	1.2
160	7.2	2.8
140	5.8	4.2
120	4.4	5.6
100	3.2	6.8
80	2.2	7.8

[109, 110] and the non-linearity of the LO vs E curve for protons at high energy can in theory be caused by the light collection efficiency effects of a tapered geometry. Therefore, as a definitive proof, the same simulation performed with gamma rays was instead repeated with protons. The obtained results are shown in Fig. 4.6 were different configuration were tested.

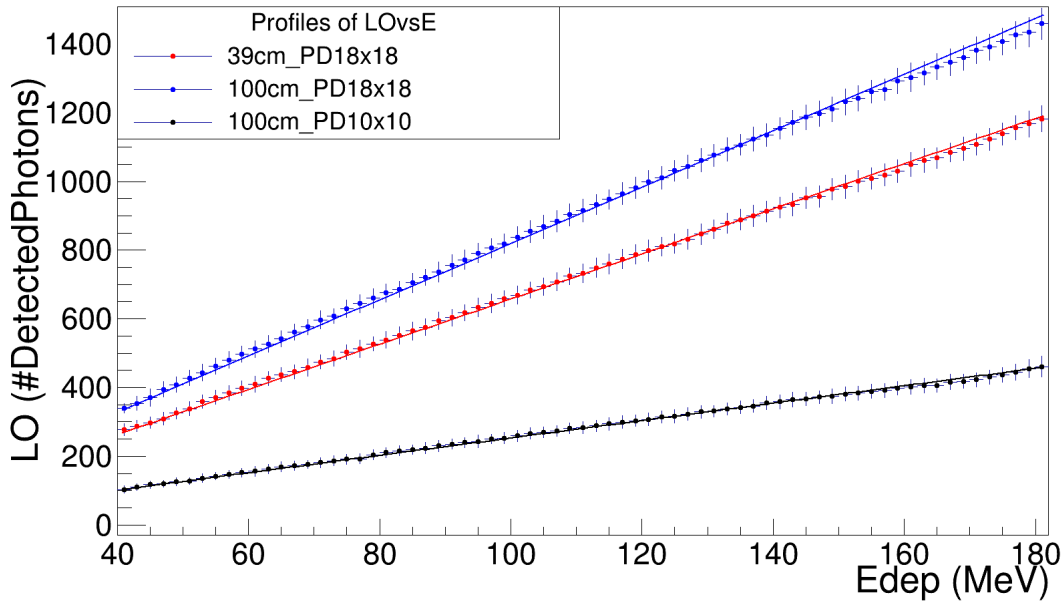

(a)

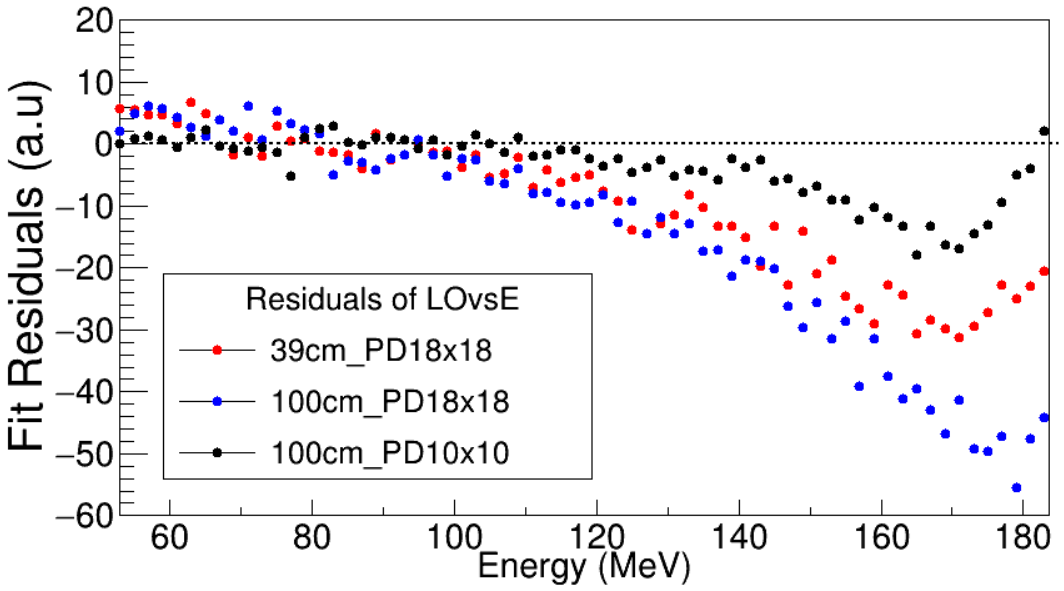

(b)

Fig. 4.6 Upper panel (a): Geant4 simulated correlation between the Light Output expressed by the number of detected photons and the proton deposited energy. The different curves represent various parametrizations for the absorption length and photodiode dimensions. The lines over the points are the linear fits performed for each curve. The geometry is that of a Fazia crystal (tapered). Bottom panel (b): residuals of the 3 fits. Only the statistical errors are considered here.

We tried to simulate the dependence of the LO with respect to both the absorption length and the photodiode dimensions. These are the two parameters which can heavily influence the results of the simulation. The blue dots in Fig. 4.6 represent ideally our experimental case. The obtained results shows that also in the simulation is present a deviation from linearity if only the light efficiency collection due to the tapered configuration is considered. We note furthermore that the starting point (around 120 MeV) of the non-linearity is correctly reproduced.

4.3.2 Efficiency

The impinging protons, while slowing-down within the crystal can experience interactions which can be summarized as:

- Elastic scattering: change of the proton direction which consequently can cause the escape from the crystal
- Inelastic scattering and/or reactions: creation of both neutral (n and γ) and secondary charged particles

Fig. 4.7 (a) (Multiple-) Elastic scattering effect. (b) Reaction and/or inelastic scattering effects. Here p stands for proton, cp for charged particles and n/γ for neutrons and gamma-rays.

The effects due to nuclear reactions in CsI(Tl), sketched in Fig. 4.7, have been reported in the past (see ref [123, 124]). They are expected to contribute in different manners to the final signal amplitude in the crystal. For example, when inelastic scattering or reactions occur, where neutrons or γ are produced, the energy deposited by the particle can be reduced because of the limited efficiency of the CsI to these particles/radiations. On the other hand, when secondary charged particles are produced the reduction of the light output is due to quenching effects which increase with charge and mass of the secondary particles. The effects due to the elastic scattering processes are usually disregarded, because their importance strongly depends on the shape of the detector. In particular, this effects is enhanced when the transversal size is narrower than the longitudinal one. The consequence of all these effects is that part of the original energy is not released in the crystal, resulting in an IED (*Incomplete Energy Deposition*) event. In Fig. 4.8, a typical ΔE-E plot, obtained with a Si-CsI telescope of the test experiment for protons of 180 MeV, is shown together with the associated locus

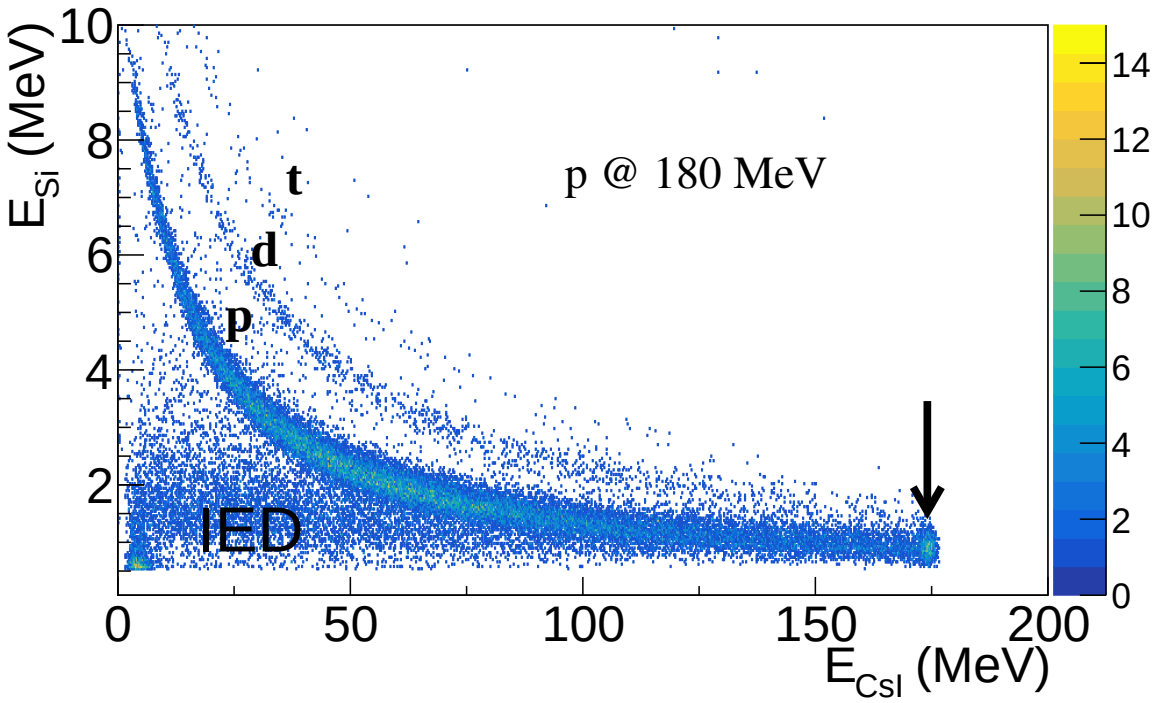

Fig. 4.8 The sum of the energies deposited in the two silicons vs. LO (calibrated) correlation for the crystal F2 in the case of 180 MeV proton beam. The vertical arrow indicates the proton elastic peak, while letters indicate the ridges of the Hydrogen isotopes and the incomplete energy deposition events (IED). Only events with an energy deposition in Silicon detectors higher than the noise level are reported.

of IED events. One can clearly recognize the IED events as those with a correct energy deposition in the Si layer(s) and a lower that expected energy deposition in the CsI(Tl) layer. Very similar plots have been often reported in the literature [124, 125].

In case of monochromatic protons with an energy E_{el}, the efficiency for a proper detection of protons can be written as:

$$\eta_{el} = \frac{N_{CED}}{N_{in}} = \frac{N_{CED}}{N_{CED} + N_{IED}} \tag{4.2}$$

where N_{in}, N_{CED} and N_{IED} are the number of protons entering the crystal with a defined energy and the complete/incomplete energy deposition subsets. In a ΔE-E telescope the selection of the N_{in} protons entering the crystal with E_{CsI} could be performed by requiring the expected deposited energy ΔE_{Si} in the silicon detector(s), while the number N_{CED} could be selected from this ensemble gating on the protons populating the elastic peak (see arrow in Fig. 4.8). However, as we anticipated, in our case we observe a sizable background due to

the passive thick collimator; the energy distribution of protons impinging on the telescope extends to values lower than the elastic peak energy (see Fig 4.8) and any selection of the deposited energy in silicons includes a non-vanishing fraction of these lower energy protons. This means that a clean selection results very difficult and we expect to have a systematic error in the efficiency evaluation. Indeed, this fact can be partially responsible

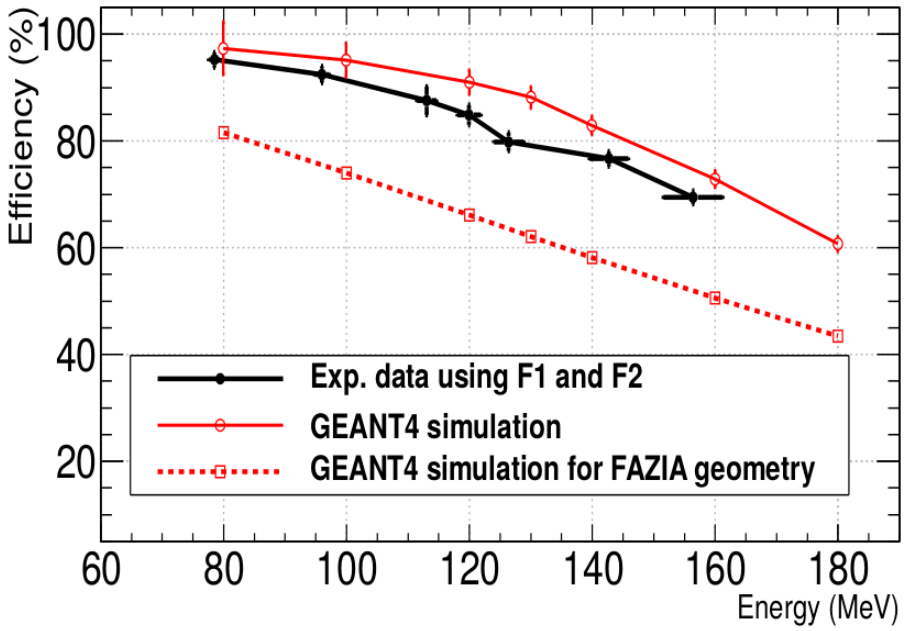

Fig. 4.9 The experimental identification efficiencies (black symbols) compared with a GEANT4 simulation (red open dots) in the collimated geometry. Open squares correspond to a GEANT4 simulation for the uncollimated geometry of FAZIA detectors. Connecting lines are to guide the eye.

for the disagreement between the measured and calculated efficiency, using the GEANT4 toolkit. This can be seen in Fig. 4.9, where the efficiency calculated from the simulation is systematically higher (continuous red line) than the experimental points (black line and points). The reasons of this mismatch are still under study. A new experiment has just been performed at CCB using this time an active collimator for a cleaner experimental condition. The analysis is still ongoing.

However, if we trust the GEANT4 simulation for our case, we can extend the calculation and obtain a first estimate of the efficiency for the FAZIA CsI crystal irradiated in the typical measurement condition which corresponds to the telescopes mounted at 100 cm from the target and without collimators. For the simulation we used the *FTFP_BERT_EMZ* [126] physics list to mimic the interaction of protons in the CsI(Tl), including also the GEANT4

option4 for optimized low-energy electromagnetic interaction. The study here briefly reported is fully described in Frosin et al. [109]. There, more details on the efficiency, errors and background estimation procedures can be found.

CHAPTER 5

MONTECARLO SIMULATIONS

In order to describe and understand the reaction dynamics of Heavy-Ion Collisions in the Fermi energy domain (20-100 MeV/u), where different phenomena can occur depending on the size of target/projectile, bombarding energies and impact parameter, different types of models with varying complexity have been devised. Among the available models, the transport models are able to give a good description of the reactions and usually the MonteCarlo simulations assume a two step reaction process. First, a dynamical phase is simulated and the interaction between projectile and target leads to the formation of one or more excited primary fragments. Subsequently, the primary fragments undergo a statistical de-excitation, often called afterburner phase, moving towards their ground state dissipating energy by means of particle emission (gamma, neutrons or charged particles) or other competitive mechanisms (fission), according to the corresponding branching ratios. Different numerical codes are available for this purpose, in particular GEMINI++ [127] and HFl [128, 129], both including the angular momentum conservation in the decay chain as it is necessary at low excitation energies, and SIMON [130], which neglects angular momentum conservation.

While the statistical de-excitation is relatively well understood and modelized using the Hauser-Feshbach formalism [131], many approaches are still being followed for the dynamical stage. The critical point is the correct accounting of many-body correlations needed to explain the complex cluster emission during the reaction at Fermi energy. In fact both should be accounted for at the same time to accurately reproduce experimental data. Two different approaches have been introduced to develop microscopic transport models for nuclear collisions; in a first family (BUU-type such as SMF [132] and BLOB [133]), the time evolution of the 1-body phase space density function is investigated while the second one is based on molecular dynamics [134]. The two "families" of models correspond to two different strategies to address the problem: roughly speaking, either introduce fluctuations and correlations through an approximate but semi-quantal approach (BUU), or exactly account

for the classical correlations but make strong hypothesis on the localization of the wave packets (MD). A different approach to the dynamical phase modelizzation consists in using a more phenomenological strategy where parameters are fitted on the experimental data and which does not correspond to the solution of a specific transport equation. This kind of method is employed for example in the HIPSE event generator [135].

In the FaziaCor experiment systems two light systems possibly reaching extreme excitation energies (from 1 AMeV up to 8 AMeV) where a multitude of exit channels can be populated (from evaporation to multifragmentation and even vaporization) are investigated. Therefore, it is challenging to find a single model able to reproduce the experimental data. As a consequence, we tried different models for both the dynamical and de-excitation phase, in order to find the description that best suits the experimental case. We decided to use primarily two combination of models. The first model we used is the Antisymmetrized Molecular Dynamics model (AMD), for the dynamical phase, and Hauser-Feshbach light (HFl) for the following statistical de-excitation. The second one is HIPSE coupled to SIMON as an afterburner. The choice in this second case was dictated by the fact that AMD cannot properly work for the lighter systems of FaziaCor (*i.e.* ^{20}Ne + ^{12}C) and is less CPU demanding in producing a simulation for the same number of events (weeks/months vs days).

The chapter is organized as following. In section 5.1 a short introduction of both AMD and HFl will be given . The same approach will be pursued also for HIPSE and SIMON in section 5.2. Finally, in the last section, the characteristics of the simulated data will be presented with a global comparison with the experimental data.

5.1 AMD and HFl

For the ^{32}S systems, we choose to adopt the AMD model due to its capability to predict in a reliable way the main features of the collisions in the Fermi energy domain, both in semi-peripheral [136, 137] and more central collisions [138–140]. The dynamical phase is assumed to be concluded at 500 fm/c from the onset of the interaction and generally the AMD calculation is been stopped at this point. For the ^{32}S+^{12}C at 25 and 50 AMeV systems we simulated approximately 60000 primary events with "b" ranging from 0 to 9 fm (i.e. from zero to the grazing parameter). The hot sources in each event are then fed to a statistical decay model. For this purpose, we employed the HFl model and for each primary event 1000 secondary events have been simulated. The results are then filtered through a software replica of the FAZIA apparatus. This kind of events will be indicated from now on by the subscript "geo". The FAZIA filter mimics the effects of the experimental angular acceptance, the energy and identification thresholds and the energy resolutions in order to be able to

perform a convincing comparison with the experimental data. When needed also the full geometry (hereafter indicated as "4π") model which will be employed to estimate important quantities such as the detection efficiency. For example at 25 AMeV the estimated event detection efficiency reaches 38% and 40% for the Ne and S beams respectively.

5.1.1 Antisymmetrized Molecular Dynamics (AMD)

Being a transport model, based on quantum molecular dynamics AMD gives the time evolution of a many-nucleon system starting from two boosted nuclei in their ground state (projectile and target) given the impact parameter and the distance between them. At each time step, the state of the system in AMD is described by a single Slater determinant of Gaussian wave packets for A nucleons [138, 139, 141, 142]:

$$\Phi(Z) = \det\left[\exp\left\{-\nu\left(\mathbf{r_j} - \frac{\mathbf{Z_i}}{\sqrt{\nu}}\right)^2 + \frac{1}{2}\mathbf{Z_i^2}\right\}\chi_{\alpha_i}(j)\right] \tag{5.1}$$

where $\mathbf{r_j}$ are the coordinates of the single particles and $\chi_{\alpha_i}(j)$ represents the spin-isospin states with α_i = p↑, p↓, n↑, or n↓. In a few words, the many-body state $\Phi(Z)$ is parametrized by a set of complex variables Z = $\mathbf{Z_i}$ with i=1,...,A. The real and imaginary parts of $\mathbf{Z_i}$ correspond to the position and momentum centroids, respectively. The width parameter ν = (2.5 fm)$^{-2}$ is a constant parameter common to all the wave packets. The time evolution of the wave packet parameters Z is determined by applying the time-dependent variational principle (see [142]):

$$\delta\int_{t_1}^{t_2}\frac{\left\langle\Phi(Z)\left|\left(i\hbar\frac{d}{dt}-H\right)\right|\Phi(Z)\right\rangle}{\langle\Phi(Z)\mid\Phi(Z)\rangle}dt = 0 \quad \text{with} \quad \delta Z(t_1) = \delta Z(t_2) = 0 \tag{5.2}$$

from which the equation of motion for Z is obtained as [140, 142]:

$$i\hbar\sum_{j\tau}C_{i\sigma,j\tau}\frac{dZ_{j\tau}}{dt} = \frac{\partial\mathscr{H}}{\partial Z^*_{i\sigma}} \quad \text{or} \quad \dot{\mathbf{Z}}_i = \{\mathbf{Z}_i, \mathscr{H}\}_{\mathrm{PB}} \tag{5.3}$$

where σ, τ = x, y, z are the labels for the components of $\mathbf{Z_i}$(i = 1, 2, ... , A) and $\mathscr{H}$ is the expectation value of the Hamiltonian operator H. The equation of motion in eq.5.4 is then solved using the Euler method with a time step Δt = 0.75 fm/c.

In addition to the mean-field effect in the equation of motion, the residual interaction needs also to be included, especially at energies of more than 10 MeV/nucleon. In a similar way to other transport models, the residual interaction has been incorporated into AMD by means of two-nucleon collisions. This effect goes beyond the mean-field approximation with

a single Slater determinant and cannot be described by a deterministic term in the equation of motion. Therefore, in the AMD model, two-nucleon collisions are implemented as stochastic transitions from an AMD state to one of the possible other AMD states. The total probability of a collision and the partial transition probabilities to specific states are calculated on the basis of the differential cross section $(\delta\sigma/\delta\Omega)_{NN}$ of the two-nucleon scattering. The NN in-medium cross section is a parameter of the model. In the version of AMD used in this work the parametrization of Coupland et al. [143] was adopted, with the screening parameter y=0.85.

Concerning the mean-field, the AMD version used in this work implements it via the effective interaction Skyrme SLy4 [144], using K_{sat} = 230 MeV for the incompressibility modulus of nuclear-matter and ρ_0= 0.16 fm^{-3} for the saturation density. For the symmetry energy, expressed as a Taylor expansion as:

$$\frac{E_{sym}(\rho)}{A} = E_{sym} + L_{sym}\cdot\left(\frac{\rho-\rho_0}{3\rho_0}\right) + \frac{1}{2}K_{sym}\cdot\left(\frac{\rho-\rho_0}{3\rho_0}\right)^2 + \ldots \tag{5.4}$$

where E_{sym} is the symmetry energy at ρ_0, L_{sym} and K_{sym} the slope and the curvature parameters, plus high order terms, two different parametrizations are available in the model. The asy-stiff, with E_{sym}= 32 MeV and L_{sym} = 108 MeV as slope parameter, and the asy-soft, with E_{sym} = 32.0 MeV and L_{sym} = 46 MeV. For our simulation, the former choice has been used since it has been demonstrated in previous studies [70, 74, 137] that it provides the most suitable description of the experimental data in the Fermi energy domain.

As stated in ref.[140], the first versions of AMD does not satisfactorily reproduce the fragmentation yields in central collisions [145, 146], underestimating the production of α particles in favor of nucleons. In the latest AMD version with cluster correlations, when two nucleons N_1 and N_2 collide with a relative velocity v_{NN}, the possibility to form a cluster is kept into account, i.e. $N_1(N_2)$ can form a cluster C_1 (C_2) with another nucleon $B_1(B_2)$ in the final state:

$$N_1\,(N_2) + B_1\,(B_2) \rightarrow C_1\,(C_2) \tag{5.5}$$

The partial differential cross section for this final channel is given by [140]:

$$v_{\mathrm{NN}} d\sigma\,(\mathrm{N_1B_1N_2B_2} \rightarrow \mathrm{C_1C_2}) = \frac{2\pi}{\hbar}\left|\left\langle \varphi_1' \mid \varphi_1^{+\mathrm{q}}\right\rangle\right|^2 \left|\left\langle \varphi_2' \mid \varphi_2^{-\mathrm{q}}\right\rangle\right|^2 |M|^2 \delta(\mathscr{H}-E)\frac{p_{\mathrm{rel}}^2 dp_{\mathrm{rel}} d\Omega}{(2\pi\hbar)^3} \tag{5.6}$$

where M is the matrix element for the two-nucleon scattering to the final state with the relative momentum p_{rel} and the scattering angle Ω in the two-nucleon center-of-mass system. The overlap matrix $\left\langle \varphi_1' | \varphi_1^{+\mathrm{q}} \right\rangle$ is taken between $|\varphi_1^{+\mathrm{q}}\rangle = e^{i\mathrm{q}\cdot\mathrm{r}_1}|\varphi_1\rangle$ and $|\varphi_1'\rangle$, where $|\varphi_1\rangle$ and

$|\varphi_1'\rangle$ are the initial and final states of the N_1 + B_1 system, respectively, and the operator $e^{iq\cdot r_1}$ gives the momentum transfer to the nucleon N_1. The clusterized states $|\varphi_1'\rangle$ and $|\varphi_2'\rangle$ are approximated by the simple harmonic oscillator $(0s)^n$ configuration with the oscillator constant associated with the wave packet width ν in AMD, so that any final state of the collision is represented by an AMD wave function. When cluster formation is turned on in the final states of two-nucleon collisions, many clusters are created in heavy-ion collisions as soon as two nuclei overlap and hard two-nucleon collisions occur. The formed clusters are then propagated by the AMD equation of motion (Eq.5.4). A cluster can be broken during the propagation either because different forces acts on the nucleons in the cluster, or more frequently because one of the nucleons in the cluster collides with another nucleon of the system.

5.1.2 Hauser-Feshbach *light*

This subsection contains a general description of the Monte Carlo Hauser-Feshbach-light code [128, 129] that has been developed in the framework of the NUCL-EX collaboration for the practical application to the problem of sequential evaporation of an excited nucleus. Hereafter, we will detail the key ingredients for the calculation of the branching ratio for the decay channels. In particular, we will describe the expression used for the decay width in a particular channel and the choice of the realistic parametrizations for the nuclear Level Density (LD). The latter has been highly constrained with experimental data and also includes all available experimental information on low-energy excitation spectra. In this way, the developed code is particularly suited to address the decay of equilibrated light nuclei, for which one expects a strong influence of nuclear structure effects even at high excitation energy. This last feature is one of the reasons for which we chose this model over other statistical models such as GEMINI++ [127]. The reliability of this code has been widely tested in the description of CN decays in the 1 to 3 AMeV excitation range [20, 31, 32, 147].

The evaporation is treated within the Hauser-Feshbach evaporation formalism [131]. The complete expression for the decay width in channel ξ for a compound nucleus in its state C (specified by the energy E and the angular momentum J) is:

$$\Gamma_\xi^C = \frac{1}{2\pi\rho_C(E^*,J)} \cdot \int_0^{E^*-Q} d\varepsilon_\xi \sum_{J_d} \sum_{j=|J-J_d|}^{J+J_d} \sum_{l=|j-s_p|}^{J} \sum_{j,s_p} (\varepsilon_\xi) \cdot \rho_d\left(E^*-Q-\varepsilon_\xi, J_d\right) \quad (5.7)$$

where ε_ξ is the relative kinetic energy of the decay products, namely the daughter nucleus labeled by the "d" subscript and the evaporated particle labeled by "p". Q represents the decay Q-value while J_d, s_p and l are the angular momentum of the daughter nucleus, the

spin of the emitted particle and the orbital angular momentum of the decay. Lastly, T is the transmission coefficient whereas $\rho_C(E^*,J)$ and $\rho_d(E^*-Q-\varepsilon_\xi,J_d)$ are the nuclear LD of the decaying nucleus and of the daughter nucleus, respectively. A simple analytical expressions is employed for light excited nuclei and the transmission coefficients are implemented as in the work of Chen and Gelbke [148]. The level density model includes in a coherent way all the available experimental information on the low energy discrete spectra. Within a phenomenological approach, the back-shifted Fermi gas model (BSFG) has been proven to well reproduce the many-body correlated nuclear level density. This model includes only two free parameters: the LD parameter $a(E^*)$ and the pairing backshift parameter E_2. In ref.[149, 150] it is shown that the BSFG model also allows an excellent fit of the complete low-lying level schemes. Therefore, the low energy level density model implemented in this Monte-Carlo simulation is the one presented in [149, 150], where the free parameters for the BSFG model have been determined for 310 nuclei (from ^{18}F to ^{251}Cf) form the fit of complete level schemes at low excitation energies and s-wave neutron resonances spacing at the neutron binding energies. Moreover, the formulas proposed by [149, 150] provide a reliable extrapolation of the LD parameters of exotic nuclei or of the nuclei which are not part of the studied data set. Nevertheless, as stated by the same authors [149, 150], the proposed model is considered trustworthy only up to energies of 15-20 MeV for nuclei with A=20. In fact, it is found that the values of the LD parameter a(E*) which well reproduce the discrete level information are normally lower than the one coming from fusion-evaporation data or evaporation-after-fragmentation studies at higher energies. To extend the LD range, the HFl Monte-Carlo code contains an expression for the a(E*, Z, N) which is able to match the formula (at low energy) with the higher energy regime. For the high excitation energy case, the functional form of Tōke and Świątecki [151] was used. Combining the two LD parametrizations with a continuous interpolation between the two energy regimes, the following functional form for the final LD a(E*) parameter was adopted:

$$a\,(E^*,A) = \begin{cases} a_D = \tilde{a}\left[1+\frac{S(Z,N)-\delta E_p}{E^*-E_2}\left(1-e^{-0.06(E^*-E_2)}\right)\right] & \text{if } E^* \leq E_m+E_2 \\ a_C = \alpha\cdot\exp\left[-\beta\,(E^*-E_2)^2\right]+a_\infty & \text{if } E^* > E_m+E_2 \end{cases} \tag{5.8}$$

where

$$a_\infty = \frac{A}{14.6}\left(1+\frac{3.114}{A^{1/3}}+\frac{5.626}{A^{2/3}}\right) \tag{5.9}$$

and S(Z, N), δE$_p$ are a shell correction term and the pairing factor [128, 129]. The α and β parameters are constrained by the matching conditions between the low energy and high

energy regimes:

$$\begin{aligned} a_D(E_m,A) &= a_C(E_m,A) \\ a_C(E_l,A) &= a_\infty \pm 10\% \end{aligned} \tag{5.10}$$

E_l represents the limiting energy at which the break-up or fragmentation regime is attained while E_m is the excitation energy marking the transition between the discrete and the continuum part of the excitation spectrum. The value of the limiting energy is fixed to 3 AMeV as this was observed to give good results for previous reactions [20, 129] in the case of A<40 nuclei. The value of E_m is fixed to approximately 10 MeV coherently with the value of the critical energy for the damping of pairing effects.

The treatment of the angular momentum is based on a semi-classical approach already used by GEMINI++ [127] where angular momenta are treated as classical vectors. At every evaporation step, a decomposition of the initial $\overrightarrow{J}$ of the decaying source into the different components is performed by taking into account the conservation of the total angular momentum. An upper limit J_{limit} for the angular momentum of a given evaporation residue with excitation energy E^* is determined by the Yrast line, namely $E^* \leq E^*_{yrast}$ with:

$$E^*_{yrast} = \frac{J_{limit}(J_{limit}-1)\hbar}{2I_d} \tag{5.11}$$

where I_d represents the moment of inertia of the daughter nucleus. In this model I_d is assumed to be that of a spherical source, thus no emission from deformed systems is considered. On the other hand, the lowest value the angular momentum can assume has to be either 0 or $1/2$ depending on the residue being an even- or odd-A nucleus. For a selected decay channel, the angular momentum J_d is obtained through a maximization of the $\rho_d(J)$ as a function of J.

With the aforementioned parameters, and the phenomenological LD, eq. 5.7 allows to calculate the widths Γ^C_ξ for all the possible decay channels and therefore the Branching Ratio associated to a particular channel ξ:

$$BR^C(\xi) = \frac{\Gamma^C_\xi}{\sum_i \Gamma^C_i} \tag{5.12}$$

This quantity simply represents the probability for the excited nucleus to decay via the ξ channel. The decay channels implemented in the code are the evaporation of light particles or of a charged fragment (always in their ground state) like: n, p, d, t, ^3He, α, ^6Li, ^7Li and ^8Be. The decay chain starting from the initial hot source is stopped whenever an excitation energy lower than the particle emission threshold (the decay Q-value) for the evaporation residue is reached. In the code, these thresholds are calculated from experimental binding

energies taken from the Audi and Wapstra online database [152]. Therefore, a complete decay chain is defined as a series of successive binary decays, in which at each step a new decaying source is formed, inheriting the characteristics of the evaporation residue of the previous step. These characteristics, such as mass, charge, excitation energy and angular momentum, come from the usual conservation laws. Once the decay channel is selected by the Monte-Carlo according to its weight BR, the relative kinetic energy of the emitted particle and the evaporation residue is extracted from the same distribution integrated for the calculation of the branching ratio. Subsequently, one checks if the ER is left with a residual excitation energy such that a discrete level of its spectrum is populated. To do so, the code accesses at each decay step a database containing all the information concerning the discrete experimental levels. This information was obtained from the online archive [106].

5.2 HIPSE and SIMON

HIPSE [135] (Heavy-Ion Phase-Space Exploration) is an event generator dedicated to the description of nuclear collisions in the Fermi energy range. It performs quite well for central and semi-peripheral collisions while it cannot account for the most peripheral reactions mechanisms such as knock-out or break-up reactions, which require the treatment of the intrinsic quantum nature of nucleons. Unlike AMD who is a microscopic transport model, HIPSE is a “phenomenological” model being somewhere in between a microscopic and statistical approach. It makes use of a geometrical hypothesis to describe the reaction which can be divided into three steps: a first approaching phase of the collision which ends when the partners of the reaction are at maximum overlap, followed by the partition formation phase and the exit channel (or after-burner) phase. The first phase is simulated by solving the classical equation of motion of the two partners in their mutual interaction potential. At this time the two nuclei are sketched as a collection of nucleons whose momentum and space distributions correspond to their ground-state boosted by the relative momentum and distance associated with maximum overlap between the two incoming nuclei. Successively, during the partition phase, a rearrangement according to the impact parameter of the reaction of the nucleons into several clusters and light particles takes place. The partition is built following simple coalescence rules in momentum and position spaces. The partition is then propagated taking into account possible re-aggregation effects due to nuclear and Coulomb interactions among the various species of the partition. Moreover, since these latter can be produced in excited states, their secondary decays are simulated by means of SIMON [130]. For the FAZIACor systems at 25 and 50 AMeV, we simulated approximately 10 million events which include both the dynamical and statistical phase with "b" ranging from 0 to the grazing value.

5.2.1 Entrance channel

Depending on the relative distance of the two nuclei different interaction approximations are used. For the phase of approach of the collision at a given beam energy E_B, a classical two-body dynamics is assumed with the interaction potential between the target and the projectile $V_{A_TA_P}(r = |\mathbf{r}_T - \mathbf{r}_P|)$.

Then a proximity potential (see [135] and reference therein) is used until the relative distance r is greater than $R_T + R_P$, where R_T and R_P are the radii of the target and the projectile, respectively. In order to obtain the potential for $r < R_T + R_P$, an interpolation has been employed for the potential between $r = 0$ and $r = R_T - R_P$. The value retained at $r = 0$ is expressed as:

$$V(r = 0) = \alpha_a V^{\text{Froz}}_{A_TA_P}(r = 0) \tag{5.13}$$

where α_a is a parameter to be fixed by comparison with experimental data defining the hardness of the potential. $V^{\text{Froz}}_{A_TA_P}(r = 0)$ is the energy of the system assuming that the two densities of the projectile and target overlap completely in the frozen density approximation. It is supposed that the collision is sufficiently fast so that the internal degrees of freedom do not have time to "re-organize" themselves and the concept of di-nuclear system persists even in the limit of overlapping target and projectile densities. In practice, the process consists in having a table for all $V^{\text{Froz}}_{A_1A_2}(r = 0)$ values for all values A_1 and A_2 using a double folding approximation [153] with the simplified Skyrme interaction of ref.[154] for the nuclear part of the interaction.

5.2.2 The partition

At the minimum distance of approach, the overlap of the two partners of the reaction depends on the impact parameter and the value assumed by the α_a parameter. As said, the spatial and momentum distributions of the (A_T, Z_T) and (A_P, Z_P) nucleons constituting the target and the projectile are assumed not to differ significantly from the ones they have in the initial ground state. This approximation, called the frozen density limit, is explicitly used to sample the positions and momenta of the nucleons in the center of mass of each partner of the reaction.

In order to define the quasi-projectile and the quasi-target fragments the so-called participant-spectator picture is employed. This corresponds to assume that nucleons which do not lie inside the overlap region constitute the quasi-projectile (QP) and quasi-target (QT) fragments. Such a simplified approach is not however exempt from flaws in the energy regime considered here. In particular, the QP and/ or QT fragments have experimental kinetic energies which are reduced with respect to the initial ones. This effect is ascribed to

the exchange of particles between the two partners during the reaction. In the model, this exchange is introduced "by hand" assuming that a fraction x_{tr} of the nucleons from the target (projectile) now located in the overlap region are transferred to the projectile (target). The number x_{tr} of transferred nucleons decreases with the beam energy. Furthermore, when the beam energy increases, pre-equilibrium emission can further deplete nucleons from this region. These light particles with large transverse momenta are generally assigned to promptly emitted particles induced by hard nucleon-nucleon collisions. Therefore, to include this phenomena, in the model has been introduced the x_{coll} parameter which represents the percentage of occurring nucleon-nucleon collisions. These collisions, whose effects increase with increasing beam energy, tend also to wash out the memory of the entrance channel, and may eventually lead to the formation of a compound-like state.

After these steps, the remaining nucleons inside the overlap region will then constitute the reservoir for building particles and/or light clusters. The method used to create fragments is based on a coalescence algorithm as follows. First, one nucleon is randomly chosen to constitute the coalescence point. Then, another randomly chosen nucleon "i" in the overlap region can be captured by the cluster according to two criteria:

1. Existence condition: test if the composite nucleus is known (in particular, its binding energy) by checking its presence in an experimental mass table.

2. Position and momentum conditions: only nucleons that are close enough in phase space to the considered fragment can be absorbed.

If the two preceding conditions are fulfilled, the nucleon is absorbed by the fragment and the position and momentum of the cluster of mass $A_1 = 2$ is recalculated according to the positions and momenta of its constituents. If one of the conditions is not met, the nucleon serves as a new coalescence point and the procedure is re-iterated.

5.2.3 Exit channel

At the end of the previously described steps, one ends up with a set of N_{frag}^{ini} fragments (including the QP and QT) with the mass number, position, momentum, and angular momentum (A_f , R_f , P_f , L_f) obtained from the characteristics of the nucleons belonging to each fragment. From this point on, a "clock" is started corresponding to t = 0 fm/c for the forthcoming dynamics which consists in the final state interaction and a re-aggregation phase. Because these fragments are created in a high density region, they can overlap during times comparable to the reaction time (typically a few tens of fm/c) and it is necessaty to propagate the partition before freeze-out is reached. This is achieved during the first 50 fm/c

according to their mutual interacting potentials. The same interaction potentials as for the entrance channel part of the reaction are used. At low incident energy, it may also happen that most of the fragments produced in a highly fragmented partition will fuse because their relative energy is lower than the fusion barrier, producing a single composite system. Thus according to the incident energy, the re-aggregation phase allows to smoothly explore mechanisms between complete or incomplete fusion up to the pure participant-spectator picture. After testing all possible fusions of fragment pairs, the chemical freeze-out is reached and modifications of fragment mass are no more possible. Moreover, the total energy balance in the center of mass frame is checked and if the excitation energy is negative the partition is rejected as it corresponds to an inaccessible phase-space region.

The following interaction between the fragments is purely Coulombian and since the fragments emerge with a sizable excitation, their further decay is described by means of a statistical evaporation code assuming a thermalization process has just taken place (after a few hundreds of fm/c). This last part is taken into account by SIMON which, much as HFl or GEMINI++, simulates all the possible decay channels from neutron evaporation up to symmetric fission.

To conclude, the HIPSE model has overall three freely adjustable parameters (α_a, x_{tr} and x_{coll}), which depend on the incident beam energy. Their energy dependence and the used values for the FAZIACor beam energies are listed in Table 5.1. We tried also to vary these parameters in an reasonable interval for each energy to see the variation with respect to the experimental data. However, the coarse nature of the reaction does not change significantly when compared with the experimental points.

Table 5.1 The values used for the corresponding beam energies of the FAZIACor experiment as determined by [155].

E_{beam}(AMeV)	α_a	x_{tr}	x_{coll}
25	0.10	0.45	0.02
50	0.20	0.30	0.05

5.3 Comparison of models and global observables

The models described above are now compared among them and with experimental data for the FAZIACor experiment. In this latter case the models are filtered with the software replica of the apparatus to take into account the geometrical and experimental threshold effects. In these model and data comparisons, although very interesting, we would like to specify

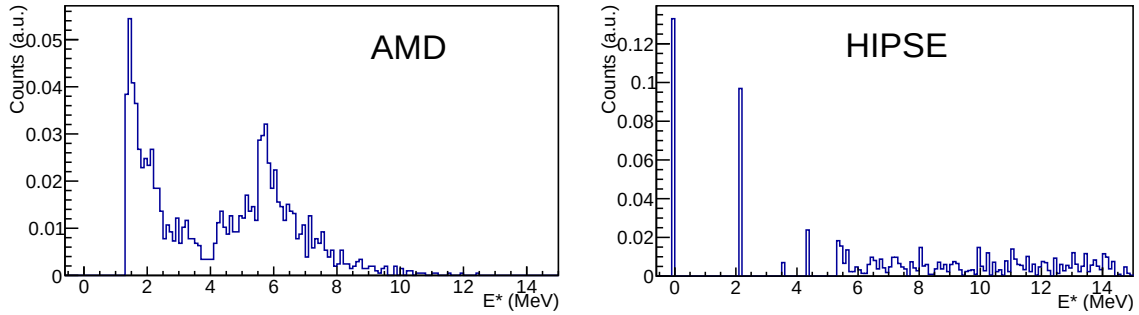

Fig. 5.1 ^{6}Li excitation spectra of primary fragments for ^{32}S+^{12}C @ 25 AMeV. Left panel shows the AMD results while the right one plots the results from HIPSE. The spectra are normalized to the total ^{6}Li events.

that model ingredients are inherently not fully comparable. In fact, AMD tries to treat the many-body time-dependent quantum problem and predicts all the observables of the whole reaction starting from nucleons interacting through a realistic though effective Hamiltonian (and getting information on this hamiltonian through the comparison with the data). This is somehow different from the phenomenological approach of the HIPSE event generator which is generally optimized to experimental data.

We start by first evaluating the differences at the primary fragments level. A striking characteristic of HIPSE is that for the primary fragments the excitation energy of the various nuclei present all the known discrete levels, while for AMD the spectra are continuous and the discrete nature is sometimes present only because of the clustering procedure (even though not associated with an existing experimental known level). In fact, one can notice (fig.5.1), for example for the ^{6}Li case, that the excitation energy spectrum for AMD starts from the d+α threshold while for HIPSE it includes also many levels starting from the ground state. This can be easily understood as AMD has a very simplified ansatz for the wave functions and can be essentially considered as a classical model (localized nucleons) that cannot explain the excited nuclear levels; while the same levels are implemented by hand in HIPSE.

Moreover, the excitation energy profile is also somehow different at this level (see fig.5.2). Here, one can clearly notice how the excitation energies per nucleon reached by the heavy (Z>5) primary fragments are much higher (as shown in fig.5.2) for HIPSE than for AMD where they are considerably lower. For example, in the SC@50AMeV system the E*/A of HIPSE easily exceeds the multifragmentation threshold (3 AMeV) going towards more central collisions. On the other hand, in AMD a sort of saturation is reached for b/b$_{gr}$<0.6 which also seems to be independent of the incident beam energy. This effect is partially due to the stopping time of the dynamical phase. For AMD this value has been chosen, on the basis of previous FAZIA experiments, to be 500 fm/c while for HIPSE is around

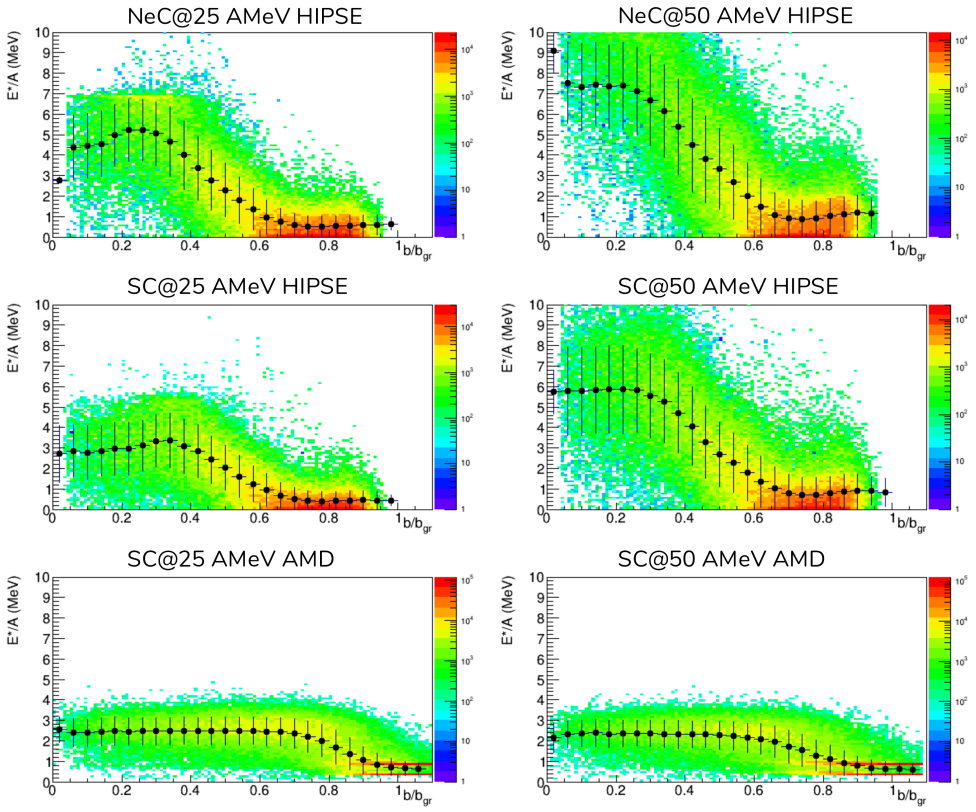

Fig. 5.2 Excitation energy per nucleon for the Z>5 primary fragments of HIPSE and AMD (4π). The systems of FAZIACor are indicated over each panel. The black points represents the x-axis profile of the E*/A variable (i.e. mean trend with b) and the associated errors are the standard error on the mean of E*/A.

150 fm/c as previously described. This means that in the former case the propagation time can be sufficiently long for the fragments to already dissipate part of their energy after the separation/fusion time of the two nuclei including processes as fragmentation or dynamical LCP emission. Looking at AMD backwards in time this becomes evident as shown in fig.5.3 for the SC@50 AMeV system screenshots at 100 and 300 fm/c are presented. However, even at 100 fm/c, the mean excitation energy of AMD is significantly lower especially for the most central collisions. Whatever one considers as an optimal choice of the stopping time of the dynamical phase, the final proof is given by the agreement of the models with the experimental data. The important thing to remember is that different afterburners have different excitation energy intervals where they provide optimized results. For example, both HFl and Gemini++ are considered reliable up to E*/A energies of 3 AMeV [127, 128, 156]. Therefore, in this last part of this section, we look at global observables considering also the afterburner phase. Both experimental and model data are shown only for events with particle

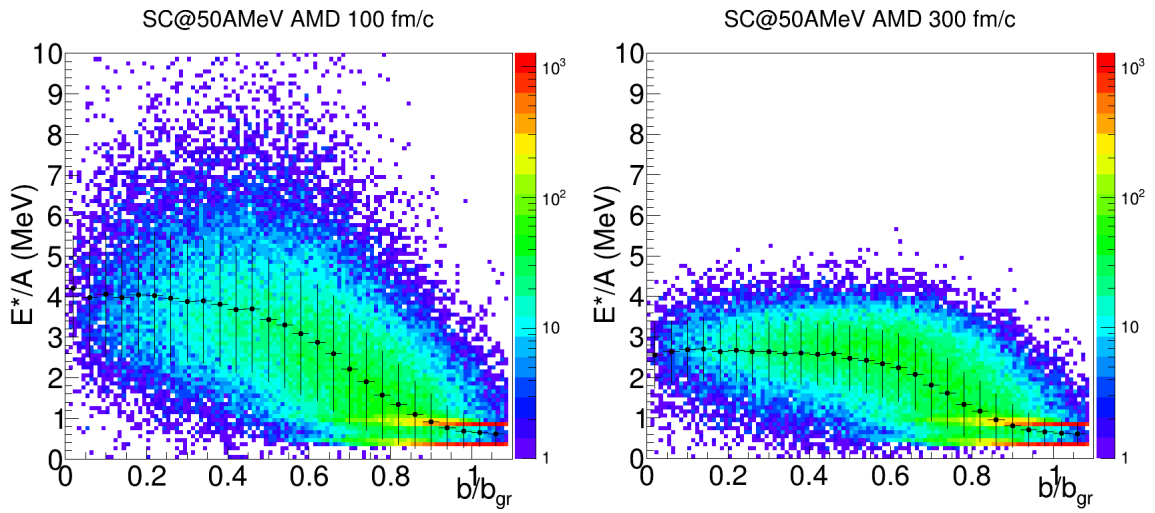

Fig. 5.3 Excitation energy per nucleon for the Z>5 primary fragments of AMD (4π) for SC@50 AMeV. The plots are identical to those of fig.5.2 just taken at 100 fm/c (left) and 300 fm/c (right).

multiplicity $M_{tot} \geq 2$ due to the acquisition trigger which required the telescope multiplicity $M_{fired} \geq 2$. Unfortunately, due to the latter trigger condition, this implies that pure single hit elastic events or one particle events (low coverage) are mainly discarded and only acquired if accompanied by noise signals which exceed the acquisition threshold. Therefore, we do not acquire the largest part of M=1 events which is clearly underestimated in the experimental data. However, from the physics point of view these events are not interesting as we cannot generate correlations or study in-depth the kinematics of the event due to the poor angular coverage. Therefore, M=1 events are rejected in the further analysis.

A convenient observable to address the kinematics and the topology of the reaction is the usual bi-dimensional correlation between the atomic number and the parallel velocity of all emitted particles. These are shown in fig.5.4 and fig.5.5 for the experimental data and model predictions, respectively. The red and black arrows indicate the center of mass and beam velocities of the respective systems as a guideline. The general trends of the experimental data are reproduced by the simulation even though some differences are clearly noticeable. First of all, it seems like the models tend to less populate the region around v_{cm}, especially for Z>6 fragments. In order to better highlight these differences the corresponding Z and Vz projections are shown in fig.5.6 and fig.5.7 where the experimental points are compared to the available model predictions. Looking at the Z distributions, one clearly sees how for the NeC systems the HIPSE model predicts a lower energy dissipation as the heavy fragment part is shifted towards heaver elements, i.e. the projectile-like elements are more populated.

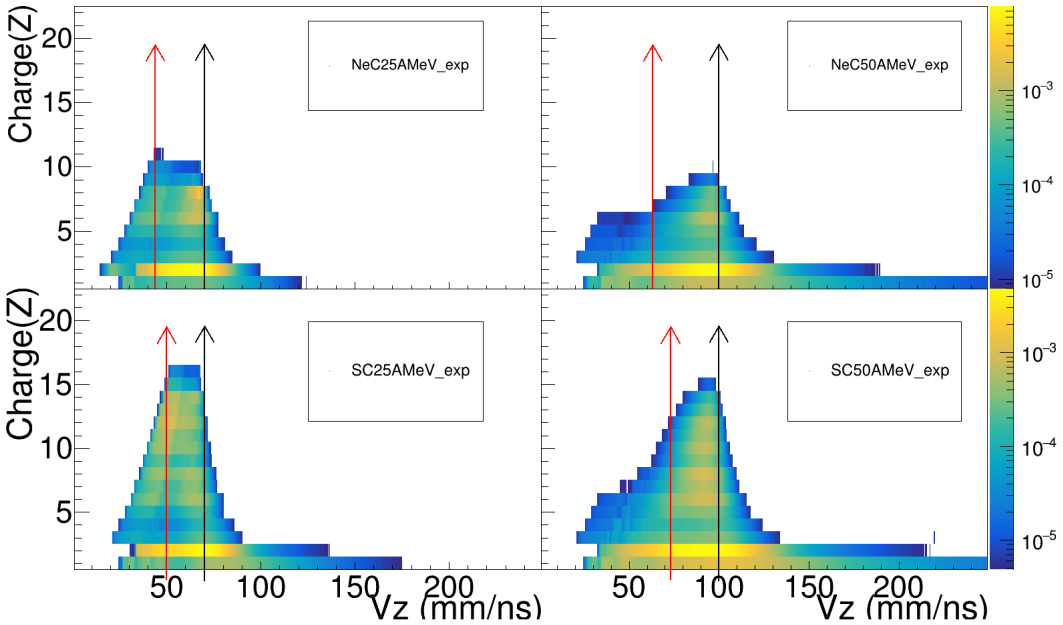

Fig. 5.4 Experimental correlations of ion charge v.s. parallel velocity in the laboratory frame for the four indicated reactions. The red and black arrows indicate the center of mass and projectile velocities respectively.

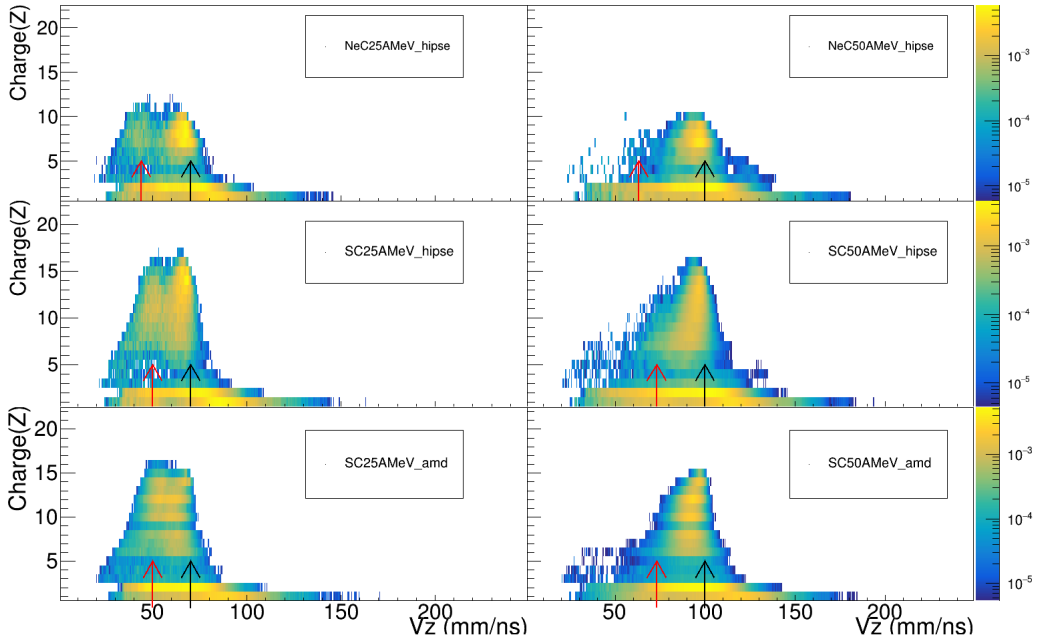

Fig. 5.5 Simulation correlations of ion charge v.s. parallel velocity in the laboratory frame for the four indicated reactions after the FAZIA filter. The red and black arrows indicate the center of mass and projectile velocities respectively.

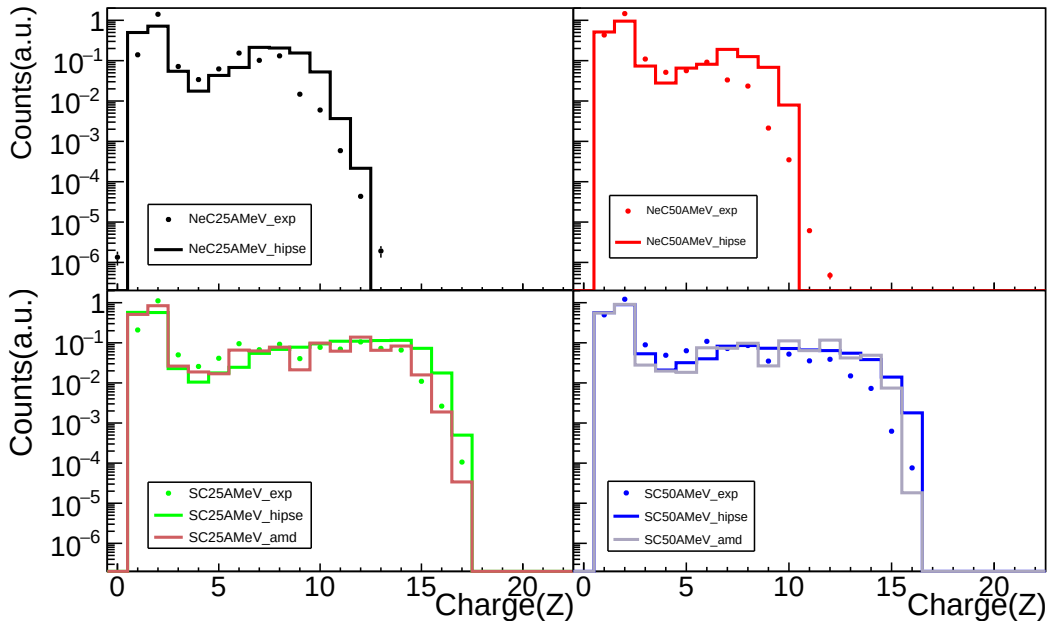

Fig. 5.6 Experimental data vs. model predictions for the Z distribution for the four reactions and available models. The distributions are normalized to the total event number.

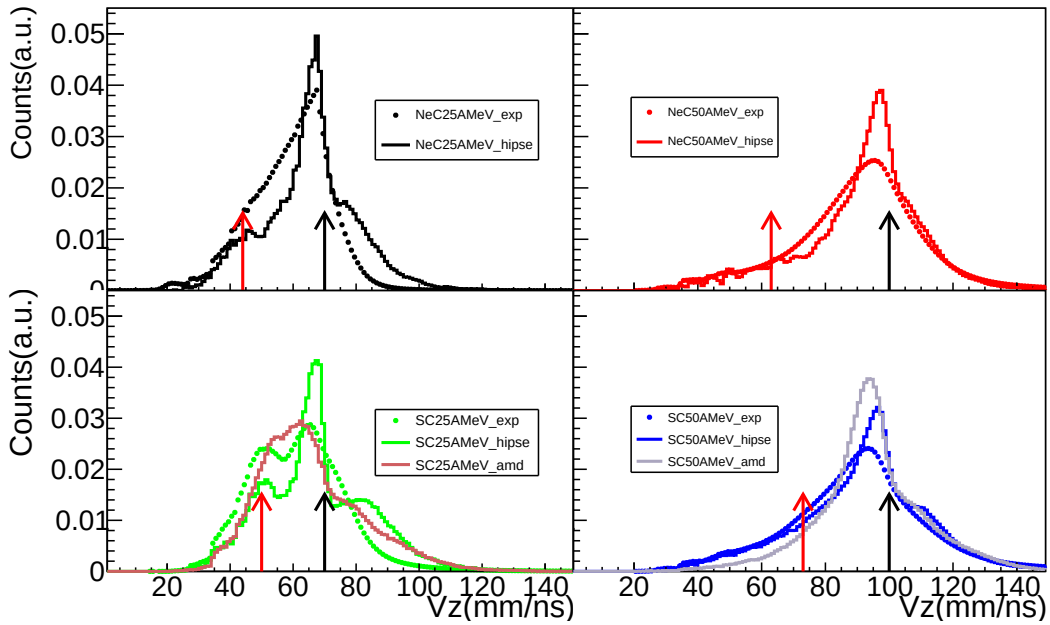

Fig. 5.7 Experimental data vs. model predictions for the Vz distribution (lab frame of reference) specified for the four indicated reactions and available models. The distributions are normalized to the integral for a better shape comparison. The red and black arrows indicate the center of mass and projectile velocities respectively.

The same considerations are true for the SC systems as far as HIPSE and AMD at 50 AMeV are regarded while AMD at 25 AMeV seems to better reproduce the overall shape and yield keeping track also of the staggering effect observed in the experimental data. However, if one looks at the Vz distribution in fig.5.7 we see how HIPSE is better at reproducing the overall shape of the particle velocities and the various peak components of the spectra although it is not totally accurate in reproducing the yields. In particular, the experimental distributions at 50 AMeV are wider and at 25 present a more pronounced center of mass peak with respect to the model prediction. Another interesting feature is that all models are underestimating the alpha particle production and overestimating the hydrogen yield. This is known to be a common characteristic of light N=Z nuclei where the alpha clustering effects may play an important role not only in the dynamical phase but also in the following statistical decay [20, 31, 105, 157]

For the following analysis, we will continue to show the comparison with both models (when available) since neither models is overwhelmingly better than the other. In the next chapter we will study the experimental data with more exclusive selections and through different observables.

CHAPTER 6

REACTION MECHANISMS AND PARTICLE CORRELATIONS

In sec.5.3, we have already presented some general measured characteristics of the FAZIACor reactions comparing them with the model results. Here we deepen the analysis on various observables related to the selected events. These are defined as events containing (at least two) particles identified both in charge and mass. The criteria adopted to deal with the different reaction channels will be presented, as well as their gross properties. In one of these channels, we show the chemical compositions of the fragments, obtained thanks to the excellent isotopic separation allowed by the FAZIA telescopes and we compare the results with those of fragments produced in other reactions at Fermi energies, in order to search for possible systematic features. Then we will try to enter more into the details of the reaction mechanisms and in particular to study incomplete and complete fusion estimating their relative/absolute cross sections with a kinematical analysis. Further information on the reaction mechanism and fragment production will be obtained by means of particle correlations as explained in the introduction. A first attempt to put into evidence possible in-medium effect is performed by comparing the resonant states population in supposed different reaction environments.

6.1 General feature of the reaction

In table 6.1 some important reaction parameters are reported as indicated in the caption. In column 8 of the table, the reaction and fusion cross sections are obtained with the old Bass model [158]. This value is an example among various estimations and we remind that it has only a weak dependence of the details of how one parameterizes the interaction

radius. In table 6.1 however we compare the value predicted by Bass and that given by the more recent parametrization of Eudes et al. [8]. In that work, the authors find that in general the calculation of Bass largely overestimates the measured cross sections by about 30%, especially at higher energies since the Bass formula was initially developed starting from low-energy reactions. Nevertheless, both parametrizations provide a reference level for our FAZIACor measurements since not many experimental values exist in this energy interval. For sake of clarity, we classify the reaction products in various subsets which

Table 6.1 Reaction parameters for the studied FAZIACor systems: center of mass energy and velocity, beam energy and velocity in the laboratory frame, grazing impact parameter and angle in the laboratory frame. The last two columns show the ratio between the reaction and fusion cross section estimated with the Bass model [158] and through the systematics of Eudes et al. [8] where the reaction cross section is given by Tripathi et al. [21].

System	E_{cm} (MeV)	v_{cm} (mm/ns)	E^{lab}_{beam} (MeV)	v^{lab}_{beam} (mm/ns)	b_{gr} (fm)	θ^{lab}_{gr} (deg)	$(\sigma_F/\sigma_R)_B$ (%)	$(\sigma_F/\sigma_R)_E$ (%)
SC 25	218	50.5	800	69.5	8.1	1.2	45	13
SC 50	436	71.4	1600	98.2	8.2	0.59	42	3
NeC 25	187	43.4	500	69.5	7.5	1.3	42	10
NeC 50	375	61.4	1000	98.2	7.7	0.64	40	1

helps understanding and separating the various reaction channels. First, we will limit the fusion cross section analysis to events containing at least one big fragment (BF), defined as a fragment from Carbon onward ($Z \geq 5$). Events with one BF can be associated with smaller ejectiles, i.e. Intermediate Mass Fragments (IMF, here from Lithium to Boron isotopes) and/or light charged particles (isotopes of Hydrogen and Helium). A more specific sample reflects our attempt to select events where the BF is also likely a quasi-projectile (QP); this is done with the additional cut $\theta_{cm}<40°$ (the projectile grazing angles in the CM reference are all below 5°). This angular limit was imposed to better focus on QP remnants while reducing big fragments coming from the most central collisions (complete/incomplete fusion events) that have a broader CM angular distribution. For the two-particle correlation analysis no selection has been imposed on the big fragment in order to retain the full spectrum of reaction mechanisms which produce the decaying nuclei. As for the model simulations, from now on, for brevity, the models will be called "HIPSE" and "AMD" meaning they already include the respective afterburners SIMON and HFl if not otherwise specified. Moreover, we underline here that the models have a twofold purpose. On the one hand we use them to derive the detection efficiency needed, for example, to measure the reaction cross section. Secondly, the simulated fragment distributions (after the inclusion of the decay and the filtering) are directly compared with the experimental observables to verify the goodness of the assumed

model ingredients, especially for AMD which contains more physical details. From this point of view it is particularly important the new coupling between the AMD code with the HFl afterburner (optimized for light nuclei) that is attempted here for the first time. Unfortunately, the AMD simulation was possible only for the S induced reactions. When simulating the Ne+C reactions, the program crashes, as it happens also for other light systems (except for C+C) and this problem has not yet been fixed.

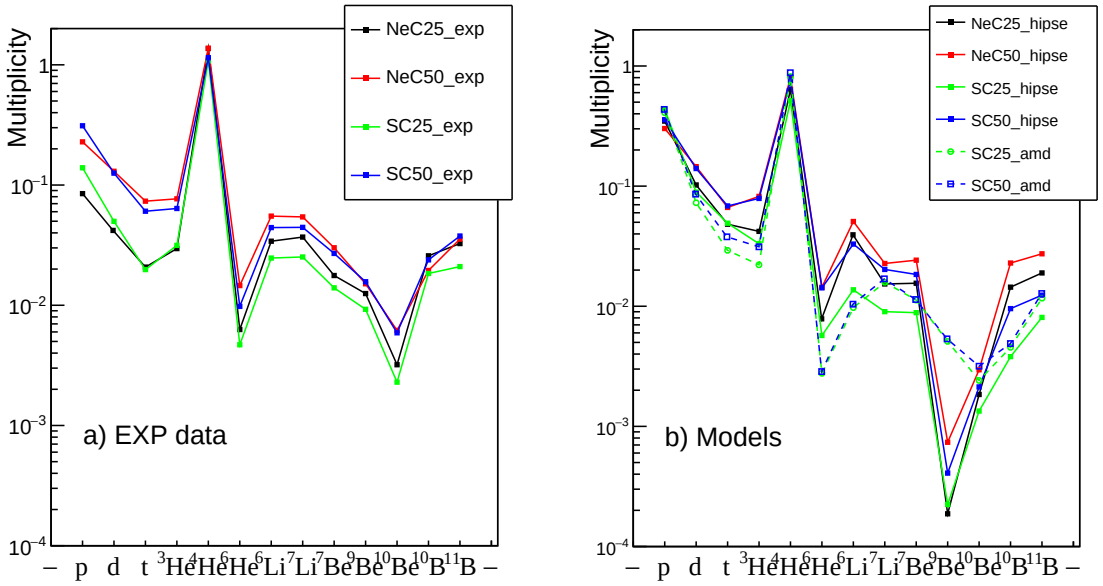

Fig. 6.1 LCP and IMF multiplicities for good events, without any specific selection, shown for the a) experimental data and b) models, respectively. Symbols according to the legend and statistical errors within the symbol sizes. The respective lines are drawn to guide the eye.

A first global overview of the reactions can be taken by comparing the observed average LCP and IMF multiplicities, as shown in fig.6.1 for the experimental data (left) and model predictions (right). The values refer here to the whole set of good events, with at least two identified particles. The data show the dominant emission of α particles, expected in these light N=Z systems: on average, more than one particle is found in each collected event. The other familiar behaviour is the scaling of p, d, t yields, tritons being only 20% of protons. We observe that hydrogen particles and ^3He are a factor 2-3 more for the higher energy reactions, possibly reflecting the enhance of fragmenting channels for more violent collisions; the larger production of fragments at 50 AMeV is seen also for Li and Be isotopes. The scaling with system size is less clear. It is basically absent for hydrogen while it appears for Li and Be. Here we see that, for a given beam energy, NeC gives more fragments that SC. This can be interpreted considering that these fragments are far from the QP (or from some composite

system) size more for SC than for NeC, thus they are reached with less probability during the decay of parents species. If we consider the models we see that the very general pattern in log-scale is caught by all of them and also some details (e.g. the general larger yields at 50 AMeV, the production of Li and Be larger in NeC than in SC). However, in absolute terms, it must be noted the too large hydrogen yield (in particular protons at low energy) and the underestimation of α emission as more clearly shown in tab.6.2 where the experimental multiplicities are compared to the calculated ones, either filtered either in 4π conditions, i.e. taking for each event all secondary products. The statistical errors are less than the last digit. One sees that HIPSE largely underestimates the α production in all cases with worse performance for the low energy case (about 50%); as pointed out in sec.5.3, overall AMD is better although its predictions are still 20% less. Finally, enhanced by log-scale, it is evident that HIPSE fails in producing n-rich Be isotopes; in this respect AMD does a better job in the region of Z=3-4, although we do not have the NeC case. This fact can be due both to the clusterization process included (by the model author) in our version of AMD (dynamical phase) and to the improved statistical emission of HFl (afterburner) including IMF emissions.

Table 6.2 α-particles multiplicities for the FAZIACor systems.

System	$M_\alpha{}^{EXP}$	$M_\alpha{}^{HIPSE}(4\pi)$	$M_\alpha{}^{AMD}(4\pi)$
SC 25	1.09	0.51(1.25)	0.82(3.01)
SC 50	1.15	0.76(1.73)	0.87(3.14)
NeC 25	1.35	0.64(1.36)	-
NeC 50	1.37	0.80(1.67)	-

We continue the general overview of the reactions considering now the heaviest fragments of the events. The event sharing according to the BF multiplicity is reported in tables 6.3,6.4 for both the experimental data and model predictions. In the experimental data, we observe a significant amount of M_{BF}=0 events, increasing with the bombarding energy($\approx$20-30%) and more abundant in the light NeC system. Various effects contribute to this result. The trend with bombarding energy can be affected by the increasing role of violent multifragmentation channels which reduce the final production of ions equal or heavier than carbon. Also, carbon ions (corresponding to arbitrary limit for the adjective "big") are surviving with larger probability in the heavier SC system than in NeC collisions. Last but not least, the acceptance which slightly differs for the two systems can have a role.

The same arguments can be applied to explain the behavior of M_{BF}=1 and M_{BF}>1 which are those relevant for this Thesis. Indeed, the cases with one BF increase with the system size while they decrease with beam energy. The events with M_{BF}>1 are anyhow a minority for these systems also due to the limited detector acceptance that plays an increasing role for

manyfold events. However this category of events strongly increases with the system size, about 8 (15) times from NeC to SC at 50 AMeV (25); indeed, any kind of break up from S-like sources tends to produce more frequently, than in the case of NeC source, two or more fragments with Z>6.

As for models, first we consider HIPSE because we have simulated events for all cases. The general partitioning is reproduced, though with the overprediction of M_{BF}=1 events in all reactions and the correlated underestimation of zero BF events. The class with M_{BF}>1 detected is strongly underestimated by HIPSE in all cases. All above, signals that HIPSE perhaps favours less multifragment events, namely the channels with only residual light clusters and particles are less than in reality. AMD code, limited to the SC reactions, very well performs at 25 AMeV, while the agreement at 50AMeV is even worse than for HIPSE.

Table 6.3 Event sorting based on the M_{BF} multiplicity for 25 AMeV systems. The experimental data (exp) are shown together with both model predictions (HIPSE-AMD) in the respective "geo" and "4π" configurations. The shown percentages are referred to the total number of events.

	M_{BF}=0 (%)				
25 AMeV	exp	HIPSE	AMD	HIPSE4π	AMD4π
NeC	55.2	31	-	16	-
SC	29.5	15.5	28.8	0.8	1
	M_{BF}=1 (%)				
25 AMeV	exp	HIPSE	AMD	HIPSE4π	AMD4π
NeC	44.4	68.8	-	59	-
SC	65.3	83.5	69.2	67	94
	M_{BF}>1 (%)				
25 AMeV	exp	HIPSE	AMD	HIPSE4π	AMD4π
NeC	0.3	0.02	-	25	-
SC	5.2	1.5	2	32	5

The comparison between the 4π and the filtered events allows us to better understand the geometry influence on the observed multiplicities. For explanation purposes, we limit ourselves to the SC reaction at 25 AMeV as shown in fig.6.2. As expected, we clearly see that the efficiency cuts shift events from high to low M_{BF} classes. For example, almost all M_{BF}=0 are not true 0-BF events but they are the consequence of the cuts on higher multiplicity events. The fact that AMD performs better than HIPSE seems to be related to the fact that it doesn't produce too many "big" fragments filling the $M_{BF} \geq 1$ groups as HIPSE does (compare dashed histograms in the figure). Overall, the above arguments on M_{BF} are in agreement with the comment on model dissipation reported in sec.5.3 where we saw the experimental sample being more dissipative as testified here also by the number of events without any big

Table 6.4 Event sorting based on the M_{BF} multiplicity for 50 AMeV systems. The experimental data (exp) are shown together with both model predictions (HIPSE-AMD) in the respective "geo" and "4π" configurations. The shown percentages are referred to the total number of events

	M_{BF}=0 (%)				
50 AMeV	exp	HIPSE	AMD	HIPSE4π	AMD4π
NeC	86.1	53	-	32	-
SC	57	41	33.9	11	3
	M_{BF}=1 (%)				
50 AMeV	exp	HIPSE	AMD	HIPSE4π	AMD4π
NeC	13.7	47	-	53	-
SC	41.4	58.8	65.8	71	95
	M_{BF}>1 (%)				
50 AMeV	exp	HIPSE	AMD	HIPSE4π	AMD4π
NeC	0.2	0	-	15	-
SC	1.6	0.2	0.3	18	2

fragment. For the 50 AMeV data, the inspection of table6.4 suggests that the failure of both models is due, again, to the too scarce average dissipativity of the reactions: too many events with one large residue, that survive the efficiency cuts, are produced. HIPSE, at this energy, performs slightly better.

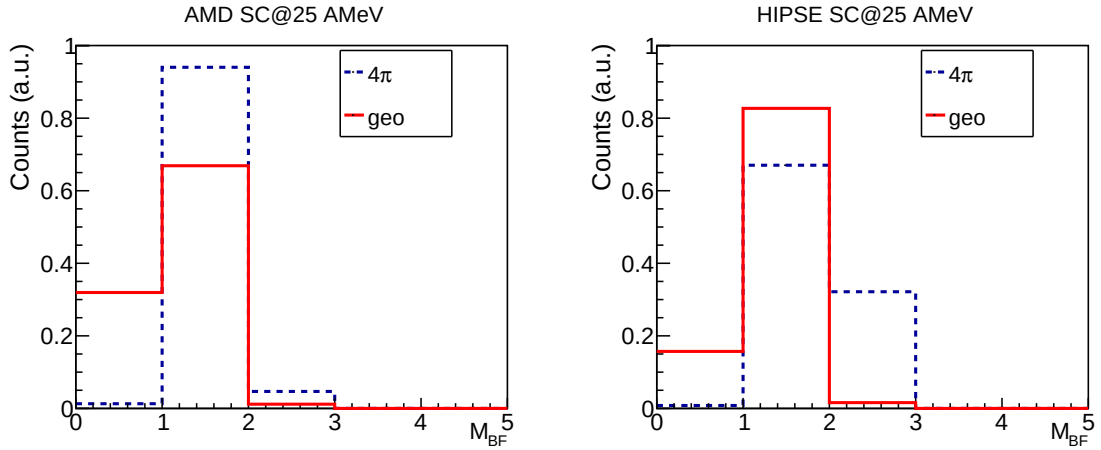

Fig. 6.2 Big fragment multiplicity for the SC@25 system in HIPSE and AMD seen before (4π) and after (geo) the filtering. Histograms are normalized to the total number of events.

Reaction features can be derived looking also at the lab velocity spectra of the main detected fragments as done in a inclusive manner in sec.5.3. The fact that we measure in reverse kinematics and with a wide coverage in the forward cone, ensures that we efficiently detect the QP fragments and, to a less extent, the quasi-fusion residues. These latter hit our

detectors if they receive a sufficient kick to deviate from their almost zero emission angle. The lab velocity for these ejectiles represents a reasonable scale for their origin, thus we discuss some specific isotopes as examples for the behaviour of FAZIACor systems. In fig.6.3, the measured velocity spectra for ^{12}C and ^{20}Ne isotopes produced in the FAZIACor systems are shown. These two isotopes are chosen as representative of different sources, depending on the system. For the SC system, Carbon and Neon are both produced in more or less damped collisions where the excited QP can break-up into two major pieces or sequentially decay towards the final measured residues. Of course the Ne-ions are closer to the original projectile size than C-ions (charge deficit respectively 6 or 10 units), thus in this latter case larger dissipation is expected. On the other hand, for NeC reactions, Ne residues can be only detected as originating from a not too excited heavier QP (which gained some mass-charge from the Carbon target) or, to a less extent, from the evaporation of fusion-like nuclei. Carbon ions, instead, could be QP remnants after rather strongly dissipative events (the charge deficit is 4 with respect to projectile). In the figure, the various cases are indicated in the legend that also reports the multiplicity per event, referring to the whole good events set for each reactions. To help the reader, the relevant velocities are indicated by corresponding vertical bars. The two continuous bars are the two beam velocities while the colored dot-dashed segments are the four CM-velocities. The spectra present some discontinuities not related to the reaction but to detection thresholds: the passage from Si1 to Si2 (around 47mm/ns only for Carbon) and the punch-through into CsI for Carbon and Neon (around 60mm/ns and 52mm/ns, respectively).

We first comment the 50AMeV reactions for which the difference between CM and beam velocities are larger. For carbon we see intense production close to (but less than) the beam velocity with a long tail extending below CM-velocities. For the SC system the maximum sits at lower values than for NeC most likely because of the larger dissipations needed to reach Z=6 from sulfur. For Neon the situation is different. Whilst for SC we detect a QP contribution of the same level (some percent) as for C, basically no Neon ions are found for the NeC. This is quite reasonable because the chance for an excited Ne-like source to survive the huge amount of deposited energy is almost zero. At low energy the pattern partially changes. The yields are similar for C in the two reactions with a broad bump from beam velocity extending with a rather intense tail well below the CM velocities, for both cases. At 25AMeV, Ne ions in SC are sizable and distributed in a structureless region from below beam velocity to below CM velocity. Instead, NeC gives only a small production of Ne towards the CM phase space. Qualitatively this corresponds to the scenario from moderate to big damping in SC, such that Ne (QP) ions can be formed in semi-peripheral to central collisions; for NeC, again, the probability to detect a beam-like Ne is almost zero (the parent

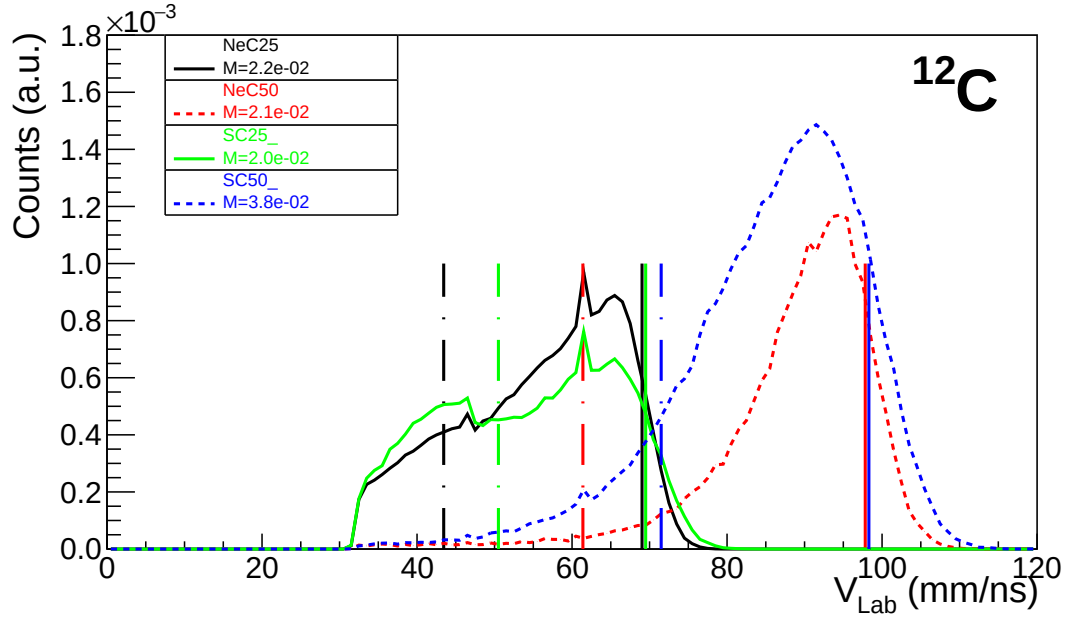

(a)

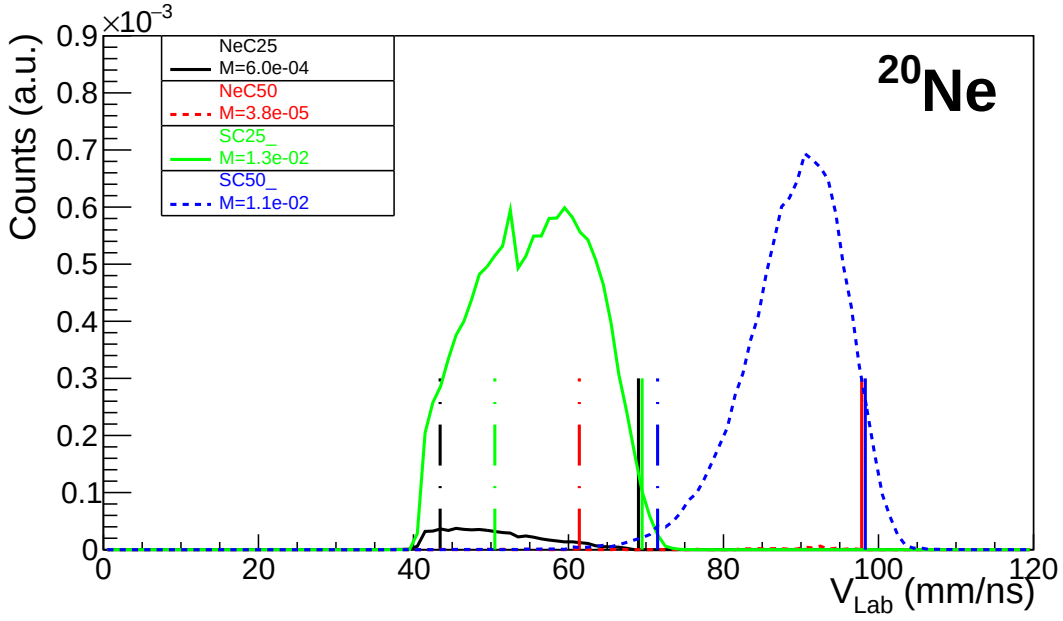

(b)

Fig. 6.3 Experimental lab velocity spectra for a) ^{12}C and b) ^{20}Ne isotopes produced in the FAZIACor systems. Colors represent each reaction as explained by the legend, also showing the average fragment multiplicities. The continuous bars represent the projectile velocities while the dashed dotted bars are the CM velocities. The NeC@50 AMeV contribution is too small to be clearly visible.

nuclei are not produced at all or, if so, they have long evaporation chains. Ne-ions can be only the result of fusion-like reactions sitting around the CM phase space.

After having had a survey of the entire data sets, we now move to analyze selected categories, essentially corresponding to A) semi-peripheral reactions with a QP plus coincident particles; B) more central collisions possibly related to incomplete fusion; C) two-particle correlation cases in order to reconstruct the parent species, also attempting to study these resonant states when occurring in the groups of collisions of type A) or B).

6.1.1 QP-like events

The FAZIACor setup, and FAZIA in general, is well suited for the identification of fast fragments at forward angles as demonstrated by our last papers[137, 156, 159]. Also in this Thesis we exploit this feature especially for QP-like events, considering that the relatively small size of the fragments and the high reaction velocities allow for the isotopic separation of most of the detected species. In general, we can have various scenarios which lead to detecting one big fragment in coincidence with LCPs and IMFs. One is associated to a BF from the evaporative decay of primary QP; as a function of the initial excitation, the final nucleus can be more or less lighter than the primary QP. In this scenario, a QP is associated only to LCP. Although the studied reactions involve light ions and thus the typical nuclear fission channel is practically absent, other break-up channels cannot be excluded

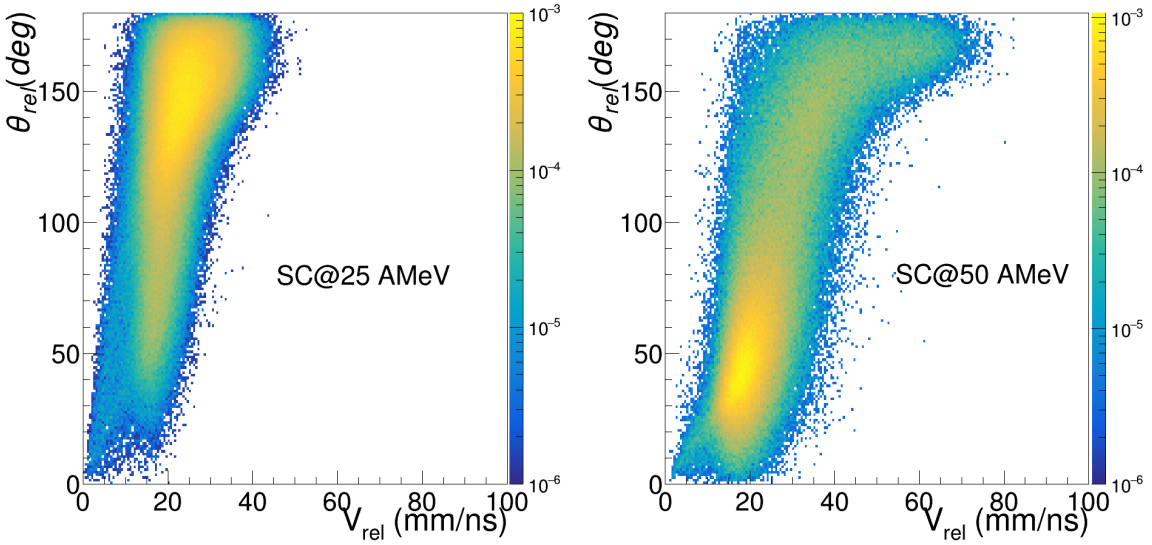

Fig. 6.4 Experimental correlation between the relative angle in the CM frame and the relative velocity of two big fragments in coincidence for the SC reactions.

(also favoured by cluster structure effects surely present in our systems): here, we can have two big fragments, or a big fragment and an IMF as also stated in the previous section.

In addition to the previous cases, one must consider that in typical binary reactions, the outgoing channel contains two major fragments, the QP and the QT. The second one is light, as coming from Carbon ions, and thus it is very probable its decay into small fragments and particles; these latter have a broad phase space that can overlap with the phase space of the QP fragments or, for more central collisions, of fusion-like residues. Therefore, also considering the non-4π acceptance, from the experimental point of view, it is very difficult to unambiguously separate the various cases. A way to help distinguishing among these scenarios is the correlation between the relative angle (θ_{rel}), measured in the CM frame, between the two detected BFs or BF and IMF and their relative velocity (v_{rel}). Such a correlation is shown for our heavier system data in fig.6.4 restricting to the cases with two BF (both Z>5). If the two fragments come from the split of a moderately hot QP, v_{rel} should correspond to a Coulomb-driven repulsion [160], less than 20mm/ns for these small systems. Moreover, the boost of the QP in the CM system makes the original back-to-back emission of the pair quite narrower (small θ_{rel} values). On the contrary, if the pair would correspond to a binary emission (QP+QT) from nearby the CM, then θ_{rel} would assume large values (towards 180°) while the relative velocity would cover the broader range related to the dissipation extent. A caution note must be given: the QP CM-velocity is rather small due to reverse kinematics and, of course, it reduces further with increasing dissipation. Therefore, dissipative QP-QT events can populate a phase space partially overlapping that of the QP break-up; in other words the two scenarios are not clearly separated. In fig.6.4 we see that for SC@ 25 AMeV, the angle-velocity correlation is populated close to 180°. However, the relative velocity is low around 20-30mm/ns. This indicates an emission of fragments from very dissipative collisions, irrespective if they were binary QP-QT collisions or they were a kind of fusion followed by break-up: the difference is very subtle, indeed. Moreover, there is scarce indication of a rather clear QP break up. At 50 AMeV, instead, the region of QP-QT is weak but it is more clearly signaled by the extension of the tail towards high velocity absolutely not compatible with Coulomb-driven ruptures. A spot appears, also, at small angles which supports the hypothesis of QP-like break-up.

The same angle-velocity correlations are displayed in fig.6.5 for all measured systems for the class of events where a BF is in coincidence with an IMF. It is clear that the emission of a Z=3, 4, 5 (IMF) with a BF is only arbitrarily distinguished from the case of two BF; indeed, the former can be only the asymmetric-mass tail for a break-up process. As a matter of fact, we observe two main different patterns for the two beam energies. At 25 AMeV the back-to-back region in the SCM is efficiently populated while it is faint at 50 AMeV

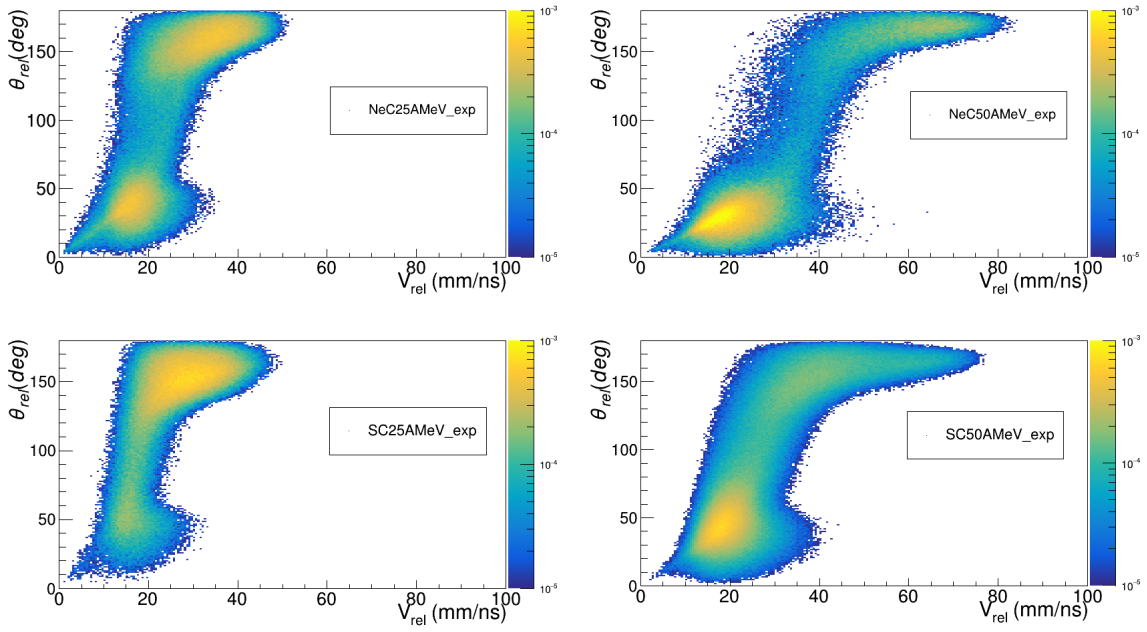

Fig. 6.5 Experimental correlation between the relative angle in the CM frame and the relative velocity of one big fragment and IMFs in coincidence for the FAZIACor systems.

although a tail of less damped events is clearly present. The region compatible with a QP break up is more intense at 50 AMeV. For the NeC case the relative angle is around 20°-30°, smaller than for SC probably due to the larger CM-velocity of the Ne-like that of the S-like (SC system is more mass asymmetric). As said, the fraction of these 2 BF or BF-IMF events is anyhow small for all cases. Therefore, although the features of the break-up channel for light nuclei in the Fermi domain are interesting to investigate, we cannot deepen further this subject with our data.

We now concentrate on the QP events, selected within the set of "good events" with the condition of only one BF (Z>5) in coincidence with LCP. To reinforce the QP selection we also require that BF is emitted at forward CM angles (θ_{cm} <40°), i.e. within the QP emission cone for most reactions from peripheral to semi-central. By observing the emission pattern of the LCP in coincidence with the (only) detected QP, we can learn about the source of emission of these light species. For example, the velocity component patterns for α particles, referred to the QP-system, are shown in fig.6.6 (experimental data) and fig.6.7 (model data). The plots, in log-Z scale, refer to the measured data without efficiency corrections so that their shape can be directly compared with the filtered simulation results drawn in the second figure. The counts, for each plot, are normalized to unity. The colored arrows signal the QP-like origin (zero value corresponds to beam velocity) and the CM origin. We can observe a large contribution with the typical Coulomb pattern i.e. with a circular symmetry centered

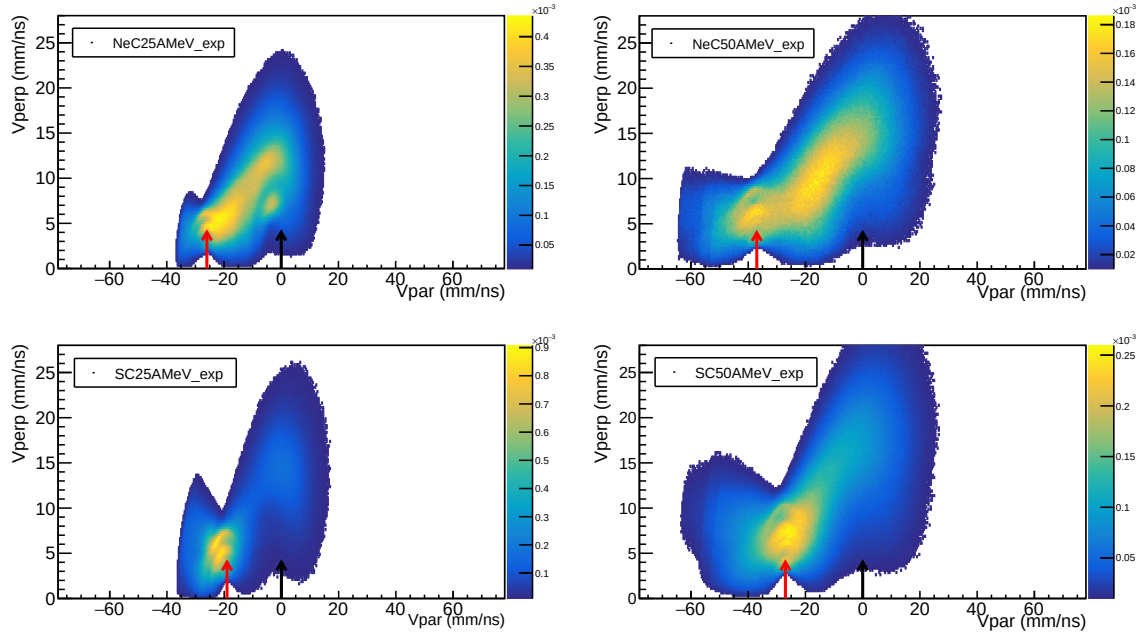

Fig. 6.6 Experimental velocity plots for alpha particles in coincidence with a QP-like source.

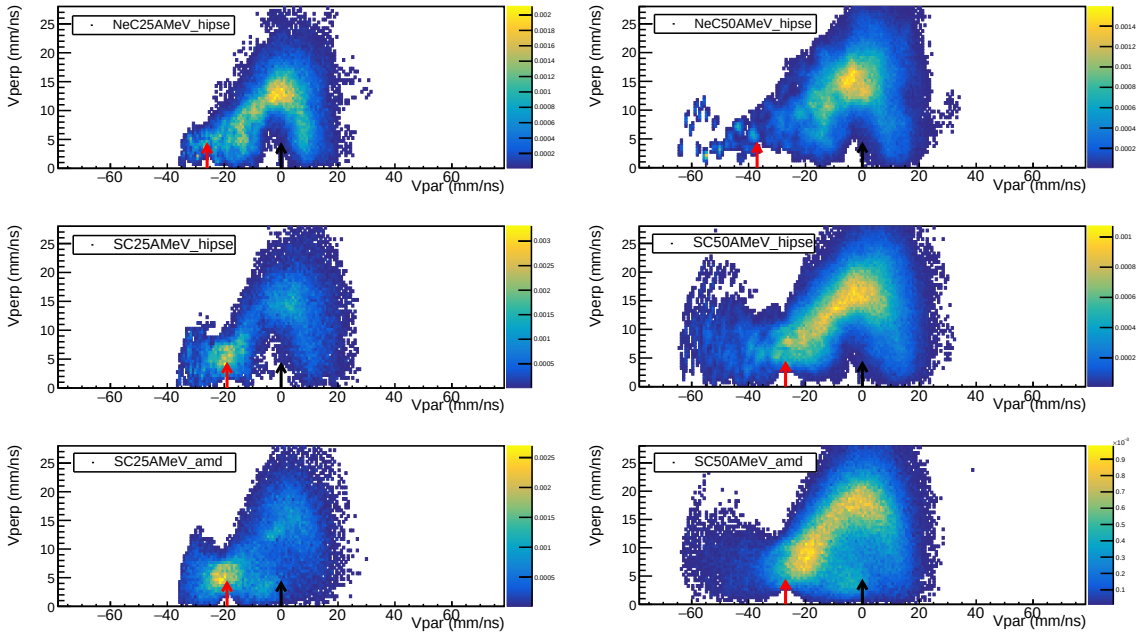

Fig. 6.7 Simulated velocity plots for alpha particles in coincidence with a QP-like source. The model type is indicated in each pad.

around the QP-origin. This is compatible with particles emitted by the QP source. A sizable spot is present also at the CM position having a shape that appears out of the main ring-like

structure. This region overlaps with the concurrent emission from QT sources. The simulated plots reveal the basically correct interpretation of the experimental results. Namely, the ring sitting around the QP source is clear in all cases; also the intensified region around the CM appears in the models, that can be due to the superposition of LCP from QT decay and/or other mechanisms (for example fast dynamical LCP emission in the overlapping region allowed in both models). We note that the model statistics is not very high, especially for HIPSE; anyway the AMD code seems to better reproduce than HIPSE the larger fluctuations that tend to smear the sharp Coulomb ring shape as seen in the data. The velocity plots for other measured LCP show similar characteristics, although protons have a broader and more uniform phase-space and the statistics for d,t,^{3}He and ^{6}He is lower.

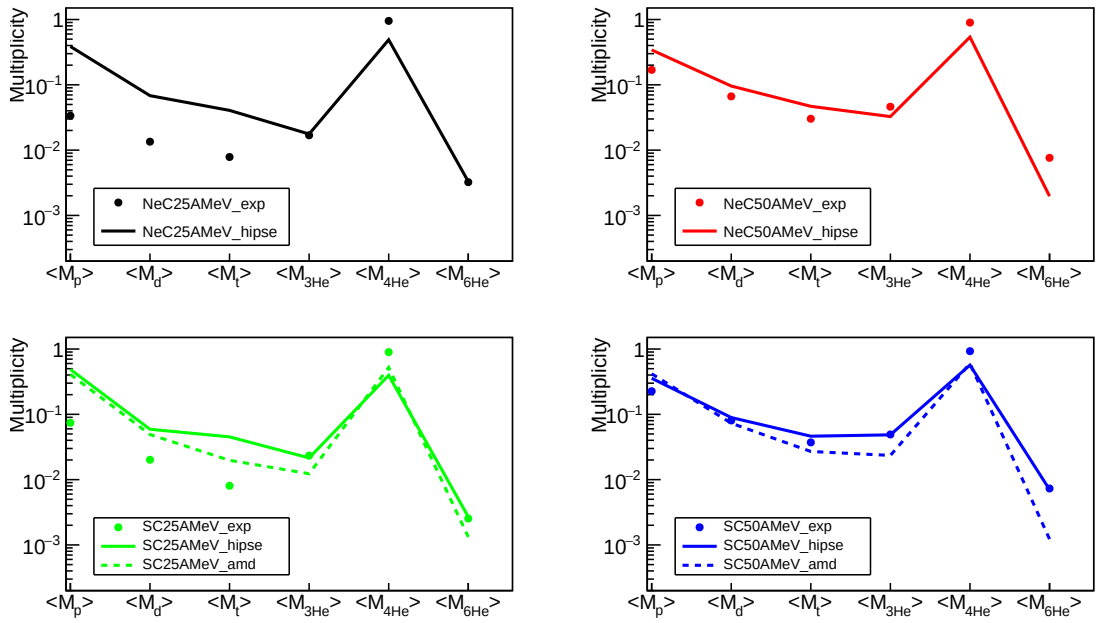

Fig. 6.8 Average LCP multiplicity for events with the selected QP. Symbols explained in the legend. Statistical errors are within the symbol size.

For these events we can extract the various LCP multiplicities. These should be ideally ascribed to the contribution of the QP decay. These values are plotted in fig. 6.8; please, note the log scale. As already anticipated in less selected events, the experimental α emission is larger than predicted by models either at 25 and 50AMeV; the opposite happens for hydrogen ions at 25AMeV while at 50AMeV the models better follow the data. Since we have seen that the QT decay can contribute to the QP coincident yield of particles, we extracted the LCP multiplicity also restricting to a safer QP-ring region, i.e. with an angular cut of $\theta_{sdrQP} < 90°$ in the QP reference. Several comments can be done. The first concerns the α multiplicity which is quite better reproduced by the models in the restricted forward

Table 6.5 LCP multiplicities in coincidence with the selected QP condition. The multiplicities are presented integrated (all), described by fig.6.8), and restricting to the QP forward cone (θ_{sdrQP} <90° , i.e. <90 in table).

		p		**d**		**t**		**^{3}He**		**^{4}He**		**^{6}He**	
		all	<90	all	<90	all	<90	all	<90	all	<90	all	<90
NeC25	EXP	0.034	0.016	0.013	0.0023	0.0078	0.00042	0.017	0.0056	0.95	0.17	0.0032	8.1e-05
	HIPSE	0.39	0.28	0.068	0.024	0.041	0.0065	0.018	0.0073	0.49	0.21	0.0033	0.00087
NeC50	EXP	0.17	0.078	0.067	0.013	0.03	0.0023	0.046	0.0098	0.9	0.18	0.0076	0.00028
	HIPSE	0.34	0.2	0.096	0.021	0.047	0.0051	0.033	0.0047	0.54	0.2	0.002	0
SC25	EXP	0.074	0.04	0.02	0.0048	0.008	0.0008	0.023	0.0053	0.9	0.17	0.0025	0.00013
	HIPSE	0.49	0.38	0.059	0.035	0.045	0.014	0.022	0.016	0.4	0.17	0.0027	0
	AMD	0.41	0.3	0.049	0.028	0.02	0.0046	0.012	0.0055	0.52	0.16	0.0013	1.7e-06
SC50	EXP	0.23	0.11	0.08	0.019	0.037	0.0038	0.049	0.015	0.93	0.18	0.0073	0.0004
	HIPSE	0.36	0.23	0.089	0.039	0.046	0.012	0.049	0.015	0.57	0.2	0.007	0.0003
	AMD	0.42	0.26	0.073	0.034	0.027	0.0081	0.023	0.0089	0.6	0.19	0.0012	5.1e-05

cone. This suggests an excess of emission in the 'mid-velocity' region, i.e. close to the CM, not well predicted by models and likely not due to the QP decay. Second, the model overestimation of protons persists even in the restricted QP-cone; the same trend holds for d, t emissions and still we observe that yields are better reproduced at the higher energy. Finally, for other He-isotopes the emission cut does not sizably change the situation.

We conclude this section with a short discussion on the average isotopic content of the QP fragments and of the coincident fragments. We refer to fig.6.9 showing the average N/Z ratio for species from Lithium to the projectile (where as usual N is the neutron number) ordered as function of the ion charge Z. The fragments from Carbon onward are the true QP (by our definition valid in discussing this section) while the IMF contribute here when coincident with a QP product. The results of the reactions studied here are compared with data obtained in an other FAZIA experiment on symmetric Ca-induce reactions (ref.[70, 159]); all cases (colors, symbols) are indicated in the legend. It is interesting to discuss some general aspects of the figure. We clearly recognize a similar path for N/Z, from the charge value corresponding to the projectile moving down to IMF. Indeed, all our systems (and the ^{40}Ca reaction) start with N/Z=1 at around Z=Z_{proj} reflecting their same starting value; the N/Z ratio smoothly grows with decreasing Z and reaches a Z-region where the values are weakly dependent of the system (and also of the bombarding energy). The region of the smooth N/Z evolution in some respect marks the passage from low to high dissipation and is more clearly evidenced for heavier systems that have a wide range of reachable (cold) fragments. In this sense it is particularly interesting to look at these three similar (shifted in Z) trends for Ne, S and Ca projectiles. Below Fluorine ions, the behaviour is much more influenced by the details of the reaction and of the fragment structure. It is anyhow remarkable that this behaviour is similar (and N/Z values are also similar) for fragments from Li to Oxygen produced in five

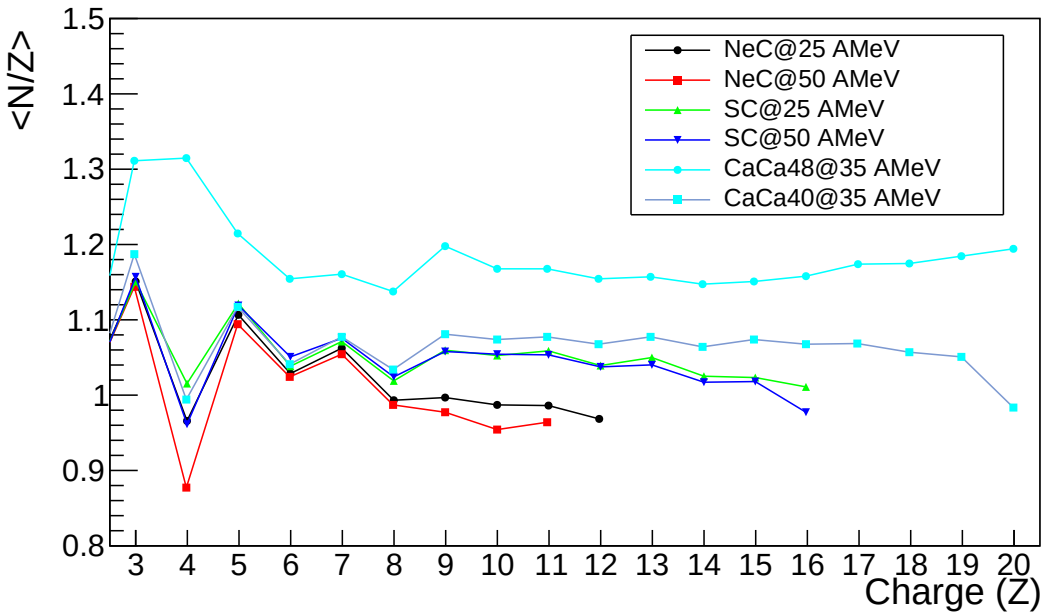

Fig. 6.9 Average isotopic content of QP fragments and of the coincident fragments as a function of Z. Statistical errors are within symbol size. The reactions are indicated according to the legend.

reactions quite different in many respects, only having the same "chemical" feature (N=Z) of the in-going channel. This last observation is reinforced in comparison with the behaviour of the n-rich Ca-system. Here we clearly see the high N/Z values around the projectile zone (around Z=19, 20) with an opposite trend to decrease still remaining definitely well above those N/Z for N=Z reactions. Also the region of intermediate fragments, while less smooth, conserves trace of the global neutron richness. These findings have been discussed in detail in ref.[70, 159].

6.2 Incomplete fusion

As anticipated, we now investigate the specific class of the detected events in which at least one big fragment is detected and attributed to a kind of complete/incomplete fusion process, for the most central collisions. As a function of the center-of-mass energy, the fusion excitation function features three general distinct regimes. Region I opens at the reaction threshold, then steadily increases, and ends by the region II, corresponding to the saturation of fusion cross section, whereas in the region III the fusion process regularly diminishes. Experimental data for systems similar to the present light ones are relatively abundant in the literature [161] at bombarding energies not far from the Coulomb barrier (region I), where

the fusion cross section is almost equal to the total reaction cross section. At higher energy (region II and region III of the excitation function) experimental data are less numerous (see the systematic study of Eudes et al. [8]), more so for light systems. In these cases the exact determination of the fusion cross section is complicated due to the opening and/or increasing overlap of other competing channels, such as incomplete fusion, deep inelastic and direct reactions. In particular, it has been found that the fraction of incomplete fusion, with respect to the complete fusion, grows with the bombarding energy, while the fusion cross section decreases almost linearly with incident energy. This trend is motivated by the increasing role of NN-collisions and in general by fast emission processes which increase with the bombarding energy and prevent the formation of a compound nucleus built up with the total system mass.

The FAZIACor energies fall well within regions II-III of the fusion excitation function, in which there is a lack of experimental data and we want to contribute adding some new results. In particular we want to estimate the ratio between complete and incomplete fusion and to compare it to the predictions, for our system, of the universal parametrization obtained by Eudes et al. [8] and reported in table 1.1. Moreover, we can also compare these ratios specifically for the SC@25 AMeV reaction to the results obtained by Pirrone et al. [16] where the same study has been performed on the same reaction although at a lower energy, i.e. SC@19.5 AMeV. We analyzed the reaction products having atomic charge number $Z > 9$ for SC@25 and $Z > 7$ for SC@50, for which we expect the major contributions from complete and incomplete fusion. Although these limits may seem a bit low (for example ref.[16] considered Z>10), the models still predict a non vanishing component of incomplete fusion also for the these lower Z ions. We will show the effect of this cut when our data will be compared to the systematics. As detailed in chapter 1, one knows that it is rather hard to disentangle the contribution of these fusion-like mechanisms from the rest of the processes taking place (i.e deep inelastic and direct reactions). This is the reason why we cautiously exclude the lighter NeC system from the present analysis on ICF. In fact, the phase-space is so compressed that the fragments to be studied are too close to both the projectile and target fragments. With this selection, on the SC reactions, we applyied a multiple component fit to the fragment velocity spectra in order to separate the fusion contribution from other reaction components; essentially, we performed a kinematical analysis of the velocity spectra for each evaporation residue (as done by Pirrone et al. [16]) well identified thanks to the good performance of our telescopes. As examples of the many fitted spectra, that we are going to discuss, we show in fig.6.10 the experimental velocity spectra for a few representative isotopes. We assume (as in ref.[16]) that the processes that contribute significantly to the observed residue yield are mainly three: complete fusion (CF), incomplete fusion (ICF),

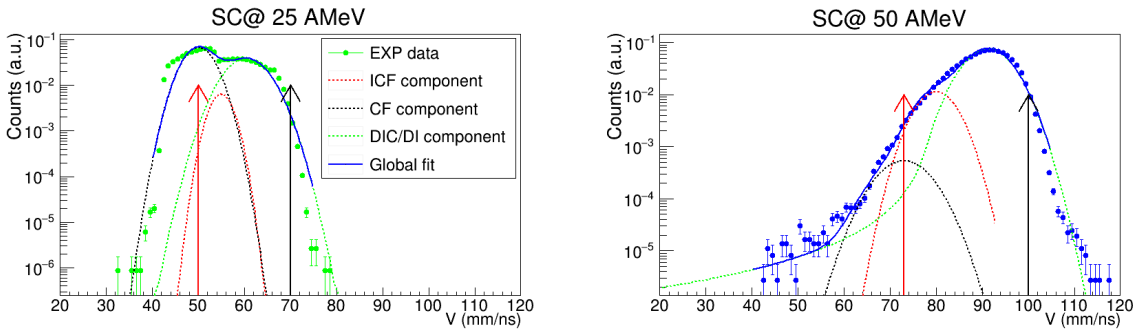

(a) ^{23}Na laboratory velocity spectra

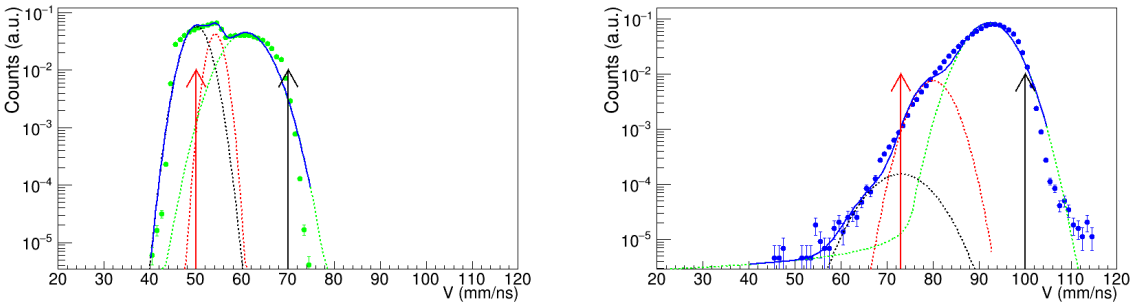

(b) ^{24}Mg laboratory velocity spectra

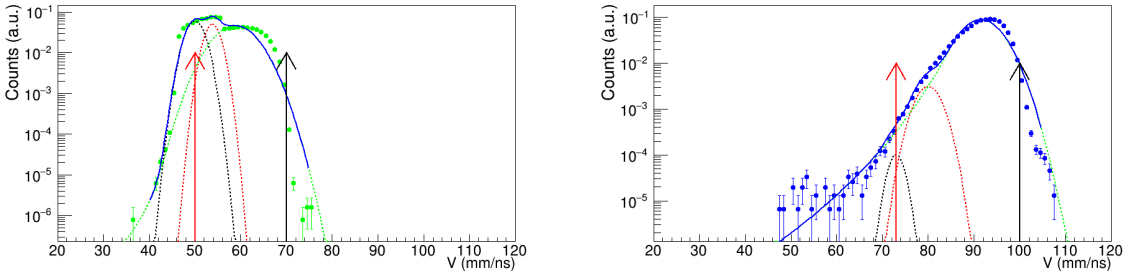

(c) ^{27}Al laboratory velocity spectra

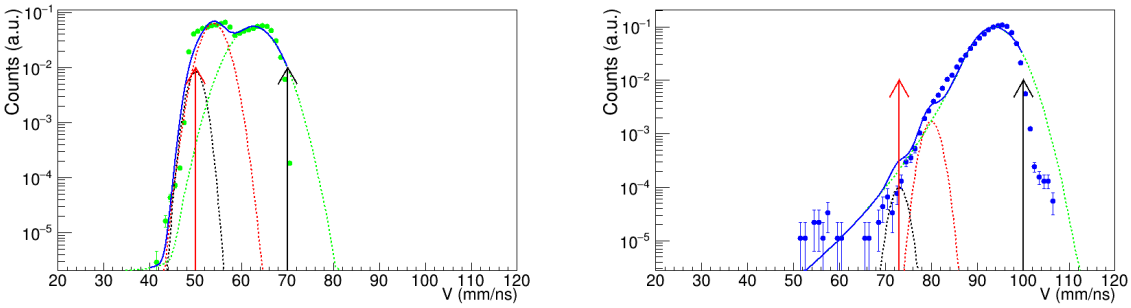

(d) ^{28}Si laboratory velocity spectra

Fig. 6.10 Laboratory velocity spectra for a few selected isotopes a) ^{23}Na b) ^{24}Mg c) ^{27}Al d) ^{28}Si for the SC systems at 25 AMeV (left) and 50 AMeV (right). Experimental data are shown by dots, the global fit is shown by the blue line and the various components are represented by the dashed lines (see legend). The red and black arrows indicate the V_{cm} and V_{beam} velocities, respectively. The experimental error are statistical and visible when greater than the symbol size.

and DIC/direct reaction. The fitting procedure consists in assuming three fit functions, two Gaussian-like shapes for the fusion components and a third different curve for the last contribution as discussed below. The first Gaussian component is centered around V_{cm} representing the complete fusion part (full momentum transfer). We remark that the SC systems are mass-asymmetric and that there is evidence, from literature, that the ICF develops as if a part of the lighter partner would not participate to the fusion. Therefore, in cases of reverse kinematics as ours, this produces a nuclear system traveling with a velocity in between that of the center of mass V_{cm} and that of the beam V_{beam} (see chap. 1 for some more details on ICF). For the CF-Gaussian we treat the calculated value of the centroid V_{cm} as a fixed parameter and allow the sigma to vary while for the ICF component both the mean value and sigma were allowed to vary in a reasonable interval. The initial values and the boundaries of the free parameters as well as the limits (in velocity) of the three contributions are critical for the convergence of the fit. Thus, the starting values and the boundaries for the ICF component are derived using the model simulations. We decided to employ AMD in particular, and not HIPSE, because of the better performance in reproducing the SC@25AMeV data as described before. The same simulation is also used to model the shape and associated parameters for the DIC/DI component which may differ more from a Gaussian distribution. In fig.6.11, we show as an example the AMD model predictions for

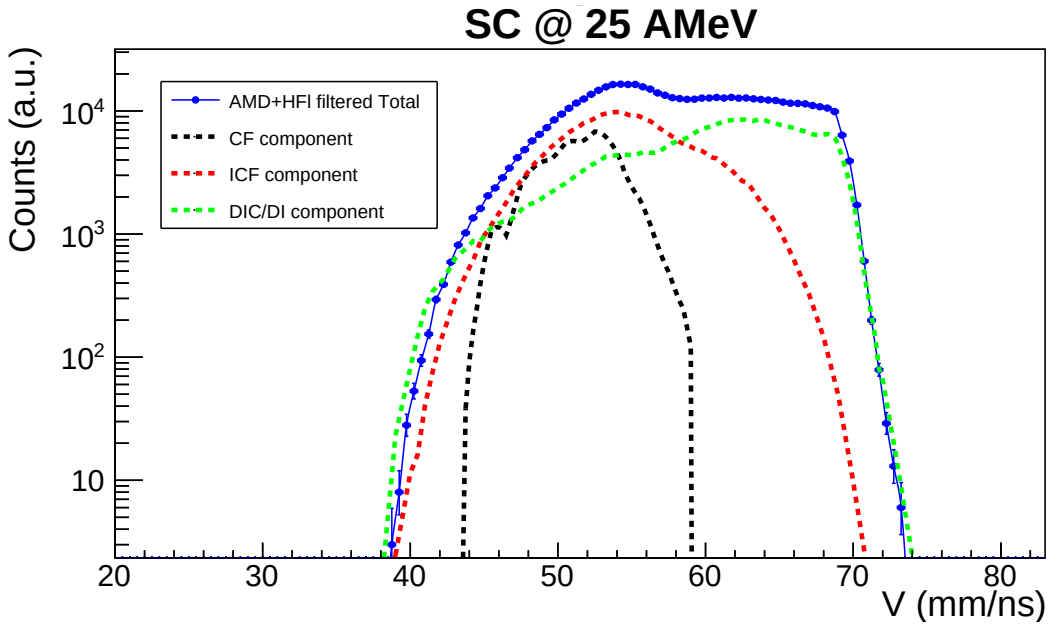

Fig. 6.11 AMD simulated laboratory velocity spectra summed for the fragments with Z>10 for the SC systems at 25 AMeV. The various components are indicated in the legend.

the three velocity components and the total shape distribution for all heavy fragments with

Z>10 in the SC@25 reaction. The selection of the processes (i.e ICF, CF and DIC/DI) in the model is made by using conditions on some quantities for primary fragments (charge, mass and excitation energy) and more global parameters such as multiplicities and impact parameter. For example, for the CF component a single excited (M_{BF}=1) source after the dynamical phase with Z_{tot}=Z_p+Z_t and A_{tot}=A_p+A_t was required also verifying that this gate indeed corresponds to central impact parameters. Following the guide of simulations, we found that the Crystalball function [98] better reproduces the actual DIC/DI component. This is basically composed of a Gaussian distribution core and a power-law low-end tail, below a certain threshold. The latter should better mimic the possible DIC/DI contamination into the experimental CF/ICF components. The power-law tail parameters, the mean and the width are left as free parameters within limits and initial guesses coming from the model indications.

The results of the fits are important to evaluate the CF and ICF contributions and, in one case, also to estimate the absolute cross sections to be compared with systematics. We remark the need to correct for the efficiency the contributions derived from the fits. Indeed, in general the efficiency is expected to vary as a function of the isotope and of the reaction mechanism. These corrections are not the same when derived from HIPSE or AMD. For example the ^{24}Mg ER has a 25% and 27% variation of the efficiency between the values calculated with the two models, respectively at 25 and 50AMeV. Since AMD globally performs better in reproducing the measured data, we used this model for our final values; the HIPSE efficiencies are considered only as a contribution of the systematics that can affect our results as discussed below. It is remarkable that for the 25 AMeV system we attempted also an absolute cross section evaluation. This is possible because during the data taking a collimated special telescope Si-Si was positioned at large distance from the target subtending a very small solid angle $\Delta\omega$ next to the beam. The polar angle was 0.99° in the lab, measured with a precision goniometer and an optical laser system. In principle, the idea behind the use of this telescope (called SiMon Silicon Monitor) was to allow for the normalization of each reaction data to the Rutherford cross section. However, for geometrical constraints, the final polar angle was above the very small grazing angles for the 50 AMeV reactions. Also, due to acquisition issues, for the first part of the experiment (NeC at 25 AMeV) SiMon was excluded from the trigger. Therefore we could use the SiMon data only for the SC@25 AMeV reaction. The method is briefly outlined. The SiMon identification plot $\Delta E - E$ was obtained for the same runs as for the main analysis. SiMon was acquired in singles without trigger reduction or bias. A cut on the plot was drawn to select the elastic scattered Sulfur ions and the integral of this region has been normalized to the Rutherford cross section calculated for the SiMon geometry. About the error on the Rutherford cross section, the main

contributions are due to the determination of the SiMon geometry; in particular the cross section is sensitive to the collimator diameter (3mm) and to the polar angle in the lab (0.99°). Assuming ±0.2mm and ± 0.05° as errors on these parameters, we estimate an error of 25% on the normalization factor. Thanks to this normalization, the respective fusion values are given in absolute value (mb) at 25AMeV. For the 50 AMeV data the applyied efficiency corrections allow us to recover a reliable estimate of the ratio ICF/CF. We attempted to go ahead in this business and obtain a result to be confronted with the Eudes systematics even at 50AMeV and notwithstanding the lack of absolute normalization. To do this we estimated with the models a global efficiency for the entire set of "good events", assuming that they rather faithfully sample the total reaction cross section. After that we can calculate the normalized and efficiency corrected ratios reported in the last row of the table6.7.

Table 6.6 Values of complete (σ_{CF}) and incomplete (σ_{ICF}) fusion cross sections for each evaporation residue for the SC@25 AMeV. In the last row we report the results summing over the above considered isotopes. The corresponding errors are taken to be around 37% as explained in the text.

	$\sigma_{CF}(mb)$	$\sigma_{ICF}(mb)$	σ_{CF}/σ_{ICF}
^{20}Ne	1.0± 0.4	0.8± 0.3	1.2± 0.4
^{21}Ne	15.1± 5.6	2.5± 0.9	6.1± 2.2
^{22}Ne	4.6 ± 1.7	0.8± 0.3	5.6± 2.1
^{22}Na	9.6± 3.6	4.9± 1.8	2.0± 0.7
^{23}Na	22.7 ± 8.4	13.6± 5.0	1.7± 0.6
^{24}Na	4.4± 1.6	2.5± 0.9	1.7± 0.6
^{24}Mg	10.6± 3.9	27.2± 10.1	0.4± 0.1
^{25}Mg	7.7± 2.9	21.4± 7.9	0.4± 0.1
^{26}Mg	3.7± 1.4	6.5± 2.4	0.6± 0.2
^{26}Al	18.3± 6.8	11.4± 4.2	1.6± 0.6
^{27}Al	16.5± 6.1	21.1± 7.8	0.8± 0.3
^{28}Al	2.8± 1.0	4.0± 1.5	0.7± 0.3
^{28}Si	10.8± 4.0	17.3± 6.4	0.6± 0.2
^{29}Si	12.7± 4.7	14.1± 5.2	0.9± 0.3
^{30}Si	3.8± 1.4	4.1± 1.5	0.9± 0.3
^{30}P	4.0± 1.5	5.0± 1.8	0.8± 0.3
^{31}P	13.1± 4.9	12.0± 4.4	1.1± 0.4
^{32}P	2.2± 0.8	3.2± 1.2	0.7± 0.3
^{32}S		3.3± 1.2	
Total	164± 61	176± 65	0.93± 0.34

Of course, the results of the three-component fit for the velocity spectra are affected by

Table 6.7 Counts of complete (*CF*) and incomplete (*ICF*) fusion counts for each evaporation residue for the SC@50 AMeV. In the last row we report the fraction of total fusion obtained summing all experimental data and normalized to the total number of events after efficiency correction. The corresponding errors are taken to be around 30% as explained in the text.

	$CF(counts)$	$ICF(counts)$	CF/ICF
^{16}O	$(2.94\pm0.88)\times10^5$	$(8.94\pm2.67)\times10^5$	0.33 ± 0.10
^{17}O	$(1.02\pm0.31)\times10^5$	$(3.12\pm0.93)\times10^5$	0.33 ± 0.10
^{18}O	$(3.62\pm1.09)\times10^4$	$(9.71\pm2.91)\times10^4$	0.37 ± 0.11
^{18}F	$(6.88\pm2.06)\times10^4$	$(3.20\pm0.96)\times10^5$	0.21 ± 0.06
^{19}F	$(6.76\pm2.03)\times10^4$	$(3.08\pm0.92)\times10^5$	0.22 ± 0.07
^{20}F	$(3.33\pm0.99)\times10^4$	$(1.03\pm0.31)\times10^5$	0.33 ± 0.10
^{20}Ne	$(5.14\pm1.54)\times10^4$	$(3.60\pm1.08)\times10^5$	0.14 ± 0.04
^{21}Ne	$(4.86\pm1.46)\times10^4$	$(3.53\pm1.05)\times10^5$	0.14 ± 0.04
^{22}Ne	$(1.87\pm0.56)\times10^4$	$(1.34\pm0.40)\times10^5$	0.14 ± 0.04
^{22}Na	$(2.63\pm0.79)\times10^4$	$(2.87\pm0.86)\times10^5$	0.09 ± 0.03
^{23}Na	$(2.52\pm0.76)\times10^4$	$(3.89\pm1.16)\times10^5$	0.06 ± 0.02
^{24}Na	$(5.96\pm1.78)\times10^3$	$(7.48\pm2.24)\times10^4$	0.08 ± 0.02
^{24}Mg	$(1.17\pm0.35)\times10^4$	$(3.16\pm0.95)\times10^5$	0.04 ± 0.01
^{25}Mg	$(8.21\pm2.46)\times10^3$	$(2.24\pm0.67)\times10^5$	0.04 ± 0.01
^{26}Mg	$(3.80\pm1.14)\times10^2$	$(3.91\pm1.17)\times10^4$	0.009 ± 0.003
^{26}Al	$(3.32\pm0.99)\times10^3$	$(1.06\pm0.31)\times10^5$	0.03 ± 0.01
^{27}Al	$(3.51\pm1.05)\times10^3$	$(8.96\pm2.69)\times10^4$	0.04 ± 0.01
^{28}Al	$(1.85\pm0.56)\times10^2$	$(2.70\pm0.81)\times10^3$	0.07 ± 0.02
^{28}Si	$(4.33\pm1.30)\times10^3$	$(5.42\pm1.63)\times10^4$	0.08 ± 0.02
^{29}Si		$(4.15\pm1.24)\times10^4$	
Total	0.0045 ± 0.0013	0.023 ± 0.008	0.19 ± 0.06

uncertainties. First, we note that the three assumed curves are only approximations of the true contributions. Moreover, the convergence values of the fit somewhat depends on the initial guesses and on the chosen velocity boundaries. The estimated errors on the parameters, in particular on the integral, due to the fit tuning conditions are around 20%. As said, a source of uncertainty is given also by the efficiency estimation for the cross section normalization. For the best shape estimation and yields correction we used AMD; however, to assign an uncertainty to the efficiency factor, we used the mean variation from AMD to HIPSE (around 20%). These values are then summed as the sum of squares to the integral error and elastic cross section normalization error to give the total error of 37% quoted in tab.6.6. For SC@ 50 AMeV the elastic cross section normalization was not available, as explained before, and the error is given just by the sum of the two previous components (6.7. Our best results for

the SC systems are listed, for the various isotopes forming the "Evaporation Residue" set, in the tables tab.6.6 and tab.6.7 for the two beam energies 25 and 50 AMeV, respectively. Some comments on the obtained values in the tables are in order. As expected various ions contribute to the CF at 25AMeV while at 50 AMeV only the lighter ones do. The same trend is true also for ICF and this trend indicates that at 50 AMeV the systems that form and decay in the collisions more rarely survive as big fragments than at 25 AMeV. It is also clear the the CF component tends to vanish from 25 to 50 AMeV, in agreement with expectations and systematics of Eudes et al. [8].

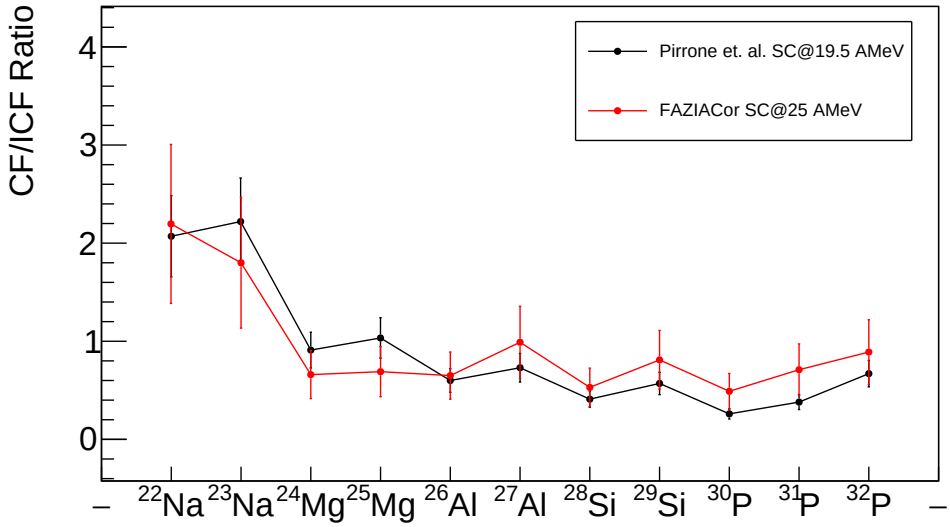

Fig. 6.12 CF/ICF ratio comparison for the most populated fragments for the to reaction SC@25 AMeV (red point) and SC@19.5 AMeV (black points).

For the SC@25 AMeV reaction our results can be compared to the ones obtained by Pirrone et al. [16] in order to have also a benchmark for our procedure. The interval of measured Z of the ER in our case goes from Z=10 to Z=16 while in ref.[16] it extends from Z=11 to Z=18. However, the absolute values for each common ER are systematically higher for the CF and ICF values obtained by ref.[16] with respect to ours. Wanting to make a more direct quantitative comparison, they quote an overall total measured CF and ICF component of 505 mb and 660 mb, respectively. These are approximately a factor 3 greater then our measured values of 164 mb and 176 mb at 25 AMeV. Of course, these two findings are to a certain degree expected given the 5 AMeV of beam energy difference. It is left to understand if the observed differences are indeed reasonable given the initial energy difference. In fig 6.12, we compare first of all the relative CF/ICF ratio between these two experiments. In this figure we plot the most populated ER common to both experiments. Within errors, we see

that the global trend is very similar in both reactions, with the CF dominating towards the lighter fragments and then slowly decreasing as the mass of the ER increases. Therefore, it seems that indeed the only major difference is given by the factor 3 scaling in the measured fusion cross sections.

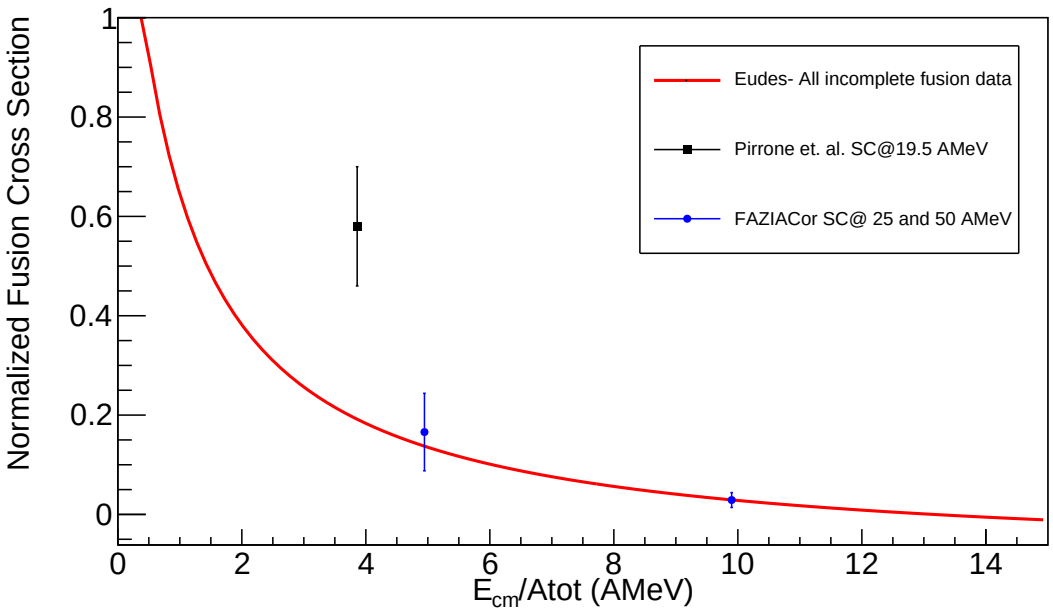

Fig. 6.13 The results of the FAZIACor S+C systems (blue points) are compared to the normalized cross section law (red line) and with the results of the S+C at 19.5 AMeV (black point).

These results are compared to the general systematics of Eudes et al. [8] derived from a rich compilation of data. The systematics gives a law for the fusion (both complete and incomplete type) cross section scaled to the reaction cross section and ordered as a function of an energy-mass variable. The law is simple:

$$f(x) = a + \frac{b}{c+x} \tag{6.1}$$

with x=E_{cm}/A_{tot} and where a, b, and c are fit parameters. As a result of the study of the cited paper, the a, b, c parameters are essentially independent of the reaction system i.e. its size, mass asymmetry, and isospin. Our results with respect to this function are shown in fig.6.13. At 25 AMeV, the fusion cross section has been normalized to the Bass reaction cross section value. In the introduction we specified that this may introduce an additional 20-30% uncertainty which is included in the final error bar. A further source of error, as we explained, can come from the choice of the Z values to be included. If we reduce the residue

range by increasing the lower limit (Z>10 as in Pirrone et al. [16] and Z>9 at 25 and 50 AMeV, respectively) the normalized fusion cross sections vary from 16.4% to 15.2% and from 2.9% to 1.5 % for 25 and 50 AMeV respectively. The variation is additionally included in the final error bars of fig 6.13. Our results well agree with the systematics predictions and this suggests the global correctness of the employed method. In fig.6.13, we also drew the Pirrone et al. [16] point for SC@19.5 AMeV beam energy. We remark that this result was not included in the global fit of Eudes because it deviates too much from the general observed trend for other reactions in the same energy range (more than 2σ away from the overall fit formula).

6.3 Analysis of particle correlations

In this section, we investigate the correlations between charged particles emitted in the FAZIACor reactions, i.e ^{20}Ne, ^{32}S+ ^{12}C at 25 and 50 AMeV beam energies, as a complementary way of studying the fragment formation and decay, possibly as a function of the collision mechanism. In these first attempts to investigate correlations between particles with the FAZIA array we naturally considered the α particles since decay chains for N=Z systems are involved and indeed more than one α per event is detected. Various arguments can be introduced to explain the choice of the candidates of this investigation. First, we look for particles coming from the decay of previously formed sources; in other words, starting from all detected species in an event, we try to reconstruct resonant states for some fragments, thus going back at least of one step toward the original population. In this respect we can access only states above the separation energies of the parent system. In this analysis, we restrict to only correlations of particle pairs, neglecting for the moment the search of multiple particle correlations (3 or more). To do so, we exploit the good isotopic resolution of FAZIA to extend the panorama of candidates for resonant states where, for instance, an α is produced together with an identified isotope with charge Z and mass A, where Z can be as high as 8 or more.

When applying the correlation technique, an experimental limitation comes from the granularity of the apparatus. Indeed, the easiest states that can be reconstructed are the most separated ones, usually not far from the separation energies. Also, with increasing size of the decaying fragments, the level spectrum becomes more complicated with many states overlapping at moderate excitation energies; this suggests that the correlation analysis is better suitable for not too heavy fragments as shown in literature [35, 36, 43, 48]. As a matter of fact, considering the collected data, we took suggestions from nuclear databases to select our best candidate pairs. The NUDAT2 [106] database indicates at first sight as good

candidates the alpha decay of ^{10}B and ^{20}Ne. They both possesses a discrete spectrum with enough separation between groups of energy levels near the decay threshold which can be seen by our apparatus. Moreover, they are representative of two groups of events that can differ much for the two systems, SC and NeC, allowing to explore different reaction regimes. Just in the spirit of what discussed about fig.6.3, we argue that B and Ne have different origin for a given system.

As already discussed in chapter 1, the two particle correlation function, 1+R(q), can be defined as:

$$1 + R(q) = C_{12} \cdot \frac{Y_{12}(\vec{p}_1, \vec{p}_2)}{Y_{12}^{uncor}(\vec{p}_1, \vec{p}_2)} \tag{6.2}$$

where $Y_{12}(\vec{p}_1, \vec{p}_2)$ is the correlated yield, $Y_{12}^{uncor}(\vec{p}_1, \vec{p}_2)$ the uncorrelated two-particles yields constructed via the so-called event-mixing technique [52, 53] and C_{12} a normalization constant which is taken to give R(∞) = 0. If two emitted particles are totally uncorrelated, the probability of detecting them in coincidence would be equal to the product of the probabilities of detecting the single yields, resulting in a rather flat correlation function, 1+R(q)=1, whatever the q value (we remind that q is the relative momentum). In our analysis, q is taken to be the relative energy E_{rel} or excitation energy E* [55, 56]. E_{rel} and E* are just connected by the Qvalue of the reaction. In fig.6.14, we show an example of the results from the data and the associated mixing technique applied to the ^{10}B→^{6}Li+α decay in the NeC@50 AMeV reaction in order to give an idea of the background component. As it can

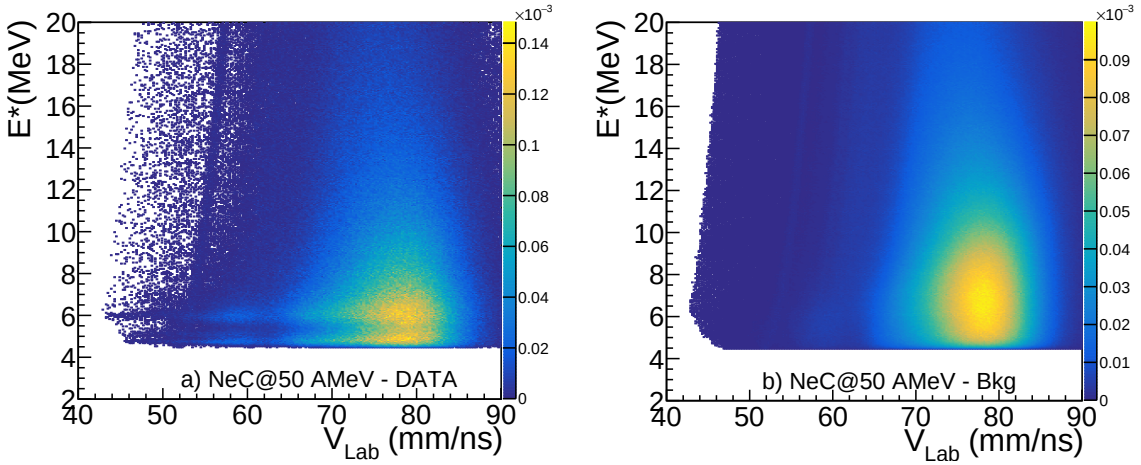

Fig. 6.14 Experimental E* vs. V_{Lab} for the reconstructed ^{10}B→^{6}Li+α decay in the NeC@50 AMeV reaction. In the left panel is shown the correlation with coincident pairs (same event) while on the right the corresponding background coming from the event mixing technique is depicted.

be seen, the phase-space population is very similar for the two cases indicating that a big

part of the experimental data is dominated by the background given by uncorrelated events. The spectrum on the right represents our best estimate for $Y_{12}^{uncor}(\vec{p}_1, \vec{p}_2)$. It is interesting to note that in the left panel of fig.6.14 two horizontal lines are clearly recognizable below E*=7MeV. These regions correspond to intrinsec properties of the parent excited fragment (here Boron) which, as it must be, do not depend on the velocity of the source.

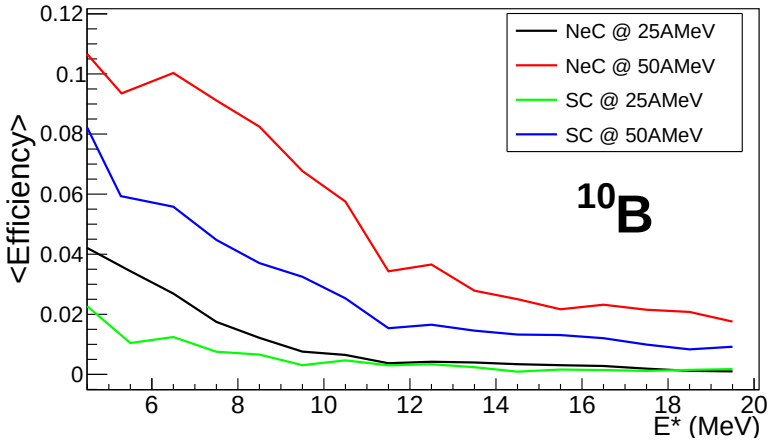

(a)

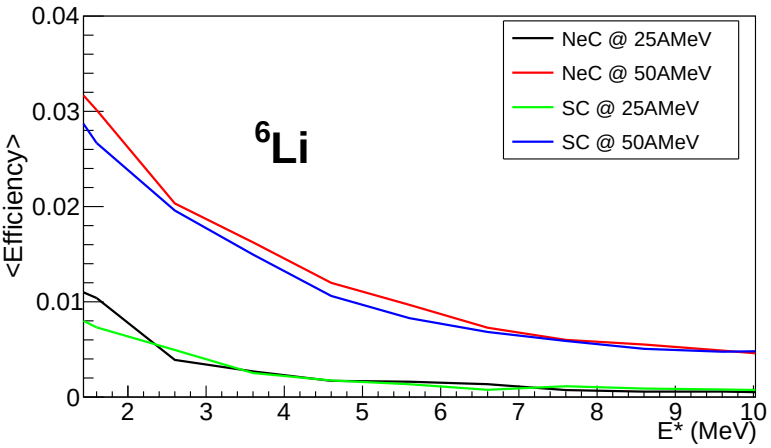

(b)

Fig. 6.15 Average efficiency calculated as a function of the reconstructed excitation energy (E_{rel}+Q_{val}) from the HIPSE simulation for a) ^{6}Li-α particles (expected for the ^{10}B decay) and b) alpha-d (expected for the ^{6}Li). We highlight that the origin of the X-axis is suppressed in these plots as the efficiency starts from the Q_{value} for the respective decay.

6.3.1 Efficiency observations and kinematical phase-space

Before going into the details of the correlation spectra we need to make some considerations on the detection efficiency and resolution of FAZIA in the angular range covered by the detector. We have calculated the efficiency of the employed apparatus for the measured correlation functions, following a similar procedure as Ref.s [35, 57]. These calculations have been made by means of the MonteCarlo-simulations introduced in chapter5, taking into account the geometry of the detectors, the energy resolution, energy thresholds and the granularity of the telescopes. The average integrated efficiency for each decay channel was calculated as the ratio between the yield of detected pairs and the number of generated pairs for each bin of relative energy. In Fig.6.15, the efficiency spectra are represented for the alpha-^{6}Li and alpha-deuteron expected for the ^{10}B and ^{6}Li correlations, respectively. Similar plots are made also for the other considered nuclei. These show how the limited acceptance heavily influences the detection of the the energy states, strongly affecting the collected statistics.

For sake of clarity, we sketch in fig.6.16a an in plane representation of a hypothetical $^{10}\mathrm{B}\rightarrow{}^6\mathrm{Li}+\alpha$ decay where we indicate the main variables which define our kinematical phase-space. The variable here represented are essentially the same that we used in discussing the QP break up (see figs.6.5,6.4). As we can qualitatively realize, due to the limited angular coverage around the beam direction (lab polar range 2-8°), the detection efficiency highly depends on various parameters, mainly on the relative velocity v_{rel} of the pair (directly related to E* of the hot fragment), on the source velocity V_R in the CM and on the α-angle, drawn in the sketch. This latter essentially represents the polarization of the decay with respect to the parent fragment flight direction and it has been largely used to characterize the fission-like process after damped collisions, also by our group [159, 162–165]. It reads:

$$\alpha = arccos\left(\frac{\vec{V_R}\cdot\vec{v_{rel}}}{|\vec{V_R}\cdot\vec{v_{rel}}|}\right) \tag{6.3}$$

We use the definition of vectors such that $\alpha = 0$ means aligned configurations with the light species emitted towards the CM. Generally speaking, decay steps from fragments fast in CM tend to be focused at forward directions, within the FAZIA acceptance independently of the α-angle. Polarizations orthogonal to the original fragment directions, instead, tend to be unfavoured, more if the excitation energy is large and/or the decaying nucleus has small CM velocity, i.e. for cases possibly related to more central collisions. From the above arguments we predict that our detectors can explore even large excitation energy for rather stretched configurations while it misses more triangular-shape velocity configurations. This

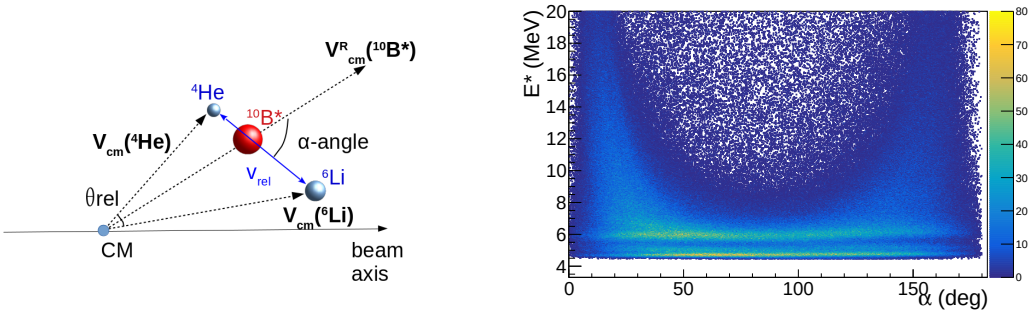

(a) (b)

Fig. 6.16 a) Schematic in plane kinematical description and variables for a possible ^{10}B$\rightarrow^{6}$Li+α decay. b) Experimental E* vs α correlation for the NeC@25 system

is exactly what is shown in the fig.6.16b where the E* vs. α matrix is represented again for the correlation pairs candidate to ^{10}B decay for the NeC reaction at 25 AMeV. We clearly see that in the region of low excitation energy the apparatus does not introduce significant deformations while resonant states above 8-10 MeV would be inaccessible for decay steps orthogonal to the parent nucleus direction. This is another reason why we cannot extend the investigation towards high energy states knowing that in any case they would intrinsically overlap more and thus would be more difficult to separate .

In this last subsections we present some preliminary attempt to discriminate the various (accessible) excitation energy levels and to comment their contribution at least comparing in a qualitative manner the four reaction cases. All plots refer to experimental data. We hereafter focus on the ^{10}B and ^{20}Ne resonances, that represent two very different cases of fragment decay, comparing both two dissipation levels in the same reaction or two reactions for a rough similar reaction type. We remark that ^{20}Ne is well within the class of QP for both systems and, to a less extent, of residues from fusion like reactions; instead Boron is an intermediate fragment that can have various origins in the four reactions. Thus the selection along the lab velocity applyied to Boron, as we propose below, must be only considered as a rough attempt to distinguish these resonances as coming more from a QP decay or from a kind of composite system.

6.3.2 ^{10}B$\rightarrow {}^{6}Li+\alpha$ channel

In fig.6.17 we show the experimental ^{6}Li+α correlation function versus E*, measured in the FAZIACor collisions for all systems. As previously seen in this section, the correlation pairs do manifest the presence of excited levels for fragment decay but also a significant background contribution is present. The Coulomb background correlation function has

been estimated using a phenomenological curve defined as in [35, 57] and described in chapter1. This phenomenological function describes well two-particle correlations which are not dominated by resonant interactions, but only by long-range Coulomb repulsion. This background curve is drawn (red continuous line) in each pad. The spectra in the four cases

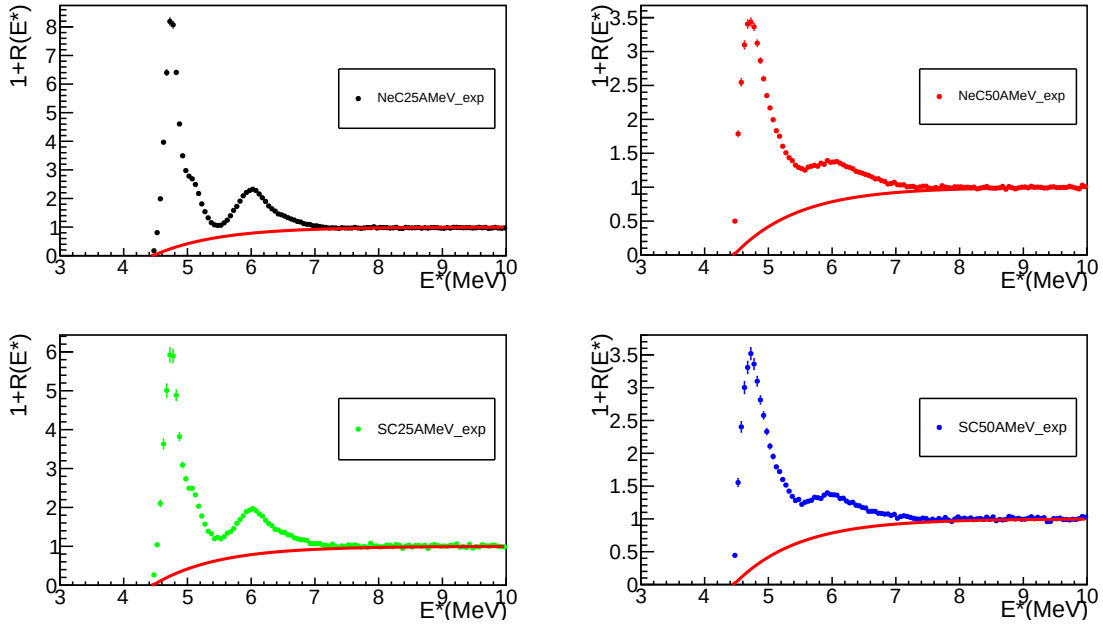

Fig. 6.17 Experimental ^{6}Li+α correlation function versus E*, measured in the FAZIACor collisions. Red lines represent the Coulomb background correlation functions introduced in [35, 57].

look very similar, starting (as expected) from the Q_{value}=4.46 MeV point; they show at least two peaks in every reaction case. At 25 AMeV beam energy, as expected, the resolution is better because of the lower effect of finite granularity on resolution for slower sources. To give an idea, the broadening of the first peak specifically increases from $FWHM_{25}$=5% to $FWHM_{50}$=10%. The observed peak structure is associated with the following groups of excited levels which cannot be further separated in this integrated (over the entire V_{Lab} range) spectra:

- First group (centered at 4.7 MeV): 4.774 ($J^{\pi}=3^{+}$)
- Second group (centered at 5.0 MeV): 5.110 ($J^{\pi}=2^{-}$), 5.163 ($J^{\pi}=2^{+}$), 5.182 ($J^{\pi}=1^{+}$)
- Third group (centered at 6.0 MeV): 5.919 ($J^{\pi}=2^{+}$), 6.024 ($J^{\pi}=4^{+}$), 6.129 ($J^{\pi}=3^{-}$)

These groups of energy levels are well visible at 25AMeV; at 50AMeV the first two groups overlap. Anyhow they qualitatively agree with results of similar particle decay correlation

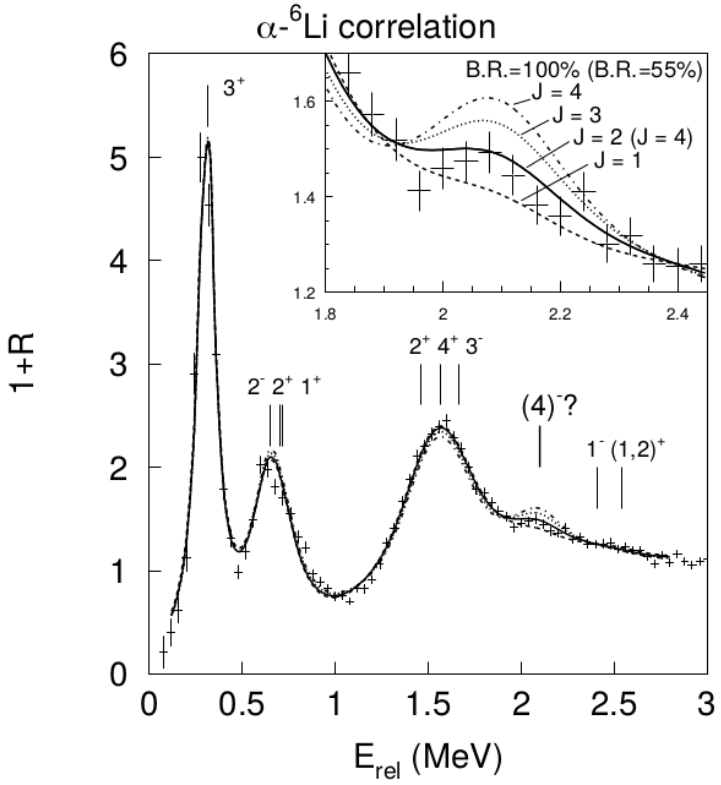

Fig. 6.18 R-function for the $^6Li+\alpha$ correlation reconstructed in ^{129}Xe+^{197}Au collisions at 50AMeV as a function of E_{rel}. In the top panel, a fit procedure was applyied to tentatively assign the spin of the 6.56 MeV state. Figure taken from ref.[55].

experiments [43, 55, 57] where the $^{10}\text{B}\rightarrow {}^6Li+\alpha$ was observed. As an example, below in fig.6.18, we show the $^6Li+\alpha$ correlation reconstructed in ^{129}Xe+^{197}Au multifragmentation collisions at 50AMeV with the large area silicon-strip/CsI detector array LASSA[166]. Hereafter, the R-function is shown as a function of E_{rel} and not E*. Nevertheless, we can clearly observe that the same levels are basically populated although with better resolution in their case. This is achieved due to the 3 mm pitch of the silicon-strip detectors corresponding to a good angular resolution of $\Delta\theta = \pm 0.43^\circ$ for this setup. Fig.6.18 can also be better compared with the next figure in fig.6.19a where the background has been removed.

As done by [43, 57], it is interesting to explore if some evolution is observed when moving from more peripheral to more central collisions. This can be done by gating the E* spectra (after the removal of the estimated background) in different regions of lab velocity for the assumed parent fragment. As previously discussed in this chapter, the lab velocity is a crude order parameter for the reaction violence, especially for light fragments as Boron. Basically, on correlations of the type of fig.6.14, we put two gates: one around the CM

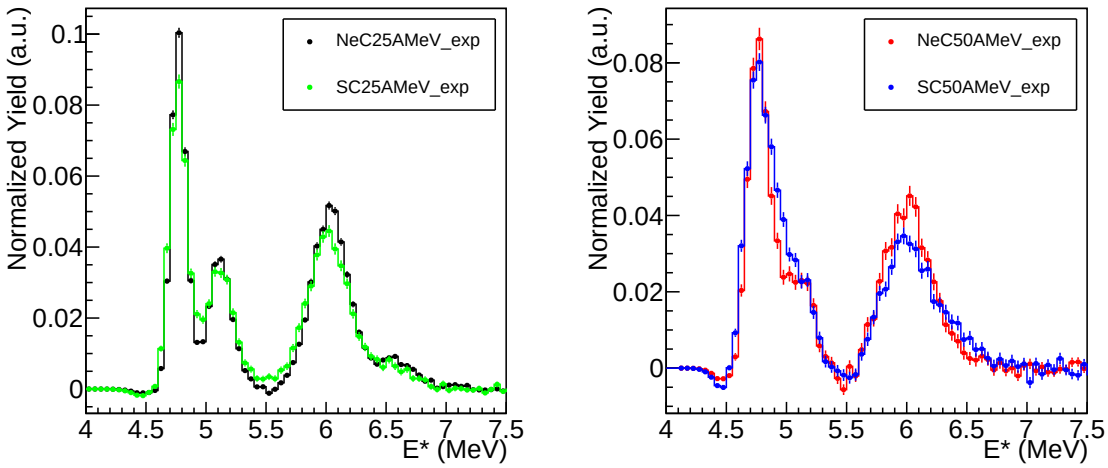

(a) Central

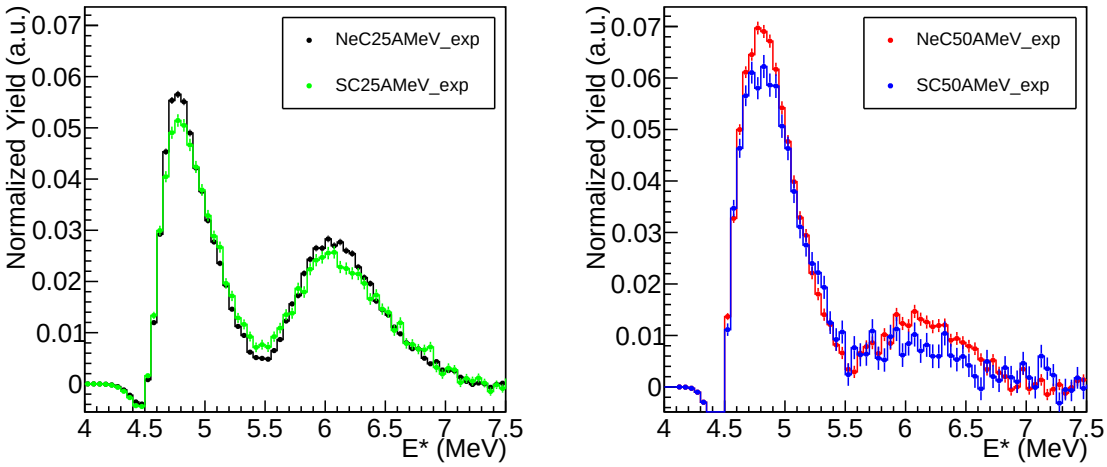

(b) Peripheral

Fig. 6.19 Background subtracted yields for the ^{6}Li+α correlation shown with two different centrality cuts: a) central collisions and b) peripheral collisions. Spectra are normalized to the integral to allow a better shape comparison between systems. Left pad represent the data at 25 AMeV and right ones the data at 50 AMeV

velocity and one centered around the projectile velocity.

The ^{10}B excitation energy plots, after the removal of the background, for the four reactions are displayed in fig.6.19a and fig.6.19b. The curves are all normalized to unity so to represent the excitation probability and to be easily compared in shape. The upper panel refers to what we call "central" collisions while we label the bottom panel as "peripheral", this corresponding to different values of the reconstructed ^{10}B velocity. We remark once more that the adjective "central" and "peripheral" are indicative of the two gates but must be taken as a rough ordering without quantitative assignment. Looking at the spectra we can do various comments. The best resolution is obtained for the central gate at the lower bombarding energy. The reconstructed levels of the excited Boron in this regions are more evidently separated and better defined. One can now easily recognize the second group at around 5.1 MeV and also the presence of a fourth peak around 6.5 MeV associated to the 6.560 ($J^{\pi}=4^{-}$) level. In fact, with this "central" gate the excitation spectra of fig.6.19a(left panel) resembles remarkably well to that of fig.6.18 obtained also in central collisions but in much heavier systems. The resolution worsens toward periphery and with increasing beam velocity, due to the stronger impact on the experimental resolutions (in energy and angle). From a general comparison of the curves, we can state that the ^{10}B excitation spectrum is quite similar in all cases, taking into account the different level resolutions. If we compare the two curves in each panel, we can clearly see that the shapes are almost identical: the excitation spectrum is not affected, for Boron, in case it is formed in S+C or Ne+C reactions, independently of energy and "centrality". This comments suggest that the fragments far from projectile size and "a fortiori" from the size of some compound-like system are produced in highly dissipative events and are populated with very similar excitation spectra. At the present level of our analysis, we cannot state any more robust or quantitative conclusion on that.

6.3.3 ^{20}Ne$\rightarrow$ $^{16}O+\alpha$ channel

The second and final example that we studied is the excitation spectrum for the ^{20}Ne, reconstructed in events with coincident pairs of ^{16}O and α. This case can be viewed as the complementary of Boron; while for the latter a similar origin can be hypothesized independent of the collision, only in Ne+C reactions ^{20}Ne is exactly the projectile isotope. In fig.6.17 we show the experimental ^{16}O+α correlation function versus E*, measured in the FAZIACor collisions for all systems as already done in fig.6.17. Even in this representation, the spectra appear very different for the two energy regimes, here zoomed in from the Q_{value}=4.73 MeV point, with a clear separation of at least three peaks at 25 A MeV and only one (and a hint for a second small contribution at around 8MeV) at 50 AMeV. The observed

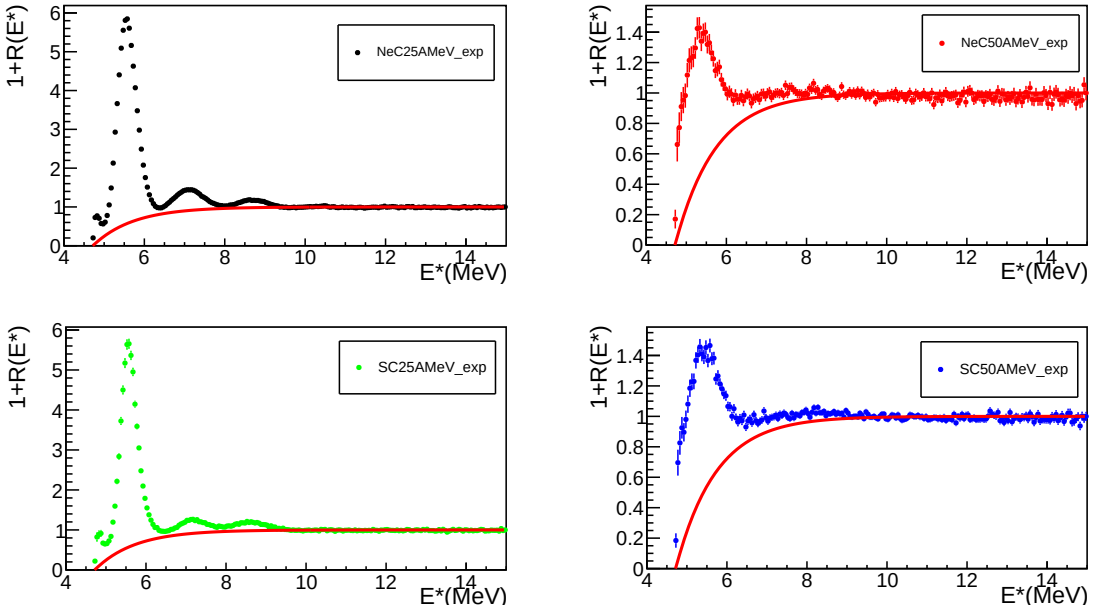

Fig. 6.20 Experimental ^{16}O+α correlation function versus E*, measured in the FAZIACor collisions. Red lines represent the Coulomb background correlation functions expressed as in [35, 57].

peak structure is associated with the following groups of excited levels which can not be further separated:

- First group (centered at 5.7 MeV): 5.621 (J^{π}=3^{-}), 5.787 (J^{π}=1^{-})
- Second group (centered at 7.2 MeV): 7.156 (J^{π}=3^{-}), 7.191 (J^{π}=0^{+}), 7.421 (J^{π}=2^{+})
- Third group (centered at 8.7 MeV): 8.708 (J^{π}=1^{-}), 8.777 (J^{π}=6^{+}), 8.820 (J^{π}=5^{-}), 8.854 (J^{π}=1^{-})

These groups of energy levels match the ones seen in literature (see [106, 167] and references therein), however they are generally obtained through elastic scattering methods and/or gamma decays. As for the Boron case, we can employ the same centrality selection by means of the reconstructed velocity. However we limit here to the 25 AMeV reactions since at 50 AMeV the level resolution is poor and the contributions above 6 MeV are seemingly very small. In fig.6.21 we show the lab velocity distributions for ^{20}Ne formed in the reaction NeC (SC) on the left (right) panel. Each panel contains the spectra of ^{20}Ne ions both directly measured (black line) and reconstructed from ^{16}O+α pairs (red line). The curves in each panel are normalized to unity for shape comparison. In the plots the arrows correspond to the relevant velocities of the beam and the CM. First we note the remarkable difference between

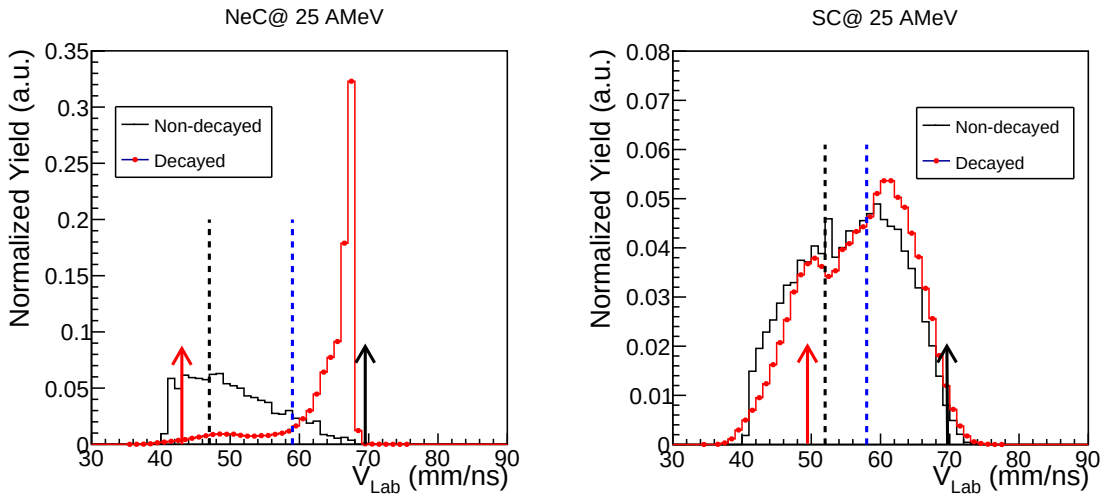

Fig. 6.21 Laboratory velocity of Neon fragments, reconstructed from the ^{16}O+α correlation (Decayed) and detected as a whole (Non-decayed). Arrows indicate the projectile velocity (black) and center of mass velocity (red). The two vertical bars represent the limits for the "central" (black dashed) and "peripheral" cut (blue dashed). See text for more details.

the NeC and the SC cases. For NeC the chance to directly detect a final ^{20}Ne ions is confined to the region of damped collisions and no such species are present close to the beam velocity. For reconstructed resonances, instead, we see that they extend over the whole velocity range with a strong enhancement towards the beam velocity. For the SC reactions, instead, we see that ^{20}Ne can be observed with similar probability as a cold fragment or as an excited one in the whole velocity range. This is consistent with the observation that ^{20}Ne can be produced as a final (cold) or almost final (excited) fragment following a enough dissipative event; it cannot be originated from too peripheral events. Following these arguments we imposed the cuts that are marked by the dashed segments in the panels; these segments represent the limits for the applyied selections; the “central” selection extends from the lower segment to below while the “peripheral” encompasses events with velocity above the higher segment. A cautious zone in between the two regions is excluded in order to reduce the possible cross-talk for the two groups.

In fig.6.22 we show the excitation spectra for the 25 AMeV collisions divided in the two mentioned gates of lab velocity of the reconstructed ^{20}Ne. Several observations can be made by comparing two reactions in the same velocity gate and by comparing the same reaction in the two gates. Let us first consider the top panel; the cut "central" should guarantee that the resonance is reconstructed having a velocity next to the CM thus probably related to violent collisions. For both systems, but more evidently for NeC, a ^{20}Ne ion represents a possible residue after some fusion-like process. The initial hot source (at most is ^{32}S for

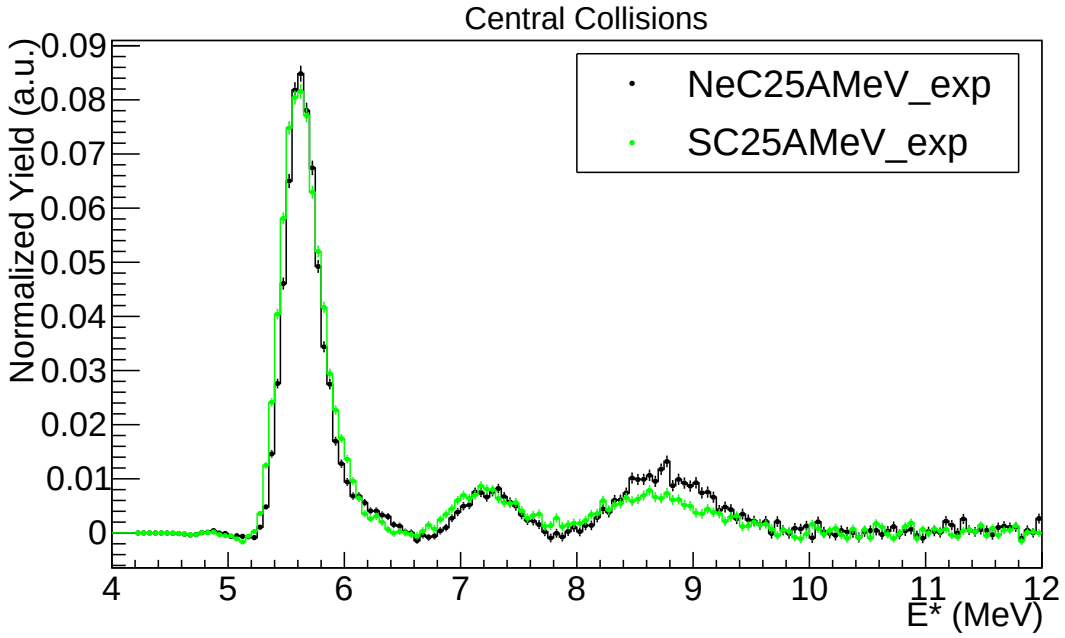

(a)

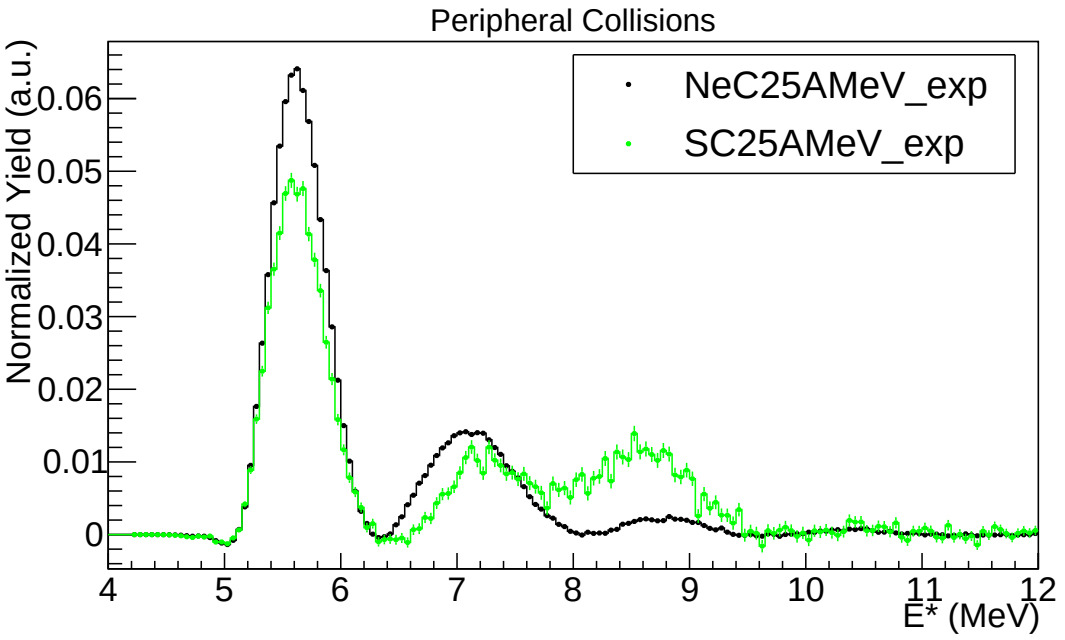

(b)

Fig. 6.22 Background subtracted excitation spectra for the ^{16}O+α correlation shown with two different centrality cuts: a) central collisions and b) peripheral collisions. Spectra are normalized to the integral to allow a better shape comparison between systems.

complete fusion in NeC) is strongly excited and decays reaching with a certain probability various channels, as for instance a ^{20}Ne even with residual excitation above the α separation energy. Thus the final step can lead to the detected pair of an α and an Oxygen ion. The level group above 8MeV is slightly more probable in NeC than SC. We remark that in a scenario assuming statistical equilibrium (where thermodynamics arguments can be valid as assumed for instance in refs.[43, 57]) the level population strongly depends on the temperature, higher energy states becoming more probable with increasing temperature. This is consistent with the fact that observing ^{20}Ne in final states (as we measure) corresponds to more damped collisions in NeC than in SC; in the former reaction we must suppose the previous formation of some fused system in order to observe ^{20}Ne ions in this gate, whilst this is not strictly the case for SC collisions where Ne ions can be QP residues. The results for the "peripheral" gate on the right bottom can be qualitatively explained with similar arguments. In NeC reactions the chance of observing resonant ^{20}Ne states can be ascribed to binary dissipative collisions close to the regime of direct reactions. The projectile becomes a QP excited via a few exchanges of mass and charge with the C-target. If the reconstructed pair has a rather high velocity this means on average a not too high excitation, otherwise the final state could not be ^{20}Ne because its size is surely close to the primary parent. Instead, for the SC reaction, the ^{20}Ne represents a final QP residue only if sufficient energy is dissipated in the QP systems. The previous arguments are consistent with the fact that the excitation spectrum is shifted to lower values in NeC than in SC; the third excited level group is approximately a factor of two less in NeC than in SC.

At the level of analysis performed so far we are not able to go ahead and derive quantitative results related to the excited state populations of these and other possible resonances. What we want to remark here in conclusion is that the FAZIA array, although not designed as a particle-fragment correlator, can offer interesting opportunities to explore multi-particle correlations with analysis gated on different impact parameter regimes. From this point of view we note that this kind of investigation is under discussion within the collaboration for the new data obtained in Ni+Ni reactions in a recent experiment. This measurement, carried on at GANIL in 2019, was based on the coupling of the entire FAZIA array (192 telescopes instead of the 64 sensors of this Thesis) with the INDRA multidetector. The very large acceptance of the entire apparatus adding to the excellent isotopic separation of FAZIA should guarantee the application of this particle correlation analysis with more accurate and reliable gates on reaction types. Thus the rich variety of particle-fragment pairs that can be recognized with FAZIA (with fragments well above magnesium, if produced) can be reconstructed and compared (possibly with good statistics) in several centrality bins.

SUMMARY AND CONCLUSIONS

As many previous other works, this thesis has been made possible in the context of the FAZIA collaboration which performs heavy ion collision experiments using cutting-edge charge particle detectors. The long R&D campaign has culminated with the development of a "recipe" for producing Si-Si-CsI telescopes, grouped in blocks, capable of excellent performances in terms of ion identification (see chapter2). A latter contribution to the characterization of the CsI layer was also given in this work as summarized here in the conclusions. The data analyzed in this Thesis was collected as part of the FAZIA collaboration program started at LNS laboratories a few years ago, where the first four complete blocks were used. Specifically, we analyzed the data of the ^{32}S,^{20}Ne+^{12}C reactions at 25 and 50 AMeV beam energies, referred to as FAZIACor.

The physical case develops around the study of the reaction mechanisms in light-ion reactions in the Fermi energy range and aims at presenting some new detailed data in this field also by employing the particle correlation tool as originally proposed. In fact, these light reaction at these energies are in itself very challenging to study due to the concurring of many effects. First due to the relative small mass and high energy deposition, the reaction evolution is more compressed and the different reactions mechanisms are harder to separate over a broad impact parameter range. Second, finite size fluctuations and structure effects as alpha-clustering (the systems are N=Z) have more influence on the outcome than for heavier systems. In particular, an interesting study in literature, that we wanted to replicate and extend to the FAZIACor systems, deals with the separation of the fusion cross section into the various competing channels, i.e. the complete and incomplete fusion, as a function of the bombarding energy. The systematics [8] present today of these two phenomena are quite detailed for the Coulomb barrier region while in the transition region of the Fermi energy, the available data is scarce and often contradictory in this light mass reactions.

As usual, in the framework of heavy-ion reactions, the comparison of experimental findings with extensive simulations based on different reaction models is essential and indeed is a central point of the thesis. For these purposes we employed the AMD [138]

and HIPSE [135] models coupled to HFl][128] and SIMON respectively for the afterburner phase. Such a comparison provides help in guiding our event selections and permits to draw some conclusions on the observed phenomena. We want to stress that such comparisons, and in particular with the dynamical AMD code, is relatively new in this light region as testified by recent papers [136, 146, 168] and up to now applied exclusively to C+C reactions. Unfortunately, it was impossible to employ this model for the NeC system as the code details are not yet optimized while luckily the SC system was within the current AMD version's reach.

After the data reduction phase, described in details in chapter3, the main achievements and findings of this thesis are reported in chap.4 and chap.6 and can be summarized as following:

- The response of the CsI crystals to energetic light particles (protons) was deeply studied and two main findings have been published [109]. First, the light output versus energy was shown to be linear in the lower portion of the investigated energy range while showing a clear deviation from linearity on the higher energy side as also observed in literature [110]. These deviations were interpreted as due to the tapered geometry of the CsI and less to doping uniformity effects. Moreover, we highlighted and estimated the effects of proton induced nuclear collisions via Pulse Shape Analysis in CsI(Tl) crystals. Experimental efficiency for proton identification in the examined energy range was deduced and compared with GEANT4 simulations. These results will provide an efficiency correction curve for future higher energies studies.

- A general comparison with the MonteCarlo models of the reaction mechanisms and fragment production for light systems underlined that although great progress have been made from the theoretical and simulation side, there are still some missing details with respect to this mass region of the Fermi energy. In particular for the FAZIACor reactions, we found that both AMD and HIPSE tend towards less dissipative collisions which overestimate the production of heavy fragments. In the performed reaction characterization, notwithstanding the limited coverage of the setup, candidates for violent collisions such as fragmentation/vaporization were found through a global classification of the events. The bad reproduction of those and in general of multi-fragment events may represent the disagreement between the observed data and model predictions. Furthermore, as already found at lower incident energies, the emission of alpha particles is underestimated by models for these N=Z systems also at Fermi energies. In the context of model comparisons, we extended the use of dynamical models to such light systems which in itself represents a challenging quest. Moreover,

for the first time we were able to couple the AMD model to the HFl afterburner, specifically optimized with low energy reactions to better include structure effects. While AMD by Ono et al. [138] is one of the best performing code in the field of ion collisions at Fermi energies, the HFl code was implemented within our collaboration years ago, to describe the statistical decay of light nuclei in a more accurate way than other models.

- Also in this Thesis we profited of the good isotopic capability of the FAZIA detectors as done in previous papers[137, 156, 159]. The apparatus was positioned at forward angle so to cover a relatively large portion of solid angle for our reactions studied in reverse kinematics. When selecting QP-like sources, the break-up mechanism was evidenced. The comparison of experimental data showed how the particular break-up channel into one big fragment (Z>5) and one/more IMF(Z=3,4,5) is easily detected with our setup. The LCP emission pattern in coincidence with a QP was also studied and compared to the results of the simulations. The AMD+HFl code reproduces rather well the LCP multiplicities. However the experimental data evidenced a significant yield of alpha particles in the midvelocity region which seems for the moment not well accounted for by the models. This means that the QT emission or some other intermediate source is not particularly well defined in the models and still left to understand.

- The reaction mechanisms of complete and incomplete fusion in the SC systems was investigated and disentangled by means of a kinematical analysis (as already done in other papers [9, 16]) for big fragments, isotopically resolved thanks to the FAZIA performances. For SC at 25 AMeV, using the data acquired by a beam monitor, the absolute values of the cross sections were given while for SC at 50 AMeV only relative values were obtained. This values were compared to the available systematics in order to test the procedure and to validate our results. Indeed we found that as the beam energy increases the component of fusion (complete and incomplete) mechanism decreases as expected , with our experimental data being within errors compatible with the prediction of the Eudes systematics [8]. Moreover, it is shown that indeed the complete fusion component is a vanishing fraction for the 50 AMeV energy. Therefore, in this context, the FAZIACor absolute and relative cross section measurements provided additional important confirmation on the Fermi domain (above 20 AMeV) where data especially for light systems are scarce.

- The feasibility of particle-particle correlations was clearly demonstrated for the FAZIA apparatus as we were able to discriminate the discrete states of few selected isotopes

(for example ^{10}B and ^{20}Ne) with relatively good precision. The various efficiency effects of the limited coverage and granularity were discussed in order to show the limits of this technique with the FAZIA setup. In particular, we showed that the discrimination of discrete levels is severely limited for the most peripheral collisions and/or for high beam energies due to the high velocity of the decaying sources; for those, the fluctuations increasing with the weight of the worse energy calibration (CsI contribution increases) and as a consequence of the finite granularity ($\Delta\theta = \pm 0.7^\circ$) do not allow sufficient level separation. Nevertheless, we put into evidence differences and similarities, in a qualitative way, for the excitation energy spectra of some resonances taken as representative within the range of final fragments. The observed shapes are consistent with the expectations basing on the various parameters under control (system size, bombarding energy and centrality selection). This kind of analysis, pioneer in the FAZIA group, suggests that we can do more in the future, by also addressing the subject of the modifications of fragment population and decay as a function of the production site (labeled often as 'in medium' effects). This is already planned in the analysis of the new data from the last experiment where FAZIA was coupled with the INDRA multidetector allowing for an almost 4π coverage.

In conclusion, in this Thesis, we presented a detailed analysis of the ^{32}S, ^{20}Ne + ^{12}C reactions at 25 and 50 AMeV beam energies with four block of the FAZIA array. The main goals were to investigate the reaction mechanism for light ion collisions and to test the particle-particle correlation capabilities of the apparatus. The reaction dynamics studies are complemented also by a study of one of the detection layer of the FAZIA detector, namely the characterization of the CsI response to energetic protons.

ACKNOWLEDGEMENTS

This work required the use of a lot of computation time for the analysis of the experimental and simulated data. I would like to thank the IN2P3 Computing Centre (or CC-IN2P3) in Lyon for the kind use of the computing infrastructure and resources.

Throughout the writing of this dissertation I have received a great deal of support and assistance. I would first like to thank my supervisors for their valuable guidance throughout my studies and invaluable experitise. I would also like to acknowledge my colleagues for their wonderful collaboration. I want to thank them for their patient support and for all the adivice I was given to further my research. Finally, I would also like to express my gratitude to the FAZIA and NUCLEX collaborations for allowing me to perform these studies.

In addition, I would like to thank my parents for their wise counsel and unconditional support. You are always there for me. Last but not least, I could not have completed this dissertation without a little help from my friends who provided stimulating discussions as well as happy distractions to rest my mind outside of my research.

REFERENCES

[1] E. Suraud D. Durand and B. Tamain. *Nuclear dynamics in the nucleonic regime*. IoP, Bristol and Philadelphia, 2000. ISBN 9780429138355. doi: doi.org/10.1201/9781420033793. URL https://doi.org/10.1201/9781420033793.

[2] J. J. Griffin. Statistical model of intermediate structure. *Phys. Rev. Lett.*, 17:478–481, Aug 1966. doi: 10.1103/PhysRevLett.17.478. URL https://link.aps.org/doi/10.1103/PhysRevLett.17.478.

[3] E. Gadioli and E. Gadioli Erba. Pre-equilibrium emission. *Nuclear Instruments and Methods*, 146(1):265 – 277, 1977. ISSN 0029-554X. doi: https://doi.org/10.1016/0029-554X(77)90521-3. URL http://www.sciencedirect.com/science/article/pii/0029554X77905213.

[4] J. Łukasik et al. Dynamical effects and intermediate mass fragment production in peripheral and semicentral collisions of xe+sn at 50 mev/nucleon. *Phys. Rev. C*, 55:1906–1916, Apr 1997. doi: 10.1103/PhysRevC.55.1906. URL https://link.aps.org/doi/10.1103/PhysRevC.55.1906.

[5] S. Piantelli, L. Bidini, G. Poggi, M. Bini, G. Casini, P. R. Maurenzig, A. Olmi, G. Pasquali, A. A. Stefanini, and N. Taccetti. Intermediate mass fragment emission pattern in peripheral heavy-ion collisions at fermi energies. *Phys. Rev. Lett.*, 88:052701, Jan 2002. doi: 10.1103/PhysRevLett.88.052701. URL https://link.aps.org/doi/10.1103/PhysRevLett.88.052701.

[6] R. Lionti, V. Baran, M. Colonna, and M. Di Toro. Imf isotopic properties in semi-peripheral collisions at fermi energies. *Physics Letters B*, 625(1):33 – 40, 2005. ISSN 0370-2693. doi: https://doi.org/10.1016/j.physletb.2005.08.044. URL http://www.sciencedirect.com/science/article/pii/S0370269305011470.

[7] V. Baran, M. Colonna, V. Greco, and M. Di Toro. Reaction dynamics with exotic nuclei. *Physics Reports*, 410(5):335 – 466, 2005. ISSN 0370-1573. doi: https://doi.org/10.1016/j.physrep.2004.12.004. URL http://www.sciencedirect.com/science/article/pii/S0370157305000025.

[8] P. Eudes, Z. Basrak, F. Sébille, V. de la Mota, and G. Royer. Comprehensive analysis of fusion data well above the barrier. *Phys. Rev. C*, 90:034609, Sep 2014. doi: 10.1103/PhysRevC.90.034609. URL https://link.aps.org/doi/10.1103/PhysRevC.90.034609.

[9] H. Morgenstern, W. Bohne, K. Grabisch, D.G. Kovar, and H. Lehr. Incomplete momentum transfer in heavy-ion fusion at 14.5 mev/nucleon. *Physics Letters B*, 113 (6):463 – 466, 1982. ISSN 0370-2693. doi: https://doi.org/10.1016/0370-2693(82)90786-9. URL http://www.sciencedirect.com/science/article/pii/0370269382907869.

[10] H. Morgenstern, W. Bohen, W. Galster, K. Grabisch, and A. Kyanowski. Influence of the mass asymmetry on the onset of incomplete and the limit to complete fusion. *Phys. Rev. Lett.*, 52:1104–1107, Mar 1984. doi: 10.1103/PhysRevLett.52.1104. URL https://link.aps.org/doi/10.1103/PhysRevLett.52.1104.

[11] W. Bohne, H. Morgenstern, K. Grabisch, T. Nakagawa, and S. Proschitzki. Critical excitation energy in fusion-evaporation reactions. *Phys. Rev. C*, 41:R5–R8, Jan 1990. doi: 10.1103/PhysRevC.41.R5. URL https://link.aps.org/doi/10.1103/PhysRevC.41.R5.

[12] B. Heusch, C. Beck, J. P. Coffin, P. Engelstein, R. M. Freeman, G. Guillaume, F. Haas, and P. Wagner. Entrance channel effect for complete fusion of o + c isotopes. *Phys. Rev. C*, 26:542–554, Aug 1982. doi: 10.1103/PhysRevC.26.542. URL https://link.aps.org/doi/10.1103/PhysRevC.26.542.

[13] S. M. Lee, T. Matsuse, and A. Arima. "statistical yrast line" in heavy-ion fusion reactions. *Phys. Rev. Lett.*, 45:165–168, Jul 1980. doi: 10.1103/PhysRevLett.45.165. URL https://link.aps.org/doi/10.1103/PhysRevLett.45.165.

[14] J.R. Birkelund, L.E. Tubbs, J.R. Huizenga, J.N. De, and D. Sperber. Heavy-ion fusion: Comparison of experimental data with classical trajectory models. *Physics Reports*, 56(3):107 – 166, 1979. ISSN 0370-1573. doi: https://doi.org/10.1016/0370-1573(79)90093-0. URL http://www.sciencedirect.com/science/article/pii/0370157379900930.

[15] R. Bass. Nucleus-nucleus potential deduced from experimental fusion cross sections. *Phys. Rev. Lett.*, 39:265–268, Aug 1977. doi: 10.1103/PhysRevLett.39.265. URL https://link.aps.org/doi/10.1103/PhysRevLett.39.265.

[16] S. Pirrone, G. Politi, G. Lanzalone, S. Aiello, N. Arena, Seb. Cavallaro, E. Geraci, F. Porto, and S. Sambataro. Fusion and competing processes in the ^{32}S+^{12}C reaction at $E(^{32}\mathrm{S}) = 19.5$ mev/nucleon. *Phys. Rev. C*, 64:024610, Jul 2001. doi: 10.1103/PhysRevC.64.024610. URL https://link.aps.org/doi/10.1103/PhysRevC.64.024610.

[17] J. A. Scarpaci, Y. Chan, D. DiGregorio, B. A. Harmon, J. Pouliot, R. G. Stokstad, and J. Suro. Central collisions in the ^{16}O+^{12}c reaction at 32.5 mev/nucleon. *Phys. Rev. C*, 52:764–774, Aug 1995. doi: 10.1103/PhysRevC.52.764. URL https://link.aps.org/doi/10.1103/PhysRevC.52.764.

[18] L Morelli, G Baiocco, M D'Agostino, F Gulminelli, M Bruno, U Abbondanno, S Appannababu, S Barlini, M Bini, G Casini, M Cinausero, M Degerlier, D Fabris, N Gelli, F Gramegna, V L Kravchuk, T Marchi, A Olmi, G Pasquali, S Piantelli, S Valdré, and Ad R Raduta. Thermal properties of light nuclei from 12C+12C fusion–evaporation reactions. *Journal of Physics G: Nuclear and Particle Physics*, 41 (7):075107, jun 2014. doi: 10.1088/0954-3899/41/7/075107. URL https://doi.org/10.1088%2F0954-3899%2F41%2F7%2F075107.

[19] L Morelli, G Baiocco, M D'Agostino, F Gulminelli, M Bruno, U Abbondanno, S Appannababu, S Barlini, M Bini, G Casini, M Cinausero, M Degerlier, D Fabris, N Gelli, F Gramegna, V L Kravchuk, T Marchi, A Olmi, G Pasquali, S Piantelli, S Valdré, and Ad R Raduta. Non-statistical decay and α-correlations in the 12C+12C fusion–evaporation reaction at 95 MeV. *Journal of Physics G: Nuclear and Particle Physics*, 41(7):075108, jun 2014. doi: 10.1088/0954-3899/41/7/075108. URL https://doi.org/10.1088%2F0954-3899%2F41%2F7%2F075108.

[20] A. Camaiani, G. Casini, L. Morelli, S. Barlini, S. Piantelli, G. Baiocco, M. Bini, M. Bruno, A. Buccola, M. Cinausero, M. Cicerchia, M. D'Agostino, M. Degelier, D. Fabris, C. Frosin, F. Gramegna, F. Gulminelli, G. Mantovani, T. Marchi, A. Olmi, P. Ottanelli, G. Pasquali, G. Pastore, S. Valdré, and G. Verde. Experimental study of precisely selected evaporation chains in the decay of excited ^{25}Mg. *Phys. Rev. C*, 97: 044607, Apr 2018. doi: 10.1103/PhysRevC.97.044607. URL https://link.aps.org/doi/10.1103/PhysRevC.97.044607.

[21] R.K. Tripathi, Francis A. Cucinotta, and John W. Wilson. Accurate universal parameterization of absorption cross sections. *Nuclear Instruments and Methods in Physics Research Section B: Beam Interactions with Materials and Atoms*, 117(4):347 – 349, 1996. ISSN 0168-583X. doi: https://doi.org/10.1016/0168-583X(96)00331-X. URL http://www.sciencedirect.com/science/article/pii/0168583X9600331X.

[22] G. Bizard, R. Bougault, R. Brou, J. Colin, D. Durand, A. Genoux-Lubain, J.L. Laville, C. Le Brun, J.F. Lecolley, M. Louvel, J. Péter, J.C. Steckmeyer, B. Tamain, A. Badala, T. Motobayashi, G. Rudolf, and L. Stuttgé. From binary fission to multifragmentation in the decay of heavy excited nuclei. *Physics Letters B*, 302(2):162 – 166, 1993. ISSN 0370-2693. doi: https://doi.org/10.1016/0370-2693(93)90377-T. URL http://www.sciencedirect.com/science/article/pii/037026939390377T.

[23] Willibrord Reisdorf. Dynamics of Multifragmentation in Heavy Ion Collisions. *Progress of Theoretical Physics Supplement*, 140:111–133, 10 2000. ISSN 0375-9687. doi: 10.1143/PTPS.140.111. URL https://doi.org/10.1143/PTPS.140.111.

[24] M. D'Agostino, M. Bruno, F. Gulminelli, F. Cannata, Ph. Chomaz, G. Casini, E. Geraci, F. Gramegna, A. Moroni, and G. Vannini. Nuclear liquid-gas phase transition: Experimental signals. *Nuclear Physics A*, 749:55 – 64, 2005. ISSN 0375-9474. doi: https://doi.org/10.1016/j.nuclphysa.2004.12.008. URL http://www.sciencedirect.com/science/article/pii/S0375947404012126. Phase transitions in strongly interacting matter. Proceedings of the 18th Nuclear Physics Division Conference of the EPS.

[25] B. Borderie and M.F. Rivet. Nuclear multifragmentation and phase transition for hot nuclei. *Progress in Particle and Nuclear Physics*, 61(2):551 – 601, 2008. ISSN 0146-6410. doi: https://doi.org/10.1016/j.ppnp.2008.01.003. URL http://www.sciencedirect.com/science/article/pii/S0146641008000045.

[26] Zhi-Yong He, L. Gingras, Y. Larochelle, D. Ouerdane, L. Beaulieu, P. Gagné, Xing Qian, R. Roy, C. St-Pierre, G. C. Ball, and D. Horn. Fragment emission time from well defined sources in ^{58}Ni+^{197}Au at 34.5 mev/nucleon. *Phys. Rev. C*, 63:011601, Dec 2000. doi: 10.1103/PhysRevC.63.011601. URL https://link.aps.org/doi/10.1103/PhysRevC.63.011601.

[27] M. Louvel, A. Genoux-Lubain, G. Bizard, R. Bougault, R. Brou, A. Buta, H. Doubre, D. Durand, Y. El Masri, H. Fugiwara, K. Hagel, T. Hamdani, F. Hanappe, S.C. Jeong, G.M. Jin, S. Kato, J.L. Laville, C. Le Brun, J.F. Lecolley, S.M. Lee, T. Matsuse, T. Motobayashi, A. Péghaire, J. Péter, R. Regimbart, F. Saint-Laurent, J.C. Steckmeyer, and B. Tamain. Rapid decrease of fragment emission time in the range of 3–5 mev/u excitation energy. *Physics Letters B*, 320(3):221 – 226, 1994. ISSN 0370-2693. doi: https://doi.org/10.1016/0370-2693(94)90648-3. URL http://www.sciencedirect.com/science/article/pii/0370269394906483.

[28] Y. Larochelle, L. Beaulieu, G. Anctil, B. Djerroud, D. Doré, R. Laforest, J. Pouliot, R. Roy, M. Samri, C. St-Pierre, G. C. Ball, D. R. Bowman, A. Galindo-Uribarri, E. Hagberg, D. Horn, D. Guinet, and P. Lautesse. Dependence of intermediate mass fragment production on the reaction mechanism in light heavy-ion collisions at intermediate energy. *Phys. Rev. C*, 53:823–837, Feb 1996. doi: 10.1103/PhysRevC.53.823. URL https://link.aps.org/doi/10.1103/PhysRevC.53.823.

[29] M. Samri, F. Grenier, G. C. Ball, L. Beaulieu, L. Gingras, D. Horn, Y. Larochelle, R. Moustabchir, R. Roy, C. St-Pierre, and D. Theriault. Fusion and reaction mechanism evolution in ^{24}Mg+^{12}C at intermediate energies. *Phys. Rev. C*, 65:061603, Jun 2002. doi: 10.1103/PhysRevC.65.061603. URL https://link.aps.org/doi/10.1103/PhysRevC.65.061603.

[30] J. B. Natowitz, R. Wada, K. Hagel, T. Keutgen, M. Murray, A. Makeev, L. Qin, P. Smith, and C. Hamilton. Caloric curves and critical behavior in nuclei. *Phys. Rev. C*, 65:034618, Mar 2002. doi: 10.1103/PhysRevC.65.034618. URL https://link.aps.org/doi/10.1103/PhysRevC.65.034618.

[31] L. Morelli, M. Bruno, M. D'Agostino, G. Baiocco, F. Gulminelli, S. Barlini, A. Buccola, A. Camaiani, G. Casini, C. Ciampi, C. Frosin, N. Gelli, A. Olmi, P. Ottanelli, G. Pasquali, S. Piantelli, S. Valdré, M. Cicerchia, M. Cinausero, F. Gramegna, G. Mantovani, T. Marchi, M. Degerlier, D. Fabris, and V. L. Kravchuk. Full disassembly of excited ^{24}Mg into six α particles. *Phys. Rev. C*, 99:054610, May 2019. doi: 10.1103/PhysRevC.99.054610. URL https://link.aps.org/doi/10.1103/PhysRevC.99.054610.

[32] M Bruno et al. Four α-particle decay of the excited ^{16}O*quasi-projectile in the ^{16}O + ^{12}C reaction at 130MeV. *Journal of Physics G: Nuclear and Particle Physics*, 2019. URL http://iopscience.iop.org/10.1088/1361-6471/ab46cd.

[33] M. Bruno et al. Garfield + RCo digital upgrade: A modern set-up for mass and charge identification of heavy-ion reaction products. *The European Physical Journal A*, 49(10):128, Oct 2013. ISSN 1434-601X. doi: 10.1140/epja/i2013-13128-2. URL https://doi.org/10.1140/epja/i2013-13128-2.

[34] F. Grenier, A. Chbihi, R. Roy, G. Verde, D. Thériault, J.D. Frankland, J.P. Wieleczko, B. Borderie, R. Bougault, R. Dayras, E. Galichet, D. Guinet, P. Lautesse, N. Le Neindre, O. Lopez, J. Moisan, L. Nalpas, P. Napolitani, M. Pârlog, M.F. Rivet, E. Rosato, B. Tamain, E. Vient, and M. Vigilante. Multi-particle correlation function to study short-lived nuclei. *Nuclear Physics A*, 811(3):233 – 243, 2008. ISSN 0375-9474. doi: https://doi.org/10.1016/j.nuclphysa.2008.07.018. URL http://www.sciencedirect.com/science/article/pii/S0375947408006416.

[35] J. Pochodzalla, C. K. Gelbke, W. G. Lynch, M. Maier, D. Ardouin, H. Delagrange, H. Doubre, C. Grégoire, A. Kyanowski, W. Mittig, A. Péghaire, J. Péter, F. Saint-Laurent, B. Zwieglinski, G. Bizard, F. Lefèbvres, B. Tamain, J. Québert, Y. P. Viyogi, W. A. Friedman, and D. H. Boal. Two-particle correlations at small relative momenta for ^{40}induced reactions on ^{197}Au at e/a=60 mev. *Phys. Rev. C*, 35:1695–1719, May 1987. doi: 10.1103/PhysRevC.35.1695. URL https://link.aps.org/doi/10.1103/PhysRevC.35.1695.

[36] L. V. Grigorenko, T. D. Wiser, K. Mercurio, R. J. Charity, R. Shane, L. G. Sobotka, J. M. Elson, A. H. Wuosmaa, A. Banu, M. McCleskey, L. Trache, R. E. Tribble, and M. V. Zhukov. Three-body decay of ^{6}Be. *Phys. Rev. C*, 80:034602, Sep 2009. doi: 10.1103/PhysRevC.80.034602. URL https://link.aps.org/doi/10.1103/PhysRevC.80.034602.

[37] W. P. Tan, W. G. Lynch, T. X. Liu, X. D. Liu, M. B. Tsang, G. Verde, A. Wagner, H. S. Xu, B. Davin, R. T. de Souza, Y. Larochelle, R. Yanez, R. J. Charity, and L. G. Sobotka. Spin determination of particle unstable levels with particle correlations. *Phys. Rev. C*, 69:061304, Jun 2004. doi: 10.1103/PhysRevC.69.061304. URL https://link.aps.org/doi/10.1103/PhysRevC.69.061304.

[38] M. Freer, N. M. Clarke, N. Curtis, B. R. Fulton, S. J. Hall, M. J. Leddy, J. S. Pople, G. Tungate, R. P. Ward, P. M. Simmons, W. D. M. Rae, S. P. G. Chappell, S. P. Fox, C. D. Jones, D. L. Watson, G. J. Gyapong, S. M. Singer, W. N. Catford, and P. H. Regan. ^{8}Be and α decay of ^{16}O. *Phys. Rev. C*, 51:1682–1692, Apr 1995. doi: 10.1103/PhysRevC.51.1682. URL https://link.aps.org/doi/10.1103/PhysRevC.51.1682.

[39] R. Ghetti G. Verde, A. Chbihi and J. Helgesson. Correlations and characterization of emitting sources. *Eur. Phys. J. A*, 30:81–108, Oct 2006. doi: 10.1140/epja/i2006-10109-6. URL https://link.springer.com/article/10.1140/epja/i2006-10109-6.

[40] D. Ardouin. A Review on recent light particle correlation data from heavy ion collisions at intermediate-energies and low-energies. *Int. J. Mod. Phys. E*, 6:391–436, 1997. doi: 10.1142/S021830139700024X.

[41] W. Bauer. Particle-particle correlations and the space-time structure of heavy ion collisions. *Progress in Particle and Nuclear Physics*, 30:45 – 64, 1993. ISSN 0146-6410. doi: https://doi.org/10.1016/0146-6410(93)90005-Z. URL http://www.sciencedirect.com/science/article/pii/014664109390005Z.

[42] P. A. DeYoung, M. S. Gordon, Xiu qin Lu, R. L. McGrath, J. M. Alexander, D. M. de Castro Rizzo, and L. C. Vaz. Emission times in low-energy heavy-ion reactions by particle-particle correlations. *Phys. Rev. C*, 39:128–131, Jan 1989. doi: 10.1103/PhysRevC.39.128. URL https://link.aps.org/doi/10.1103/PhysRevC.39.128.

[43] F. Zhu et al. Thermalization in nucleus nucleus collisions. *Phys. Lett. B*, 282:299–304, 1992. doi: 10.1016/0370-2693(92)90642-H.

[44] R.HANBURY BROWN and R.Q.TWISS. Correlation between photons in two coherent beams of light. *Nature*, 177:27–29, Jan 1956. doi: 10.1038/177027a0. URL https://doi.org/10.1038/177027a0.

[45] R.HANBURY BROWN and R.Q.TWISS. A test of a new type of stellar interferometer on sirius. *Nature*, 178:1046–1048, Nov 1956. doi: 10.1038/1781046a0. URL https://doi.org/10.1038/1781046a0.

[46] Gerson Goldhaber, Sulamith Goldhaber, Wonyong Lee, and Abraham Pais. Influence of bose-einstein statistics on the antiproton-proton annihilation process. *Phys. Rev.*, 120:300–312, Oct 1960. doi: 10.1103/PhysRev.120.300. URL https://link.aps.org/doi/10.1103/PhysRev.120.300.

[47] Steven E. Koonin. Proton pictures of high-energy nuclear collisions. *Physics Letters B*, 70(1):43 – 47, 1977. ISSN 0370-2693. doi: https://doi.org/10.1016/0370-2693(77)90340-9. URL http://www.sciencedirect.com/science/article/pii/0370269377903409.

[48] G. Verde, P. Danielewicz, W.G. Lynch, C.F. Chan, C.K. Gelbke, L.K. Kwong, T.X. Liu, X.D. Liu, D. Seymour, R. Shomin, W.P. Tan, M.B. Tsang, A. Wagner, H.S. Xu, D.A. Brown, B. Davin, Y. Larochelle, R.T. de Souza, R. Yanez, R.J. Charity, and L.G. Sobotka. d–α correlation functions and collective motion in xe+au collisions at e/a=50 mev. *Physics Letters B*, 653(1):12 – 17, 2007. ISSN 0370-2693. doi: https://doi.org/10.1016/j.physletb.2007.07.031. URL http://www.sciencedirect.com/science/article/pii/S0370269307008532.

[49] O. Schapiro and D.H.E. Gross. Imf-imf correlations 3–4-fragment correlations reveal details of the breaking process. *Nuclear Physics A*, 576(3):428 – 440, 1994. ISSN 0375-9474. doi: https://doi.org/10.1016/0375-9474(94)90252-6. URL http://www.sciencedirect.com/science/article/pii/0375947494902526.

[50] O. Schapiro, A.R. DeAngelis, and D.H.E. Gross. Imf-imf correlations. *Nuclear Physics A*, 568(2):333 – 349, 1994. ISSN 0375-9474. doi: https://doi.org/10.1016/0375-9474(94)90206-2. URL http://www.sciencedirect.com/science/article/pii/0375947494902062.

[51] Scott Pratt and M. B. Tsang. Viewing the liquid-gas phase transition by measuring proton correlations. *Phys. Rev. C*, 36:2390–2395, Dec 1987. doi: 10.1103/PhysRevC.36.2390. URL https://link.aps.org/doi/10.1103/PhysRevC.36.2390.

[52] D. Drijard, H.G. Fischer, and T. Nakada. Study of event mixing and its application to the extraction of resonance signals. *Nuclear Instruments and Methods in Physics Research*, 225(2):367 – 377, 1984. ISSN 0167-5087. doi: https://doi.org/10.1016/0167-5087(84)90275-8. URL http://www.sciencedirect.com/science/article/pii/0167508784902758.

[53] R. Trockel, U. Lynen, J. Pochodzalla, W. Trautmann, N. Brummund, E. Eckert, R. Glasow, K. D. Hildenbrand, K. H. Kampert, W. F. J. Müller, D. Pelte, H. J. Rabe, H. Sann, R. Santo, H. Stelzer, and R. Wada. Correlated fragment production in ^{18}O-induced reactions at $\frac{E}{A} = 84$ mev. *Phys. Rev. Lett.*, 59:2844–2847, Dec 1987. doi: 10.1103/PhysRevLett.59.2844. URL https://link.aps.org/doi/10.1103/PhysRevLett.59.2844.

[54] W. G. Gong, W. Bauer, C. K. Gelbke, N. Carlin, R. T. de Souza, Y. D. Kim, W. G. Lynch, T. Murakami, G. Poggi, D. P. Sanderson, M. B. Tsang, H. M. Xu, S. Pratt,

D. E. Fields, K. Kwiatkowski, R. Płaneta, V. E. Viola, and S. J. Yennello. Intensity-interferometric test of nuclear collision geometries obtained from the boltzmann-uehling-uhlenbeck equation. *Phys. Rev. Lett.*, 65:2114–2117, Oct 1990. doi: 10.1103/PhysRevLett.65.2114. URL https://link.aps.org/doi/10.1103/PhysRevLett.65.2114.

[55] Tan Wanpeng. *Probing the freezeout mechanisms and isospin effect in multifragmentation*. PhD thesis, Michigan State University, 2002. URL https://groups.nscl.msu.edu/nscl_library/Thesis/Tan,%20Wanpeng.pdf.

[56] Luca Morelli. *Competition between evaporation and fragmentation in nuclear reactions at 15-20 AMeV beam energ*. PhD thesis, Universita' di Bologna, 2011. URL http://amsdottorato.unibo.it/3537/.

[57] T. K. Nayak, T. Murakami, W. G. Lynch, K. Swartz, D. J. Fields, C. K. Gelbke, Y. D. Kim, J. Pochodzalla, M. B. Tsang, H. M. Xu, F. Zhu, and K. Kwiatkowski. Emission temperatures from the decay of particle unstable complex nuclei. *Phys. Rev. C*, 45:132–161, Jan 1992. doi: 10.1103/PhysRevC.45.132. URL https://link.aps.org/doi/10.1103/PhysRevC.45.132.

[58] M. D'Agostino, M. Bruno, F. Gulminelli, L. Morelli, G. Baiocco, L. Bardelli, S. Barlini, F. Cannata, G. Casini, E. Geraci, F. Gramegna, V.L. Kravchuk, T. Marchi, A. Moroni, A. Ordine, and Ad.R. Raduta. Towards an understanding of staggering effects in dissipative binary collisions. *Nuclear Physics A*, 875:139 – 159, 2012. ISSN 0375-9474. doi: https://doi.org/10.1016/j.nuclphysa.2011.11.011. URL http://www.sciencedirect.com/science/article/pii/S0375947411006671.

[59] Schröder Wolf-Udo. *Nuclear Particle Correlations and Cluster Physics*. WORLD SCIENTIFIC, 2017. doi: 10.1142/10429. URL https://www.worldscientific.com/doi/abs/10.1142/10429.

[60] J. Pouthas et al. Indra, a 4π charged product detection array at ganil. *Nuclear Instruments and Methods in Physics Research Section A: Accelerators, Spectrometers, Detectors and Associated Equipment*, 357(2):418 – 442, 1995. ISSN 0168-9002. doi: https://doi.org/10.1016/0168-9002(94)01543-0. URL http://www.sciencedirect.com/science/article/pii/0168900294015430.

[61] R. Bougault et al. The FAZIA project in Europe: R&D phase. *The European Physical Journal A*, 50(2):47, Feb 2014. ISSN 1434-601X. doi: 10.1140/epja/i2014-14047-4. URL https://doi.org/10.1140/epja/i2014-14047-4.

[62] W. von Ammon. Neutron transmutation doped silicon — technological and economic aspects. *Nuclear Instruments and Methods in Physics Research Section B: Beam Interactions with Materials and Atoms*, 63(1):95 – 100, 1992. ISSN 0168-583X. doi: https://doi.org/10.1016/0168-583X(92)95176-R. URL http://www.sciencedirect.com/science/article/pii/0168583X9295176R. Proceedings of the E-MRS 1991 Spring Meeting, Symposium F on Nuclear Methods in Semiconductor Physics Strasbourg, France, May 28-30, 1991.

[63] L. Bardelli et al. Influence of crystal-orientation effects on pulse-shape-based identification of heavy-ions stopped in silicon detectors. *Nuclear Instruments*

and Methods in Physics Research Section A: Accelerators, Spectrometers, Detectors and Associated Equipment, 605(3):353 – 358, 2009. ISSN 0168-9002. doi: https://doi.org/10.1016/j.nima.2009.03.247. URL http://www.sciencedirect.com/science/article/pii/S0168900209007451.

[64] C.A.J. Ammerlaan, R.F. Rumphorst, and L.A.Ch. Koerts. Particle identification by pulse shape discrimination in the p-i-n type semiconductor detector. *Nuclear Instruments and Methods*, 22:189 – 200, 1963. ISSN 0029-554X. doi: https://doi.org/10.1016/0029-554X(63)90248-9. URL http://www.sciencedirect.com/science/article/pii/0029554X63902489.

[65] S. Barlini et al. New digital techniques applied to a and z identification using pulse shape discrimination of silicon detector current signals. *Nuclear Instruments and Methods in Physics Research Section A: Accelerators, Spectrometers, Detectors and Associated Equipment*, 600(3):644 – 650, 2009. ISSN 0168-9002. doi: https://doi.org/10.1016/j.nima.2008.12.200. URL http://www.sciencedirect.com/science/article/pii/S0168900209000023.

[66] L. Bardelli et al. Progresses in the pulse shape identification with silicon detectors within the fazia collaboration. *Nuclear Instruments and Methods in Physics Research Section A: Accelerators, Spectrometers, Detectors and Associated Equipment*, 654(1): 272 – 278, 2011. ISSN 0168-9002. doi: https://doi.org/10.1016/j.nima.2011.06.063. URL http://www.sciencedirect.com/science/article/pii/S0168900211011879.

[67] M. Mutterer, W. H. Trzaska, G. P. Tyurin, A. V. Evsenin, J. von Kalben, J. Kemmer, M. Kapusta, V. G. Lyapin, and S. V. Khlebnikov. Breakthrough in pulse-shape based particle identification with silicon detectors. In *1999 IEEE Nuclear Science Symposium. Conference Record. 1999 Nuclear Science Symposium and Medical Imaging Conference (Cat. No.99CH37019)*, volume 1, pages 148–151 vol.1, Oct 1999. doi: 10.1109/NSSMIC.1999.842465.

[68] S. Valdré et al. Time of flight identification with FAZIA. *Nuovo Cimento C*, 41(5): 167, Sep 2019. doi: 10.1393/ncc/i2018-18167-7. URL https://ui.adsabs.harvard.edu/abs/2019NCimC..41..167V.

[69] Giuseppe Pastore. *Study of the reaction $^{80}Kr+^{48,40}Ca$ at 35 MeV/u with the FAZIA detector array*. PhD thesis, Universita' Di Firenze, 2018. URL http://www.infn.it/thesis/thesis_dettaglio.php?tid=11924.

[70] Alberto Camaiani. *Complete isotopic characterization of projectile fragments in Ca+Ca reactions at Ferni energies with the FAZIA array*. PhD thesis, Universita' Di Firenze, 2020. URL http://www.infn.it/thesis/thesis_dettaglio.php?tid=11924.

[71] Pietro Otanelli. *Study of the $^{40,48}Ca+^{12}C$ at 25,40 MeV/u reaction*. PhD thesis, Universita' Di Firenze, 2020.

[72] S. Valdré et al. The FAZIA setup: A review on the electronics and the mechanical mounting. *Nuclear Instruments and Methods in Physics Research Section A: Accelerators, Spectrometers, Detectors and Associated Equipment*, 930:27 – 36, 2019. ISSN 0168-9002. doi: https://doi.org/10.1016/j.nima.2019.03.082. URL http://www.sciencedirect.com/science/article/pii/S0168900219304243.

[73] James M. Lattimer and Madappa Prakash. The equation of state of hot, dense matter and neutron stars. *Physics Reports*, 621:127 – 164, 2016. ISSN 0370-1573. doi: https://doi.org/10.1016/j.physrep.2015.12.005. URL http://www.sciencedirect.com/science/article/pii/S0370157315005396. Memorial Volume in Honor of Gerald E. Brown.

[74] S. Piantelli et al. Isospin transport phenomena in semiperipheral heavy ion collisions at Fermi energies. *Nuovo Cimento C*, C42(2-3-3):104, 2019. doi: 10.1393/ncc/i2019-19104-0.

[75] A. Camaiani et al. Isotopic composition of quasi-projectile fission fragments for the systems ^{40,48}Ca + ^{40,48}Ca at 35 AMeV. *Nuovo Cimento C*, 41(5):172, Sep 2019. doi: 10.1393/ncc/i2018-18172-x. URL https://ui.adsabs.harvard.edu/abs/2019NCimC..41..172C.

[76] L. Bardelli, G. Poggi, G. Pasquali, and M. Bini. A method for non-destructive resistivity mapping in silicon detectors. *Nuclear Instruments and Methods in Physics Research Section A: Accelerators, Spectrometers, Detectors and Associated Equipment*, 602(2):501 – 505, 2009. ISSN 0168-9002. doi: https://doi.org/10.1016/j.nima.2009.01.033. URL http://www.sciencedirect.com/science/article/pii/S0168900209000631.

[77] N. Le Neindre et al. Comparison of charged particle identification using pulse shape discrimination and $\Delta E - E$ methods between front and rear side injection in silicon detectors. *Nuclear Instruments and Methods in Physics Research Section A: Accelerators, Spectrometers, Detectors and Associated Equipment*, 701:145 – 152, 2013. ISSN 0168-9002. doi: https://doi.org/10.1016/j.nima.2012.11.005. URL http://www.sciencedirect.com/science/article/pii/S0168900212012764.

[78] M F Rivet, E Bonnet, B Borderie, R Bougault, P Edelbruck, N Le Neindre, S Barlini, S Carboni, G Casini, E Rosato, and G Tortone and. Status and performances of the FAZIA project. *Journal of Physics: Conference Series*, 420:012160, mar 2013. doi: 10.1088/1742-6596/420/1/012160. URL https://doi.org/10.1088%2F1742-6596%2F420%2F1%2F012160.

[79] D. Bédérède, E. Bougamont, Ph. Bourgeois, F.X. Gentit, Y. Piret, and G. Tauzin. Performances of the csi(tl) detector element of the glast calorimeter. *Nuclear Instruments and Methods in Physics Research Section A: Accelerators, Spectrometers, Detectors and Associated Equipment*, 518(1):15 – 18, 2004. ISSN 0168-9002. doi: https://doi.org/10.1016/j.nima.2003.10.011. URL http://www.sciencedirect.com/science/article/pii/S0168900203026937. Frontier Detectors for Frontier Physics: Proceedin.

[80] F. Salomon et al. Front-end electronics for the FAZIA experiment. *Journal of Instrumentation*, 11(01):C01064–C01064, jan 2016. doi: 10.1088/1748-0221/11/01/c01064. URL https://doi.org/10.1088%2F1748-0221%2F11%2F01%2Fc01064.

[81] H. Hamrita et al. Charge and current-sensitive preamplifiers for pulse shape discrimination techniques with silicon detectors. *Nuclear Instruments and Methods in Physics Research Section A: Accelerators, Spectrometers, Detectors and Associated Equipment*, 531(3):607 – 615, 2004. ISSN 0168-9002. doi: https://doi.org/10.1016/j.nima.2004.05.112. URL http://www.sciencedirect.com/science/article/pii/S0168900204011106.

[82] G. Pasquali, R. Ciaranfi, L. Bardelli, M. Bini, A. Boiano, F. Giannelli, A. Ordine, and G. Poggi. A dsp equipped digitizer for online analysis of nuclear detector signals. *Nuclear Instruments and Methods in Physics Research Section A: Accelerators, Spectrometers, Detectors and Associated Equipment*, 570(1):126 – 132, 2007. ISSN 0168-9002. doi: https://doi.org/10.1016/j.nima.2006.10.008. URL http://www.sciencedirect.com/science/article/pii/S0168900206017669.

[83] A. Pagano et al. Fragmentation studies with the chimera detector at lns in catania: recent progress. *Nuclear Physics A*, 734:504 – 511, 2004. ISSN 0375-9474. doi: https://doi.org/10.1016/j.nuclphysa.2004.01.093. URL http://www.sciencedirect.com/science/article/pii/S0375947404001137.

[84] I. Lombardo et al. Use of large surface microchannel plates for the tagging of intermediate energy exotic beams. *Nuclear Physics B - Proceedings Supplements*, 215(1):272 – 274, 2011. ISSN 0920-5632. doi: https://doi.org/10.1016/j.nuclphysbps.2011.04.028. URL http://www.sciencedirect.com/science/article/pii/S0920563211002672. Proceedings of the 12th Topical Seminar on Innovative Particle and Radiation Detectors (IPRD10).

[85] W. von Oertzen, V. Zherebchevsky, B. Gebauer, Ch. Schulz, S. Thummerer, D. Kamanin, G. Royer, and Th. Wilpert. Fission decay of $n = z$ nuclei at high angular momentum: ^{60}Zn. *Phys. Rev. C*, 78:044615, Oct 2008. doi: 10.1103/PhysRevC.78.044615. URL https://link.aps.org/doi/10.1103/PhysRevC.78.044615.

[86] M. Bini, G. Casini, A. Olmi, G. Poggi, A.A. Stefanini, L. Bardelli, A. Bartoli, L. Bidini, C. Coppi, P. Del Carmine, A. Mangiarotti, P.R. Maurenzig, G. Pasquali, S. Piantelli, S. Poggi, N. Taccetti, and E. Vanzi. Fiasco: a multidetector optimized for semiperipheral heavy ion collisions at fermi energies. *Nuclear Instruments and Methods in Physics Research Section A: Accelerators, Spectrometers, Detectors and Associated Equipment*, 515(3):497 – 523, 2003. ISSN 0168-9002. doi: https://doi.org/10.1016/j.nima.2003.07.064. URL http://www.sciencedirect.com/science/article/pii/S0168900203023088.

[87] Glenn F. Knoll. *Radiation Detection and Measurement, 4th Edition*. John Wiley & Sons, New York, September 2010.

[88] G. Pausch, W. Bohne, D. Hilscher, H.-G. Ortlepp, and D. Polster. Particle identification in a wide dynamic range based on pulse-shape analysis with solid-state detectors. *Nuclear Instruments and Methods in Physics Research Section A: Accelerators, Spectrometers, Detectors and Associated Equipment*, 349(1):281 – 284, 1994. ISSN 0168-9002. doi: https://doi.org/10.1016/0168-9002(94)90634-3. URL http://www.sciencedirect.com/science/article/pii/0168900294906343.

[89] J.B.A. England, G.M. Field, and T.R. Ophel. Z-identification of charged particles by signal risetime in silicon surface barrier detectors. *Nuclear Instruments and Methods in Physics Research Section A: Accelerators, Spectrometers, Detectors and Associated Equipment*, 280(2):291 – 298, 1989. ISSN 0168-9002. doi: https://doi.org/10.1016/0168-9002(89)90920-0. URL http://www.sciencedirect.com/science/article/pii/0168900289909200.

[90] P.A. Tove and W. Seibt. Plasma effects in semiconductor detectors. *Nuclear Instruments and Methods*, 51(2):261 – 269, 1967. ISSN 0029-554X. doi: https://doi.org/10.1016/0029-554X(67)90012-2. URL http://www.sciencedirect.com/science/article/pii/0029554X67900122.

[91] W. Bohne, W. Galster, K. Grabisch, and H. Morgenstern. The influence of plasma effects on the timing properties of surface-barrier detectors for heavy ions. *Nuclear Instruments and Methods in Physics Research Section A: Accelerators, Spectrometers, Detectors and Associated Equipment*, 240(1):145 – 151, 1985. ISSN 0168-9002. doi: https://doi.org/10.1016/0168-9002(85)90398-5. URL http://www.sciencedirect.com/science/article/pii/0168900285903985.

[92] Gruyer Diego. *Aspects dynamiques de la desexcitation nucleaire : de la fission a la multifragmentation*. PhD thesis, Universitè de Caen Normandie, 2014. URL http://www.theses.fr/2014CAEN2057.

[93] G. Pastore et al. Isotopic identification using pulse shape analysis of current signals from silicon detectors: Recent results from the fazia collaboration. *Nuclear Instruments and Methods in Physics Research Section A: Accelerators, Spectrometers, Detectors and Associated Equipment*, 860:42 – 50, 2017. ISSN 0168-9002. doi: https://doi.org/10.1016/j.nima.2017.01.048. URL http://www.sciencedirect.com/science/article/pii/S0168900217301092.

[94] F. Benrachi, B. Chambon, B. Cheynis, D. Drain, C. Pastor, D. Seghier, K. Zaid, A. Giorni, D. Heuer, A. Llères, C. Morand, P. Stassi, and J.B. Viano. Investigation of the performance of csi(tl) for charged particle identification by pulse-shape analysis. *Nuclear Instruments and Methods in Physics Research Section A: Accelerators, Spectrometers, Detectors and Associated Equipment*, 281(1):137 – 142, 1989. ISSN 0168-9002. doi: https://doi.org/10.1016/0168-9002(89)91225-4. URL http://www.sciencedirect.com/science/article/pii/0168900289912254.

[95] William R. Leo. *Techniques for Nuclear and Particle Physics Experiments, 2nd Edition*. Springer-Verlag Berlin Heidelberg GmbH, 1994.

[96] IN2P3 Computing Center. URL https://cc.in2p3.fr/en/qui-sommes-nous/le-cc-in2p3/.

[97] KaliVeda. URL http://indra.in2p3.fr/kaliveda/.

[98] ROOT. URL https://root.cern.ch/.

[99] GitHub. URL https://github.com/kaliveda-dev/kaliveda-dev.github.io.

[100] VedaLoss. URL http://indra.in2p3.fr/kaliveda/KVedaLossDoc/KVedaLoss.html.

[101] L.C. Northcliffe and R.F. Schilling. Range and stopping-power tables for heavy ions. *Atomic Data and Nuclear Data Tables*, 7(3):233 – 463, 1970. ISSN 0092-640X. doi: https://doi.org/10.1016/S0092-640X(70)80016-X. URL http://www.sciencedirect.com/science/article/pii/S0092640X7080016X.

[102] F. Hubert, R. Bimbot, and H. Gauvin. Range and stopping-power tables for 2.5–500 MeV/nucleon heavy ions in solids. *Atom. Data Nucl. Data Tabl.*, 46:1–213, 1990. doi: 10.1016/0092-640X(90)90001-Z.

[103] M. Pârlog et al. Response of CsI(Tl) scintillators over a large range in energy and atomic number of ions. Part i: recombination and δ-electrons. *Nuclear Instruments and Methods in Physics Research Section A: Accelerators, Spectrometers, Detectors and Associated Equipment*, 482(3):674 – 692, 2002. ISSN 0168-9002. doi: https://doi.org/10.1016/S0168-9002(01)01710-7. URL http://www.sciencedirect.com/science/article/pii/S0168900201017107.

[104] M. Pârlog et al. Response of CsI(Tl) scintillators over a large range in energy and atomic number of ions. Part ii: calibration and identification in the INDRA array. *Nuclear Instruments and Methods in Physics Research Section A: Accelerators, Spectrometers, Detectors and Associated Equipment*, 482(3):693 – 706, 2002. ISSN 0168-9002. doi: https://doi.org/10.1016/S0168-9002(01)01712-0. URL http://www.sciencedirect.com/science/article/pii/S0168900201017120.

[105] L Morelli, M Bruno, M D'Agostino, G Baiocco, F Gulminelli, U Abbondanno, S Barlini, M Bini, G Casini, M Cinausero, M Degerlier, D Fabris, F Gramegna, J Mabiala, T Marchi, A Olmi, G Pasquali, S Piantelli, and S Valdré. The $12C^{*}hoylestateintheinelastic12C+12Creactionandin24Mg^{*}$ decay. *Journal of Physics G: Nuclear and Particle Physics*, 43(4):045110, feb 2016. doi: 10.1088/0954-3899/43/4/045110. URL https://doi.org/10.10882F0954-38992F432F42F045110.

[106] NUDAT2. URL https://www.nndc.bnl.gov/nudat2/getdatasetClassic.jsp?nucleus=6LI&unc=nds.

[107] S. Carboni et al. Particle identification using the $\Delta E - E$ technique and pulse shape discrimination with the silicon detectors of the fazia project. *Nuclear Instruments and Methods in Physics Research Section A: Accelerators, Spectrometers, Detectors and Associated Equipment*, 664(1):251 – 263, 2012. ISSN 0168-9002. doi: https://doi.org/10.1016/j.nima.2011.10.061. URL http://www.sciencedirect.com/science/article/pii/S0168900211020134.

[108] M.S. Wallace et al. The high resolution array (hira) for rare isotope beam experiments. *Nuclear Instruments and Methods in Physics Research Section A: Accelerators, Spectrometers, Detectors and Associated Equipment*, 583(2):302 – 312, 2007. ISSN 0168-9002. doi: https://doi.org/10.1016/j.nima.2007.08.248. URL http://www.sciencedirect.com/science/article/pii/S016890020701947X.

[109] C. Frosin, S. Barlini, G. Poggi, et al. Energy response and identification efficiency of csi(tl) crystals irradiated with energetic protons. *Nuclear Instruments and Methods in Physics Research Section A: Accelerators, Spectrometers, Detectors and Associated Equipment*, 951:163018, 2020. ISSN 0168-9002. doi: https://doi.org/10.1016/j.nima.2019.163018. URL http://www.sciencedirect.com/science/article/pii/S016890021931383X.

[110] D. Dell'Aquila et al. Non-linearity effects on the light-output calibration of light charged particles in CsI(Tl) scintillator crystals. *Nuclear Instruments and Methods in Physics Research Section A: Accelerators, Spectrometers, Detectors and Associated Equipment*, 929:162 – 172, 2019. ISSN 0168-9002. doi: https://doi.org/10.1016/j.nima.2019.03.065. URL http://www.sciencedirect.com/science/article/pii/S0168900219303961.

[111] A.V. Gektin, B.V. Grinyov, D.I. Zosim, and A.Yu. Boyarintsev. Light output tuning for the long-length csi(tl) scintillators. *Nuclear Instruments and Methods in Physics Research Section A: Accelerators, Spectrometers, Detectors and Associated Equipment*, 598(1):270 – 272, 2009. ISSN 0168-9002. doi: https://doi.org/10.1016/j.nima.2008.08.123. URL http://www.sciencedirect.com/science/article/pii/S0168900208012436. Instrumentation for Collding Beam Physics.

[112] N. Grassi, G. Casini, M. Frosini, G. Tobia, and T. Marchi. Pixe characterization of csi(tl) scintillators used for particle detection in nuclear reactions. *Nuclear Instruments and Methods in Physics Research Section B: Beam Interactions with Materials and Atoms*, 266(10):2383 – 2386, 2008. ISSN 0168-583X. doi: https://doi.org/10.1016/j.nimb.2008.03.012. URL http://www.sciencedirect.com/science/article/pii/S0168583X08002735. Accelerators in Applied Research and Technology.

[113] M. M. Hamada, F. E. Costa, M. C. C. Pereira, and S. Kubota. Dependence of scintillation characteristics in the csi(tl) crystal on tl/sup +/ concentrations under electron and alpha particles excitations. *IEEE Transactions on Nuclear Science*, 48(4):1148–1153, Aug 2001. ISSN 0018-9499. doi: 10.1109/23.958740.

[114] L.N Trefilova, A.M Kudin, L.V Kovaleva, B.G Zaslavsky, D.I Zosim, and S.K Bondarenko. Concentration dependence of the light yield and energy resolution of nai:tl and csi:tl crystals excited by gamma, soft x-rays and alpha particles. *Nuclear Instruments and Methods in Physics Research Section A: Accelerators, Spectrometers, Detectors and Associated Equipment*, 486(1):474 – 481, 2002. ISSN 0168-9002. doi: https://doi.org/10.1016/S0168-9002(02)00756-8. URL http://www.sciencedirect.com/science/article/pii/S0168900202007568. Proceedings of the 6th International Conference on Inorganic Scin tillators and their Use in Scientific and Industrial Applications.

[115] Stefan Diehl et al. Measurement and optimization of the light collection uniformity in strongly tapered pwo crystals of the panda detector. *Nuclear Instruments and Methods in Physics Research Section A: Accelerators, Spectrometers, Detectors and Associated Equipment*, 857:1 – 6, 2017. ISSN 0168-9002. doi: https://doi.org/10.1016/j.nima.2017.03.021. URL http://www.sciencedirect.com/science/article/pii/S0168900217303583.

[116] A. Knyazev et al. Properties of the csi(tl) detector elements of the califa detector. *Nuclear Instruments and Methods in Physics Research Section A: Accelerators, Spectrometers, Detectors and Associated Equipment*, 940:393 – 404, 2019. ISSN 0168-9002. doi: https://doi.org/10.1016/j.nima.2019.06.045. URL http://www.sciencedirect.com/science/article/pii/S0168900219308903.

[117] W.G. Gong et al. Resolution tests of csi(tl) scintillators read out by pin diodes. *Nuclear Instruments and Methods in Physics Research Section A: Accelerators, Spectrometers, Detectors and Associated Equipment*, 268(1):190 – 199, 1988. ISSN 0168-9002. doi: https://doi.org/10.1016/0168-9002(88)90605-5. URL http://www.sciencedirect.com/science/article/pii/0168900288906055.

[118] J. Bea et al. Simulation of light collection in scintillators with rough surfaces. *Nuclear Instruments and Methods in Physics Research Section A: Accelerators, Spectrometers, Detectors and Associated Equipment*, 350(1):184 – 191, 1994. ISSN 0168-9002. doi: https://doi.org/10.1016/0168-9002(94)91162-2. URL http://www.sciencedirect.com/science/article/pii/0168900294911622.

[119] I.V. Kilimchuk, V.A. Tarasov, and I.D. Vlasova. Study of light collection as a function of scintillator surface roughness. *Radiation Measurements*, 45(3):383 – 385, 2010. ISSN 1350-4487. doi: https://doi.org/10.1016/j.radmeas.2010.01.027. URL http://www.sciencedirect.com/science/article/pii/S1350448710000284. Proceedings of the 7th European Conference on Luminescent Detectors and Transformers of Ionizing Radiation (LUMDETR 2009).

[120] E. Auffray et al. A comprehensive systematic study of coincidence time resolution and light yield using scintillators of different size, wrapping and doping. In *2011 IEEE Nuclear Science Symposium Conference Record*, pages 64–71, Oct 2011. doi: 10.1109/NSSMIC.2011.6154402.

[121] Ali Taheri and Reza Gholipour Peyvandi. The impact of wrapping method and reflector type on the performance of rod plastic scintillators. *Measurement*, 97:100 – 110, 2017. ISSN 0263-2241. doi: https://doi.org/10.1016/j.measurement.2016.10.051. URL http://www.sciencedirect.com/science/article/pii/S0263224116306121.

[122] S. Agostinelli et al. Geant4—a simulation toolkit. *Nuclear Instruments and Methods in Physics Research Section A: Accelerators, Spectrometers, Detectors and Associated Equipment*, 506(3):250 – 303, 2003. ISSN 0168-9002. doi: https://doi.org/10.1016/S0168-9002(03)01368-8. URL http://www.sciencedirect.com/science/article/pii/S0168900203013688.

[123] G. Poggi et al. Large volume detector telescopes for charged particles at the SIS/ESR accelerator. *Nuclear Instruments and Methods in Physics Research Section A: Accelerators, Spectrometers, Detectors and Associated Equipment*, 324(1):177 – 190, 1993. ISSN 0168-9002. doi: https://doi.org/10.1016/0168-9002(93)90975-N. URL http://www.sciencedirect.com/science/article/pii/016890029390975N.

[124] A. Siwek et al. Incomplete energy deposition in long CsI(Tl) crystals. *NUKLEONIKA*, 47(4):141 – 145, 2002. ISSN 0029-5922. doi: http://www.ichtj.waw.pl/nukleonikaa/?p=685. URL http://www.ichtj.waw.pl/nukleonikaa/?p=685.

[125] V Avdeichikov, A.S Fomichev, B Jakobsson, A.M Rodin, and G.M Ter-Akopian. Reaction losses of light charged particles in csi, bgo and gso scintillators. *Nuclear Instruments and Methods in Physics Research Section A: Accelerators, Spectrometers, Detectors and Associated Equipment*, 437(2):424 – 431, 1999. ISSN 0168-9002. doi: https://doi.org/10.1016/S0168-9002(99)00774-3. URL http://www.sciencedirect.com/science/article/pii/S0168900299007743.

[126] J. Allison et al. Recent developments in Geant4. *Nuclear Instruments and Methods in Physics Research Section A: Accelerators, Spectrometers, Detectors and Associated Equipment*, 835:186 – 225, 2016. ISSN 0168-9002. doi: https://doi.org/10.1016/j.nima.2016.06.125. URL http://www.sciencedirect.com/science/article/pii/S0168900216306957.

[127] R. J. Charity. Systematic description of evaporation spectra for light and heavy compound nuclei. *Phys. Rev. C*, 82:014610, Jul 2010. doi: 10.1103/PhysRevC.82.014610. URL https://link.aps.org/doi/10.1103/PhysRevC.82.014610.

[128] Giorgio Baiocco. *Towards a reconstruction of thermal properties of light nuclei from fusion-evaporation reactions*. PhD thesis, Università di Bologna and University of Caen - Lower Normandy, 2012. URL http://amsdottorato.unibo.it/4295/1/baiocco_giorgio_tesi.pdf.

[129] G. Baiocco et al. α-clustering effects in dissipative ^{12}C+^{12}C reactions at 95 Mev. *Phys. Rev. C*, 87:054614, May 2013. doi: 10.1103/PhysRevC.87.054614. URL https://link.aps.org/doi/10.1103/PhysRevC.87.054614.

[130] D. Durand. An event generator for the study of nuclear collisions in the fermi energy domain (i). formalism and first applications. *Nuclear Physics A*, 541(2):266 – 294, 1992. ISSN 0375-9474. doi: https://doi.org/10.1016/0375-9474(92)90097-4. URL http://www.sciencedirect.com/science/article/pii/0375947492900974.

[131] Walter Hauser and Herman Feshbach. The inelastic scattering of neutrons. *Phys. Rev.*, 87:366–373, Jul 1952. doi: 10.1103/PhysRev.87.366. URL https://link.aps.org/doi/10.1103/PhysRev.87.366.

[132] M. Colonna, M. Di Toro, A. Guarnera, S. Maccarone, M. Zielinska-Pfabé, and H.H. Wolter. Fluctuations and dynamical instabilities in heavy-ion reactions. *Nuclear Physics A*, 642(3):449 – 460, 1998. ISSN 0375-9474. doi: https://doi.org/10.1016/S0375-9474(98)00542-9. URL http://www.sciencedirect.com/science/article/pii/S0375947498005429.

[133] P. Napolitani and M. Colonna. Bifurcations in boltzmann–langevin one body dynamics for fermionic systems. *Physics Letters B*, 726(1):382 – 386, 2013. ISSN 0370-2693. doi: https://doi.org/10.1016/j.physletb.2013.08.005. URL http://www.sciencedirect.com/science/article/pii/S037026931300631X.

[134] H. Feldmeier. Fermionic molecular dynamics. *Nuclear Physics A*, 515(1):147 – 172, 1990. ISSN 0375-9474. doi: https://doi.org/10.1016/0375-9474(90)90328-J. URL http://www.sciencedirect.com/science/article/pii/037594749090328J.

[135] Denis Lacroix, Aymeric Van Lauwe, and Dominique Durand. Event generator for nuclear collisions at intermediate energies. *Phys. Rev. C*, 69:054604, May 2004. doi: 10.1103/PhysRevC.69.054604. URL https://link.aps.org/doi/10.1103/PhysRevC.69.054604.

[136] G. Tian, R. Wada, Z. Chen, R. Han, W. Lin, X. Liu, P. Ren, F. Shi, F. Luo, Q. Sun, L. Song, and G. Q. Xiao. Nuclear stopping and light charged particle emission in $^{12}\mathbf{C} + ^{12}\mathbf{C}$ at 95 mev/nucleon. *Phys. Rev. C*, 95:044613, Apr 2017. doi: 10.1103/PhysRevC.95.044613. URL https://link.aps.org/doi/10.1103/PhysRevC.95.044613.

[137] S. Piantelli, A. Olmi, P. R. Maurenzig, A. Ono, M. Bini, G. Casini, G. Pasquali, A. Mangiarotti, G. Poggi, A. A. Stefanini, S. Barlini, A. Camaiani, C. Ciampi, C. Frosin, P. Ottanelli, and S. Valdré. Comparison between calculations with the amd code and experimental data for peripheral collisions of ^{93}Nb + ^{93}Nb,^{116}Sn at 38

mev/nucleon. *Phys. Rev. C*, 99:064616, Jun 2019. doi: 10.1103/PhysRevC.99.064616. URL https://link.aps.org/doi/10.1103/PhysRevC.99.064616.

[138] Akira Ono, Hisashi Horiuchi, Toshiki Maruyama, and Akira Ohnishi. Antisymmetrized Version of Molecular Dynamics with Two-Nucleon Collisions and Its Application to Heavy Ion Reactions. *Progress of Theoretical Physics*, 87(5): 1185–1206, 05 1992. ISSN 0033-068X. doi: 10.1143/ptp/87.5.1185. URL https://doi.org/10.1143/ptp/87.5.1185.

[139] A. Ono, H. Horiuchi, T. Maruyama, and A. Ohnishi. Fragment formation studied with antisymmetrized version of molecular dynamics with two-nucleon collisions. *Phys. Rev. Lett.*, 68:2898–2900, May 1992. doi: 10.1103/PhysRevLett.68.2898. URL https://link.aps.org/doi/10.1103/PhysRevLett.68.2898.

[140] Akira Ono. Cluster correlations in multifragmentation. *Journal of Physics: Conference Series*, 420:012103, mar 2013. doi: 10.1088/1742-6596/420/1/012103. URL https://doi.org/10.10882F1742-65962F4202F12F012103.

[141] Akira Ono and Hisashi Horiuchi. Antisymmetrized molecular dynamics of wave packets with stochastic incorporation of the vlasov equation. *Phys. Rev. C*, 53:2958–2972, Jun 1996. doi: 10.1103/PhysRevC.53.2958. URL https://link.aps.org/doi/10.1103/PhysRevC.53.2958.

[142] Akira Ono. Antisymmetrized molecular dynamics with quantum branching processes for collisions of heavy nuclei. *Phys. Rev. C*, 59:853–864, Feb 1999. doi: 10.1103/PhysRevC.59.853. URL https://link.aps.org/doi/10.1103/PhysRevC.59.853.

[143] D. D. S. Coupland, W. G. Lynch, M. B. Tsang, P. Danielewicz, and Yingxun Zhang. Influence of transport variables on isospin transport ratios. *Phys. Rev. C*, 84:054603, Nov 2011. doi: 10.1103/PhysRevC.84.054603. URL https://link.aps.org/doi/10.1103/PhysRevC.84.054603.

[144] E. Chabanat, P. Bonche, P. Haensel, J. Meyer, and R. Schaeffer. A skyrme parametrization from subnuclear to neutron star densities. *Nuclear Physics A*, 627(4):710 – 746, 1997. ISSN 0375-9474. doi: https://doi.org/10.1016/S0375-9474(97)00596-4. URL http://www.sciencedirect.com/science/article/pii/S0375947497005964.

[145] O. Lopez, D. Durand, G. Lehaut, B. Borderie, J. D. Frankland, M. F. Rivet, R. Bougault, A. Chbihi, E. Galichet, D. Guinet, M. La Commara, N. Le Neindre, I. Lombardo, L. Manduci, P. Marini, P. Napolitani, M. Pârlog, E. Rosato, G. Spadaccini, E. Vient, and M. Vigilante. In-medium effects for nuclear matter in the fermi-energy domain. *Phys. Rev. C*, 90:064602, Dec 2014. doi: 10.1103/PhysRevC.90.064602. URL https://link.aps.org/doi/10.1103/PhysRevC.90.064602.

[146] G. Tian, Z. Chen, R. Han, F. Shi, F. Luo, Q. Sun, L. Song, X. Zhang, G. Q. Xiao, R. Wada, and A. Ono. Cluster correlation and fragment emission in $^{12}C + ^{12}C$ at 95 mev/nucleon. *Phys. Rev. C*, 97:034610, Mar 2018. doi: 10.1103/PhysRevC.97.034610. URL https://link.aps.org/doi/10.1103/PhysRevC.97.034610.

[147] L Morelli et al. The ^{12}C* hoyle state in the inelastic ^{12}C+^{12}C reaction and in ^{24}Mg* decay. *Journal of Physics G: Nuclear and Particle Physics*, 43(4):045110, feb 2016. doi: 10.1088/0954-3899/43/4/045110. URL https://doi.org/10.1088%2F0954-3899%2F43%2F4%2F045110.

[148] Z. Chen and C. K. Gelbke. Sequential feeding and temperature determinations from the relative populations of widely separated states in ^{4}He, ^{5}Li, and ^{8}Be nuclei. *Phys. Rev. C*, 38:2630–2639, Dec 1988. doi: 10.1103/PhysRevC.38.2630. URL https://link.aps.org/doi/10.1103/PhysRevC.38.2630.

[149] Till von Egidy and Dorel Bucurescu. Systematics of nuclear level density parameters. *Phys. Rev. C*, 72:044311, Oct 2005. doi: 10.1103/PhysRevC.72.044311. URL https://link.aps.org/doi/10.1103/PhysRevC.72.044311.

[150] Till von Egidy and Dorel Bucurescu. Erratum: Systematics of nuclear level density parameters [phys. rev. c 72, 044311 (2005)]. *Phys. Rev. C*, 73:049901, Apr 2006. doi: 10.1103/PhysRevC.73.049901. URL https://link.aps.org/doi/10.1103/PhysRevC.73.049901.

[151] J. Tōke and W.J. Świątecki. Surface-layer corrections to the level-density formula for a diffuse fermi gas. *Nuclear Physics A*, 372(1):141 – 150, 1981. ISSN 0375-9474. doi: https://doi.org/10.1016/0375-9474(81)90092-0. URL http://www.sciencedirect.com/science/article/pii/0375947481900920.

[152] The AME2012 Atomic Mass Evaluation. URL https://www.nndc.bnl.gov/masses/.

[153] W. Nörenberg. *Heavy-Ion Collisions Vol.2*. North-Holland, Amsterdam, 1980.

[154] D. Vautherin, J. Treiner, and M. Vénéroni. Evolution of hot compressed nuclei in the time-dependent hartree-fock approximation. *Physics Letters B*, 191(1):6 – 10, 1987. ISSN 0370-2693. doi: https://doi.org/10.1016/0370-2693(87)91311-6. URL http://www.sciencedirect.com/science/article/pii/0370269387913116.

[155] Michal Mocko. *Rare isotope production*. PhD thesis, Michigan State University, 2006. URL https://groups.nscl.msu.edu/nscl_library/Thesis/.

[156] A. Camaiani, S. Piantelli, A. Ono, G. Casini, B. Borderie, R. Bougault, C. Ciampi, J. A. Dueñas, C. Frosin, J. D. Frankland, D. Gruyer, N. LeNeindre, I. Lombardo, G. Mantovani, P. Ottanelli, M. Parlog, G. Pasquali, S. Upadhyaya, S. Valdré, G. Verde, and E. Vient. Influence of fast emissions and statistical de-excitation on the isospin transport ratio. *Phys. Rev. C*, 102:044607, Oct 2020. doi: 10.1103/PhysRevC.102.044607. URL https://link.aps.org/doi/10.1103/PhysRevC.102.044607.

[157] Catalin Frosin. The 16O+ 12C reaction at 90.5, 110 and 130 MeV beam energy . Master's thesis, Università di Bologna, 2017. URL https://amslaurea.unibo.it/13511/.

[158] R. Bass. Nucleus-nucleus potential deduced from experimental fusion cross sections. *Phys. Rev. Lett.*, 39:265–268, Aug 1977. doi: 10.1103/PhysRevLett.39.265. URL https://link.aps.org/doi/10.1103/PhysRevLett.39.265.

[159] A. Camaiani, G. Casini, S. Piantelli, A. Ono, E. Bonnet, R. Alba, S. Barlini, B. Borderie, R. Bougault, C. Ciampi, A. Chbihi, M. Cicerchia, M. Cinausero, J. A. Dueñas, D. Dell'Aquila, Q. Fable, D. Fabris, C. Frosin, J. D. Frankland, F. Gramegna, D. Gruyer, K. I. Hahn, M. Henri, B. Hong, S. Kim, A. Kordyasz, M. J. Kweon, H. J. Lee, J. Lemarié, N. LeNeindre, I. Lombardo, O. Lopez, T. Marchi, S. H. Nam, P. Ottanelli, M. Parlog, G. Pasquali, G. Poggi, J. Quicray, A. A. Stefanini, S. Upadhyaya, S. Valdré, and E. Vient. Isospin diffusion measurement from the direct detection of a quasiprojectile remnant. *Phys. Rev. C*, 103:014605, Jan 2021. doi: 10.1103/PhysRevC.103.014605. URL https://link.aps.org/doi/10.1103/PhysRevC.103.014605.

[160] V. E. Viola, K. Kwiatkowski, and M. Walker. Systematics of fission fragment total kinetic energy release. *Phys. Rev. C*, 31:1550–1552, Apr 1985. doi: 10.1103/PhysRevC.31.1550. URL https://link.aps.org/doi/10.1103/PhysRevC.31.1550.

[161] J. J. Kolata, R. A. Racca, P. A. DeYoung, E. Aguilera-Reyes, and M. A. Xapsos. Structure in the fusion yield for ^{32}s+^{12}c. *Phys. Rev. C*, 32:1080–1082, Sep 1985. doi: 10.1103/PhysRevC.32.1080. URL https://link.aps.org/doi/10.1103/PhysRevC.32.1080.

[162] S. Piantelli, G. Casini, A. Ono, G. Poggi, G. Pastore, S. Barlini, A. Boiano, E. Bonnet, B. Borderie, R. Bougault, M. Bruno, A. Buccola, A. Camaiani, A. Chbihi, M. Cicerchia, M. Cinausero, M. D'Agostino, M. Degerlier, J. A. Dueñas, Q. Fable, D. Fabris, J. D. Frankland, C. Frosin, F. Gramegna, D. Gruyer, M. Henri, A. Kordyasz, T. Kozik, N. Le Neindre, I. Lombardo, O. Lopez, G. Mantovani, T. Marchi, L. Morelli, A. Olmi, P. Ottanelli, M. Pârlog, G. Pasquali, A. A. Stefanini, G. Tortone, S. Upadhyaya, S. Valdré, G. Verde, E. Vient, M. Vigilante, R. Alba, and C. Maiolino. Dynamical fission of the quasiprojectile and isospin equilibration for the system ^{80}Kr + ^{48}Ca at 35 mev/nucleon. *Phys. Rev. C*, 101:034613, Mar 2020. doi: 10.1103/PhysRevC.101.034613. URL https://link.aps.org/doi/10.1103/PhysRevC.101.034613.

[163] E. De Filippo, A. Pagano, P. Russotto, F. Amorini, A. Anzalone, L. Auditore, V. Baran, I. Berceanu, B. Borderie, R. Bougault, M. Bruno, T. Cap, G. Cardella, S. Cavallaro, M. B. Chatterjee, A. Chbihi, M. Colonna, M. D'Agostino, R. Dayras, M. Di Toro, J. Frankland, E. Galichet, W. Gawlikowicz, E. Geraci, A. Grzeszczuk, P. Guazzoni, S. Kowalski, E. La Guidara, G. Lanzalone, G. Lanzanò, N. Le Neindre, I. Lombardo, C. Maiolino, M. Papa, E. Piasecki, S. Pirrone, R. Płaneta, G. Politi, A. Pop, F. Porto, M. F. Rivet, F. Rizzo, E. Rosato, K. Schmidt, K. Siwek-Wilczyńska, I. Skwira-Chalot, A. Trifirò, M. Trimarchi, G. Verde, M. Vigilante, J. P. Wieleczko, J. Wilczyński, L. Zetta, and W. Zipper. Correlations between emission timescale of fragments and isospin dynamics in ^{124}sn+^{64}ni and ^{112}sn+^{58}ni reactions at 35*a* mev. *Phys. Rev. C*, 86:014610, Jul 2012. doi: 10.1103/PhysRevC.86.014610. URL https://link.aps.org/doi/10.1103/PhysRevC.86.014610.

[164] B. Davin, R. Alfaro, H. Xu, L. Beaulieu, Y. Larochelle, T. Lefort, R. Yanez, S. Hudan, A. L. Caraley, R. T. de Souza, T. X. Liu, X. D. Liu, W. G. Lynch, R. Shomin, W. P. Tan, M. B. Tsang, A. Vander Molen, A. Wagner, H. F. Xi, C. K. Gelbke, R. J. Charity, and L. G. Sobotka. Fragment production in noncentral collisions of intermediate-energy heavy ions. *Phys. Rev. C*, 65:064614, Jun 2002. doi: 10.1103/PhysRevC.65.064614. URL https://link.aps.org/doi/10.1103/PhysRevC.65.064614.

[165] A. B. McIntosh, S. Hudan, J. Black, D. Mercier, C. J. Metelko, R. Yanez, R. T. de Souza, A. Chbihi, M. Famiano, M. O. Frégeau, J. Gauthier, J. Moisan, R. Roy, S. Bianchin, C. Schwarz, and W. Trautmann. Short-lived binary splits of an excited projectile-like fragment induced by transient deformation. *Phys. Rev. C*, 81:034603, Mar 2010. doi: 10.1103/PhysRevC.81.034603. URL https://link.aps.org/doi/10.1103/PhysRevC.81.034603.

[166] B Davin, R.T de Souza, R Yanez, Y Larochelle, R Alfaro, H.S Xu, A Alexander, K Bastin, L Beaulieu, J Dorsett, G Fleener, L Gelovani, T Lefort, J Poehlman, R.J Charity, L.G Sobotka, J Elson, A Wagner, T.X Liu, X.D Liu, W.G Lynch, L Morris, R Shomin, W.P Tan, M.B Tsang, G Verde, and J Yurkon. Lassa: a large area silicon strip array for isotopic identification of charged particles. *Nuclear Instruments and Methods in Physics Research Section A: Accelerators, Spectrometers, Detectors and Associated Equipment*, 473(3):302 – 318, 2001. ISSN 0168-9002. doi: https://doi.org/10.1016/S0168-9002(01)00295-9. URL http://www.sciencedirect.com/science/article/pii/S0168900201002959.

[167] D.R. Tilley, C.M. Cheves, J.H. Kelley, S. Raman, and H.R. Weller. Energy levels of light nuclei, a = 20. *Nuclear Physics A*, 636(3):249 – 364, 1998. ISSN 0375-9474. doi: https://doi.org/10.1016/S0375-9474(98)00129-8. URL http://www.sciencedirect.com/science/article/pii/S0375947498001298.

[168] R. Han, Z. Chen, R. Wada, A. Ono, G. Tian, F. Shi, X. Zhang, B. Liu, and H. Sun. Effects of cluster correlations on fragment emission in $^{12}C + ^{12}C$ at 50 mev/nucleon. *Phys. Rev. C*, 102:064617, Dec 2020. doi: 10.1103/PhysRevC.102.064617. URL https://link.aps.org/doi/10.1103/PhysRevC.102.064617.